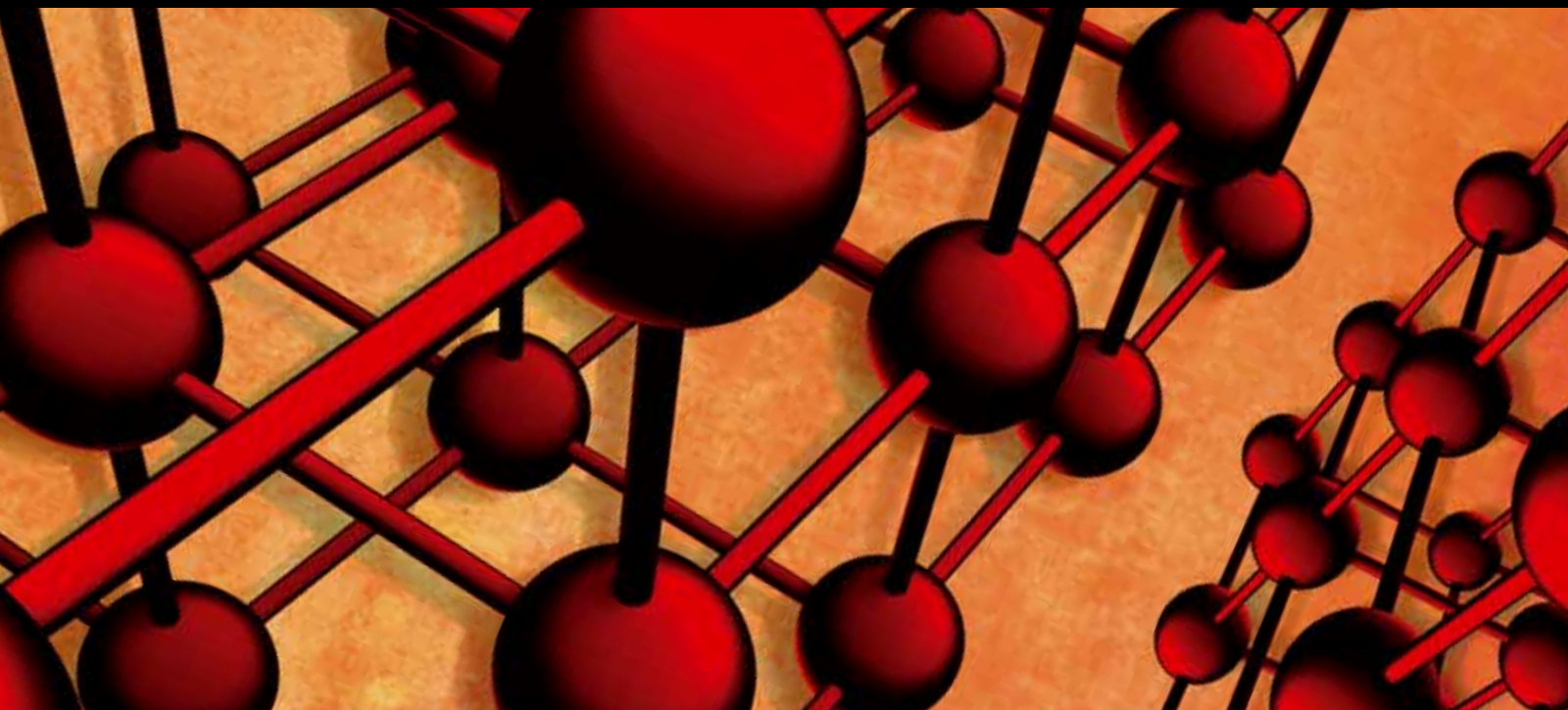


# Sustainable Composites

Guest Editors: Belal F. Yousif, Md Mainul Islam, and Mohd Sapuan Salit





---

# **Sustainable Composites**

Advances in Materials Science and Engineering

---

## **Sustainable Composites**

Guest Editors: Belal F. Yousif, Md Mainul Islam,  
and Mohd Sapuan Salit



---

Copyright © 2013 Hindawi Publishing Corporation. All rights reserved.

This is a special issue published in “Advances in Materials Science and Engineering.” All articles are open access articles distributed under the Creative Commons Attribution License, which permits unrestricted use, distribution, and reproduction in any medium, provided the original work is properly cited.

## Editorial Board

K. G. Anthymidis, Greece  
Robert S. Averbach, USA  
A. Bandyopadhyay, USA  
Z. Barber, UK  
Yucel Birol, Turkey  
Susmita Bose, USA  
Steve Bull, UK  
Peter Chang, Canada  
Daolun Chen, Canada  
M. U. Chhowalla, USA  
Martin Crimp, USA  
Jie Dai, Singapore  
C. K. Das, India  
J. Paulo Davim, Portugal  
Seshu B. Desu, USA  
Yong Ding, USA  
Chunying Duan, China  
Nadia El-Masry, USA  
John W. Gillespie, USA  
Hiroki Habazaki, Japan  
Richard Hennig, USA  
Dachamir Hotza, Brazil  
Chun-Hway Hsueh, Taiwan  
Rui Huang, USA  
Shyh-Chin Huang, Taiwan  
Wei Huang, China  
Jacques Huot, Canada  
William A. Jesser, USA  
Jaehwan Kim, Korea  
S. Komarneni, USA  
Prashant Kumta, USA  
Pavel Lejcek, Czech Republic

Markku Leskela, Finland  
Bin Li, China  
Hai Lin, China  
Yuanhua Lin, China  
Ying Liu, USA  
Gang Liu, China  
Yuan Liu, China  
Zhimin Liu, China  
Meilin Liu, Georgia  
Jun Liu, China  
Tao Liu, China  
Maria A. Loi, The Netherlands  
Hai Lu, China  
Peter Majewski, Australia  
Abdel S. H. Makhlof, Germany  
S. Miyazaki, Japan  
Paul Munroe, Australia  
Korukonda L. Murty, USA  
Ali Nazari, Iran  
Luigi Nicolais, Italy  
Tsutomu Ohzuku, Japan  
Xiaoqing Pan, USA  
G. Ramanath, USA  
Raju V. Ramanujan, Singapore  
Manijeh Razeghi, USA  
Mohd Sapuan Salit, Malaysia  
Chinnappa Sanjeeviraja, India  
Jainagesh A. Sekhar, USA  
Jiangbo Sha, China  
Liyuan Sheng, China  
You Song, China  
Aloysius Soon, Korea

Charles C. Sorrell, Australia  
Steven L. Suib, USA  
Sam-Shajing Sun, USA  
Wen-Hua Sun, China  
Weihua Tang, China  
Achim Trampert, Germany  
An-Pang Tsai, Japan  
Vladimir Tsukruk, USA  
Krystyn Van Vliet, USA  
Rui Vilar, Portugal  
Kunpeng Wang, China  
Min Wang, China  
Jrg M K Wiezorek, USA  
Wei Wu, USA  
Gongnan Xie, China  
Aiguo Xu, China  
Jenn-Ming Yang, Taiwan  
Jianqiao Ye, UK  
Yadong Yin, USA  
Guan-Jun Zhang, China  
Jian Zhang, Singapore  
Rui Zhang, China  
Tao Zhang, China  
Kai Zhang, China  
Ming-Xing Zhang, Australia  
Bin Zhang, China  
Jing Zhang, China  
Kai Zhang, China  
Yufeng Zhang, China  
Jun Zhang, China

# Contents

**Sustainable Composites**, Belal F. Yousif, Md Mainul Islam, and Mohd Sapuan Salit  
Volume 2013, Article ID 142718, 1 page

**Sustainable Use of Tepetate Composite in Earthen Structure**, T. López-Lara, Juan Bosco Hernandez-Zaragoza, Jaime Horta, Eduardo Rojas Gonzalez, Carlos Lopez-Cajun, and Gerson Ramirez  
Volume 2013, Article ID 806387, 6 pages

**A Review on Tribological Behaviour of Polymeric Composites and Future Reinforcements**, B. Aldousiri, A. Shalwan, and C. W. Chin  
Volume 2013, Article ID 645923, 8 pages

**Manufacture of Green-Composite Sandwich Structures with Basalt Fiber and Bioepoxy Resin**, J. P. Torres, R. Hoto, J. Andrés, and J. A. García-Manrique  
Volume 2013, Article ID 214506, 9 pages

**Materials Selection, Synthesis, and Dielectrical Properties of PVC Nanocomposites**, Youssef Mobarak, M. Bassyouni, and M. Almutawa  
Volume 2013, Article ID 149672, 6 pages

**Experimental and Theoretical Investigations of the Impact Localization of a Passive Smart Composite Plate Fabricated Using Piezoelectric Materials**, M. M. S. Dezfouli, Mohd Roshdi Hassan, Mohd Hafidz Ruslan, Sohif Mat, and B. Bakhtyar  
Volume 2013, Article ID 326713, 12 pages

**Biopolymer Doped with Titanium Dioxide Superhydrophobic Photocatalysis as Self-Clean Coating for Lightweight Composite**, Anika Zafiah M. Rus, S. R. Mohid, S. Nurulsaidatulasyida, and N. Marsi  
Volume 2013, Article ID 486253, 9 pages

**Mechanical Properties of Palm Fibre Reinforced Recycled HDPE**, B. Aldousiri, M. Alajmi, and A. Shalwan  
Volume 2013, Article ID 508179, 7 pages

**Reinforcement of Recycled Foamed Asphalt Using Short Polypropylene Fibers**, Yongjoo Kim and Tae-Soon Park  
Volume 2013, Article ID 903236, 9 pages

**Effects of Fiber Orientation and Material Isotropy on the Analytical Elastic Solution of a Stiffened Orthotropic Panel Subjected to a Combined Loading**, S. K. Deb Nath  
Volume 2013, Article ID 710143, 13 pages

**Behavior of Concrete Columns Repaired with Polymer Mortar and Epoxy Fiber Panel**, Sunghnam Hong and Sun-Kyu Park  
Volume 2013, Article ID 748294, 13 pages

## *Editorial*

# **Sustainable Composites**

**Belal F. Yousif,<sup>1</sup> Md Mainul Islam,<sup>1</sup> and Mohd Sapuan Salit<sup>2</sup>**

<sup>1</sup> Faculty of Health, Engineering and Sciences, University of Southern Queensland, Toowoomba, QLD 4350, Australia

<sup>2</sup> Department of Mechanical and Manufacturing Engineering, Universiti Putra Malaysia, UPM, 43400 Serdang, Selangor, Malaysia

Correspondence should be addressed to Belal F. Yousif; [belal.yousif@usq.edu.au](mailto:belal.yousif@usq.edu.au)

Received 10 September 2013; Accepted 10 September 2013

Copyright © 2013 Belal F. Yousif et al. This is an open access article distributed under the Creative Commons Attribution License, which permits unrestricted use, distribution, and reproduction in any medium, provided the original work is properly cited.

In the current era, the world is suffering from several environmental issues which have been raised by different academic, industrial, and environmental sectors. One of the main concerns is the large amount of nonsustainable productions and the way of their disposal. Due to this, the combination of the environmental regulation and industrial demands urges the researchers to develop alternative and sustainable materials. In the recent years, there have been new research areas that are being developed covering different types of sustainable materials for different mechanical, civil, electrical and even medical applications.

In this special issue, a number of articles related to the sustainable composite materials and their applications have been discussed. In particular, sustainable use of tepetate composite in earthen structure has been presented in an article. This article also includes the characterization of the mechanical and physicochemical properties of the sustainable tepetate composites. A detailed review on tribological behaviour of polymeric composites and their future reinforcements has been conducted in a separate article. The article reviews several factors which control the wear and frictional characteristics of such materials, that is, additives, fibres, interfacial adhesion, tribology environment, operating parameters, and composite geometry. Manufacturing of a green type of composite sandwich structures with basalt fiber and bioepoxy resin has also been articulated here, which includes some useful finite element analyses. In another article, materials selection process, synthesis, and dielectric properties of PVC nanocomposites have been discussed for electrical insulation application. The impact of localization of a passive smart composite plate fabricated using piezoelectric materials has been investigated experimentally and theoretically in a separate article. The development of a lightweight

composite based on Portland cement concrete with waste lightweight aggregate additive has also been carried out and discussed to improve the sustainability and environmental impact and to offer potential cost savings without sacrificing strength. In another paper, an attempt has been made to enhance the mechanical properties of recycled high-density polyethylene (HDPE) with chopped strand mat glass fibres as a synthetic reinforcement and with short oil palm fibres as a biodegradable reinforcement. A paper has presented the reinforcing effects of the inclusion of short polypropylene fibers on recycled foamed asphalt mixture. Effects of fiber orientation and material isotropy on the analytical elastic solution of a stiffened orthotropic panel subjected to a combined loading have been discussed in a separate article. Finally, an investigation on the behavior of concrete columns repaired with polymer mortar and epoxy fiber panel considering underground and underwater conditions has been presented in this special issue.

*Belal F. Yousif  
Md Mainul Islam  
Mohd Sapuan Salit*

## Research Article

# Sustainable Use of Tepetate Composite in Earthen Structure

**T. López-Lara, Juan Bosco Hernandez-Zaragoza, Jaime Horta, Eduardo Rojas Gonzalez, Carlos Lopez-Cajun, and Gerson Ramirez**

*Postgraduate Division, Faculty of Engineering, Autonomous University of Queretaro, Cerro de las Campanas S/N, Colonia Niños Héroes, 76010 Querétaro, QRO, Mexico*

Correspondence should be addressed to T. López-Lara; lolte@uaq.mx

Received 20 March 2013; Accepted 18 June 2013

Academic Editor: Mohd Sapuan Salit

Copyright © 2013 T. López-Lara et al. This is an open access article distributed under the Creative Commons Attribution License, which permits unrestricted use, distribution, and reproduction in any medium, provided the original work is properly cited.

One of the best indicators for construction sustainability is the use of earthy local materials which are completely recyclable and savers of energy during their life cycle. Tepetate is an underestimated earth-natural material, vast and economic, used only in a compacted form in backfills for layers of low resistance in pavements and platforms of buildings. This volcanic soil, named in different ways in several countries, is found in the central region of Mexico. Its resistance as compacted material is very low, of the order of 0.08 MPa. In this work, an improved sustainable-tepetate composite, using CaOH, is presented. This research includes the determination of mechanical properties as well as the physicochemical characterization of the sustainable-tepetate composite behavior. It can be concluded that the strength of the proposed composite increases significantly, immediately after treatment and with time. X-Ray Diffraction shows that all the mineralogical phases prevail in the natural tepetate and only a new phase appeared (calcite), which increases with time. This and the reaction of CaOH with clay content are very likely associated with the continuous strength increase of the composite.

## 1. Introduction

Construction based on earthy materials is the most important, since these are natural, sustainable, and plenty in any region of the world. Unfortunately, the applications of an earthy material, in general, depend on their mechanical properties in their pure natural form. This fact makes them of limited applications, which leads to be used only as fills in platforms. One example of this kind of materials is the *tepetate*. However, there is a potential of being used as a composite via the use of other economical and sustainable materials for constructions such as the CaOH. Indeed, CaOH is a material being used from ancient times. There are several antique constructions as bridges, castles, and aqueducts built with stones and CaOH as joining material. These constructions have lasted for centuries and they still can be seen nowadays. The previous shows their long useful life.

Moreover, CaOH has a wide field of applications, both, in industry (paper, paints, etc.) and construction (it decreases soils expansion and increases strength on pavements). It is also used as fertilizer, metallurgy, water treatment, glass manufacture, and so forth.

In this work, CaOH was used to improve the mechanical properties of natural *tepetate*. This is an economic and vast volcanic soil used in construction only as backfill material.

## 2. Background

The use of earth on site as a building material saves manufacturing cost, time, energy, environmental pollution, and transportation cost. Earth can also be used in the construction of low cost sustainable houses which is significantly cheaper than using conventional bricks. Selected soil (sand and clay) is mixed with water to the correct proportions and then placed in a hydraulic or hand operated compressing machine to produce compressed blocks, which, after curing, is used for building walls [1, 2].

Tepetates have been reported in several countries, mainly in Latin America. They have been denoted with different names such as silcrete in the USA; talpetate in Nicaragua; hardpan, duripan, and cangahua in Colombia and Ecuador; cancagua, moromoro, toasca, and ñadis in Chile; hardpan in Perú; and kora and masa in Japan [3].

Tepetate is a word derived from the Nahuatl *tepétlatl*, whose root *tel* means stone and *pétlatl*, petate. Literally it has been translated as “stone-petate,” “stone-like,” or “soft-rock.” For the aztecs, this word was included within their classification of materials of a type of soil for agriculture, hard to work [4]. However, when the Spaniards arrived to Mexico, the word tepetate was synonymous of agriculture-useless because of its low quality [5].

In Mexico there exists a great amount of materials denoted as tepetates. These occupy approximately 30% of the surface of the whole country [6, 7], either on the surface or in the first meter deep [8]. Tepetates are interstratified volcanic banks, including paleosoils of different nature characterized by horizontal boundaries and well defined between the layers. Tepetates of the Mexican central plateau have been described as massive, compacted and hard, natural formations, and cemented for several chemical agents, including clays and silicates [3]. Tepetates classification has been based on the type of cementing substance. When the cementing substance is mainly silica ( $\text{SiO}_2$ ), the tepetates are denoted “duripan”; when is calcium carbonate ( $\text{CaCO}_3$ ), the tepetates are denoted “petrocalcic” type; when is calcium sulfate ( $\text{CaSO}_4$ ), they are denoted “petrogypsic” type; when are salts, they are denoted “petrosalt” type; when is iron, they are denoted “petroferic” type and when is clay, they are denoted “fragipan” type. Tepetates are originated basically from volcanic materials that have been cemented or compacted, as consequence of three main processes: (1) consolidation of mineral particles provoking compaction; (2) nature of the pyroclastic materials consolidated at the instant of being deposited; (3) hardening by pedologic (sedimentary) processes which produce cementing substances in solution [6, 7].

Several works on Mexican tepetates have been reported in the literature. Most of them have been based in their physical and chemical characterization [9–11]. In most of those it reports is assessed that tepetate is a matrix composed of sand, lime, and small percentages of clays. However, once in a while they can exhibit high content of clays. This variability leads to a problem for work-rehabilitation of tepetates for each textural type generates an independent physical and mechanical behavior. Clearly, this fact requires a specific investigation. Some of their reports were based on micromorphological characteristics [12] which have a distribution related to gross and fine particles, simple porphyritic, and morphology of peds in subangular blocks suggesting a reorganization of the basal mass. There are also reports focused on the cementing substance identification, the use of soil, and its ecological significance [6, 7].

Some authors have made reference to the relief, climate, and pedologic origin of tepetates [13, 14]. As a matter of fact, it has been determined that the secondary hardening happens under template or semiarid conditions, this climate condition allows the liberation of compounds. The liberated compounds are lixiviated and deposited and then, they act as cementing substance (free silica, calcium carbonate) in the soil. These are particularly efficient if in the matrix of the horizon where they are deposited, are absorbed by clay. Tepetates are formed, preferably, in subhumid climates (annual precipitation less than 800 mm), characterized for a

dry season lasting from four to six months [14], where, in general, evapotranspiration is greater than the precipitation.

There are also a great amount of studies about its agrological properties (important for agronomy). Indeed, since the pre-Hispanic age there have been some attempts for using them in agriculture, by breaking them up and fertilizing them [15]. This is so because they have a very low content of organic matter, nitrogen, and phosphorous, which makes it difficult for using them in agricultural production [16]. Some studies have been on tepetate taxonomy; for example, [17] reported that in the lower level, known as generic, there were kinds of soils that can be located in the group of work soils as well as in the nonwork soils. This double inclusion is exemplified with the materials named as tepetates. About its classification and geological origin [6, 18], tepetates are originated from old deposits of volcanic ashes, deposited *in situ* or reworked, which were subjected to both processes, namely, diagenesis (hydroconsolidation) and pedogenesis that contributed to its compaction and/or cementation.

On the other hand, tepetates below soils produce lithological discontinuity that block the water infiltration and favor the lateral leakage, marking a surface where slides are prone. As well, tepetate could favor erosion and prevent aquifers reloading [19].

In 1996, while the III International Symposium of Hardened Volcanic Soils was celebrated at Quito, Ecuador, it was proposed to characterize tepetates as a hardened horizon, of volcanic origin, whose material is basically composed of pyroclastic materials, or fluids, or else as degraded volcanic soils.

Based on research done for several authors [9–11], it is possible to infer that, independently of its origin, tepetates always show common physical, mechanical, and chemical properties among them. Its compaction or cementation should be highlighted, which are reflected in high apparent densities ( $16.67\text{--}18.63 \text{ KN/m}^3$ ), low porosity (from 13% to 24%), and its hydraulic conductivities and holding low humidity. These characteristics limit significantly the fast incorporation of primary plants, and generate a constant soil erosion.

Llerena [20] and García [21] considered tepetates of the Mexican Valley as pumite fragments of the Terciary or Cenozoic in process of weathering. Valdés [22] mentioned that tepetates of the Mexico were formed due to the alluvial sediments that lately were consolidated. Rodríguez et al. [23] noticed that the results reported by the aforementioned author lack sufficient precision and left questions about the hardened layers, concluding that tepetates may have diverse origins.

Zebrowski [3] states two geological processes for explaining the horizons hardening, as follows.

(A) Simple consolidation-compaction or by the hydroconsolidation of volcanic materials transported by the water. In both cases, there always exists an increase of the apparent density material, a greater hardness, and consequently, a decrease of porosity.

(B) Hardening of volcanic materials at the instant of their deposit and posterior cooling (pyroclastic flows) is another.

These natural deposits, called tepetate in Mexico, have very low permeability and the overlying soil erodes rapidly when cultivated. Unconfined compression varied from 0.29 to 15.7 MPa, and the mean was 2.42 MPa. The strongest, most indurated tepetate appears to occur when disseminated carbonates combine with silica as cementing substances [24]. The reported properties are circumstantial and depend on the geological consolidation and type of cementing substance.

As construction material, the properties of tepetates show a wide range of values, thus making it less reliable as homogeneous material for construction. Adding, it has a very low strength as construction material [25]. The properties of Tepetate depend on the volcanic origin of this material, mainly through phreatomagmatic eruptions. As construction material, 80% of the tepetates are classified as silty sand according to the Unified System of Soil Classification with no plasticity [26].

About problematic soils used in embankments for sustainable pavements, there is a study for bituminous sand materials where their high bitumen content makes oil sand materials problematic for field operations [27]. Then, about expansive soils there is a study on their engineering properties as subgrade when stabilized by using different percentage of hydrated lime on thickness of pavement structural system. The results suggest that the highly strength, lowest swelling and small thickness of pavement were determined with an optimum percentage of lime content of 6% [28].

CaOH is a natural linking material in the preparation of mortars for construction. Indeed their usage goes back to ancient times. Developed countries specify for construction in seismic zones the compulsory use of CaOH in mortars because of their unique features of adherence and strength for sustaining diagonal tensions.

Up to the industrial revolution and the cement discovery in 1824 at Portland, UK, CaOH had been the main link for construction in mortars, stuccos, and paints. Due to the limited facility of transportation, constructors applied the local material but they knew a wide spectrum of tricks for correcting the effects of each of the found CaOH and producing the mortars with the required quality in each application case, such as the control of speed for solidification, hardness, and the degree of waterproofing [29].

Lime treatment in clay soils can be explained by two types of chemical reactions that occur when lime is added to a wet soil: short-term reactions known as soil improvement or modification consisting of cation exchange and flocculation and the long-term reaction known as stabilization/solidification: the pozzolanic activity. During the cation exchange, the highly alkaline environment produced by the addition of lime causes silica and alumina to be dissolved out of the structure of the clay minerals and to combine with the calcium to produce new cementitious compounds: calcium silicate hydrates, calcium aluminate hydrates, and calcium aluminosilicate hydrates. The calcium hydrosilicates contribute substantially to the strength of the stabilized soil material and are of varying composition. These reactions contribute to flocculation by bonding adjacent soil particles together and strengthen the soil with curing time [30, 31].

### 3. Experimental Methodology

**3.1. Soils Samplings.** Tepetate was taken from one of the large active banks of Queretaro, QRO, Mexico. It should be pointed out that this location was selected because tepetate was being used for backfills in residential areas and also as layers for base or subbase of pavements. The place is known as “Mompani,” having geographical coordinates: latitude  $20^{\circ}39'6.90''$ N, longitude  $100^{\circ}28'29.61''$ W, and a height of 1905 m above sea level. The CaOH used was of the commercial type.

**3.2. Procedure.** After extracting the material from “Mompani,” the index and mechanical properties were determined, following the procedure set by the American Society for Testing and Materials (ASTM):

- (i) gradation (size of aggregates) [32];
- (ii) liquid limit, plastic limit, and index limit (material plasticity) [33];
- (iii) classification by the Unified System for Soil Classification (it defines soil type) [34];
- (iv) proctor Standard Compaction (it determines the maximum dry density and optimum humidity of the material for obtaining the greater strength) [35];
- (v) unconfined compressive strength (material strength) [36].

Then, the physicochemical behavior of the sustainable-tepetate composite using CaOH was studied, by performing the tests listed as follows:

- (i) proctor Standard Compaction [35];
- (ii) unconfined compressive strength at different ages [36].

Finally the physicochemical characterization of natural tepetate and the sustainable-tepetate composite was done via X-Ray Diffraction.

### 4. Results

**4.1. Index and Mechanical Properties of the Natural Tepetate under Study.** Gradation was made by the dry mechanical method. It was determined using sieve analysis. With this method, the particles distribution can be quantified starting from the larger ones (75 microns, retained in sieve N°200) [32]. The results of soil gradation were graves (23.22%), sands (42.55%), and fines (34.23%).

The plasticity properties (Liquid Limit, LL, Plastic Limit, PL, and Plastic Index, PI) were determined for the bank of selected material [33]. The values obtained were LL = 32.45%, PL = 31.38%, and PI = 1.07%. The soil classification was obtained by the plasticity chart. From this, one had that the fines are limes of low plasticity (ML). Then, with the plasticity properties and the gradation (45.5% sands and 32.36% of fines) the soil can be classified as a silty sand (SM) [34]. Since tepetate is a material placed and compacted in the construction site, its ideal compaction was determined via

TABLE 1: Materials standard compaction.

Material	Maximum dry unit weight (KN/m <sup>3</sup> )	Optimum moisture (%)
Natural tepetate	12.67	28.5
Tepetate-CaOH 2%	12.47	27.5
Tepetate-CaOH 4%	12.55	28
Tepetate-CaOH 6%	12.73	27.8
Tepetate-CaOH 8%	12.94	26.5
Tepetate-CaOH 10%	12.79	27.5
Tepetate-CaOH 12%	12.81	28.5
Tepetate-CaOH 15%	13.09	26.5
Tepetate-CaOH 20%	13.19	25.5

Proctor Standard test [35]. The maximum specific dry weight was 12.67 KN/m<sup>3</sup> with an optimum humidity of 28.5%. The strength of natural tepetate was measured to 0 days and was 0.082 MPa [36].

#### 4.2. Properties of the Sustainable-Tepetate Composite

**4.2.1. Proctor Standard Compaction.** The Proctor Standard test [35] was made for the sustainable-tepetate composite with different percentages of CaOH (2%, 4%, 6%, 8%, 10%, 12%, 15%, and 20%, with respect to the soil dry weight). These are shown in Table 1. From that table, it can be seen that, in general with the increase of CaOH, the optimum humidity tends to decrease and its maximum specific-dry weight increases slowly. Moreover, it can be seen that the increment of CaOH disintegrates tepetate, easing and increasing the compaction. The optimum moisture of most of the composites is between 26–28.5%, and from 12.47 to 13.18 KN/m<sup>3</sup> of maximum dry unit weight.

**4.2.2. Unconfined Compression Strength of Sustainable-Tepetate Composite.** The Unconfined Compression Strength Standard test [36] was made for the sustainable-tepetate composite with different percentages of CaOH. Probes of sustainable-tepetate composites were compacted for different CaOH percentages. For this, their dry unit weight and optimum humidity, obtained by the Proctor standard, were applied. Probes were prepared for several periods of time, namely, for 0, 7, 14, 28, 42, 56, 70, 112, and 126 days, as shown in Table 2 and Figure 1. Tepetate strength test was made only to 0 days and the result was 0.08 MPa.

From Figure 1, it is apparent that the strength increases when the amount of CaOH in the composite also increases. The increase of strength with time is also noticeable, and the same happens with clays [37]. However, there is an optimum amount (10%) of CaOH leading to the maximum strength. As time goes on, the composite strength increases significantly, reaching to 2.94 MPa at 28 days and up to 4.21 MPa at 56 days, stabilization time. The increase of resistance of the tepetate is very likely for its clay content. The treatment of clay with lime increases its resistance with the time due to the formation of calcium silicate hydrates, calcium aluminate hydrates, and

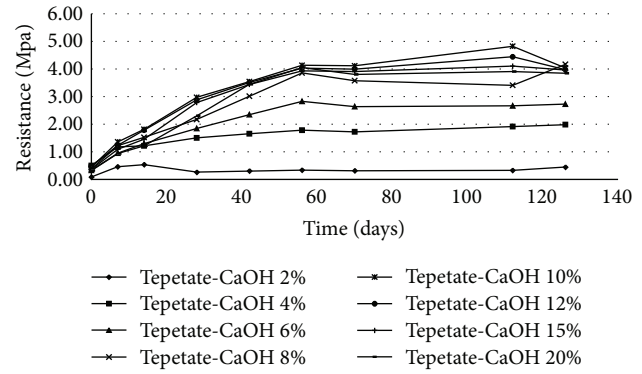


FIGURE 1: Strength time variation of the sustainable-tepetate composite.

calcium aluminosilicate hydrates. These reactions contribute to flocculation by bonding adjacent soil particles together and strengthen the soil with curing time.

**4.3. X-Ray Diffraction (XRD).** X-Ray Diffraction was done with a diffractometer Bruker D8-Advance at 30 KV and 30 mA. Samples of natural tepetate and the sustainable-tepetate composite at 15 and 30 days were analyzed for identifying minerals at the outset and those formed after some time.

**Natural Tepetate.** X-Ray Diffraction to natural tepetate was done. The study shows that several minerals as the halloysite, hematite, and quartz can be identified. The halloysite is a type of clay with plasticity much greater than the kaolinite. Hematite is a product of contact metamorphism and iron formations and is a common cementing substance in sedimentary rocks, frequently abundant in weathered iron minerals. This is an outcome of the goethite decomposition, which was found in the composite.

Quartz was another mineral found. Actually, this is the main component of sands [6] and was also identified at the tepetate XRD.

**Sustainable-Tepetate Composite at 15 Days.** The diffractogram of better sustainable-tepetate composite (10% CaOH) at 15 days shows that all the phases of the natural tepetate are present, among them, quartz, hematite, and halloysite (from white to light gray), but a new phase (calcite) appeared as result of the reaction of the CaOH with water.

The use of CaOH with expansive-clay soils, a treatment applied generally to inhibit volumetric instability, showed an increase of strength. Additionally, it is known that such a mixture generates calcite formation, which increases with time [37]. Therefore, it is very likely that the calcite is responsible of the strength composite.

The light gray and white colors of the tepetate seem to be originated by the absence of weathering of the original rock of gray and white colors, deposits of CaCO<sub>3</sub>, arising from salts or as result of iron removal, leaving great amount of minerals rich in SiO<sub>2</sub> as quartz, feldspar, and kaolinite [6, 7].

TABLE 2: Resistance of sustainable-tepetate composite in time.

Resistance material (MPa)	Time (days)								
	0	7	14	28	42	56	70	112	126
Tepetate-CaOH 2%	0.09	0.46	0.53	0.27	0.30	0.34	0.31	0.33	0.45
Tepetate-CaOH 4%	0.50	1.18	1.21	1.50	1.66	1.78	1.72	1.92	1.98
Tepetate-CaOH 6%	0.33	0.95	1.29	1.85	2.35	2.83	2.64	2.66	2.73
Tepetate-CaOH 8%	0.38	1.22	1.52	2.17	3.02	3.86	3.58	3.41	4.17
Tepetate-CaOH 10%	0.44	1.36	1.82	2.97	3.54	4.14	4.12	4.83	4.04
Tepetate-CaOH 12%	0.47	1.24	1.78	2.88	3.51	4.03	4.00	4.44	3.97
Tepetate-CaOH 15%	0.36	1.09	1.46	2.79	3.44	3.93	3.91	4.10	3.96
Tepetate-CaOH 20%	0.32	0.93	1.22	2.30	3.45	4.05	3.80	3.91	3.85

*Sustainable-Tepetate Composite at 30 Days.* The diffractogram of the sustainable-tepetate composite (10% CaOH) at 30 days shows that all the phases of the natural tepetate are present, but the calcite shows an increment with respect to 15 days, because the deflection or peak of the calcite grows in the diffractogram [37].

## 5. Conclusions

The strength of the natural tepetate was 0.08 MPa. It was constituted by graves (23.22%), sands (42.55%), and fines (34.23%).

The mechanical behavior of the sustainable-tepetate composite was improved with a maximum 10% of CaOH. Indeed with this percentage of CaOH, the maximum strength was obtained. After this percentage the strength showed no improvement. Additionally, a significant increase of strength was recorded as time went on. In fact, at 28 days the strength was 2.94 MPa whereas at 56 days, time for stabilization, the strength was 4.21 MPa. Thus, it is apparent that the inclusion of CaOH produced an optimum strength of the tepetate, by improving their mechanical properties in structures of compacted soils. This methodology creates a new sustainable composite using tepetate.

From the X-Ray Diffraction it was inferred that the natural tepetate was constituted mainly by halloysite, quartz, and hematite. These correspond to the gradation of soil with a better definition (weathered sands and halloysite clay). Since there was presence of iron minerals (hematite) and clay (halloysite), the tepetate could be classified as of the petroferic type with some halloysite clay. In the sustainable-tepetate composite with CaOH, all the phases of natural tepetate appeared. However, a new phase formed (calcite), which increased with time, could be associated very likely with the increase of strength of the composite with time. At the same time, the reactions of CaOH with clay content contribute to flocculation by bonding adjacent soil particles together and strengthen the soil with curing time.

The sustainable-composite tepetate offers an alternative construction material because of local construction material, being lasting, resistant, and economical, of low consumption energy in its preparation. Moreover, it is one hundred percent recyclable and thus can be used for reinforced platforms or for block elements.

## References

- [1] M. S. Zami and A. Lee, "Using earth as a building material for sustainable low cost housing in Zimbabwe," *The Built & Human Environment Review*, vol. 1, pp. 40–55, 2008.
- [2] R. Sangeeta and C. Swaptik, "Earth as an energy efficient and sustainable building material," *International Journal of Chemical, Environmental & Biological Sciences*, vol. 1, no. 2, pp. 257–261, 2013.
- [3] C. Zebrowski, "Los suelos volcánicos endurecidos de América Latina," *Terra Latinoamérica*, vol. 10, pp. 15–23, 1992.
- [4] Ch. Gibson, *Los Aztecas Bajo El Dominio Español, 1519–1810*, Siglo XXI, Coyoacán, México, 13 edition, 1996.
- [5] C. A. Ortiz-Solorio, *Los levantamientos etnoedafológicos [Ph.D. thesis]*, Colegio de Postgraduados, Instituto de Recursos Naturales, Montecillo, México, 1999.
- [6] D. Flores-Román, A. González-Velázquez, J. R. Alcalá-Martínez, and J. E. Gama-Castro, "Los tepetates," *Revista De Geografía*, vol. 3, no. 4, pp. 37–42, 1991.
- [7] D. Flores-Román, A. González-Velázquez, J. R. Alcalá-Martínez, and J. E. Gama-Castro, "Duripans in the subtropical and temperate subhumid climate of the Trans-Mexico Volcanic Belt," *Revista Mexicana De Ciencias Geológicas*, vol. 13, no. 2, pp. 228–239, 1996.
- [8] E. G. Guerrero, M. J. L. Luna, and O. E. Caballero, "Distribución de los tepetates de la República Mexicana escala 1:4 000 000," *Terra*, vol. 10, pp. 131–136, 1992.
- [9] G. Miehlich, "Formation and properties of tepetate in the central highlands of Mexico," *Terra*, vol. 10, pp. 137–144, 1992.
- [10] H. D. Peña, M. E. Miranda, C. Zebrowski, and M. H. Arias, "Resistencia de los tepetates de la vertiente occidental de la Sierra Nevada," *Terra*, vol. 10, pp. 164–177, 1992.
- [11] D. J. Etchevers, M. Rosa, López-Claude, C. Zebrowski, and D. Peña, "Características químicas de tepetates de referencia de los estados de México y Tlaxcala, México," *Terra*, vol. 10, pp. 171–182, 1992.
- [12] R. Hessmann, "Micromorphological investigations on "tepetate" formation in the "toba" sediments of the state of Tlaxcala (México)," in *Suelos Volcánicos Endurecidos*, vol. 10 of *Terra*, pp. 145–150, 1992.
- [13] A. Geissert, "Los tepetates de Xalapa, Veracruz México: relación con el relieve modelado actual y esquema cronológico," *Terra*, vol. 10, pp. 221–225, 1992.
- [14] D. Dubroeuq, P. Quantin, and C. Zebrowski, "Los tepetates de origen volcánico en Mexico. Esquema Preliminar de clasificación," *Terra*, vol. 7, pp. 1–13, 1989.

- [15] S. Rodríguez-Tapia, C. A. Ortiz-Solorio, C. Hidalgo-Moreno, and M. C. Gutiérrez-Castorena, "Los tepetates de la ladera oeste del cerro Tlálloc: saprolita, sin endurecimiento pedológico," *Terra Latinoamérica*, vol. 22, no. 1, pp. 11–21, 2004.
- [16] J. D. Álvarez-Solís, R. Terrera-Cerrato, and J. D. Etchevers-Barra, "Actividad microbiana en tepetate con incorporación de residuos orgánicos," *Agrociencia*, vol. 34, no. 5, pp. 523–532, 2000.
- [17] B. J. Williams and C. A. Ortiz-Solorio, "Middle American folk soil taxonomy," *Annals, Association of American Geographers*, vol. 71, no. 3, pp. 335–358, 1981.
- [18] T. J. Nimlos and C. Ortiz-Solorio, "Tepetate: the rock mat," *Journal of Soil & Water Conservation*, vol. 42, no. 2, pp. 83–86, 1987.
- [19] J. E. Gama-Castro, E. McClung de Tapia, E. Solleiro-Rebolledo et al., "Incorporation of ethnopedological knowledge in the study of soils in the Teotihuacan Valley, Mexico," *Eurasian Soil Science*, vol. 38, no. 1, pp. S95–S98, 2005.
- [20] L. D. Llerena, *El distrito de conservación del suelo y agua de Chapingo, México [Ph.D. thesis]*, Escuela Nacional de Agricultura, Chapingo, México, 1947.
- [21] E. A. García, *Estudio de los suelos tepetatosos y las posibilidades de recuperación agrícola [Ph.D. thesis]*, Escuela Nacional de Agricultura, Chapingo, México, 1961.
- [22] L. A. Valdés, *Características morfológicas y mineralógicas de los suelos de tepetate de la Cuenca de México [M.S. thesis]*, Colegio de Postgraduados, Escuela Nacional de Agricultura, Chapingo, México, 1970.
- [23] S. Rodríguez, M. C. Gutiérrez-Castorena, C. Hidalgo, and C. A. Ortiz-Solorio, "CIntemperismo en Tepetates y en cenizas volcánicas y su influencia en la formación de Andisoles," *Terra*, vol. 17, pp. 97–108, 1999.
- [24] T. J. Nimlos, "The density and strength of Mexican tepetate (duric materials)," *Soil Science*, vol. 147, no. 1, pp. 23–27, 1989.
- [25] T. López-Lara, J. B. Hernández-Zaragoza, J. Horta-Rangel, E. Rojas, C. López-Cajún, and D. Rosales-Hurtado, "Tepetate as construction material," *Journal of Materials in Civil Engineering*, 2012.
- [26] T. López-Lara, J. B. Hernández-Zaragoza, J. Horta-Rangel, E. Rojas, and D. Rosales-Hurtado, "Geocharacterisation of "Tepetates,"" *European Journal of Environmental and Civil Engineering*, 2013.
- [27] J. Anochie-Boateng, E. Tutumluer, and S. H. Carpenter, "Case study: dynamic modulus characterization of naturally occurring bituminous sands for sustainable pavement applications," *International Journal of Pavement Research and Technology*, vol. 3, no. 6, pp. 286–294, 2010.
- [28] A. A. M. Adam, I. A. Ibrahim, A. J. Alhardllo, A. M. Hadi, and M. Y. Ibrahim, "Effect of hydrated lime on behavior of expansive soil as subgrade of flexible pavement structural system," in *Sustainable Construction Materials*, S. Wu, L. Mo, B. Huang, and B. F. Bowers, Eds., pp. 64–76, American Society of Civil Engineers, 2012.
- [29] O. F. Arredondo, *Estudio De Materiales: VI. Cerámica Y Vidrio*, Instituto Eduardo Torroja de la Construcción y el Cemento, Madrid, Spain, 9nd edition, 1980.
- [30] J. A. Lasledj and M. Al-Mukhtar, "Effect of hydrated lime on the engineering behavior and the microstructure of highly expansive clay," in *Proceedings of the 12th International conference of International Association for Computer Methods and Advances in Geomechanics*, pp. 3590–3598, Goa, India, 2008.
- [31] J. Ninov, I. Donchev, A. Lenchev, and I. Grancharov, "Chemical stabilization of sandy-silty illite clay," *Journal of the University of Chemical Technology and Metallurgy*, vol. 42, no. 1, pp. 67–72, 2007.
- [32] Standard Test Method for Particle-Size Analysis of Soils, ASTM D422-63, *Annual Book of ASTM Standards*, 2007.
- [33] Standard Test Methods for Liquid Limit, Plastic Limit and Plasticity Index of soils, ASTM D4318-10, *Annual Book of ASTM Standards*, 2010.
- [34] Standard Test Method for Classification of Soils for Engineering Purposes, ASTM D 2487-93, *Annual Book of ASTM Standards*, 1993.
- [35] Standard Test Methods for Laboratory Compaction Characteristics of Soil Using Standard Effort (12400ft-lbf/ft<sup>3</sup>(600kN-m/m<sup>3</sup>)), ASTM D698-00a, *Annual Book of ASTM Standards*, 2000.
- [36] Standard Test Method for Unconfined Compressive Strength of Cohesive Soil, ASTM D2166-00, *Annual Book of ASTM Standards*, 2000.
- [37] T. López-Lara, J. Horta-Rangel, J. B. Hernández-Zaragoza, and V. M. Castaño, "Properties of waste soil-hydrated lime composite," *Mechanics of Time-Dependent Materials*, vol. 10, no. 2, pp. 155–163, 2006.

## Review Article

# A Review on Tribological Behaviour of Polymeric Composites and Future Reinforcements

B. Aldousiri,<sup>1</sup> A. Shalwan,<sup>2,3</sup> and C. W. Chin<sup>4</sup>

<sup>1</sup> Department of Power & Desalination Plants, Ministry of Electricity, Kuwait, Kuwait

<sup>2</sup> Mechanical Production Engineering Department, College of Technological Studies, PAAET, Kuwait, Kuwait

<sup>3</sup> Centre of Excellence in Engineered Fiber Composites (CEEFC), Faculty of Engineering and Surveying, University Southern Queensland, Toowoomba, QLD 4350, Australia

<sup>4</sup> Faculty of Engineering and Technology, Multimedia University, Melaka, Malaysia

Correspondence should be addressed to A. Shalwan; [abdullah.alajmi@usq.edu.au](mailto:abdullah.alajmi@usq.edu.au)

Received 28 May 2013; Accepted 2 June 2013

Academic Editor: Belal F. Yousif

Copyright © 2013 B. Aldousiri et al. This is an open access article distributed under the Creative Commons Attribution License, which permits unrestricted use, distribution, and reproduction in any medium, provided the original work is properly cited.

Many different families of polymers are used in industries and engineering applications. The demands for studying the tribological behaviour of polymers and their composites are recently increased. This article briefs the most recent studies on the tribological behaviour of polymeric materials based on synthetic fibres. It reviews several factors which control the wear and frictional characteristics of such materials, that is, additives, fibres, interfacial adhesion, tribology environment, operating parameters, and composite geometry. In addition to that, new bioreinforcement (fibre) is introduced associated with preliminary results. The results showed that there is high potential of replacing the conventional reinforcement with the bioones.

## 1. Introduction

The simplest definition of a polymer is something made of many units since the basic unit is made of carbon, hydrogen, oxygen, and/or silicon. Polymers have been with us since the beginning of time such things as tar and shellac. They are processed with heat and pressure into useful articles like gears, bearings, bushes, and current engineering applications. All polymers materials are used in nearly every industry; natural and synthetic polymers can be produced with a wide range of stiffness, strength, heat resistance, crystallinity, density, and even price [1–4]. The volume of polymer consumed each year is already greater than that of steel [5]. According to ASTM D883 80c, polymers are divided into two groups with regard to their chemical and technological behaviour [1, 5]: thermosetting and thermoplastic. Figure 1 describes the polymer classifications and the possible reinforcements.

## 2. Thermoplastic

It becomes soft under heating condition and hard under cooling regardless of how many times the process is repeated

by heating and cooling conditions, thermoplastics can be rubber-like liquid, and in hard state it is glassy or partially crystalline. The properties of the thermoplastic polymers can be changed by changing length of individual chain, changing the form of the individual chains [1]. There are several major classics of thermoplastic material [6].

*2.1. Polyethylene (PE).* There are two types of PE, which are high-density polyethylene (HDPE) and low-density polyethylene (LDPE). LDPE is flexible and tough; HDPE is much stronger and stiffer than LDPE. It is used for sheeting, bags “squeeze” bottles, ballpoint pen tubing, and wires and cable insulation. HDPE is mainly used for piping, toys, household ware, and it is used as ultrathin film for the wrapping, in supermarkets and as the carrier bags.

UHMWPE (ultrahigh molecular weight polyethylene) is commonly used as an insert for one of the load bearing, articulating surfaces in orthopedic implants, such as the acetabular cup in the hip or tibial tray insert in the knee. This particular type of polyethylene is used because it has excellent biocompatibility and has a lower wear rate and coefficient

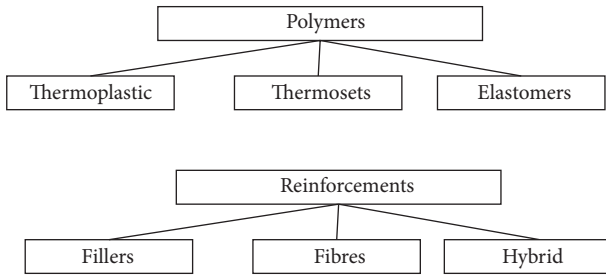


FIGURE 1: Classification and reinforcements of polymers.

of friction than other polymers. UHMWPE composites have a wide use in products. UHMWPE has been used in total joint replacement for the last three decades. Despite the recent advancements in prosthesis design, the wear of UHMWPE remains a serious problem [7]; controlling the quality of the polyethylene is essential to improve its wear resistance [7]. Some of studies have found that the tribological behaviour of the pure UHMWPE is lower than UHMWPE with composites [5–8]. UHMWPE and polypropylene (PP) were blended for enhancing the tribology behaviour of UHMWPE. By using sliding wear tests against steel ring, it is shown that antiwear properties of UHMWPE were improved notably by blending with appropriated content of polypropylene (PP) [8]. The coefficients of friction and wear rate of UHMWPE/PP blend were much lower than those of pure UHMWPE during sliding [8]. Kaolin and UHMWPE-based composite were prepared by means of polymerization filling and melt mixing, respectively. The study found that the kaolin filling greatly improves the tribology behaviour of UHMWPE. It is also found that the composites of UHMWPE with kaolin prepared by polymerization have much better tribological behaviour than the ones prepared by mixing with the same components and are promising self-lubricated material candidates for engineering application [9]. UHMWPE is induced by ion implantation aiming to increase the wear resistance of UHMWPE [10]. As a result, wear resistance of UHMWPE increases of about 76% after the ion implantation [10].

**2.2. Polypropylene (PP).** It is mainly used in its crystalline form for crates, containers, fans, car fascia panels, cabinets for radios and TV sets, toys, and chair shells.

Tribology behaviour of PP has been conducted in many researches [4–8]. Recently, it is found that the wear behaviour of PP is affected by the drawing ratio. The wear loss values dramatically increase with an increase in draw ratio when PP pin slides are normal to the drawing direction. These values of wear loss decrease to about 50% when the pin slides are parallel to the drawing direction. The use of grease lubricant reduces the wear loss to 10% of that achieved for dry motion [11]. Some developments have been carried out to increase the resistance of the PP against wear; mineral fillers are added to the PP for that purpose. The addition of mineral fillers to the polypropylene matrix decreases the wear resistance under severe abrasive conditions. Under mild abrasive conditions

the shape and size of the reinforcing filler influence the wear performance [12].

**2.3. Polyvinyl Chloride (PVC).** PVC is a linear-chain polymer with bulky chlorine side group; a range of plastics could be created with different additives to the PVC. It is a hard and rigid material, but the addition of the plasticiser can give it a flexible form. PVC is extruded to give sheet, film pipe, cable covering, and so forth. The rigid form (unplasticised) of PVC is used for piping for waste and soil drainage systems, rainwater pipes, and so forth. In addition, a copolymer is made by mixing PVC and vinyl acetate in a mass ratio of about 85% to 15% to give a rigid material, while a ration of 95% to 5% to give a flexible material. The rigid form of the copolymer is used for casing and covers, while flexible form of the copolymer is calendered to produce floor tiles. PVC is now the second most commonly used plastic material in terms of volume. Great achievements have been made in modifying its structure, behavior, and properties by including miscellaneous additives. Aspects of mechanical, thermal, and electrical properties of PVC composites were intensively studied in some researches [11, 12]. Wear of pure PVC has been tested [13] it shows that the additives (fillers) have different effects on the wear resistance of PVC composites according to the properties of the additives and the amount added. SiC and  $Al_2O_3$  as fillers improved the wear resistance of PVC significantly. Si and wollastonite also enhanced the wear resistance. Fly ash and  $B_4C$  reduced wear of PVC only when over 10% of fly ash or 7% of  $B_4C$  is added. Surprisingly, PVC filled with  $CaCO_3$  or  $SiO_2$ , the most commonly used fillers in industrial PVC materials, gave rise to a very low wear resistance [13]. PVC is in the flooring materials since the wear behaviour of flooring materials such as rubber, PVC (polyvinyl chloride), and cork was studied in detail [14].

**2.4. Ethylene-Vinyl Acetate Copolymer (EVA).** EVA copolymers are flexible, resilient, tough with good resistance to atmospheric degradation. The properties of EVA depend on the presence of the constituents since increasing vinyl acetate makes the copolymer more flexible. EVA is used for road-marker cones, ice-cube trays, medical and surgical ware, and as a major constituent in hot-melt adhesives.

**2.5. Polystyrene (PS).** PS has a lot of forms, generally; PS is brittle and transparent with a smooth surface finish material; toughened or high-impact PS is a blend of PS with rubber particles. It is used to make cups, vending machines, and casing. Expanded PS is a foamed polymer; it is a rigid form which is used for insulation and packaging. PS can be dissolved in petrol, dry cleaning agents, greases, oxidizing acids, and some oils. Exposure to detergents can cause stress cracking.

**2.6. Acrylnitrite Butadiene Styrene Terpolymer (ABS).** ABS is made by a combination of styrene-acrylonitrile copolymer (SAN), which is brittle in nature with polybutadiene; it makes ABS tougher. Upon the combination polybutadiene produces two forms: a graft terpolymer and a small rubber spheres

dispersed in the terpolymer and SAN matrix. ABS is an amorphous material. It is tough, stiff, and abrasion resistant; it is widely used as the casing boat shells and food containers.

**2.7. Polycarbonate (PC).** PC is below its glass transition at room temperature and so it is amorphous. PC is tough, stiff, strong, and transparent and retains properties well with increasing temperature. It has reasonable outdoor weathering resistance. Due to its tough properties, it is used where resistance to impact abuse and high temperatures encountered.

The static and kinetic contact of a PC against steel ball is experimentally examined to study its friction and wear behavior [15]. It is known that the wear takes place during the initial period; the steady stage is reached after sliding for 8 min, corresponding to the results of friction coefficient; and the wear volume shows a little increase due to the abrasion of the wear debris [15]. The utilization of block polycarbonate containing siloxane segments is well known to be of great interest for surface modifications [16]. The friction coefficient is strongly dependent not only on the surface enrichment of siloxane but also on the molecular weight of siloxane block segment. The initial friction coefficient has a little influence on the overall wear resistance due to the rapid wear process of the uppermost surface [16]. The reinforced polycarbonate resin Lexan 341R-739, containing 40% of weight of short glass fibres, is well known for their abrasive character [17].

**2.8. Acrylics.** Acrylics are mainly based on polymethyl methacrylate (PMMA), which has amorphous structure. They have stiff, strong material with outstanding weather resistance. Due to their transparency and weather resistance, they were used for light fittings, canopies, and lenses for car lights, signs, and nameplates. Opaque acrylic sheet is used for domestic baths, shower cabinets, basins, and lavatory cisterns.

**2.9. Polyamides (Nylons or PA).** PA is known as nylons, which has crystalline structure. There are a number of common PAs like nylon 6, nylon 6.6, nylon 6.10, and nylon 6.11. The two mostly used were nylon 6 and nylon 6.6 since nylon 6.10 has a higher melting point than the former and is also stronger and stiffer, and nylon 11 has a lower melting point and is more flexible. Nylons in general are strong, tough, and with high melting points. Glass spheres or fibers were added to give improved strength and stiffness. Molybdenum disulphide is an additive to nylon 6 to make it obtain low frictional properties. Nylons were used for the manufacture of fibers for clothing, gears, bearings, bushes, housings for domestic and power tools, electric plugs, and sockets.

PAs form a major class of tribopolymers used in almost all types of wear situations [18]. Abrasive wear studies on several types of PAs have been studied in a single pass condition by abrading a polymer pin against a waterproof silicon carbide (SiC) abrasive paper under various loads [18].  $\text{CH}_2/\text{CONH}$  ratio has a significant influence on various mechanical properties of elongation to break, fracture toughness, and fracture energy and, therefore, on the abrasive wear performance;  $\text{CH}_2/\text{CONH}$  ratio and various mechanical properties do

not show linear relation in most of the cases, while the specific wear rate as a function of some mechanical properties showed good correlation [18]. Currently, PA 11 and its three composites containing short glass fibres (GF) and metallic powdery fillers such as bronze and copper were investigated; GF reinforcement greatly improved the friction and wear performance of PA 11. Incorporation of bronze and copper powders in GF-reinforced composite further improves the friction and wears behaviour of PA 11. Copper proved to be beneficial filler than the bronze in this context [19]. The fundamental mechanisms of abrasion of 40 m diameter polyamide fibres have been reported [20] which shows that the abrasive process is responsible for a continuous diminution of the fibre cross-section until the creep failure stress is achieved locally [20]. The gear of a carbon fiber (CF) reinforced polyamide 12 (PA12) has been investigated in comparison with those of CF-reinforced polyamides such as polyamide 6 (PA6), polyamide 66 (PA66), and polyamide 46 (PA46). PA 12/CF gear has an excellent wear property under the condition that grease exists at the engagement region. PA12/CF gear indicated the highest load capability, excellent noiseless property, and the lowest water absorption among all polyamides investigated [21].

**2.9.1. Polyesters.** Polyesters have both thermoset and thermoplastic forms. The main thermoplastic form is polyethylene terephthalate (PET). It has similar properties to nylon; it is widely used in fiber form for the production of clothes. In industry, applications of glass-fibre-reinforced composite were increasing and plain polyester resin [22]. The wear behaviour of a glass-fibre-reinforced composite and plain polyester resin were experimentally investigated under several conditions and different parameters [22]. Short E-glass fibre-reinforced polyester composites with and without filler also were studied for the low stress abrasive wear behaviour in two and three body abrasions [23]. The abrasive wear of the composite depends on the entire test parameters like applied load, sliding speeds and abrasive particle size [22, 23]. The size of the abrasive particle and applied load tends to increase abrasive wear volume of the composites, whereas wear rate tends to decrease with increasing sliding velocity at constant applied load and particles of size ranging 200–300  $\mu\text{m}$ . Secondly, higher weight fraction of glass fibres in the composite improves the abrasive wear resistance because high energy is required to facilitate failure in glass fibres [23]. Polyester is used in making composite material, which is used for bearing applications [24]. Unidirectional reinforcements by linen and jute fibres were used, each in turn, in unsaturated polyester resin; the experimental results show the reinforcement volume fraction as well as orientation has considerable effect on the friction and wear of polyester composites [24]. An increase of fibre volume fraction to 33% increased the coefficient of friction of the tested material by about 14% and decreased its wear rate by about 95% at both low and high values of pressure velocity product (PV limit) when the fibres were oriented normal to the specimen surface [24]. The same increase in volume fraction of the fibres when oriented in the longitudinal and transverse directions

resulted in almost the same increase in the coefficient of friction (16%) while the wear rate decreased only by 65% at low PV value. For the same orientations at high PV value, the results showed no significant effect on the coefficient of friction while the wear rate decreased by 72% [24]. The proportion by weight of fiberglass used for the reinforcement of the polymer was conducted from 0 to 50% to investigate the tribology behaviour [25].

**2.9.2. Polyphenylene Oxide (PPO).** It is strong, rigid and has good dimensional stability. It can be mixed with polystyrene, which could be used for electrical fittings, dishwasher, and car fascia panels.

The influence of speed on the friction and wear of polyphenylene oxide (PPO) are determined and compared with polyetheretherketone (PEEK) and polytetrafluoroethylene (PTFE) in two sliding configurations under both dry and lubricated conditions [26]. With a line-contact geometry, the effects of debris aggregation on wear play a more important role than with a distributed contact. In lubricated conditions, with PPO in line-contact conditions, there is a "dwell period" in which lubrication persists following the removal of excess fluid from the contact, and this is shown to result from the formation of an aggregated layer of plasticized wear debris on the polymer surface [26].

The techniques of ion implantation were employed for improving surface hardness and wear resistance of polyphenylene oxide (PPO) [27]. The samples of PPO were implanted separately with Al, Ti, and Fe ions to three doses of  $2 \times 10^{15}$ ,  $1 \times 10^{16}$ , and  $1 \times 10^{17}$  ions/cm<sup>2</sup>. The result shows that wear resistance of PPO is improved significantly and friction coefficient is reduced. The  $1 \times 10^{16}$  ions/cm<sup>2</sup> Ti ion implantation produces the largest improvement in tribological properties, and wear resistance of  $1 \times 10^{16}$  ions/cm<sup>2</sup> Ti-implanted PPO improved over 270 times and friction coefficient is reduced by 40%. Nanohardness increased from 0.369 GPa for the plain PPO to 1.433 GPa for  $1 \times 10^{16}$  ions/cm<sup>2</sup> Ti-implanted PPO. TRIM96 (transport of ions in matter, version 1996) calculation revealed that ionization energy loss and energy loss difference between ionization and vacancies of Ti were more than those of Al and Fe beneath 50 nm ion implantation range, which were related to the largest improvement of surface properties for Ti ion implantation. IR spectra of  $1 \times 10^{16}$  ions/cm<sup>2</sup> Ti-implanted PPO indicated that the surface of samples is moisture-retentive and formed the carbonyl group [27].

The wear behaviour of a high temperature, composite plastic bearing material (polyphenylene sulphide, PTFE, lead oxide, and graphite in the ratio 55 : 25 : 10 : 10) were studied in journal bearing configuration against steel. The composition of the rubbing surfaces is studied using electron probe microanalysis (EPMA), and the physical properties of the composition at operating temperature were determined from shear modulus measurements. The results reveal a high lead content of is due to that rubbing involves the lamellar shearing of a lead oxide and possibly also a graphite layer which is aided by a relatively soft matrix containing PTFE [28].

**2.10. Polyacetals or Polyoxymethylene (POM).** One of the main forms is polyoxymethylene (POM), which is referred to sometimes as acetal homopolymer. In general polyacetals are strong, stiff, and have good impact resistance, low coefficients of friction and good abrasion resistance. Glass-filled acetal is used when higher stiffness is required.

Polyacetals are typical of thermoplastic polymers for sliding applications because of their frictional and wear characteristics [29]. Their wear mechanisms in composite and homogeneous form were investigated experimentally [29]. Subsurface deformation is found in all polyacetals tested. Crack nucleation at the matrix/glass fibre interfaces, crack propagation parallel to the surface, and cracks shearing to the surface were found in the composites. The results were consistent with previous results on nylons. Little is known about the first stages of this material transfer. Therefore, measurements was performed with polymers sliding onto steel were slightly investigated [30].

**2.10.1. PTFE.** Polytetrafluoroethylene (PTFE) is a linear polymer with high crystallinity. It is quite an expensive material. PTFE is tough and flexible and can be used over a wide range of temperatures, 250°C down to almost zero, and still retains its nature of being not attacked by any reagent or solvent. It is usually used where its special properties of low coefficient of friction is needed.

The tribological behavior of polytetrafluoroethylene (PTFE) and PTFE composites with filler materials such as carbon, graphite, E glass fibers, MoS<sub>2</sub>, and poly-p-phenylene terephthalamide (PPDT) fibers is studied [31]. The present filler additions found to increase hardness and wear resistance in all composites studied [31]. The highest wear resistance is found for composites containing (i) 18% carbon + 7% graphite, (ii) 20% glass fibers + 5% MoS<sub>2</sub>, and (iii) 10% PPDT fibers. Wear testing and SEM analysis show that three-body abrasion is probably the dominant mode of failure for PTFE + 18% carbon + 7% graphite composite, while fiber pull out and fragmentation caused failure of PTFE + 20% glass fiber + 5% MoS<sub>2</sub> composite. The composite with 10% PPDT fibers caused wear reduction due to the ability of the fibers to remain embedded in the matrix and preferentially support the load [31]. The results indicated that composites with higher heat absorption capacity exhibited improved wear resistance [31].

Adding glass fibres, the surface characteristics become better at least till 30%, but concentration of 30–40% produces wear as high as the polymer under the same testing conditions [32]. The friction and wear behavior of high performance polyimide (PI) and its composites reinforced with short cut carbon fiber and solid lubricants such as graphite, MoS<sub>2</sub>, and polytetrafluoroethylene (PTFE) are evaluated [33]. In order to gain greater insight into the relation between the wear rate, counterface surface topography, and the characteristics of the transfer layer formed of PTFE, a series of wear experiments were performed with a commercial POM – 20% PTFE composite sliding against hardened tool steel counterface [34]. The steady-state wear rate of the polymer is found to be influenced by both the surface topography of the steel

counterface and by the characteristics of the transfer layer formed after running in [34].

**2.11. Cellulosics.** The most common cellulosic materials are cellulose acetate (CA), cellulose acetate butyrate (CAB), and cellulose acetate propionate (CAP). CA is hard, stiff, and tough but has poor-dimensional stability due to its high absorption of water. CAB is tougher and more resistant to water uptake and hence more dimensionally stable. CAP is slightly harder, stiffer, and stronger. CA is widely used for spectacle frames, tool handles, keyboard keys, and toys. CAB is used for internally illuminated roadside signs, extruded piping, pens, and containers. CAP is used for toothbrush handles, pens, knobs, steering wheels, toys, and film for blister packing.

**2.12. Possible Tribological Behaviour of Thermoplastic and Fibre Thermoplastic Composites.** Summary of the tribological behaviour thermoplastic materials can be summarized and explained with the aid of Figure 2. In the case of the neat thermoplastic, the possibility of film transfer is very high. However, due to the fact that the sliding will take place between two polymers from the same type, high frictional force is expected in the interface which lead to high heat. The presence of the heat in the interface could deteriorate the soft surface when it exceeded the softening temperature ( $T_g$ ). The addition of the fillers and/or fibres will have two influences. Either it will reduce the heat in the interface by reducing the interaction between the asperities at which the film transfer will not be adhered well and detachments may occur. Another possibility is the strong film transfer made of polymer and debris of fibre may be formed on the metal surface. In this case, there are two possible surface properties which are either smooth surface or rough. In the case of the smooth surface, low friction and wear will be achieved. In the case of the rough surface, high wear rate may be obtained with high frictional force as well.

### 3. Thermosets

In general, thermosets are the materials which suffer of burning under high temperature. There is no melting phenomenon can occur on such polymer [5]. Thermosetting polymers are stronger and stiffer than thermoplastics and generally can be used at higher temperature. It is shaped directly from the raw polymer material, and no further processing is possible except machining which limits the possible processes to just moulding. Most of the moulding processes involve the addition of chemicals so that the cross-linked chains are produced while the material is in the mould. Thermosets have high thermal stability, high dimensional stability, high-stiffness, good resistance to creep, low densities, and high electrical and thermal insulating properties [1].

**3.1. Phenolics.** Its first synthetic polymer is phenol formaldehyde; it is supplied in the form of moulding powder, which includes resin, fillers, and other additional substance. The

filler is about 50 to 80% of the weight of the moulding powder. Applications for any composite material that has phenolic resin with paper or open weave fabric like glass fiber fabrics are gears, bearings, and electrical insulator parts.

**3.2. Amino Formaldehydes.** Amino formaldehydes include many materials such as urea formaldehydes and melamine formaldehyde. Both are highly cross-linked polymers; the widely used fillers are cellulose and wood flour. It has hard, and rigid, high-strength properties. Both are used for tableware such as cups, saucers, knobs, handles, light fittings and toys. Composites with open weave fabrics are used as building panels.

**3.3. Epoxides.** Epoxy resins become a thermosetting material if they are combined with a hardener since they are usually associated with glass or other fibers to give a hard and strong composite material. Epoxy resins have high adhesive strength, high hardness, chemical resistance; composites with glass fiber fabrics are used for boat hulls and tabletops.

A preliminary investigation into certain tribological aspects of filled epoxy-based plain-bearing composites was carried out [35] which shows that indiscriminate additions of irregularly shaped hard inorganic fillers may have a deleterious effect on the wear characteristics of the composite-metal pair. In addition there is evidence that minimization of the interactions between the epoxide matrix and the metallic counterface is necessary if a mild-wearing couple is to be realized [35]. The effect of counterpart material (hardened steel, austenitic steel, and  $Al_2O_3$ ), internal lubricant (PTFE, graphite,  $MoS_2$ , and  $SnS_2$ ), and fibre reinforcement (glass and carbon fibres) on the wear of epoxy-based composites has been investigated. Under dry conditions the high chromium austenitic steel led to a lower composite wear than the bearing steel, and only PTFE leads to a remarkable wear reduction. For wet conditions the  $Al_2O_3$  ceramic seems to be most promising. The carbon fibre reinforced version has the best wear performance under aqueous conditions [36]. The wear behavior of epoxy matrix composites filled with uniform sized submicron spherical silica particles is discussed [37]. The spherical silica particles could improve the wear resistance of the epoxy matrix even though the content of the fillers was at a relatively low level (0.5–4.0 wt.%). And it was found that the filler with smaller size seemed to be more effective in the improvement of the wear resistance of the composites [37].

**3.4. Polyurethane.** It is used to produce rigid foam. The advantage of using it over expanded polystyrene is that it has lower density, lower thermal conductivity, and better oil, grease, and heat resistance. The rigid foam can be formed in suit like in wall cavities for thermal insulation. Its applications were in refrigerators, structural sandwich panels in buildings, and marine buoyancy.

**3.5. Possible Tribological Behaviour of Thermoset and Fibre Thermoset Composites.** Summary of the tribological behaviour thermoset materials can be summarized and

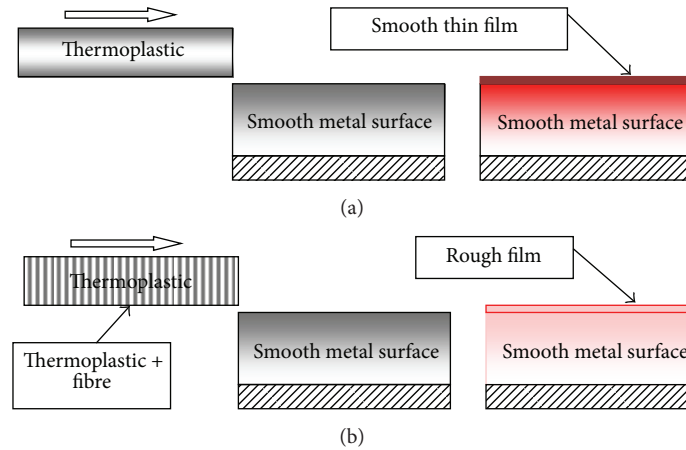


FIGURE 2: The possible film transfer when thermoplastics or fibre thermoplastic composites sliding condition on metal surface.

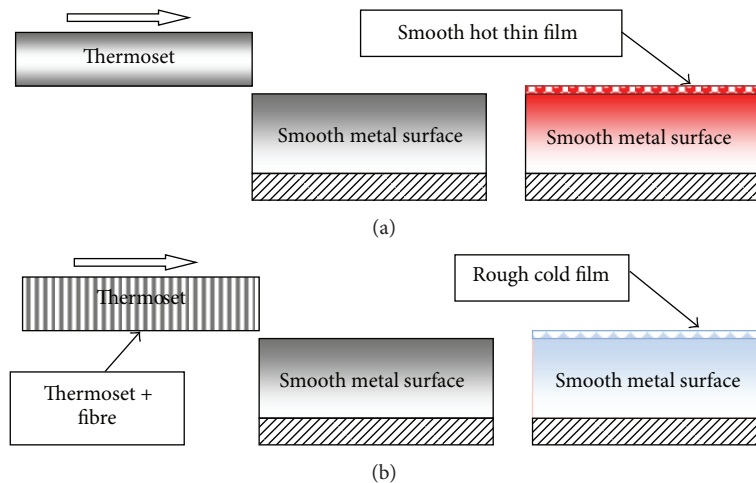


FIGURE 3: The possible film transfer when thermosets or fibre thermoplastic composites sliding condition on metal surface.

explained with the aid of Figure 3. In the case of the neat thermoset, the possibility of film transfer is lower than the thermoplastic since the thermoset is much harder than the thermoplastic. Another reason is the fact that the thermoset polymer has less plasticity than the thermoplastic. This leads to the conclusion that there is less possibility of plastic deformation, that is, forming the film on the counterface. However, most of the reported works mentioned that there is film transfer generated during the thermoset sliding against metal surfaces. In the case of the neat thermoset, it can be illustrated that the film transfer is rougher than the thermoplastic film, but the surface is cooler than the thermoplastic since the frictional force is less and there is possible of rolling debris in the interface. On the other hand, the thermoplastic has very high adhesive behaviour on the metal surface. In the case of the fibre/thermoset composites, the presence of the fibres will higher assist in cooling the interface and strengthen the exposed layer of the thermoset. However, in the case of fibre presence in the interface, the modification on the film transfer is high which could lead to

low friction due to the rolling of the debris and high wear due to the transition from adhesive to abrasive wear.

#### 4. Conclusion and Recommendations

There are several recommendations that can be withdrawn from this work as follows.

- (1) Thermoplastic materials have the ability of forming a thin film transfer on the metal counterface which assists in reducing the friction coefficient. However, at high level of interface temperature, plastic deformation occurs which deteriorate the soft surface leading to high damage. Reinforcing the thermoplastic materials will assist in reducing the wear rate of the materials which in turn can achieve good frictional and wear properties for bearings and bushes applications.
- (2) Despite the fact that thermoset materials are harder than the thermoplastic, the possibility of generating

the film transfer on the counterface is less and the property of this film is harder and can sustain high temperature. The addition of abrasive fibres to the thermosets could enhance the wear and the friction properties. However, the composites will suffer from instability condition during the serves. An attention should be put and comprehensive investigation need to be conducted in this area.

- (3) There are many polymers that have not yet studied in terms of tribology. Due to the importance of these properties which is equal to the mechanical properties, it is highly recommended for comprehensive study for such important materials.

The following can be concluded.

- (1) There is no general wear and/or frictional trend for either thermoset or thermoplastic under adhesive wear loading condition. However, most of the thermoplastic polymers generate a film transfer on the metal counterface which assists to enhance the wear and frictional performance of the materials. In the case of the thermosets, the modification occurred on the wear track that determines the wear and frictional performance of the materials. Therefore, it is highly recommended to study the wear track and its characteristics to comprehensively understand the wear behaviour of thermosets materials.
- (2) The addition of the fillers or fibres to either thermoset or thermoplastic materials assists in strengthening the surface which will result in enhancing the tribological behaviour of the polymer especially the thermoplastic. This is the general understanding for the adhesive wear loading conditions under dry contact conditions. Under wet contact condition, contradict thought was reported and further investigation is required.

## References

- [1] J. F. Shackelford, *Introduction To Material Science For Engineering*, Prentice Hall, Upper Saddle River, NJ, USA, 2000.
- [2] W. Bolton, *Engineering Materials Technology*, Butterworth Heinemann UK, 3rd edition, 1998.
- [3] E. H. Cornish, *Materials and Designer*, Cambridge University Press, Cambridge, UK, 1999.
- [4] S. K. De and J. R. White, *Short Fiber-Polymer Composites*, Woodhead, Cambridge, UK, 1996.
- [5] M. Alauddin, I. A. Choudhury, M. A. El Baradie, and M. S. J. Hashmi, "Plastics and their machining: a review," *Journal of Materials Processing Tech*, vol. 54, no. 1-4, pp. 40-46, 1995.
- [6] C. A. Keyser, *Material Science in Engineering*, Charles E. Merit, 1986.
- [7] S. Affatato, G. Bersaglia, D. Emiliani et al., "The performance of gamma- and EtO-sterilised UHMWPE acetabular cups tested under severe simulator conditions—part 2: wear particle characteristics with isolation protocols," *Biomaterials*, vol. 24, no. 22, pp. 4045-4055, 2003.
- [8] G. Liu, Y. Chen, and H. Li, "A study on sliding wear mechanism of ultrahigh molecular weight polyethylene/polypropylene blends," *Wear*, vol. 256, no. 11-12, pp. 1088-1094, 2004.
- [9] G. Guofang, Y. Huayong, and F. Xin, "Tribological properties of kaolin filled UHMWPE composites in unlubricated sliding," *Wear*, vol. 256, no. 1-2, pp. 88-94, 2004.
- [10] A. Valenza, A. M. Visco, L. Torrisi, and N. Campo, "Characterization of ultra-high-molecular-weight polyethylene (UHMWPE) modified by ion implantation," *Polymer*, vol. 45, no. 5, pp. 1707-1715, 2004.
- [11] N. E. Bekhet, "Tribological behaviour of drawn polypropylene," *Wear*, vol. 236, no. 1-2, pp. 55-61, 1999.
- [12] B. M. Sole and A. Ball, "On the abrasive wear behaviour of mineral filled polypropylene," *Tribology International*, vol. 29, no. 6, pp. 457-465, 1996.
- [13] F. Yang and V. Hlavacek, "Improvement of PVC wearability by addition of additives," *Powder Technology*, vol. 103, no. 2, pp. 182-188, 1999.
- [14] A. P. M. Baptista and M. do Carmo Vaz, "Comparative wear testing of flooring materials," *Wear*, vol. 162-164, pp. 990-995, 1993.
- [15] J. H. Lee, G. H. Xu, and H. Liang, "Experimental and numerical analysis of friction and wear behavior of polycarbonate," *Wear*, vol. 250-251, no. 2, pp. 1541-1556, 2001.
- [16] Y. S. Kim, J. Yang, S. Wang, A. K. Banthia, and J. E. McGrath, "Surface and wear behavior of bis-(4-hydroxyphenyl) cyclohexane (bis-Z) polycarbonate/polycarbonate-polydimethylsiloxane block copolymer alloys," *Polymer*, vol. 43, no. 25, pp. 7207-7217, 2002.
- [17] J. Bergstrom, F. Thuvander, P. Devos, and C. Boher, "Wear of die materials in full scale plastic injection moulding of glass fibre reinforced polycarbonate," *Wear*, vol. 250-251, no. 2, pp. 1511-1521, 2001.
- [18] J. J. Rajesh, J. Bijwe, and U. S. Tewari, "Abrasive wear performance of various polyamides," *Wear*, vol. 252, no. 9-10, pp. 769-776, 2002.
- [19] J. J. Rajesh and J. Bijwe, "Influence of fillers on the low amplitude oscillating wear behaviour of polyamide 11," *Wear*, vol. 256, no. 1-2, pp. 1-8, 2004.
- [20] J. Cayer-Barrioz, D. Mazuyer, P. Kapsa, A. Chateauminois, and F. Bouquerel, "On the mechanisms of abrasive wear of polyamide fibres," *Wear*, vol. 255, no. 1-6, pp. 751-757, 2003.
- [21] M. Kurokawa, Y. Uchiyama, T. Iwai, and S. Nagai, "Performance of plastic gear made of carbon fiber reinforced polyamide 12," *Wear*, vol. 254, no. 5-6, pp. 468-473, 2003.
- [22] H. Pihtili and N. Tosun, "Investigation of the wear behaviour of a glass-fibre-reinforced composite and plain polyester resin," *Composites Science and Technology*, vol. 62, no. 3, pp. 367-370, 2002.
- [23] N. Chand, A. Naik, and S. Neogi, "Three-body abrasive wear of short glass fibre polyester composite," *Wear*, vol. 242, no. 1-2, pp. 38-46, 2000.
- [24] A. A. El-Sayed, M. G. El-Sherbiny, A. S. Abo-El-Ezz, and G. A. Aggag, "Friction and wear properties of polymeric composite materials for bearing applications," *Wear*, vol. 184, no. 1, pp. 45-53, 1995.
- [25] S. Bahadur and Y. Zheng, "Mechanical and tribological behavior of polyester reinforced with short glass fibers," *Wear*, vol. 137, no. 2, pp. 251-266, 1990.
- [26] P. M. Dickens, J. L. Sullivan, and J. K. Lancaster, "Speed effects on the dry and lubricated wear of polymers," *Wear*, vol. 112, no. 3-4, pp. 273-289, 1986.

- [27] J. San, J. Liu, B. Zhu, Z. Liu, C. Dong, and Q. Zhang, "Tribological properties of ion-implanted polyphenylene oxide (PPO)," *Wear*, vol. 250-251, no. 2, pp. 1504-1510, 2001.
- [28] I. D. Graham and G. H. West, "Wear mechanism of a composite plastic bearing," *Wear*, vol. 36, no. 1, pp. 111-117, 1976.
- [29] M. Clerico, "Tribological behaviour of polyacetals," *Wear*, vol. 64, no. 2, pp. 259-272, 1980.
- [30] Y. J. Mergler, R. P. Schaake, and A. J. Huis in't Veld, "Material transfer of POM in sliding contact," *Wear*, vol. 256, no. 3-4, pp. 294-301, 2004.
- [31] J. Khedkar, I. Negulescu, and E. I. Meletis, "Sliding wear behavior of PTFE composites," *Wear*, vol. 252, no. 5-6, pp. 361-369, 2002.
- [32] L. Tomescu, M. Ripă, E. Vasilescu, and C. Georgescu, "Surface profiles of composites with PTFE matrix," *Journal of Materials Processing Technology*, vol. 143-144, no. 1, pp. 384-389, 2003.
- [33] J. H. Jia, H. D. Zhou, S. Q. Gao, and J. M. Chen, "A comparative investigation of the friction and wear behavior of polyimide composites under dry sliding and water-lubricated condition," *Materials Science and Engineering A*, vol. 356, no. 1-2, pp. 48-53, 2003.
- [34] S. E. Franklin and A. de Kraker, "Investigation of counterface surface topography effects on the wear and transfer behaviour of a POM-20% PTFE composite," *Wear*, vol. 255, no. 1-6, pp. 766-773, 2003.
- [35] M. Rubenstein and M. Burdekin, "Wear assessment of epoxy composites used for machine slideways," *Wear*, vol. 55, no. 1, pp. 131-142, 1979.
- [36] O. Jacobs, R. Jaskulka, F. Yang, and W. Wu, "Sliding wear of epoxy compounds against different counterparts under dry and aqueous conditions," *Wear*, vol. 256, no. 1-2, pp. 9-15, 2004.
- [37] X. S. Xing and R. K. Y. Li, "Wear behavior of epoxy matrix composites filled with uniform sized sub-micron spherical silica particles," *Wear*, vol. 256, no. 1-2, pp. 21-26, 2004.

## Research Article

# Manufacture of Green-Composite Sandwich Structures with Basalt Fiber and Bioepoxy Resin

J. P. Torres,<sup>1</sup> R. Hoto,<sup>2</sup> J. Andrés,<sup>3</sup> and J. A. García-Manrique<sup>2</sup>

<sup>1</sup> Instituto de Ciencia y Tecnología de Materiales, Universidad Nacional de Mar del Plata, Av. J.B. Justo 4302, B7608FDQ Mar del Plata, Argentina

<sup>2</sup> Universidad Politécnica de Valencia, Camino Vera s/n, 46022 Valencia, Spain

<sup>3</sup> Universitat Jaume I, Avenida de Vicent Sos Baynat, 12071 Castellón, Spain

Correspondence should be addressed to J. A. García-Manrique; [jugarcia@mcm.upv.es](mailto:jugarcia@mcm.upv.es)

Received 8 March 2013; Accepted 7 May 2013

Academic Editor: Belal F. Yousif

Copyright © 2013 J. P. Torres et al. This is an open access article distributed under the Creative Commons Attribution License, which permits unrestricted use, distribution, and reproduction in any medium, provided the original work is properly cited.

Nowadays, there is a growing interest for the use and development of materials synthesized from renewable sources in the polymer composites manufacturing industry; this applies for both matrix and reinforcement components. In the present research, a novel basalt fibre reinforced (BFR) bioepoxy green composite is proposed as an environmentally friendly alternative to traditional petroleum-derived composites. In addition, this material system was combined with cork as core material for the fabrication of fibre composite sandwich structures. Mechanical properties of both skin and core materials were assessed through flexural and tensile tests. Finite element (FEM) simulations for the mechanical stress analysis of the sandwich material were carried out, and a maximum allowable shear stress for material failure under bending loads was established. Permeability measurements of the basalt fabrics were carried out in order to perform numerical simulations of liquid composite moulding (LCM) processes on the PAM-RTM software. The proposed green-composite sandwich material was used for the fabrication of a longboard as a case study for a sports equipment application. Numerical simulations of the mould filling stage allowed the determination of an optimal mould filling strategy. Finally, the load-bearing capacity of the board was studied by means of FEM simulations, and the presented design proved to be acceptable for service.

## 1. Introduction

Nowadays, there is a growing need for the production and development of materials synthesized from renewable sources and to decrease the world's dependence on petroleum. In the fiber reinforced polymer composites (FRPCs) manufacturing industry, these tendencies have recently led to the investigation of possible substitutes, both for matrix and reinforcement components. Recently, bio-based matrix materials have received considerable attention mainly for being nonpetroleum-dependent. These systems can be obtained from sustainable sources such as vegetable oil, cellulose, and soy protein, among others. In the case of bio-based thermosetting resins, much research is still pending since mechanical properties comparable with those of petroleum-based counterparts are very difficult to achieve [1]. One of the main drawbacks of using plant oil as

a precursor for bio-based resins is that its chemistry can lead to a low crosslink density network which produces a polymer with low glass transition temperature (lower than 90°C), poor stiffness (lower than 2 GPa), and inferior thermo-physical properties, compared to the traditional petroleum-based polymers. However, this same feature can lead to a superior toughness by providing additional deformation mechanisms for energy absorption before failure in impact loading situations [2]. Altogether, a compromise solution can be the combination of both synthetic and bio-based materials [3, 4] in such a way that a superior material is obtained from a cost-performance standpoint.

With respect to fiber reinforcements, basalt fibers (BFs) have been recently studied as sustainable alternative for fiber reinforcement since the earth has practically unlimited basalt reserves [5]. BFs are produced from basalt rock, the most common rock found in the earth crust. Also,

basalt is biologically inert, and its weathering increases the mineral content of soil. BFs are manufactured by melting at 1300–1700°C and subsequent spinning. This manufacturing process requires no precursor or additives, which results in a decrease of its environmental impact and production costs [6]. Regarding mechanical performance, it has been reported that BFs have higher modulus and strength than glass fibers (GFs) [7]. In addition, basalt has much higher chemical resistance than glass: it can be used for the transportation and storage of corrosive liquids and gases. It also provides much better electrical insulating properties and thermal-stability than glass [6]. Other advantages of basalt are its high UV radiation and seawater resistance. Finally, reduction of risk of environmental pollution like high-toxic metals and oxides can be achieved by replacing GFs with BFs. All of these features make BFs a suitable substitute for GFs. On the other hand, when comparing BFs against carbon fibers (CFs), BFs are more attractive from an environmental protection perspective since they offer sustainability and independence from petroleum at significantly lower costs (even though they have lower strength and stiffness). Finally, it is important to remark that basalt fiber interface interaction with polymeric resins is not completely understood [7] and a subject of further investigation in order to gain a precise knowledge of its effect on mechanical properties.

The objective of this paper is to investigate the possibility of using a novel BFR bio-based epoxy green composite system as a potential substitute for traditional petroleum-derived composites. For this, composite panels were manufactured using the VARTM technique. Also, sandwich-structured panels were made combining the green composite for the sandwich skin, with natural cork for the sandwich core. Mechanical behaviour of the proposed material system was assessed by means of flexural and uniaxial tensile tests together with FEM simulations. To perform numerical simulations of the processing stage, the fiber permeability was measured using an especially designed characterization setup. A case study for the fabrication of a sandwich-structured sports longboard was carried out. The fabrication stage was modelled using the PAM-RTM software along with the permeability values determined experimentally. The load-bearing capability of the board was studied by means of FEM stress analysis, and the board dimensions were determined in order to satisfy the maximum allowable stress values established in the mechanical characterization stage.

## 2. Materials and Methods

*2.1. Overview on Liquid Composite Molding (LCM) Manufacturing Methods.* LCM is a manufacturing method that consists in the impregnation of a fabric with a low viscosity resin. It is currently considered as one of the most viable and ecofriendly process in the manufacturing of high quality parts. Depending on the characteristics of the mould and the applied pressure gradient, there are a number of different types of LCM process among which are Resin Transfer Moulding (RTM), Vacuum Assisted Resin Transfer Moulding (VARTM), Reactive Injection Moulding (RIM),

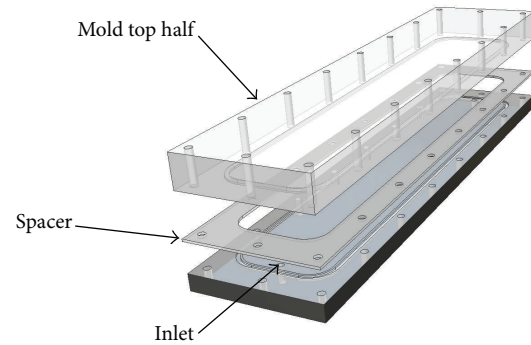


FIGURE 1: Mould assembly for the characterization of fiber preform permeability.

and Structural Reactive Injection Moulding (SRIM). One disadvantage in LCM methods is that defects such as voids and dry spots can be induced during the impregnation stage [8]. These defects are considered to be the largest source of quality and reproducibility problems. They are often caused by unbalanced resin flows, which are directly related to the fiber permeability and the impregnation velocity. As a consequence, an accurate prediction of resin flow behaviour in the fiber impregnation process is of great importance for the optimization of LCM parts quality. Currently, there are a number of computer simulation tools available for the modelling of LCM processes, which provide a remarkable advantage over the (cost and time consuming) trial-and-error methods traditionally used in the industry. In order to perform LCM modelling, one of the most critical input parameters for the mathematical models is the reinforcement permeability. In the past 20 years, a number of studies [9–11] have focused on the development of a reliable and standardized procedure for the accurate characterization of fiber permeability.

*2.2. Experimental Setup for Permeability Measurements.* Figure 1 shows the basic design of the experimental setup used for the unidirectional measurement of permeability. The bottom half of the mould was machined from a 1000 × 280 × 25 mm aluminium plate. The length of the mould was chosen according to the concept of “Minimum Injection Length” developed by Ferland et al. [10]. For the inlet and vent, two threaded holes (10 mm diameter) were machined and fitted with secure hydraulic connectors. The top-half of the mould was made from a machined methacrylate plate to allow visual observation of the flow front advance during experiments. The inner mould cavity consists of a 3 mm spacer and a rectangular silicon gasket to provide sealing. The entire mould assembly was then placed in a specially designed hydraulic press with a maximum clamping force of 5 tonnes (Figure 2). The top-half was mounted on a special frame which permits vertical displacement for the mould opening and closing operations.

A low cost data acquisition device (DATAQ DI-194RS), together with a high accuracy pressure transducer (mounted

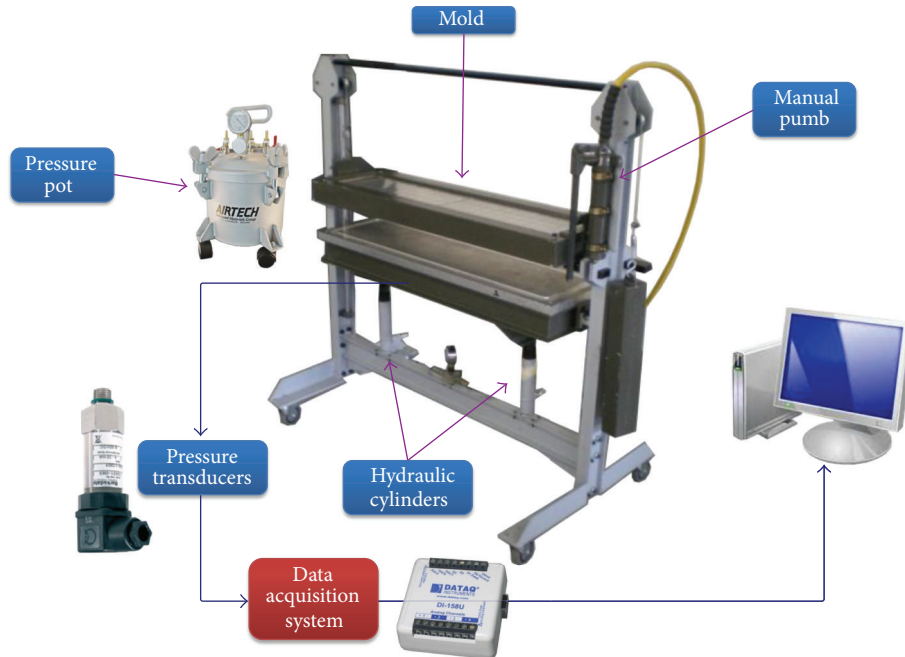


FIGURE 2: Setup for permeability measurements.

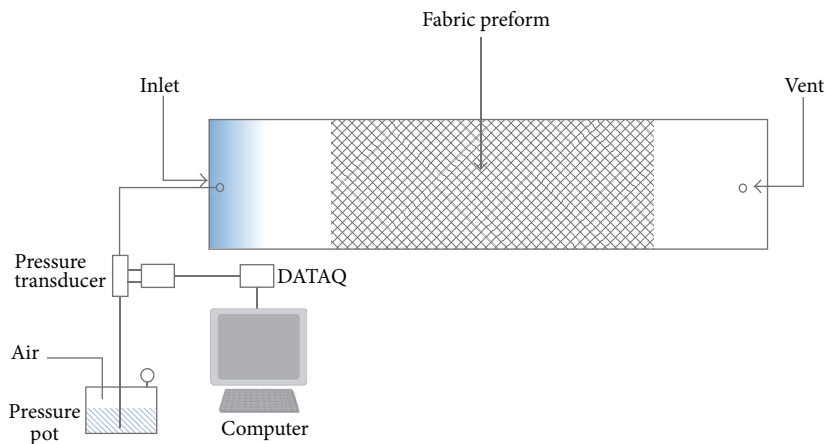


FIGURE 3: Schematic representation of the experimental setup.

on a “T” fixture), was used to measure the exerted pressure near the inlet gate of the mould (Figure 3). The DI-194 RS card was connected through a digital channel to a manual trigger which allowed manual scanning of the flow front progression. As a consequence, value pairs for the inlet pressure and flow front position could be measured at different time intervals. These recorded values were then used in the derivation of fiber permeability following the procedure established in [9].

**2.3. Manufacturing of Green Composite and Sandwich Panels.** For the present work, BFR bio-based epoxy green composites were manufactured using the VARTM technique. The fabric preform was placed over a glass tool previously coated with a release agent. Then, the reinforcements were covered with the peel ply, the bleeder material, and finally the plastic

bag. The plastic bag is attached to the glass tool using double side tape. This provides a perfect seal for the whole arrangement. An inlet tube is placed for resin infusion, and finally, an outlet tube, connected to a vacuum pump, provides the channel both for excess resin and for air evacuation. 500 mm × 900 mm plates were made using 8 plies of plain weave 6 basalt fabric laminates and the SUPER SAP 100/1000 bio-based epoxy (made by Entropy Bio-Resins Co [12]). This epoxy resin is made from up to 37% biocontent obtained as coproducts of other green industries such as wood pulp and biofuels production. The resin has a total calculated biomass of 50% [13]. The resulting panels had a 2 mm thickness. After demoulding, the panels were cured at ambient temperature for 24 hours, followed by curing at 50°C for two hours in an electrical furnace.

TABLE 1: Configuration for mechanical tests.

Test type	Thickness (mm)	Width (mm)	Length (mm)
Compression (cork)	5.0	20 (diameter)	—
Tensile (BFPC)	2.0	25	180
Flexural (BFPC)	2.0	22	60 (support span)
Flexural (sandwich)	7.0	22	60 (support span)

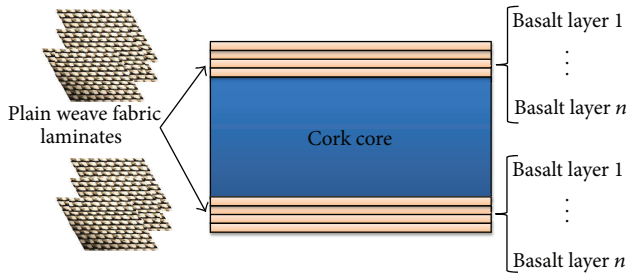


FIGURE 4: Composite sandwich structure panel.

On the other hand, sandwich-structured composites panels were also manufactured. Sandwich structured composites are a special class of composite materials which consist of thin high strength skins bonded to a thicker light weight core (Figure 4). This configuration provides high bending stiffness while keeping an overall low density. These properties, together with wide design versatility, make sandwich structured composites a choice of great interest in the field of LCM manufactured FRPC [14]. In the present investigation, a green-composite sandwich structure is proposed for the manufacturing of sandwich panels for engineering applications requiring flexural stiffness at low weight. Cork and a BFR bio-based composite were used as core and skin materials, respectively. The sandwich panels were made using the VARTM technique. For this, a two-layered BFR bioepoxy skin and a 5 mm thickness cork core were used.

**2.4. Mechanical Characterization and FEM Simulations.** In order to determine the mechanical properties of the basalt fibre bioepoxy composites, tensile and flexural coupons were obtained by waterjet cutting of VARTM manufactured flat panels. Cork compression samples were obtained from cork panels using a puncher. All mechanical tests were performed on an INSTRON 3365 testing machine (Figure 5). Table 1 shows specimen dimensions employed in every case.

In order to assess the stress states developed in the sandwich material under flexural loads, FEM simulations of the flexural test were carried out in ABAQUS/Implicit 6.10. This study will later serve as a validation stage in the design process for the optimization of part geometry and sandwich configuration for an actual part, as discussed in Section 4. The flexural test was modelled using SC8R8-node quadrilateral continuum shell elements for the basalt fiber skin and C3D8R 8-node linear brick element for the cork core. The supports

and loading tip were modeled as analytical solids. Contact interaction properties were simplified assuming frictionless behavior and “hard” contact normal behavior. Figure 6 shows the part geometry and mesh distribution employed. The cork material was modelled as an isotropic hyperelastic material using the hyperfoam option in ABAQUS. The basalt-reinforced skin was modelled as a linear orthotropic solid. Material parameters employed are shown in Table 2, and Poisson’s ratio values were obtained from the literature [5].

### 3. Results and Discussion

**3.1. Mechanical Properties and Stress Analysis.** Mechanical properties for each material are presented in Table 2. For the BFPC, linear elastic response with brittle rupture was observed as expected (Figure 7(a)). Flexural testing on BFPC showed a linear response up to a point where stress starts to present small and continuous drops (Figure 7(b)). It was observed that these drops corresponded to material failure occurring in the upper face of the test coupon, which is under a compressive stress state (Figure 8).

Flexural testing of the composite sandwich showed a nonlinear stress-strain evolution up to a point where there is a significant stress drop followed by an approximately constant stress region (Figure 9). This point corresponds to material failure associated with shear failure of the cork core material as can be seen in Figure 10. Figure 11(a) shows the finite element results for the simulation of the test along with a representation of the corresponding normal stress profile along the symmetry plane of the sample (plane  $yz$ , where  $z$  is the loading axis). Shear stresses in the cork core are approximately homogeneous in the thickness, while they are assumed negligible in the skin material since it was modeled as a shell. Figure 11(b) shows the evolution of shear stresses in the cork material as a function of distance from the axis of symmetry. Its value is 0 along the symmetry plane and increases to a maximum value located at approximately the middle point between the loading tip and the support. This fact is also confirmed in the observations of tested samples (Figure 11). Both Figures 11(a) and 11(b) are very useful for understanding how stress and deformation distribution occur in composite sandwich under flexural loads. For the purpose of mechanical design, a maximum allowable shear stress ( $\tau_{max}$ ) assumption was made. This simplification arises from the fact that, for the intended application, the sandwich structure will carry predominantly flexural loads. A critical value of 33 MPa for the shear stress in the cork core was obtained from the finite element simulation shear stress profile.

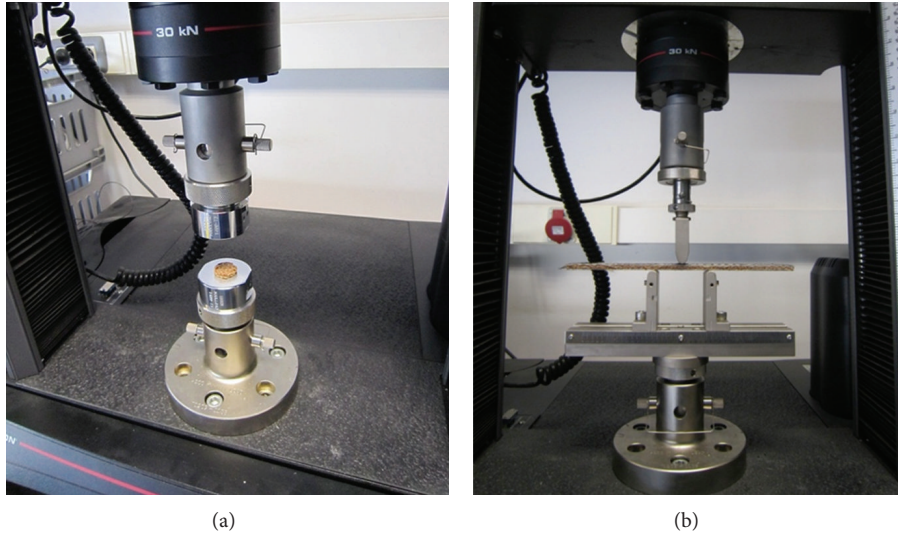


FIGURE 5: (a) Setup for compression testing of cork. (b) Specimen configuration for flexural testing of the composite sandwich.

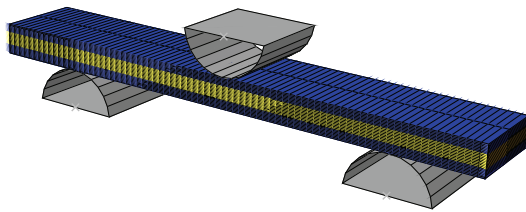


FIGURE 6: Finite element mesh used for the simulation of the 3 point-bending flexural tests.

TABLE 2: Mechanical properties obtained for sandwich components.

Test type	Young modulus (MPa)	Strength (MPa)
Compression (cork)	4.5	—
Tensile (BFPC)	54,776	513
Flexural (BFPC)	56,455	462

#### 4. Case Study: Manufacturing and Stress Analysis of a Green-Composite Sandwich Longboard

The proposed green-composite sandwich system was studied as an environmentally sustainable alternative material for a sports equipment application, namely, longboarding. Longboards consist of a specially designed board, which have the same shape as skateboards but are longer (up to 120 cm). Longboards are nowadays frequently used as an ecofriendly way to move around the city.

In order to choose the proper manufacturing strategy, two-dimensional flow simulations were performed using the commercial software PAM-RTM. The principal permeability [11] values ( $K_1 = 1.56E - 11 \text{ m}^2$  and  $K_2 = 1.49E - 11 \text{ m}^2$ )

determined from the permeability measurements were employed. The bioepoxy resin viscosity was obtained from the supplier technical data sheet [12]. The part was modelled as a sandwich laminate composed by 4 layered upper and bottom skins and a 5 mm cork panel as core material. Two mould filling strategies were tested. In the first one (see Figure 12, left) the inlet is the symmetrical axis perpendicular to the longitudinal axis of the longboard, which leads to a larger resin path to complete the filling process. The second strategy, consisting of a longitudinal inlet oriented parallel to the axis of the board, conducts to a shorter resin path (see Figure 12, right). The simulation results show that, as it was expected, the second strategy is the most appropriate because it gives a shorter filling time. In the first filling strategy, the filling time exceeded the resin gel time (22 min—when crosslinking begins to dominate the nature of the resin and it solidifies into a gel-. Therefore, this strategy was discarded.

On the other hand, the second strategy leads to a total filling time of about 12 minutes. The final part quality of the resulting polymerized skins was assessed by scanning electron microscopy (SEM). SEM micrographs (Figure 14) showed complete fiber impregnation and total absence of voids both at the macroscale (between the bundles) and at microscale (inside bundles). Figure 13 shows the final part obtained after curing for 24 hours at ambient temperature before demolding and then cured in an oven at 50°C. The final part was obtained by milling the longboard shape with a CNC machine.

Stress analysis for the longboard under loading conditions was performed by running finite element simulations on ABAQUS/Explicit 6.10. The failure criteria presented in the previous section was used to evaluate the mechanical stability of the longboard. An extreme loading situation was modelled considering the fall of a 90 kg weight person from a 1-meter height over the board. This was simplified by applying two loads, over an area approximately equal to the size of a shoe, in the two points midway between the center and

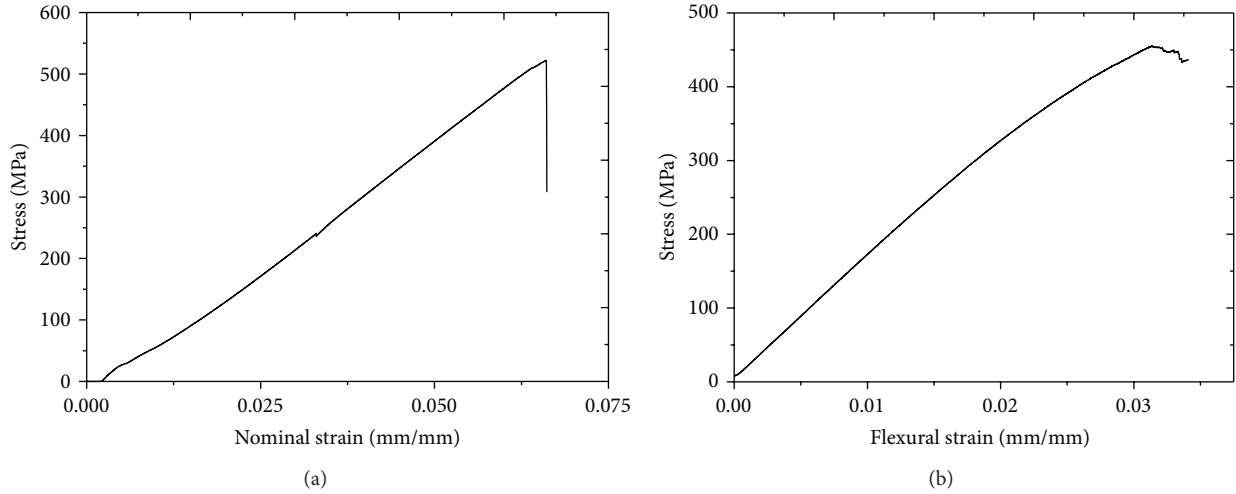


FIGURE 7: Stress-strain curves for BFPC: (a) tensile test; (b) flexural test.

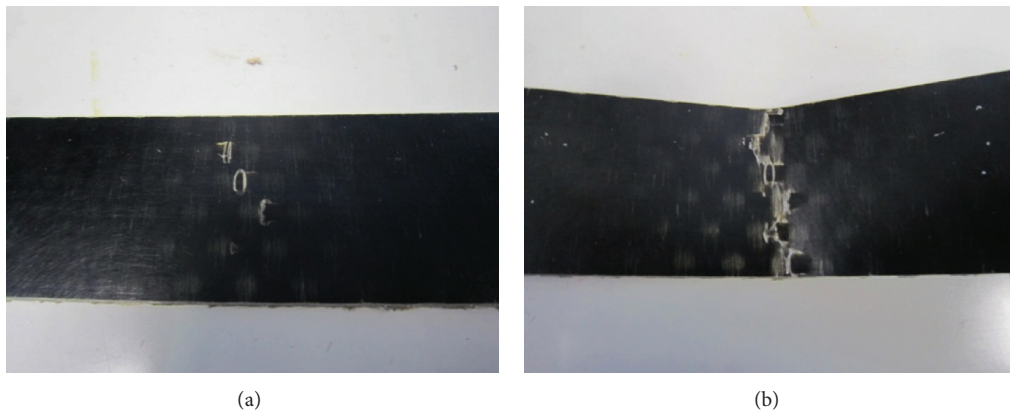


FIGURE 8: Successive stages of BFPC compressive failure in flexural tests.

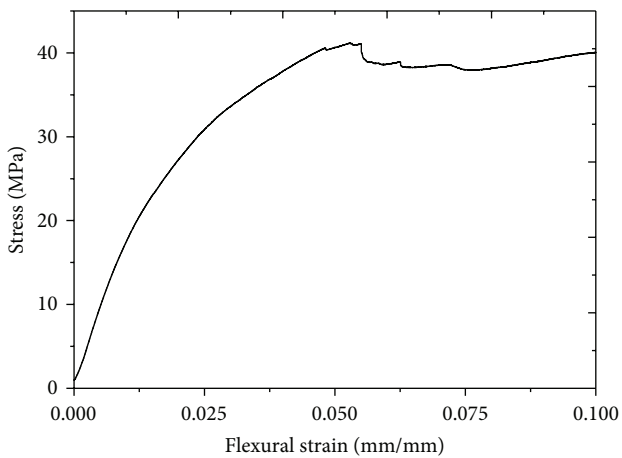


FIGURE 9: Stress-strain results for the composite sandwich flexural test.

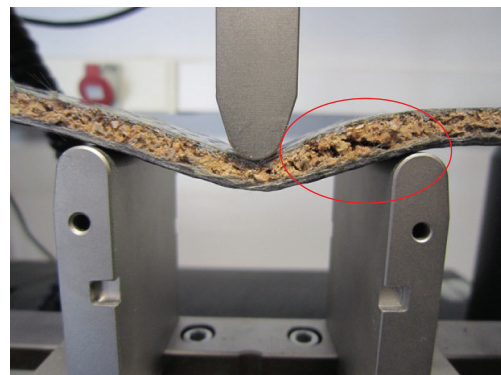


FIGURE 10: Critical failure of the sandwich sample by shear cavitation in the cork core.

the end of the part. The resulting stress distribution is shown in Figure 15. The stress analysis allows for the determination of the skin thickness by providing a lower bound below

which deflections are so large that the cork core fails by shear cavitation. For the designed longboard, a 1mm skin thickness resulted admissible since it leads to a maximum shear stress 5 times lower than the maximum allowed value determined previously.

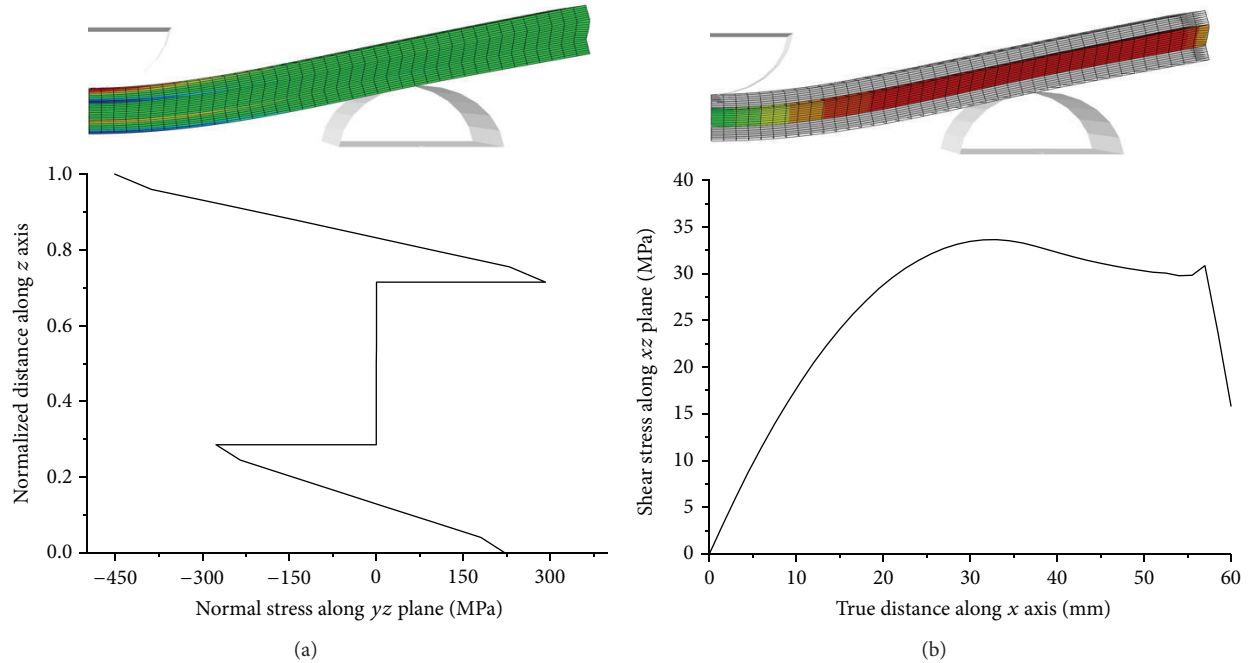


FIGURE 11: (a) Normal stress profile along the symmetry plane. (b) Shear stress evolution along the x axis in the cork core.

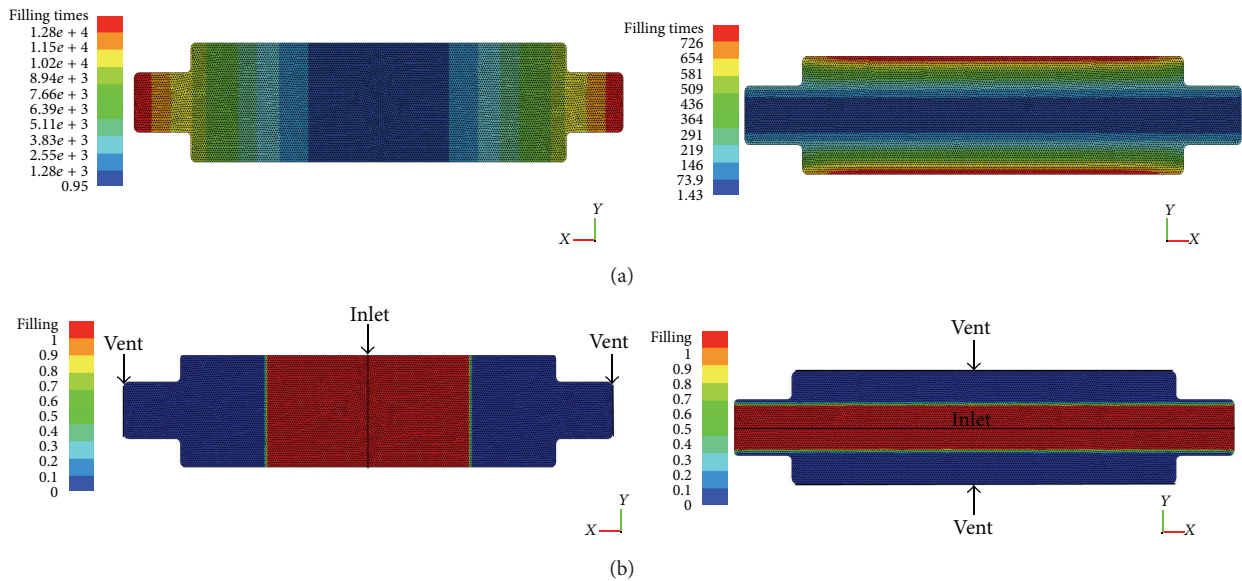


FIGURE 12: PAM-RTM simulation results for the two resin infusion strategies proposed for the fabrication of a longboard: (a) filling time; (b) flow front direction.

### 5. Conclusions

A novel BFR bioepoxy green composite is proposed as an environmentally friendly alternative to traditional petroleum-derived composites. This green composite was combined with natural cork as core material for the fabrication of sandwich-structured composite parts. Mechanical performance under tensile and flexural loads of the sandwich and its separate constituents was assessed on an INSTRON machine. It was found that the critical material failure mode

is associated with cork shear rupture. As a consequence, FEM simulation results were used to determine a maximum allowable shear stress for its later use on design of sandwich parts.

As a case study for the manufacturing and performance of the material under service conditions, a longboard part was manufactured using the VARTM technique. The results from the permeability characterization allowed for the simulation of the mould filling stage. It was found that a complete filling with absence of defects could be accomplished by employing

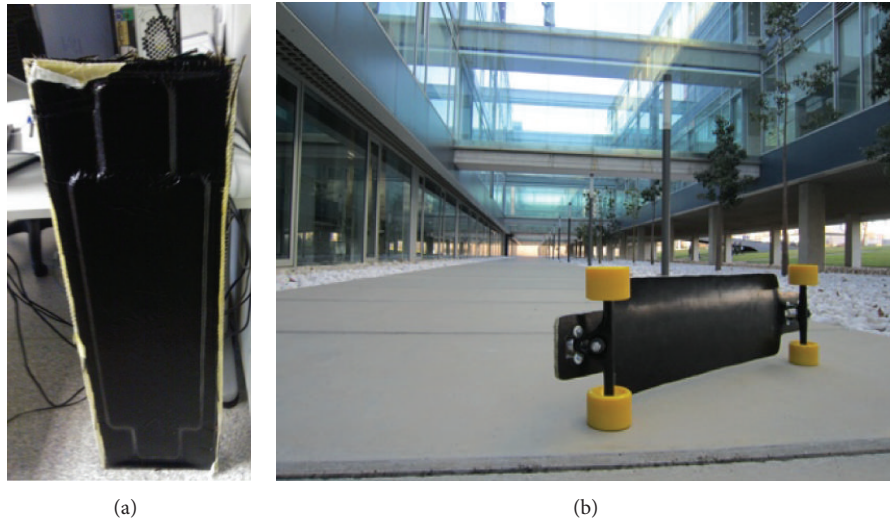


FIGURE 13: Longboard before demoulding and final obtained part.

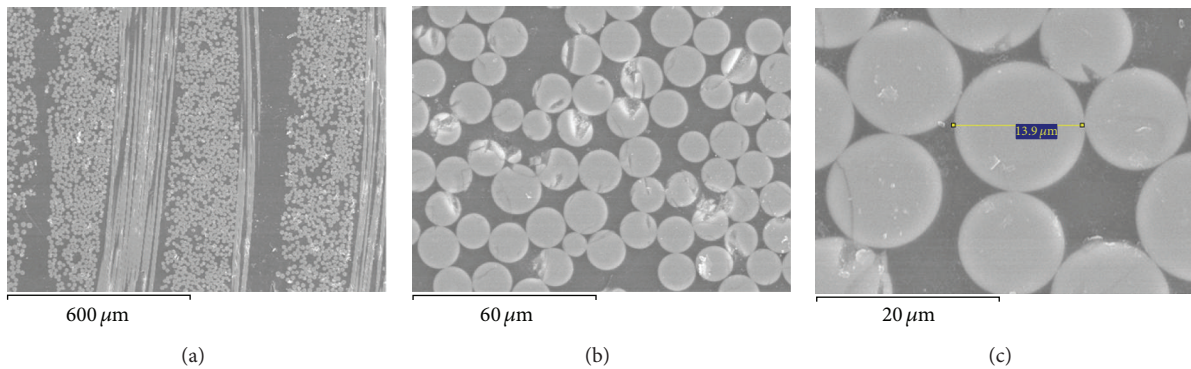


FIGURE 14: SEM micrograph taken from the polymerized samples showing complete fiber impregnation and the absence of voids.

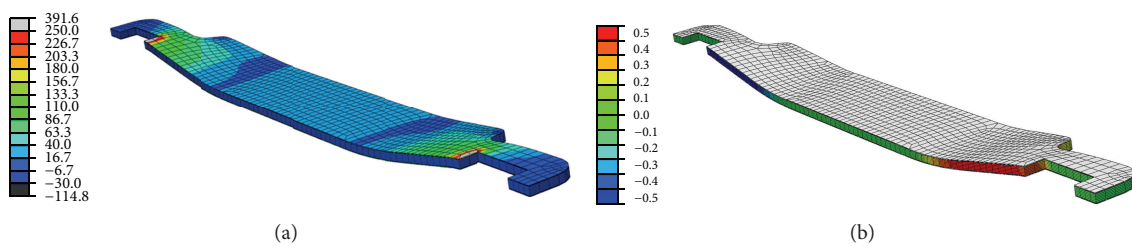


FIGURE 15: Simulation results for the longboard under normal service loads: (a) principal stress value; (b) shear stress distribution.

a longitudinal inlet parallel to the axis of the board. Stress analysis of the board was assessed by FEM simulations and the proposed design proved to satisfy the failure criteria and be acceptable for service conditions.

### Acknowledgments

This research work is supported by the Spanish Ministerio de Ciencia e Innovación, Project DPI2010-20333, and the Generalitat Valenciana through Programme PROMETEO/2009/063.

### References

- [1] X. Q. Liu, W. Huang, Y. H. Jiang, J. Zhu, and C. Z. Zhang, "Preparation of a bio-based epoxy with comparable properties to those of petroleum-based counterparts," *Express Polymer Letters*, vol. 6, no. 4, pp. 293–298, 2012.
- [2] D. Ratna, "Mechanical Properties and Morphology of epoxidized sybean-oil-modified epoxy resin," *Polymer International*, vol. 50, pp. 179–184, 2001.
- [3] M. Haq, R. Burgueño, A. K. Mohanty, and M. Misra, "Processing techniques for bio-based unsaturated-polyester/clay

- nanocomposites: tensile properties, efficiency, and limits,” *Composites A*, vol. 40, no. 4, pp. 394–403, 2009.
- [4] H. Miyagawa, A. K. Mohanty, R. Burgueño, L. T. Drzal, and M. Misra, “Novel biobased resins from blends of functionalized soybean oil and unsaturated polyester resin,” *Journal of Polymer Science B*, vol. 45, no. 6, pp. 698–704, 2007.
- [5] Q. Liu, *Basalt fiber reinforced polymer composites [Ph.D. thesis]*, University of Connecticut, 2006.
- [6] V. Fiore, G. Di Bella, and A. Valenza, “Glass-basalt/epoxy hybrid composites for marine applications,” *Materials and Design*, vol. 32, no. 4, pp. 2091–2099, 2011.
- [7] V. Lopresto, C. Leone, and I. De Iorio, “Mechanical characterization of basalt fibre reinforced plastic,” *Composites Part B*, vol. 42, no. 4, pp. 717–723, 2011.
- [8] J. A. García, L. Gascón, E. Cueto, I. Ordeig, and F. Chinesta, “Meshless methods with application to Liquid Composite Molding simulation,” *Computer Methods in Applied Mechanics and Engineering*, vol. 198, no. 33–36, pp. 2700–2709, 2009.
- [9] R. Arbter, J. M. Beraud, C. Binetruy et al., “Experimental determination of the permeability of textiles: a benchmark exercise,” *Composites A*, vol. 42, no. 9, pp. 1157–1168, 2011.
- [10] P. Ferland, D. Guittard, and F. Trochu, “Concurrent methods for permeability measurement in resin transfer molding,” *Polymer Composites*, vol. 17, no. 1, pp. 149–158, 1996.
- [11] K. Hoes, D. Dinescu, H. Sol et al., “New set-up for measurement of permeability properties of fibrous reinforcements for RTM,” *Composites A*, vol. 33, no. 7, pp. 959–969, 2002.
- [12] <http://www.entropyresins.com/products/super-sap-1001000>.
- [13] R. Masoodi, R. F. El-Hajjar, K. M. Pillai, and R. Sabo, “Mechanical characterization of cellulose nanofiber and bio-based epoxy composite,” *Materials and Design*, vol. 36, pp. 570–576, 2012.
- [14] J. R. Vinson, *The Behavior of Sandwich Structures of Isotropic and Composite Materials*, CRC Press, 1999.

## Research Article

# Materials Selection, Synthesis, and Dielectrical Properties of PVC Nanocomposites

Youssef Mobarak,<sup>1,2</sup> M. Bassyouni,<sup>3,4</sup> and M. Almutawa<sup>5</sup>

<sup>1</sup> Electrical Engineering Department, King Abdulaziz University, Rabigh 21911, Saudi Arabia

<sup>2</sup> Electrical Engineering Department, Faculty of Energy Engineering, Aswan University, Sahari City 81528, Egypt

<sup>3</sup> Chemical and Materials Engineering Department, King Abdulaziz University, Rabigh 21911, Saudi Arabia

<sup>4</sup> Chemical Engineering Department, Higher Technological Institute, Tenth of Ramadan City 11111, Egypt

<sup>5</sup> Faculty of Science, King Abdulaziz University, Jeddah 21589, Saudi Arabia

Correspondence should be addressed to M. Bassyouni; [migb2000@hotmail.com](mailto:migb2000@hotmail.com)

Received 12 March 2013; Revised 20 May 2013; Accepted 21 May 2013

Academic Editor: Mohd Sapuan Salit

Copyright © 2013 Youssef Mobarak et al. This is an open access article distributed under the Creative Commons Attribution License, which permits unrestricted use, distribution, and reproduction in any medium, provided the original work is properly cited.

Materials selection process for electrical insulation application was carried out using Cambridge Engineering Selector (CES) program. Melt mixing technique was applied to prepare polyvinyl-chloride- (PVC-) nanofumed silica and nanomontmorillonite clay composites. Surface analysis and particles dispersibility were examined using scanning electron microscope. Dielectrical properties were assessed using Hipot tester. An experimental work for dielectric loss of the nanocomposite materials has been investigated in a frequency range of 10 Hz–50 kHz. The initial results using CES program showed that microparticles of silica and clay can improve electrical insulation properties and modulus of elasticity of PVC. Nano-montmorillonite clay composites were synthesized and characterized. Experimental analyses displayed that trapping properties of matrix are highly modified by the presence of nanofillers. The nanofumed silica and nanoclay particles were dispersed homogenously in PVC up to 10% wt/wt. Dielectric loss tangent constant of PVC-nanoclay composites was decreased successfully from 0.57 to 0.5 at 100 Hz using fillers loading from 1% to 10% wt/wt, respectively. Nano-fumed silica showed a significant influence on the electrical resistivity of PVC by enhancing it up to  $1 \times 10^{11}$  Ohm-m.

## 1. Introduction

Nanocomposites represent a very attractive route to upgrade and diversify properties of the polymers. Nanofiller-filled polymers might be differentiated from microfiller-filled polymers in three major aspects that the nanocomposites normally contain smaller amounts, are in range of nanometers in size, and have tremendously large specific surface area. All these characteristics are reflected in their material properties [1–3]. Fillers are added to polymeric materials in order to enhance physical and mechanical properties [4–7]. Over the past few years, there have been few numbers of researches on the effect of fillers on di-electric properties of polymers [8–10]. The shift from ceramic electrical insulating materials (e.g., porcelain and glass) and from oil-paper insulations to polymeric materials has been the major change in the field of

high voltage insulation technology [11–13]. Today polymers are widely used in most of the high voltage equipment, for example, power transformers, insulators, capacitors, reactors, surge arresters, current and voltage sensors, bushings, power cables, and terminations. The huge scenarios of new polymer composites in high voltage technology inspire the researchers of the field to innovate new materials and to study their properties [14–16]. There is a need for developing a range of compact devices and accessories, for both outdoor and indoor conditions, in which novel and more reliable insulation systems will play the key role [17–19]. Nanomaterials, in form of polymeric nanocomposites, are foreseen as excellent candidates which are able to fulfill the new requirements [20–22]. Elemental properties are usually integrated over macroscopic volumes to reach explanations for macroscopic properties [23–26]. The new developments in nanoscience

TABLE 1: Physical and mechanical properties of polyvinyl chloride.

Physical and mechanical properties of polyvinyl chloride (Sabic, Saudi Arabia)	
Young's modulus	3.2 MPa
Shear modulus	1.2 MPa
Bulk modulus	1.8 GPa
Poisson's ratio	0.49
Yield strength (elastic limit)	10 MPa
Tensile strength	10 MPa
Compressive strength	20 MPa
Flexural strength (modulus of rupture)	11 MPa
Hardness—Shore D	12
Heat deflection temperature at 455 KPa	-30°C

and technology stop short of the final integration and consider what special properties are present at the nanometric level and how they might be exploited [26, 27].

PVC is widely used in industrial applications. Chemically, PVC has a structure which is similar to that of PE but instead of several hydrogen atoms, it has chlorine atoms, which are attached to the molecular chains at the side in a random manner [28–30]. Also, it has excellent forming properties, is suitable for extreme thermoforming requirements, chemically resistant, UV-stabilized, weather resistant, and has increased impact resistance [31–33]. PVC is stronger and more rigid than other general purpose thermoplastic materials. It has a high tensile strength and modulus of elasticity. Additives are used to further specific end use, such as thermal stabilizers, lubricity, impact modifiers, and pigmentation. PVC is basically tough and strong, resists water and abrasion, and is an excellent electrical insulator [34–36].

## 2. Experimental

**2.1. Materials Selection for Electrical Insulation and Mechanical Properties Using CES Program.** Effect of silica and clay particles on the performance of PVC can be governed by the mechanical and electrical properties. CES program (Granta Design Company) was initially used to predict the desired properties of PVC composites using different fillers (microscale)/matrix mixing ratio. Synthesis and manufacturing of PVC composites were carried out based on the obtained results using CES program.

**2.2. Raw Materials and Equipment.** Polyvinylchloride (PVC) was received from petrochemical company (Sabic, Saudi Arabia). Physical and mechanical properties of PVC are listed in Table 1. Treated nano-montmorillonite clay was purchased from Sigma Aldrich. It is montmorillonite clay (Nanomer 1.30E), clay surface modified with 25–30 wt% octadecylamine. Spherical particle shape is the most important characteristic of nanoclay for polymer applications. The platy nature of clay fillers has a greater effect on properties such as viscosity, stiffness, and strength. Using clay as nanofiller gives

high levels of flame retardancy to produced composite. Nano-fumed silica powder was obtained from Sigma Aldrich.

Hipot Tester (HIOKI 3522-50 LCR Hi-tester) device is used to measure electrical parameters of nanocomposites at various frequencies:  $|Z|$ ,  $|Y|$ ,  $\theta$ , Rp (DCR), Rs (ESR, DCR), G, X, B, Cp, Cs, Lp, Ls, D ( $\tan \delta$ ), and Q. Specification of LCR is power supply: 100, 120, 220, or 240 V ( $\pm 10\%$ ) AC (selectable), 50/60 Hz, frequency: DC, 1 mHz to 100 kHz, and display. Voltage rating is 220 V AC 50 Hz, test voltage is 0~5 KV (adjustable), and output capacity is up to 1 KVA, cutoff current. PVC was mixed and pressed with nanofillers using two roll mills made of cast iron rolls, barrel dimensions 6"  $\times$  16", working length 14", and motor capacity 7.5 HP. The samples were dried using vacuum-drying oven, at 100°C for 12 hours. Samples morphology was analyzed using scanning electron microscope (JEOL model JXA 840A (ADS+OM-Japan)). Monolayer of gold atoms was induced using gold sputter coater (S150 from Edwards for 6 min vacuum at 40 mA).

**2.3. Synthesis of Polyvinylchloride Composites.** Two sets of PVC composites were prepared. In the first set, PVC was composited with nano-fumed silica (1–10% wt/wt). Fumed silica was mixed and heated up to 200°C for 8 min using corotating twin-screw extruder (Berstorff ZE25A, Hannover, Germany) at 300 rpm. The compounded materials were ground and rolled at 185°C to obtain thin film (thickness of  $1 \pm 0.01$  mm). PVC-fumed silica composites were obtained under 25 MPa and 185°C for 5 min using hot press. In the second set, polyvinylchloride nanomontmorillonite clay was obtained using typical techniques and operating conditions.

**2.4. Characterization of PVC Composites.** Electrical and surface analysis of PVC-nanostructured material specimen were carried out. This was achieved by measuring dielectric properties losses, electrical resistivity, and SEM analysis. These tests are able to identify the best combination of polymers—nanofillers in addition to the optimum fillers loading, in terms of improved dielectric strength and smaller space charge accumulation.

**2.4.1. Electrical Properties.** Dielectric spectroscopy is a powerful experimental method to investigate the dynamical behavior of a sample through the analysis of its frequency-dependent dielectric response. This technique is based on the measurement of the dielectric loss constants as a function of frequency of a sample sandwiched between two electrodes. The  $\tan \delta$  and susceptance (B) were measured as a function of frequency in the range from 10 Hz to 50 kHz at 25°C for all test specimens. The measurements were made using high resolution dielectric spectroscopy.

**2.4.2. SEM Analysis.** The morphology and dimensions of the PVC composites were tested using scanning electron microscopy. Specimens were cut in liquid nitrogen and then coated with nanogold layers using a sputter coater to make them conductive.

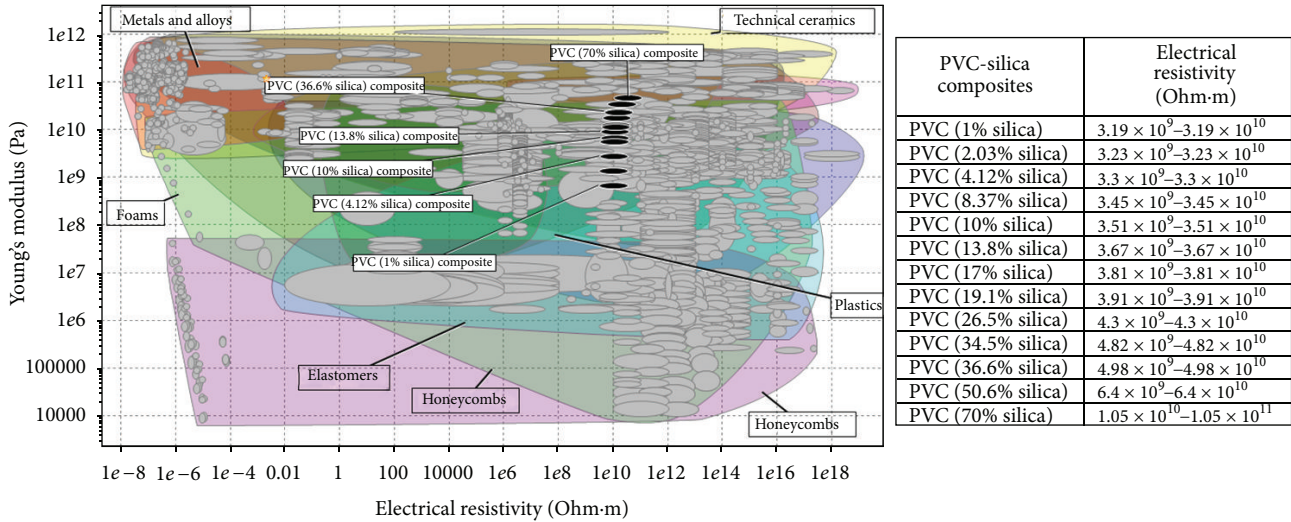


FIGURE 1: Electrical resistivity and mechanical properties of PVC-silica using CES program.

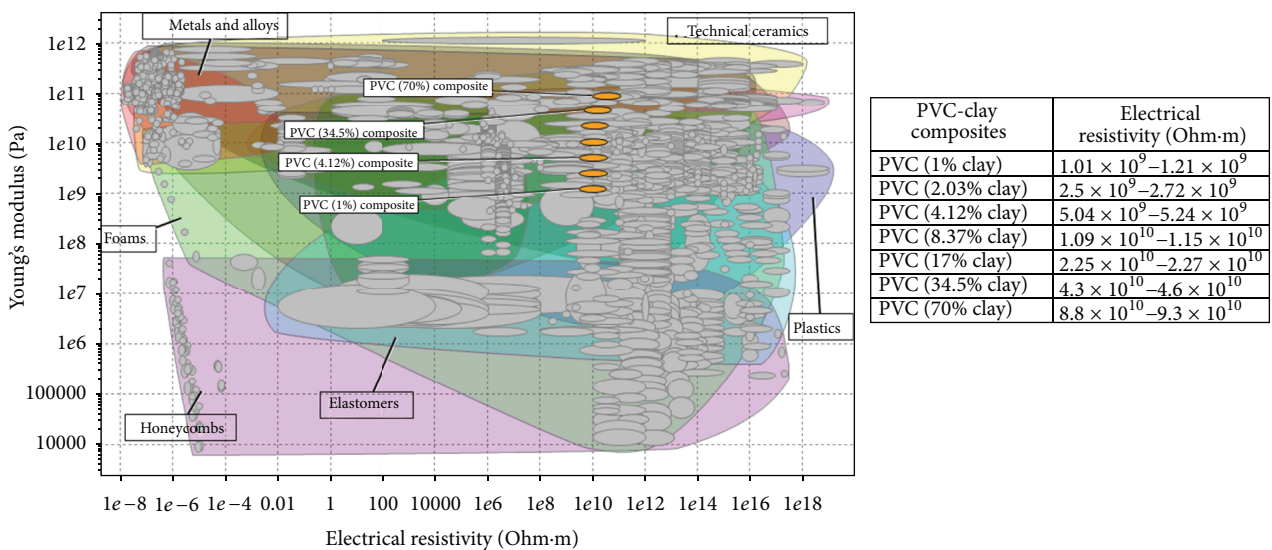


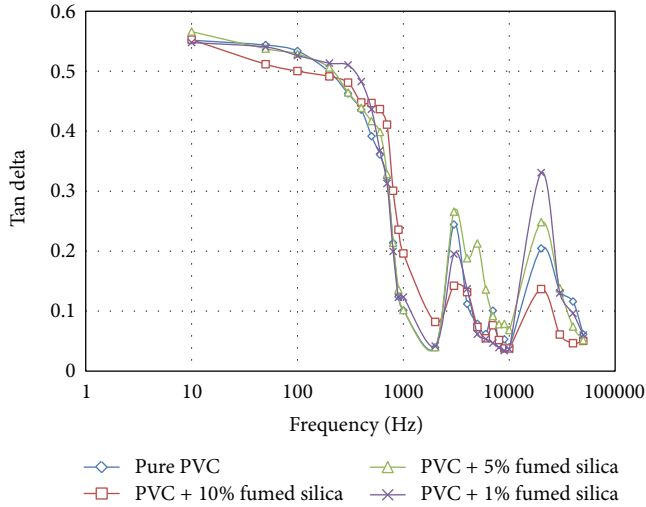
FIGURE 2: Electrical resistivity and mechanical properties of PVC-clay using CES program.

### 3. Results and Discussion

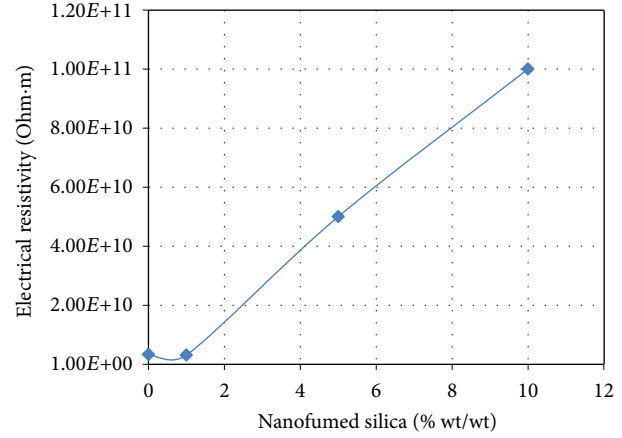
**3.1. Predictable Mechanical and Electrical Behavior of PVC-Silica Composites.** Figure 1 illustrates the electrical and mechanical properties of PVC-silica composites using CES software. Addition of silica to PVC leads to improving the electrical resistivity of PVC. It is detected that the electrical resistivity can be increased up to  $5.0 \times 10^{10}$  Ohm-m (mean value) using 70% silica wt/wt. This can be attributed to the high electrical resistivity of silica ( $1.0 \times 10^{12}$ – $1.0 \times 10^{13}$  Ohm-m) comparing with lower electrical resistivity value of PVC matrix ( $3.16 \times 10^9$ – $3.16 \times 10^9$  Ohm-m). Modulus of elasticity of PVC was increased from 3 GPa to 72 GPa in the presence of 70% wt/wt silica.

**3.2. Predictable Electrical and Mechanical Behavior of PVC-Clay Composites.** Figure 2 illustrates the electrical and mechanical properties of PVC-clay composites using CES software. The initial results using the predictable model (CES software) showed that addition of clay particles to PVC can cause an increase in the electrical resistivity and modulus of elasticity. The clay fillers loading is between 1 and 70% wt/wt. Electrical resistivity was increased from  $1.1 \times 10^9$  to  $9 \times 10^{10}$  Ohm-m (mean value). Modulus of elasticity was improved significantly from 3.190 GPa to 93.30 GPa with respect to clay fillers loading 1 to 70% wt/wt.

**3.3. Effect of Nanofumed Silica on Electrical Insulation of PVC.** Figure 3(a) shows loss tangent as a function of frequency

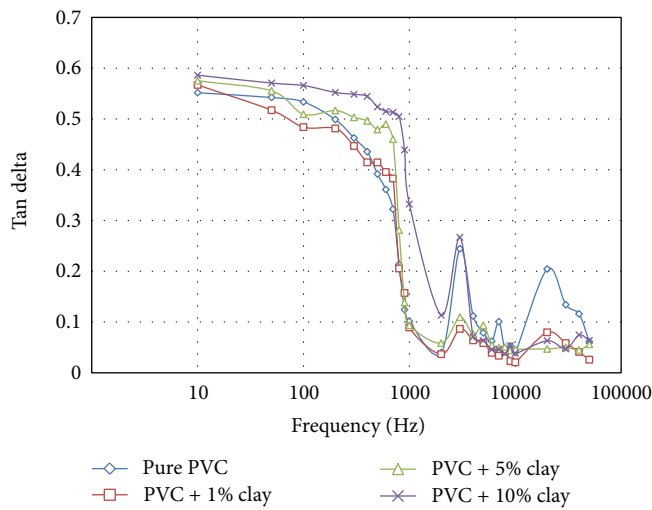


(a)

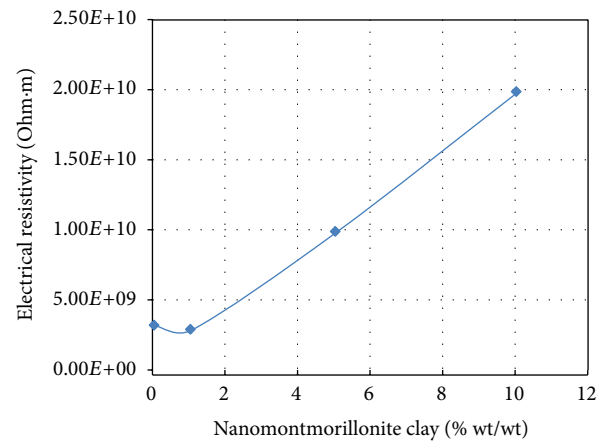


(b)

FIGURE 3: Measured loss tangent (a) and resistivity of PVC nano fumed silica.



(a)



(b)

FIGURE 4: Measured loss tangent (a) and resistivity of PVC-nano montmorillonite clay.

PVC-nano fumed silica at room temperature (25°C). It is depicted that the loss tangent of PVC nanocomposites increased with increasing the fumed silica loading. The addition of nano-fumed silica from 5 to 10% wt/wt effectively improved the loss tangent values. However, it can be observed that the loss tangent does not enhance below 5 wt%. This can be attributed to the presence of voids at PVC-nano fumed silica interphase due to low melt flow around the nanofumed silica [36]. Electrical resistivity of PVC-nano fumed silica showed higher values than the CES program results (see Figure 3(b)). This can be attributed to the influence of using nanoscale fillers (larger specific area).

**3.4. Effect of Nanomontmorillonite Clay on PVC Electrical Properties.** Figure 4(a) shows loss tangent as a function of frequency for PVC-nanomontmorillonite clay composites at

room temperature (25°C). It is clear that the loss tangent of PVC nanocomposites decreases with the increasing frequency, while it increases with increasing clay percentage of nanofillers up to 10% wt. This can be attributed to low response of the PVC dipole to follow the system variations at high frequency [37]. Figure 4(b) shows resistivity as a function of nano-montmorillonite clay loading at room temperature 25°C. The electrical resistivity of PVC-nanomontmorillonite clay composites increases with increasing nanoclay. It is noticed that the resistivity was decreased below 1% nanomontmorillonite clay which has the same behavior as PVC-nano fumed silica composite.

**3.5. SEM Analysis.** Microstructure studies were carried out in order to detect voids or agglomerates which can be formed through polymer composite processing. SEM images

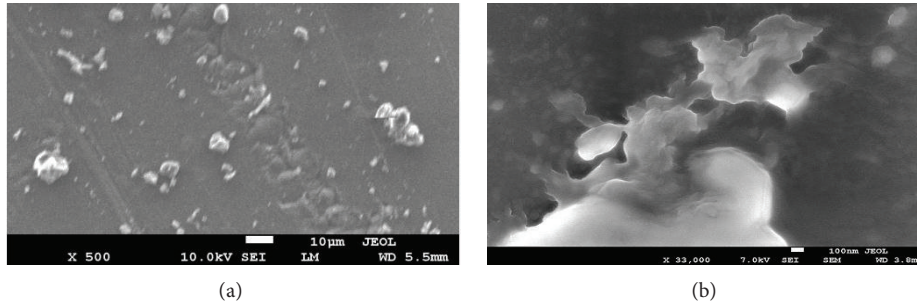


FIGURE 5: SEM analysis of PVC nanocomposites (10% wt/wt): (a) nanoclay composites, (b) nanofumed silica.

for PVC composites with nano-montmorillonite and nanofumed silica fillers have been obtained as shown in Figures 5(a) and 5(b). It is depicted that nano fillers are homogenously dispersed up to 10% wt/wt. Nanoclay surface treatment using octadecylamine promotes better dispersion of the nanoclay fillers in PVC matrix.

#### 4. Conclusions

As the electrical insulation of PVC composites contribute to its tan delta value, the variation of tan delta value in net PVC nanocomposites in lower frequency range may result in the electrical insulation of the nanocomposites having been affected by the presence of nanosize fillers. As this study was carried out under constant temperature, the influence of the relaxation time of the charge carriers on the electrical insulation of PVC nanocomposites can be ignored. Thus, the number of charge carriers and applied frequency become dominating factors of the electrical insulation of PVC nanocomposites. The presence of nanosize fillers inside PVC will restrict the chain mobility and result in increasing electric insulation as such restriction limited the generation of mobile charge and the movement of charge carriers in polymer dielectrics, especially at a lower frequency range where the insulation will play an important role. Thus, the variation of tan delta value at low frequency range may be due to the influence of inorganic fillers' electrical insulation.

#### Acknowledgment

The present work was supported by the Deanship of Scientific Research, King Abdulaziz University, Saudi Arabia, Project ID: 1432/829/388.

#### References

- [1] T. Lan and T. J. Pinnavaia, "Clay-reinforced epoxy nanocomposites," *Chemistry of Materials*, vol. 6, no. 12, pp. 2216–2219, 1994.
- [2] W. Feng, A. Ait-kadi, and B. Riedl, "Polymerization compounding: epoxy-montmorillonite nanocomposites," *Polymer Engineering and Science*, vol. 42, no. 9, pp. 1827–1835, 2002.
- [3] M. Sh. Zoromba, M. Bassyouni, and A. Dahshan, "Preparation and mechanico-optical properties of ultraviolet-curable transparent polyurethane elastomer nanocomposites," *Journal of Nanotechnology in Engineering and Medicine*, vol. 3, no. 1, Article ID 011008, 5 pages, 2012.
- [4] M. Bassyouni, S. A. Sherif, M. A. Sadek, and F. H. Ashour, "Synthesis and characterization of polyurethane—treated waste milled light bulbs composites," *Composites B: Engineering*, vol. 43, no. 3, pp. 1439–1444, 2012.
- [5] M. Bassyouni, I. Taha, S. M.-S. Abdel-Hamid, and L. Steuernagel, "Physico-mechanical properties of chemically treated polypropylene rice straw bio-composites," *Journal of Reinforced Plastics and Composites*, vol. 31, no. 5, pp. 303–312, 2012.
- [6] S. A. Gutub, M. Bassyouni, and S. M. S. Abdel-Hamid, "Dissolved solids adsorption of freshwater using synthesized bio-foam composite," *Life Science Journal*, vol. 10, no. 2, pp. 464–471, 2013.
- [7] S. A. Sheriff, M. A. Sadek, F. H. Ashour, and M. Bassyouni, "Effects of surface treatment of ground rice husk on the polyurethane based on castor oil," *Polymers and Polymer Composites*, vol. 17, no. 8, pp. 481–485, 2009.
- [8] A. Z. Simeões and C. S. Riccardi, "Dielectric spectroscopy analyses of SrBi4Ti4O 15 films obtained from soft chemical solution," *Advances in Materials Science and Engineering*, vol. 2009, Article ID 928545, 6 pages, 2009.
- [9] C. Y. Lai, S. M. Sapuan, M. Ahmad, N. Yahya, and K. Z. H. M. Dahlan, "Mechanical and electrical properties of coconut coir fiber-reinforced polypropylene composites," *Polymer - Plastics Technology and Engineering*, vol. 44, no. 4, pp. 619–632, 2005.
- [10] T. Imai, F. Sawa, T. Yoshimitsu, T. Ozaki, and T. Shimizu, "Preparation and insulation properties of epoxy-layered silicate nanocomposite," in *Proceedings of IEEE Conference on Electrical Insulation and Dielectric Phenomena (CEIDP '04)*, pp. 402–405, October 2004.
- [11] D. A. Bolon, "Epoxy chemistry for electrical insulation," *IEEE Electrical Insulation Magazine*, vol. 11, no. 4, pp. 10–18, 1995.
- [12] R. S. Gorur, E. A. Cherney, and J. T. Burnham, *Outdoor Insulators*, Ravi S Gorur, Phoenix, Ariz, USA, 1999.
- [13] R. Hackam, "Outdoor HV composite polymeric insulators," *IEEE Transactions on Dielectrics and Electrical Insulation*, vol. 6, no. 5, pp. 557–585, 1999.
- [14] L. H. Meyer, E. A. Cherney, and S. H. Jayaram, "The role of inorganic fillers in silicone rubber for outdoor insulation—alumina tri-hydrate or silica," *IEEE Electrical Insulation Magazine*, vol. 20, no. 4, pp. 13–21, 2004.
- [15] T. J. Lewis, "Nanometric dielectrics," *Philosophical Transactions of the Royal Society, London*, vol. A247, pp. 529–551, 1994.
- [16] C. Green and A. Vaughan, "Nanodielectrics—how much do we really understand?" *IEEE Electrical Insulation Magazine*, vol. 24, no. 4, pp. 6–16, 2008.

- [17] B. Venkatasulu and M. J. Thomas, "Erosion resistance of silicone rubber nanocomposites at lower filler loadings," in *Proceedings of International Symposium on High Voltage Engineering (ISH '09)*, pp. 1–6, 2009.
- [18] B. Venkatesulu and M. J. Thomas, "Studies on the tracking and erosion resistance of RTV silicone rubber nanocomposite," in *Proceedings of Annual Report Conference on Electrical Insulation and Dielectric Phenomena (CEIDP '08)*, pp. 204–207, October 2008.
- [19] I. Ramirez, E. A. Cherney, S. Jayaram, and M. Gauthier, "Silicone rubber nanocomposites for outdoor insulation applications," in *Proceedings of Annual Report Conference on Electrical Insulation and Dielectric Phenomena (CEIDP '07)*, pp. 384–387, October 2007.
- [20] G. Iyer, R. S. Gorur, R. Richert, A. Krivda, and L. E. Schmidt, "Dielectric properties of epoxy based nanocomposites for high voltage insulation," *IEEE Transactions on Dielectrics and Electrical Insulation*, vol. 18, no. 3, pp. 659–666, 2011.
- [21] M. S. Naidu and V. Karamaju, *High Voltage Engineering*, Tata McGraw-Hill, Noida, India, 3rd edition, 2004.
- [22] R. I. Buhl, J. Brandrup, M. Bitterner, W. Michaeli, and G. Menges, *Recycling and Recovery of Plastics*, Carl Hanser, Munich, Germany, 1996.
- [23] M. E. Bassiouni, F. Al-Shamy, N. K. Madi, and M. E. Kassem, "Temperature and electric field effects on the dielectric dispersion of modified polyvinyl chloride," *Materials Letters*, vol. 57, no. 9–10, pp. 1595–1603, 2003.
- [24] X.-L. Xie, R. K.-Y. Li, Q.-X. Liu, and Y.-W. Mai, "Structure-property relationships of in-situ PMMA modified nano-sized antimony trioxide filled poly(vinyl chloride) nanocomposites," *Polymer*, vol. 45, no. 8, pp. 2793–2802, 2004.
- [25] M. M. Ueki and M. Zanin, "Influence of additives on the dielectric strength of high-density polyethylene," *IEEE Transactions on Dielectrics and Electrical Insulation*, vol. 6, pp. 876–881, 1999.
- [26] G. Wypych, *Handbook of Fillers*, Transcontinental Printing, Quebec, Canada, 2nd edition, 1999.
- [27] N. Fuse, Y. Ohki, and T. Tanaka, "Comparison of nano-structure effects in polypropylene among four typical dielectric properties," *IEEE Transactions on Dielectrics and Electrical Insulation*, vol. 17, no. 3, pp. 671–677, 2010.
- [28] M. Takala, H. Ranta, P. Nevalainen et al., "Dielectric properties and partial discharge endurance of polypropylene-silica nanocomposite," *IEEE Transactions on Dielectrics and Electrical Insulation*, vol. 17, no. 4, pp. 1259–1267, 2010.
- [29] M. Ambid, D. Mary, G. Teyssedre et al., "Effect of filler concentration on dielectric behaviour and on charge trapping in PP/clay nanocomposites," in *Proceedings of Annual Report Conference on Electrical Insulation and Dielectric Phenomena (CEIDP '04)*, pp. 389–392, October 2004.
- [30] L. Bois, F. Chassagneux, S. Parola et al., "Growth of ordered silver nanoparticles in silica film mesostructured with a triblock copolymer PEO-PPO-PEO," *Journal of Solid State Chemistry*, vol. 182, no. 7, pp. 1700–1707, 2009.
- [31] A. Usuki, Y. Kojima, M. Kawasumi et al., "Synthesis of nylon 6-clay hybrid," *Journal of Materials Research*, vol. 8, no. 5, pp. 1179–1184, 1993.
- [32] M. Ochi, R. Takahashi, and A. Terauchi, "Phase structure and mechanical and adhesion properties of epoxy/silica hybrids," *Polymer*, vol. 42, no. 12, pp. 5151–5158, 2001.
- [33] P. O. Henk, T. W. Kortsens, and T. Kvarts, "Increasing the electrical discharge endurance of acid anhydride cured DGEBA epoxy resin by dispersion of nanoparticle silica," *High Performance Polymers*, vol. 11, no. 3, pp. 281–296, 1999.
- [34] A. Thabet and Y. A. Mobarak, "A model for dielectric characterization of nanocomposite polymeric industrial materials," *Journal of Engineering Sciences*, vol. 40, no. 5, 2012.
- [35] A. Thabet and Y. A. Mobarak, "Experimental study for dielectric strength of new nanocomposite polyethylene industrial materials," *International Journal of Electrical Engineering and Technology*, vol. 3, no. 1, pp. 553–564, 2012.
- [36] A. Thabet and Y. A. Mobarak, "Dielectric characteristics of new nano-composite industrial materials," in *Proceedings of International Conference on High Voltage Engineering and Application (ICHVE '10)*, pp. 568–571, New Orleans, La, USA, October 2010.
- [37] V. Raja, A. K. Sharma, and V. V. R. N. Rao, "Impedance spectroscopic and dielectric analysis of PMMA-CO-P4VPNO polymer films," *Materials Letters*, vol. 58, no. 26, pp. 3242–3247, 2004.

## Research Article

# Experimental and Theoretical Investigations of the Impact Localization of a Passive Smart Composite Plate Fabricated Using Piezoelectric Materials

**M. M. S. Dezfouli,<sup>1</sup> Mohd Roshdi Hassan,<sup>2</sup> Mohd Hafidz Ruslan,<sup>1</sup> Sohif Mat,<sup>1</sup> and B. Bakhtyar<sup>3</sup>**

<sup>1</sup> *Solar Energy Research Institute (SERI), National University of Malaysia (UKM), 43600 Bangi, Selangor, Malaysia*

<sup>2</sup> *Department of Mechanical and Manufacturing Engineering, University Putra Malaysia, 43400 Serdang, Selangor, Malaysia*

<sup>3</sup> *SEFB, COB, University Utara Malaysia (UUM), 6010 Sintok, Kedah, Malaysia*

Correspondence should be addressed to M. M. S. Dezfouli; [salehi.solar@yahoo.com](mailto:salehi.solar@yahoo.com)

Received 18 February 2013; Revised 6 May 2013; Accepted 8 May 2013

Academic Editor: Mohd Sapuan Salit

Copyright © 2013 M. M. S. Dezfouli et al. This is an open access article distributed under the Creative Commons Attribution License, which permits unrestricted use, distribution, and reproduction in any medium, provided the original work is properly cited.

Two passive smart composite plates are fabricated using one and two PZT patches that are cheaper than the PZT wafer. The composite plate is fabricated in low temperature through the hand lay-up method to avoid PZT patch decoupling and wire spoiling. The locus of the impact point is identified using the output voltage to identify the impact location using one sensor. The output voltages of the sensors are analyzed to identify the impact location using two sensors. The locations of the impacts are determined based on the crossing points of two circles and the origin of an intended Cartesian coordinate system that is concentric with one of the sensors. This study proposes the impact location identification of the passive smart composite using the low-cost PZT patch PIC155 instead of common embedded materials (wafer and element piezoelectric).

## 1. Introduction

Structural health monitoring systems have recently been developed for various applications. Numerous studies on the different aspects of smart structure systems have been conducted by physicists and engineers in the fields of aerospace, mechanics, and civil engineering [1]. The smart structure system comprises both the host structure, including a laminate composite beam, and the sensing elements (actuators), including piezoceramic patches [2]. The widespread development regarding these systems is caused by the importance and variety of applications of the system in different engineering sciences such as aircraft wing, submarine sterns, and vibration control [3].

One of the most important applications of the systems is the evaluation of the structures of the composite for impact damage and Acoustic Emission (AE), which is applied in damage detection [4, 5]. Numerous researchers have evaluated acoustic wave propagation and damage detection

by embedding or bonding PZT (lead zirconate titanate or piezoelectric ceramic material) sensors/actuators in the composite structure. Studies in the field of damage detection on the use of the PZT sensors/actuators can be divided to active and piezocomposite categories [6].

Active systems use a sensor to detect damage and an actuator. The actuator receives an input voltage and actuates the structure of the composite plate. The resulting acoustic wave is propagated in the composite. The PZT sensor shows an output signal after receiving the AE wave. If the composite structure has damage, the output signal of the PZT signal is changed. The changes of the signal are evaluated and analyzed by comparing the signal waves before and after the damage [7, 8]. Passive systems only use the PZT sensor because the AE created by the impact is propagated through the structure of the composite [9]. The damage detection is analyzed after the PZT sensor receives the AE wave [9]. Guan and Yang monitored the impact damages in the composite laminate to evaluate the output acoustic wave [10]. These researchers

proved that the AE wave caused by impact includes important information that describes the composite structure based on the availability or unavailability of the damage. Evaluating the impact behavior of the composite laminate to detect the structural properties of the composite is very complicated; thus, different analysis methods were employed by numerous researchers. Sung et al. analyzed [11] the output signal on the time-frequency domains through the wavelet transform (WT) method and by monitoring the impact on a composite laminate that includes a bonded PZT sensor. In this method, the characteristics of the AE waves made by impact were analyzed in the passive sending diagnosis (PSD) system on time-frequency domains. Red et al. evaluated the damage detection by the expressing WT as a signal process technique that includes Fourier transforms. Su et al. [12] evaluated the damage identification system, which includes a bonded PZT on a composite bead, based on the acoustic wave propagated by the impact damage.

Diamanti et al. successfully detected the impact damage on a carbon-fiber-reinforced plastic (CFRP) laminate using a PZT patch attached on the composite surface [13]. These researchers detected impact damage by investigating the propagation of the lamb wave and through finite element analysis. Ghoshal et al. evaluated the damage detection based on stress wave parameters by simulating the acoustic wave propagation on a quasi-isotropic glass-epoxy plate that includes a bonded PZT patch based [14]. The previous studies revealed that the PZT patch bonded on the composite plate and embedded piezoelectric materials [15–20], which were used in the previous studies [20–24], could replace other kinds of piezoelectric materials, such as the wafer, that are more expensive than the PZT patch. Therefore, this study fabricates a piezocomposite plate, including four fiberglass layers with one embedded PZT patch through its two intermediate layers through the cut-out method. This paper also investigates the output voltage from the PZT patch through the impact force on the piezocomposites with one PZT patch and two PZT patches.

## 2. Material and Methods

Three methods are available for inserting the PZT patch through composite layers:

- (1) smart layer;
- (2) inserting without cut-cut;
- (3) cut-out method.

Previous studies on embedding piezoelectric materials mainly focused on the application of the PZT wafer using the cut-out method and the application of PZT element using the smart layer method. The current study accordingly employs a PZT patch to embed the materials in the composite layers through the cut-out method by presenting a cost effective design. The cut-out method used in this study to fabricate smart plate and composite materials includes PZT patches, fiberglass rowing, and epoxy.

The piezoelectric materials are the PZT patch PIC155—PI Ceramic GmbH (from Germany) is a circular disc with

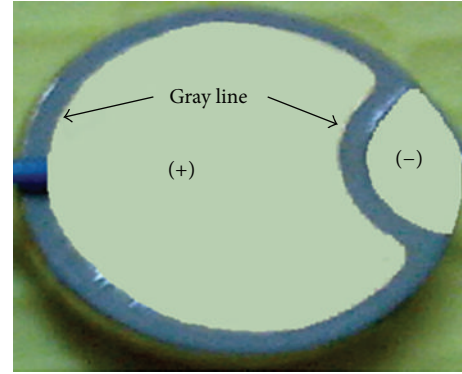


FIGURE 1: PZT patch sensor (PIC155).

TABLE 1: Physical and dielectric properties PIC 155.

Parameter	Abbreviation	PIC 155 (PZT)
Density	$\rho$ (g/cm <sup>3</sup> )	7.80
Curie temperature	$T_c$ (°C)	345
Permittivity		
In the polarization direction	$\epsilon_{33}^T$	1450
Perpendicular to the polarity	$\epsilon_{11}^T$	1400
Dielectric loss factor	$\tan \delta$ ( $10^{-3}$ )	20

TABLE 2: Mechanical properties of epoxy BBT 7892.

Mechanical properties	Amount
Tensile strength (psi)	9,800
Tensile modulus (psi)	420,000
Elongation at break (%)	4.9
Flexural strength (psi)	147,000
Flexural modulus (psi)	510,000
Compress strength (psi)	11,900

a 1 mm thickness and 10 mm diameter as shown in Figure 1. A gray line shaped like an incomplete circle separates the positive pole (+) of sensor from the negative pole (-).

The interior of the gray circle is the positive pole. The exterior and the sheet behind the sensor are the negative pole. Table 1 shows the physical and dielectric properties of PIC 155.

The fiberglass is an E-glass fiber woven roving (04 XINGDA-DIY Trade-from China) with a 0.25 mm thickness for each of the layers. The epoxy resin is Epoxy BBT 7892 (Berjaya Bintang Timur Sdn, Bhd Malaysia). Epoxy BBT-7892 is a two-component liquid epoxy system specially designed for the wet lay-up laminating process in composite applications. This epoxy resin provides good wetting to most of the composite materials. The details of the properties of BBT-7892 are shown in Table 2.

The process of fabricating the composite plate with the embedded PZT patch has five steps: (i) preparing the mold and epoxy resin, (ii) cut-out fiberglass, (iii) soldering the PZT sensor to the wire, (iv) embedding the PZT sensor into

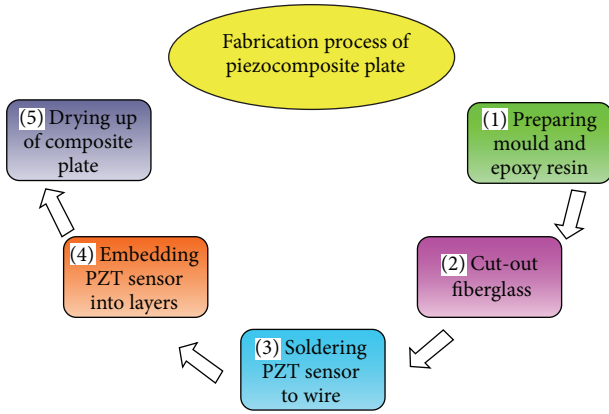


FIGURE 2: Flowchart of fabrication process of piezocomposite plate.

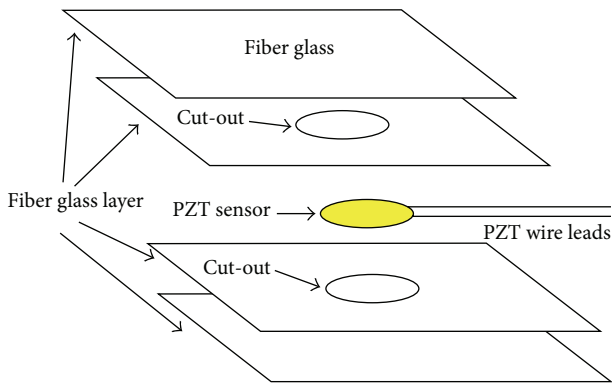


FIGURE 3: Schematic of the embedded piezoelectric into the composite by cut-out method.

layers, and (v) drying up the composite plate. Figure 2 shows the flowchart of the fabrication process of the piezocomposite plate.

Three piezocomposite plates with different specifications were fabricated in this study based on the fabrication process of the composite plate with embedded PZT.

**2.1. Fabrication of Piezocomposite Plate with One PZT Patch.** The first sample plate included one PZT patch and four layers. The fibers of the first and fourth layers had an angle of  $45^\circ$  with the fibers of second and third layers ( $45^\circ/90^\circ/90^\circ/45^\circ$ ). In this study, this sample will be called “Sample 1.”

One symmetric point in the middle layers of the composite plate was purposely cut-out with the same size as the PZT sensors to embed the sensor in the composite plate (Figure 3).

The plastic sheet holder of the first composite layer was placed on the mold. Next, the second and third layers (cut-out layers) were placed on the first layer, where the fibers of second and third layers had an angle of  $45^\circ$  with the fibers of the first layer (Figure 4).

**2.2. Fabrication of Piezocomposite Plate with Two PZT Patches.** The second sample plate had two PZT patches and four

fiberglass layers. The lay-up of layers was similar to that of Sample 1. In this research, this sample will be called “Sample 2”. Two symmetric points with a distance of 12.5 cm in the middle layers of the composite plate were purposely cut-out in the same size as the PZT sensors to embed the sensors in the composite plate. The PZT patches were then completely inserted through the empty space between the intermediate layers during lay-up processing. Finally, the last layer was placed on the top. After placing each layer, the empty spaces and the bubbles between the layers were reduced using a pressing roller. The last layering step was the placement of the fourth layer on the three layers. The fiber on the fourth layer had an angle of  $45^\circ$  with the second and third layers. The lay-up of the composite plate had four layers, and the fibers of the first and the fourth layers had an angle of  $45^\circ$  with the fibers of the second and third layers. Finally, the product was dried in environmental temperature ( $30^\circ\text{C}$ ) based on the sensitivity of the PZT sensor to the temperature. After dry-up step, a  $14\text{ cm} \times 19.5\text{ cm}$  composite plate was fabricated; thus, the distance of each sensor to the edge of the composite was 3 cm and the distance between the two sensors was 12.5 cm.

### 3. Experimental Setup

One of the aims of this study is to investigate the behavior of the output signal because of the impact test on the composite plate with the embedded PZT sensor. The process of the impact test included the production of force using an impact test machine on the composite plate to study the behavior of the composite and the embedded PZT sensor. Figure 5 shows the impact test process, which includes four steps. In the first step, impact was produced using the impact machine on the piezocomposite plate. In the second step, the stress caused by the impact as a mechanical wave was propagated in the plate until reaching the PZT sensor.

In the third step, the crystal structure of the PZT sensor was strained by the effect of the stress because of the impact and made an electrical flow. In the fourth step, the output electrical flow was monitored on the oscilloscope screen in the form of a signal wave (Figure 6).

If an impact happens on point A of the composite with the PZT Patch, stress is produced. This stress is propagated in form of a mechanical wave through the composite plate and reaches point B near the PZT patch. If the pressure on point A and B is equal to  $P_A$  and  $P_B$ , respectively,  $P_B$  is less than  $P_A$  ( $P_B < P_A$ ). This relation is proven through an analysis of the deformation of an element in the one-dimensional stress in Section 3.2.

**3.1. Impact Load.** Figure 7 shows that the impact on the composite plate is produced by releasing rod from a certain height ( $h$ ) on the composite plate. The approach velocity of the rod can be obtained using (1)

$$V^2 - V_0^2 = 2g(h - h_0), \quad (1)$$

where  $V$  is the velocity of the rod striking the composite plate,  $V_0$  is the velocity of rod released at zero (m/s),  $h$  is the height

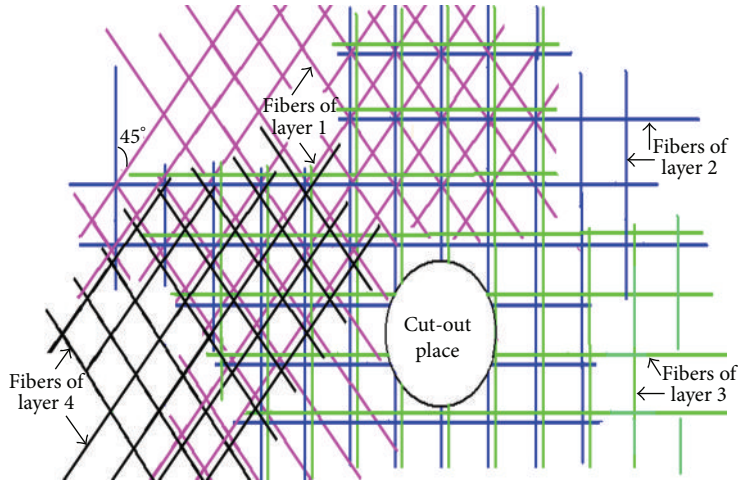


FIGURE 4: Schematic of the Sample 2 structure.

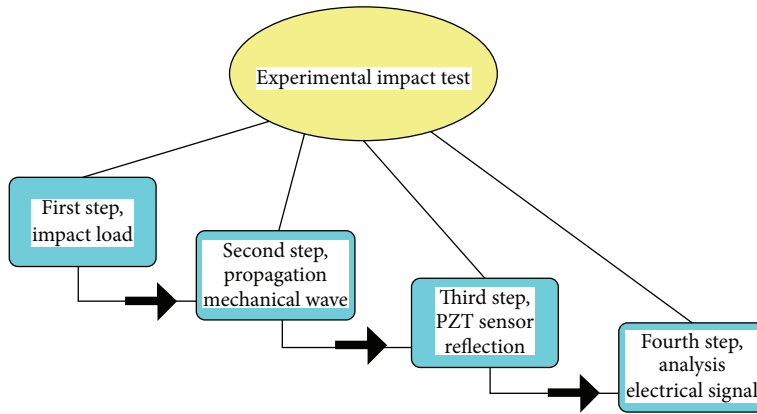


FIGURE 5: Schematic of experimental impact test process.

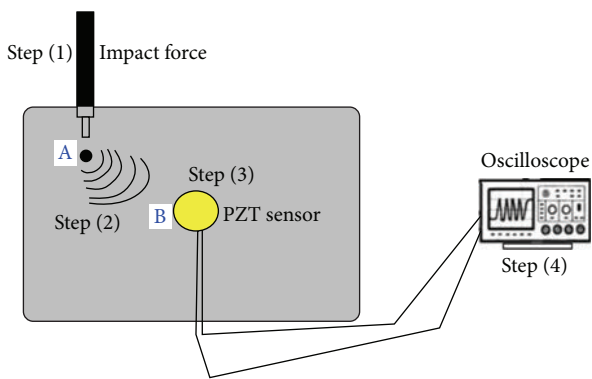


FIGURE 6: Propagation stress wave from impact point (A) to sensor (B).

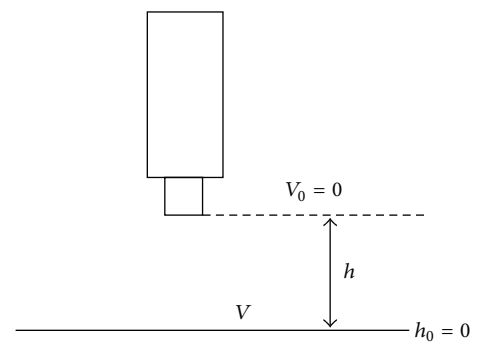


FIGURE 7: Release of the rod on the composite plate.

of rod from the composite plate, and  $h_0$  is the height of the composite plate considered as zero in this study.

$h_0 = 0$  and  $V_0 = 0$  are substituted into (1):

$$V = \sqrt{2gh}. \tag{2}$$

Newton's law of motion states that  $F = ma$  (force equals mass times acceleration) and  $a = V/t$  (acceleration equals velocity divided time). Therefore, Newton's laws of motion can be written as

$$F = m \cdot \frac{V}{t} \quad \text{or} \quad F \cdot t = m \cdot V. \tag{3}$$

TABLE 3: Force and pressure values at impact point.

$h$ (m)	$F$ (N)	$P_0$ (Pa)
0.01	0.110	5642.607
0.02	0.157	7979.852
0.03	0.192	9773.282
0.04	0.221	11285.215
0.05	0.248	12617.254
0.06	0.271	13821.509
0.07	0.293	14928.936

In this study, the time value of the impact test for each point is proposed to be 1 s (unit of time).

Therefore, the force equation is obtained by (4) by substituting the mass of rod (in this study mass of rod is  $m = 0.25$  kg), time value ( $t = 1$  s), and (2) into (3),

$$F = 0.25\sqrt{2gh}. \quad (4)$$

The pressure at the impact point on the composite plate ( $P_0$ ) can be calculated using (5):

$$P_0 = \frac{F}{A} = \frac{0.25\sqrt{2gh}}{\pi r^2} = 127.3\sqrt{2gh}, \quad (5)$$

where  $F$  is force (N),  $A$  is the area of the cross-section of the rod ( $m^2$ ),  $r$  is the radius of cross-section of the rod (m), and  $P_0$  is the pressure at the impact point on the composite plate. In this study, the radius of the cross-section of the rod is  $r = 0.025$  m.

Table 3 shows the force and pressure values at the impact point by changing the releasing height of the rod from the composite plate based on (4) and (5).

**3.2. Propagation Mechanical Wave.** The waves in the one-dimensional longitudinal strain are not the only type of wave motion for a purely longitudinal disturbance. The second type is provided by the wave motion in one-dimensional stress, where the longitudinal normal stresses, for example,  $\sigma$ , which is only a function of  $x$  and  $t$ , is the one nonvanishing stress component. All other stress components vanish [25].

The deformation of an element in the one-dimensional stress is sketched in Figure 8. The figure shows that the cross-section decreases if the element is in tension.  $U(x, t)$  is the longitudinal displacement for the case of one-dimensional stress and is related by [25]

$$\sigma = E\varepsilon_x, \quad (6)$$

where  $E$  is Young's modulus. Writing the equation of motion for an element leads to

$$\frac{\partial \sigma}{\partial x} = \rho \frac{\partial^2 u}{\partial t^2}. \quad (7)$$

The substitution of (6) into (7) yields

$$\frac{\partial^2 u}{\partial x^2} = \frac{1}{c_b^2} \frac{\partial^2 u}{\partial t^2}, \quad (8)$$

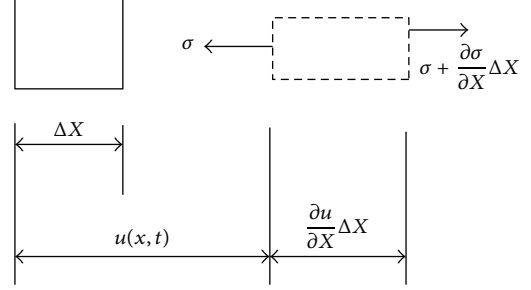


FIGURE 8: Deformation in one-dimensional stress [26].

where

$$c_b^2 = \frac{E}{\rho}. \quad (9)$$

The velocity  $c_b$  is usually called the bar velocity. In this study, Young's modulus of composite plate was achieved through the tensile test,  $E = 3.2$  GPa, and the density of composite plate was  $\rho = 1230$  kg/m<sup>3</sup>. Therefore, (8) reveals that the velocity of wave propagation in composite plate is  $c_b = 1.62$ .

If a semi-infinite thin rod ( $x \geq 0$ ) is subjected at  $x = 0$  to a pressure  $p(t)$ , the resulting stress wave is

$$\sigma = -P_0 \left( t - \frac{x}{c_b} \right), \quad (10)$$

where  $\sigma$  is the produced stress using  $P_0$  with a distance of ( $x$ ) from the impact point,  $t$  is the time that the stress reaches the point with a distance of  $x$  from an impact point, and  $c_b$  is the propagation velocity of the wave in the composite plate. Equation (10) was rewritten as

$$\sigma = -P_0 \left( \frac{c_b t - x}{c_b} \right) = -P \left( \frac{\Delta x}{c_b} \right). \quad (11)$$

The substitution of  $x_A$  (impact point) instead of  $x$  and  $c_b t$  instead of  $x_B$  yields

$$P_B = \frac{\sigma \cdot c_b}{\Delta x}, \quad (12)$$

where  $P_B$  is the pressure at point B, which has a distance of  $\Delta x$  from impact point (A);  $\sigma$  is the stress because of the pressure  $P_A$  in the impact point; and  $\Delta x$  is the distance between points A and B.

The Equation of normal stress is [27]:

$$\sigma = \frac{F}{A}, \quad (13)$$

where  $F$  is impact force (N) and  $A$  is area of cross-section of the rod ( $m^2$ ). Equation (13) is substituted into (12), which yields (10)

$$P_B = \frac{F \cdot c_b}{\Delta x \cdot A}. \quad (14)$$

In this study  $A = 19.625 \times 10^{-6}$ .  $c_b$  is 1.62. Equation (14) shows that the pressure at point B has an inverse relationship

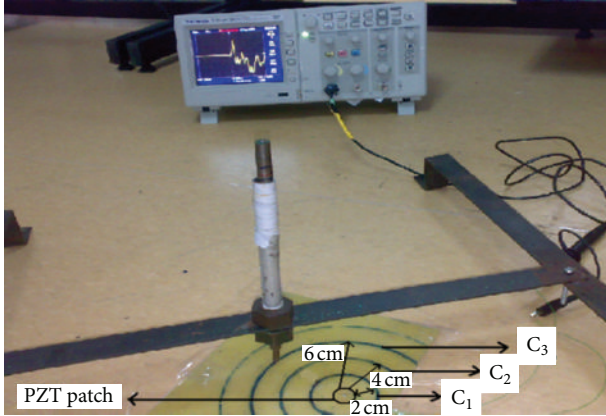


FIGURE 9: Experimental tests with different force values in different points on the composite plate.

with the distance of the impact point from the sensor, which means that the pressure value decreases with the increase of the distance of the impact point ( $\Delta x$ ). Therefore,  $P_B$  is less than  $P_A$ .

**3.3. PZT Reflection.** The values of the pressure on the sensors caused by the impacts were calculated by substituting the output voltages in [28]:

$$P = \frac{16}{3} \frac{\epsilon_{33}}{d_{31}} \frac{h}{D^2} \frac{1}{(1-\nu)} V, \quad (15)$$

where  $\epsilon_{33}$  is the dielectric constant,  $d_{31}$  is the piezoelectric constant,  $D$  is the diameter of the PZT sensor,  $h$  is the thickness of the PZT sensor,  $P$  is the pressure,  $V$  is the output voltage, and  $\nu$  is the Poisson ratio. In this study,  $\epsilon_{33} = 2.124 \times 10^{-9}$  F/m,  $d_{31} = -1.65 \times 10^{-10}$  (m/V),  $h = 0.001$  (m),  $D = 0.01$  (m), and  $\nu = 0.3$ .

**3.4. Electrical Signals from Oscilloscope.** The model of the oscilloscope is TEKTRONIX-TDS2012B with a 100 MHz Bandwidth, 1.0 GS/s sample rate, and two channels. The data were collected while the oscilloscope voltage selector was set on 10 mV/div. The sensitivity of TEKTRONIX-TDS2012B is 2 mV/div. The impact tests were done on the floor in fixed conditions.

## 4. Experimental Procedures

**4.1. Composite Plate with One PZT Patch.** Figure 9 shows the experimental procedure on the piezocomposite plate. The impact test on the three circles with radii of 2, 4, and 6 cm ( $C_1$  with radii 2 cm,  $C_2$  with radii 4 cm, and  $C_3$  with 6 cm), respectively, with their center as the sensor. The relationship between the force and pressure on the sensor was evaluated. Seven forces were placed on the three points with 2, 4, and 6 cm distance from the sensor by changing the releasing height of the rod from the composite plate ( $h_1 = 1, 2, \dots, 7$  cm).

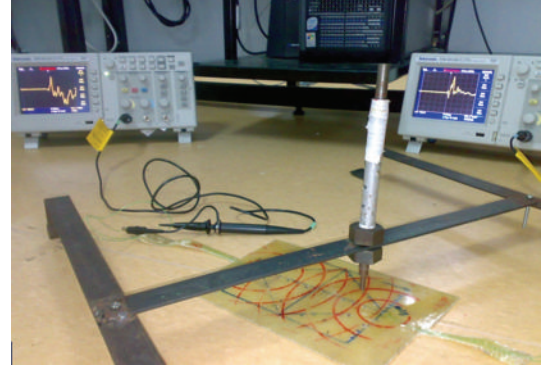


FIGURE 10: Experimental setup on the composite plate with two sensors.

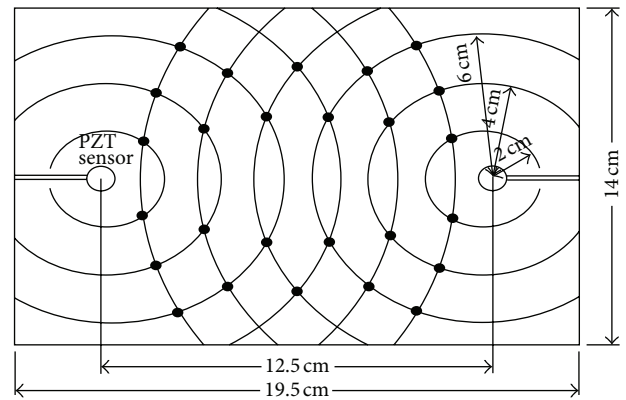


FIGURE 11: Schematic of impact points in the composite plate with two sensors.

Each force on each point caused an output voltage from the sensor. Therefore, seven output voltages existed from each point.

**4.2. Composite Plate with Two PZT Patches.** Figure 10 shows the experimental setup on the composite plate with two sensors. The principal aim of the current study, which is to localize the impacts, was preceded by drawing the circles with radii of 2, 4, 6, 8, 10, and 12 cm (the positions of the centers of the sensors) on the composite plate that holds two embedded sensors.

The circles crossed each other in two points (Figure 11). The impact tests were performed on the crossing points. The sensors calibration process was carried out by detecting the impact voltages at the cross points of the circles. The output voltages of the sensors ( $V_1, V_2$ ) were recorded using the oscilloscope to manage the possible error in the experiments for sixfold iterations. The acoustic wave is propagated on the surface of the composite as a result of the application of impact on the smart plate. When the stress wave reached the PZT sensor, the crystal structure of the sensor changed and showed an output signal. The PZT sensor had a symmetrical hexagonal crystal structure that changes with the strain of the stress wave (AE). The output is a free electron in form of a voltage. The oscilloscope displays the measured voltage in the

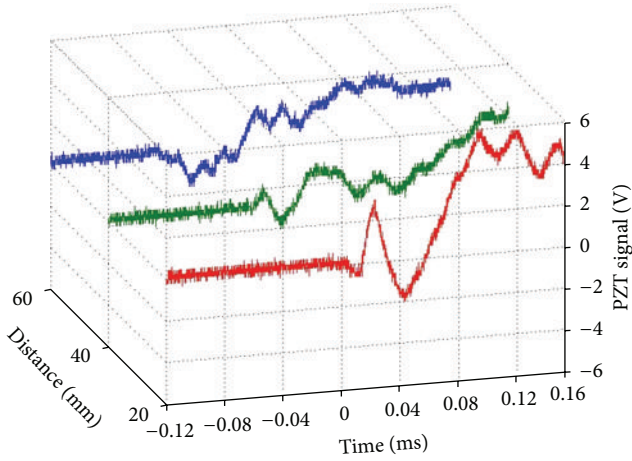


FIGURE 12: First packet of wave output voltage from PZT sensor.

shape of a sinusoidal waveform. The location of the impact load can be determined through the impact monitoring process. The acoustic wave caused by impact should be evaluated and determined in different parts of smart plate to reach the aim of the study.

### 5. Results and Discussion

The results of the impact test on the composite plates with embedded PZT patch are analyzed and evaluated. In the first step, the results of the impact on the two fabricated samples (sample 1 and sample 2) are analyzed. The analysis of the two samples aims to study the manner of the output voltage from the embedded PZT patch by the impact test. In the next step, the result of the impact on the composite plate with two embedded PZT patches (sample 3) is analyzed to find the impact location.

Figure 12 shows that the domain of the first packet of wave decreased by performing the impact test and distancing from the PZT sensor. The first packet of wave with a distance of 20 mm from the PZT sensor was the maximum. The first packet of the wave with a distance of 60 mm from the PZT sensor was minimum. Therefore, the domain of the first packet of wave (PK-PK) and the external voltage decreased with the increase of the distance of the impact point from PZT sensor. The cause of this state is demonstrated through the comparison of the theoretical and experimental results.

Figure 13 shows the impact forces versus the pressures on the PZT sensor (experimental results and theoretical results) in which the horizontal axis is the force value for impact and vertical axis is the pressure on the PZT sensor. C<sub>1</sub>, C<sub>2</sub>, and C<sub>3</sub> are the names of the three circles with radii of 2, 4, and 6 cm from the PZT sensor. On each line, 7 points (force values) were made to impact on each circle (2, 4, and 6 cm from the PZT sensor). The results of the experimental and theoretical impact on the 7 points on each circle (C) are shown as two lines (experimental and theoretical results). Three lines each for the experimental and theoretical results indicate the relationship between the pressure on the sensor

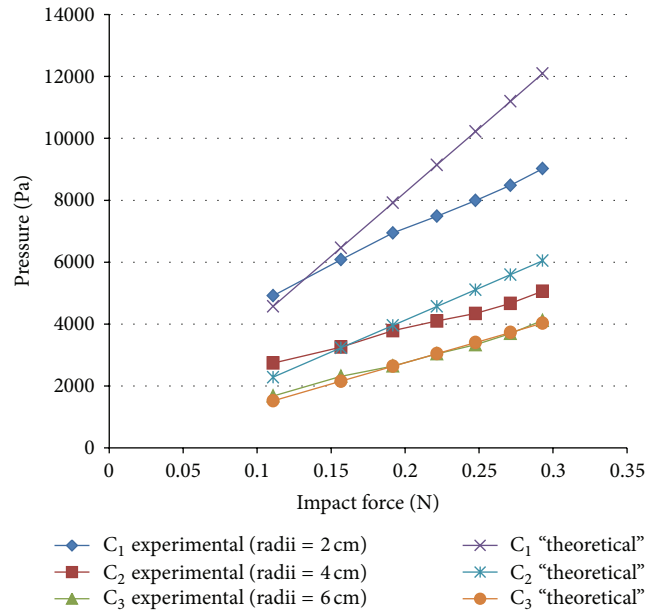


FIGURE 13: Experimental and theoretical results of the pressure on the sensor versus the impact force values.

and the forces on the points with 2, 4, and 6 cm distances from the sensor.

The theoretical results were attained through the mentioned equations and the force values in Table 2. These lines have an increasing trend, where the pressure on the sensor increases with the increase of the impact force value on different points of the composite plate.

Therefore, the pressure on the sensor has a direct relationship with the force caused by impact. The difference between lines C<sub>1</sub> experimental and C<sub>2</sub> experimental is larger than that between lines C<sub>2</sub> experimental and C<sub>3</sub> experimental. The impact point recedes the sensor (supposing that force is constant). The pressure on the sensor decreases, and the ratio of the reduction of the pressure decreases. Therefore, the pressure on the sensor has an indirect relationship with the distance of impact point from the sensor. A few points can be gleaned by comparing experimental and theoretical results, which are explained later.

The difference between lines C<sub>1</sub> theoretical and C<sub>1</sub> experimental increases with the increase of the impact force value. Increasing the impact force value with a distance of 2 cm from PZT sensor increases the difference of the experimental and theoretical results of pressure on the sensor. Increasing the impact force value also increases the difference between lines C<sub>2</sub> theoretical and C<sub>2</sub> experimental, which means that the difference of experimental and theoretical results of pressure on the sensor also increases by increasing the impact force value with a distance of 4 cm from PZT sensor. The lines of C<sub>3</sub> theoretical and C<sub>3</sub> experimental are almost close to one another, which means that the experimental and theoretical results of pressure on the sensor are almost the same by increasing the impact force value with a distance of 6 cm from PZT sensor. Therefore, the difference of the experimental and

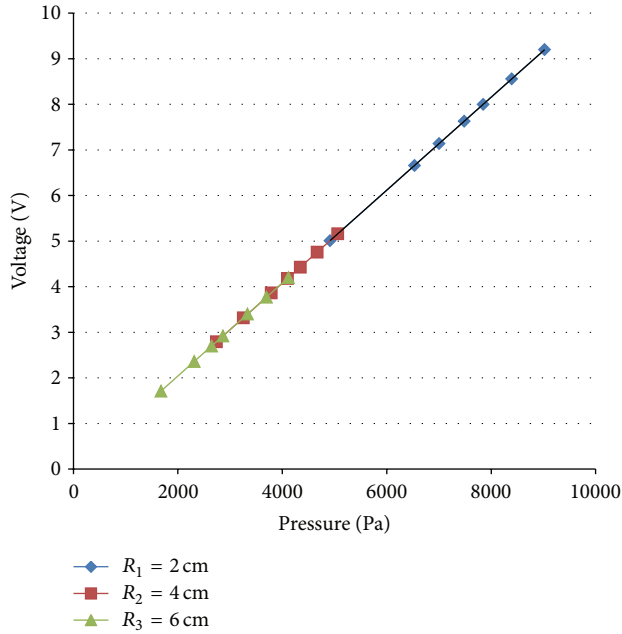


FIGURE 14: Output voltages from the PZT sensor versus pressure on sensor.

theoretical results decreases with the increase of the distance of the impact point from PZT sensor because the sensitivity of the PZT sensor will decrease.

The output voltages from the sensors versus the pressure on the sensor were evaluated using (4) because the pressures on the sensor caused output voltages from the sensor. In Figure 14, the horizontal axis is the pressure on the sensor and the vertical axis is the output voltage. The lines have an increasing trend, which means that the output voltage increases by increasing the pressure on the sensor. The calibration constant is 980.78, which means that  $P = 980.78 \times V$ .

Therefore, pressure has a direct relationship with voltage. Line  $R_2$  is below line  $R_1$ , and line  $R_3$  is below line  $R_2$ , which means that the pressure on the sensor and the output voltage decreases when the impact points recede the sensor. Therefore, the output voltage has an indirect relationship with the distance of the impact point from the sensor.

Figure 15 shows that the locus of the impact point can be identified through the output voltage if the impact occurs on random points of the composite to determine location of impact on the composite plate with a PZT Patch. The locus of the impact was a circle with  $R$  as the radius, the sensor as the center.  $R$  was obtained from (16):

$$R = 0.104V + 10.01, \quad (16)$$

where  $V$  is the output voltage from the PZT sensor.

**5.1. Composite Plate with Two PZT Patches.** The impact test on the composite plate with two sensors showed how the output voltage of the two sensors changed because of the change of the distance of the impact point from two sensors. Figure 16 shows the impact points on the composite plate.

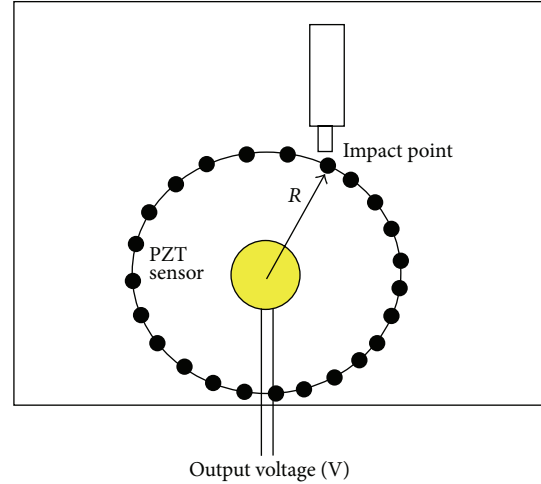


FIGURE 15: Locus of the impact point on the piezocomposite plate with a PZT sensor.

The behaviors of the output voltages of impact points 1 to 6 are similar to those of impact points 1' to 6'. Therefore, the results of impact points 1 to 6 are similar to the results of impact points 1' to 6'. Figures 17(a) and 17(b) show that the output voltage of sensor one ( $V_1$ ) is the maximum and the output voltage of sensor two ( $V_2$ ) is the minimum if the impact point is the crossing point of the two circles with radii of 2 cm from sensor one and 12 cm from sensor two. When the impact point distances from sensor one increase and sensor two decrease,  $V_1$  decreases and  $V_2$  increases, respectively. In these figures, the horizontal axis is the radius of the circles and the vertical axis is voltage. When the impact point distance to both sensors is equal,  $V_1$  and  $V_2$  are almost the same.

$V_1$  and  $V_2$  are the minimum and maximum, respectively, if the impact point is the crossing point of the two circles with radii of 2 cm from sensor one and 12 cm from sensor two. The analysis of the results of the impact test on the crossing points of the circles showed that the output voltage of PZT sensor had an adverse relationship with the distance of the impact point from the sensors. An impact test using two sensors was conducted across the different points of the composite plate with the aim of impact localization through test data analysis. The impact test data include the output voltages of the two sensors in terms of the distances of the impact points from the sensors. In a composite plate with two sensors, the distances of the impact point to sensors 1 ( $R_1$ ) and 2 ( $R_2$ ) and the value of the output voltage from the sensors 1 ( $V_1$ ) and 2 ( $V_2$ ) are shown in Figure 18. An impact on a point on the page between the two sensors occurred. Two values of voltage from the two sensors were obtained. The results from the impact on different parts of composite plate showed that the voltage values from each sensor could determine the impact point distance to each sensor.

The Output voltage of the first sensor ( $V_1$ ) indicates the location of the impact point in terms of the radial distance ( $R_1$ ) from the first sensor. The output voltage of ( $V_2$ ) indicates the location of the impact point in terms of the radial distance ( $R_2$ ) from the second sensor. The impact locations

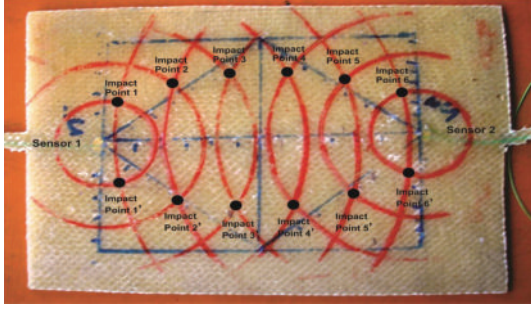


FIGURE 16: Impact points on the composite plate with two PZT sensors.

are obtained as two symmetric points generated because of the intersection of the circles. Therefore, the coordinates of the impact locus point had to be calculated to obtain the position of the impact locus point using two sensors. The origin of the coordinates was intended on the sensor 1; thus, the  $X$ -axis was matched on the center line of the two sensors and the  $Y$ -axis was perpendicular to the sensor. The distance between sensors 1 and 2 was 12.5 cm. The impact locus points were assumed to be  $A(x, -y)$  and  $A(x, y)$  to determine these two points.

The equation of the intersection of the two circles intersection was written as (17), where  $(x, y)$  is the coordinate of point A,  $R_1$  is the radius to the center of sensor 1, and  $R_2$  is the radius to the center of sensor 2,

$$\begin{aligned} x^2 + y^2 &= R_1^2, \\ (x - 12.5)^2 + y^2 &= R_2^2. \end{aligned} \quad (17)$$

Equation (17) is written as

$$\begin{aligned} y^2 &= R_1^2 - x^2, \\ x^2 + y^2 - 25x + 156.25 &= R_2^2. \end{aligned} \quad (18)$$

The calculation of (18) results to (19) and (20):

$$x = \frac{R_2^2 - R_1^2 - 156.25}{25}, \quad (19)$$

$$y = \pm \sqrt{R_1^2 - x^2}. \quad (20)$$

Therefore, (19) and (20) show that the values of radius  $R_1$  and  $R_2$  had to be determined to determine the values of  $x$  and  $y$ . The values of the output voltage from the two sensors ( $V_1$  and  $V_2$ ) were examined and analyzed through two methods.

*Method 1.* The distance values of the impact point from each sensor were considered using the voltage from the same sensor to determine  $R_1$  and  $R_2$ . For instance, the relation between  $R_1$  and  $V_1$  was obtained by analyzing the distance values of the impact point to sensor 1 through the voltage resulting from sensor 1 ( $V_1$ ),

$$R_1 = -3.807 \ln(V_1) + 7.3467. \quad (21)$$

Equation (21) shows that the distance of the impact point to sensor 1 was obtained by acquiring the output voltage from sensor 1. The relation of  $R_2$  with  $V_2$  was also determined by analyzing the distance values of the impact point to sensor 2 through the voltage from sensor 2,

$$R_2 = -2.647 \ln(V_2) + 5.9979. \quad (22)$$

Equation (22) shows that the distance of impact point to sensor 2 was obtained by acquiring the output voltage from sensor 2. Therefore, the distance value of the impact point can be determined from each sensor using the output voltage from each sensor through (21) and (22).  $R_1$  and  $R_2$  according to (21) and (22) are determined from (21) and (22) by obtaining  $V_1$  and  $V_2$  from the impact. The coordinates  $(x, y)$  of the impact point are determined by inserting the value of  $R_1$  and  $R_2$  in (19) and (20).

*Method 2.* The relationship between the distance of the impact point from each sensor with two variables of  $V_1$  and  $V_2$  was determined to obtain an impact location with a higher accuracy than the method 1. For example, the distance values of the impact point to sensor 1 ( $R_1$ ) obtained by achieving the values from the two sensors ( $V_1, V_2$ ) were analyzed. Figure 19 shows that the vertical axis is the distance of the impact point to sensor 1 ( $R_1$ ), the horizontal axis is the output voltage from sensor 1 ( $V_1$ ), and the perpendicular axis to the page is the output voltage from sensor 2 ( $V_2$ ). Therefore, the inverse relationship of the voltage change with a change in the distance of the impact point from the sensor in this page holds true. For instance, a decrease in the distance of the impact point from sensor 1 ( $R_1$ ) from point A to point B caused by the short distance of the impact point to sensor 1 leads to an increase in the output voltage from sensor 1 ( $V_1$ ). The output voltage from sensor 2 also decreases because the impact point is farther from sensor 2 ( $R_2$ ). Therefore, the relation of  $R_1$  with the two variables of  $V_1$  and  $V_2$  was analyzed through MATLAB and was written as

$$R_1 = 7.404 - 0.88V_1 + 0.83V_2. \quad (23)$$

Therefore, (23) shows that  $R_1$  can be calculated if  $V_1$  and  $V_2$  are obtained from the impact on each point of composite page. Equation (23) detected the distance of the impact point from sensor 1 ( $R_1$ ); thus,  $V_1$  and  $V_2$  were the output voltages from sensors 1 and 2, respectively. In the next step, the distance values of the impact point to sensor 2 ( $R_2$ ), acquired by obtaining the values from the two sensors ( $V_1, V_2$ ), were analyzed. Figure 20 shows that the vertical axis is the distance of the impact point from sensor 2 ( $R_2$ ), the horizontal axis is the output voltage from sensor 2 ( $V_2$ ), and the perpendicular axis on a page is output voltage from sensor 2 ( $V_1$ ).

The page was drawn using three variables ( $R_2, V_1$ , and  $V_2$ ); thus, the indirect relation of the voltage change with distance change of the impact point from the sensor holds true. For example, the voltage of sensor 2 decreases if the distance of the impact point to sensor 2 from point A to point B increases in this page because the impact point moves farther from sensor 2. The voltage of sensor 1 ( $V_1$ ) also increases because the impact point moves nearer to sensor 1. Therefore,

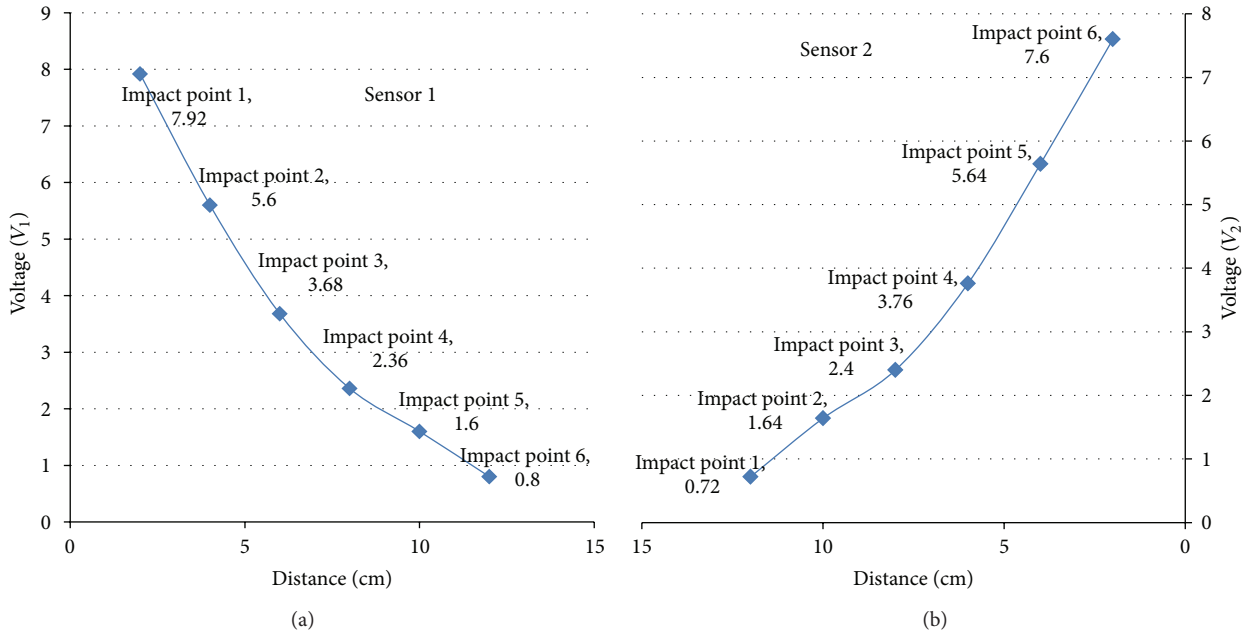


FIGURE 17: Behavior of output voltage from the two sensors.

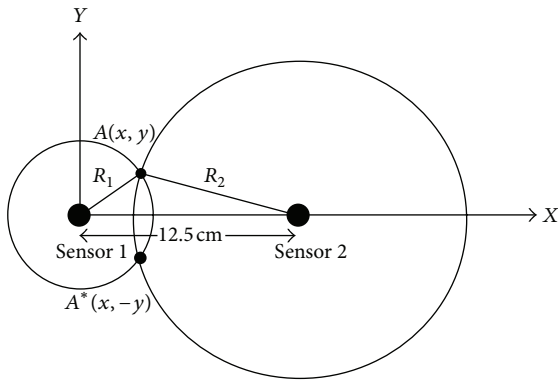


FIGURE 18: Intersection of two circles to detect impact location.

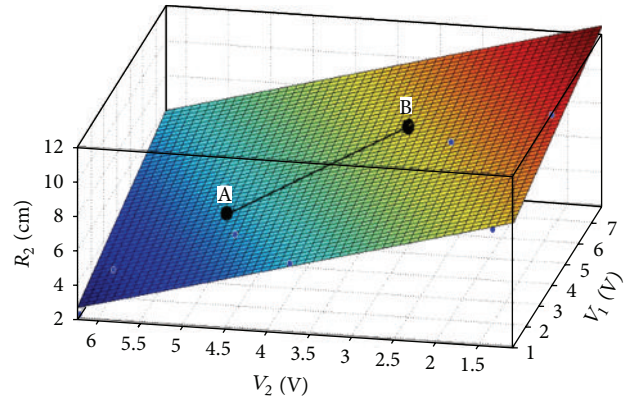


FIGURE 20: Distance of the impact point from sensor 2 ( $R_2$ ) versus the two output voltages from the two sensors ( $V_1$  and  $V_2$ ).

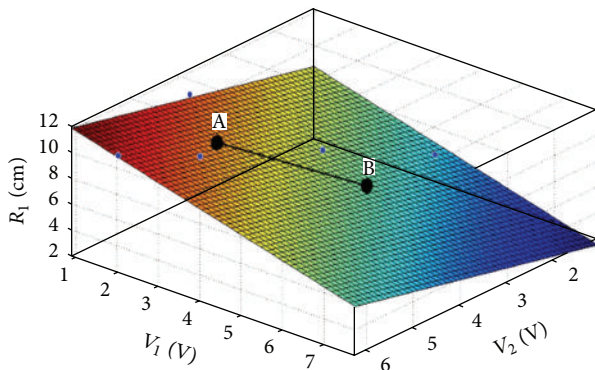


FIGURE 19: Distance of the impact point from sensor 1 ( $R_1$ ) versus the two output voltages from the two sensors ( $V_1$  and  $V_2$ ).

the relationship of  $R_2$  with the two variables of  $V_1$  and  $V_2$  was analyzed through MATLAB, which achieved (17):

$$R_2 = 10.2 + 0.476V_1 - 1.286V_2. \quad (24)$$

Therefore, the distance of the impact point from each sensor ( $R_1$ ,  $R_2$ ) is obtained by achieving the output voltage from the two sensors ( $V_1$ ,  $V_2$ ) and inserted (17) or (24) if an impact is inserted between the two sensors on a composite plate. The coordinates  $(x, y)$  or  $(x, -y)$  of the impact point can also be achieved by inserting the values of  $R_1$  and  $R_2$  in (19) and (20).

Embedding PZT into the composite technique as a passive smart structure is suitable in damage detection. Passive approaches do not affect any actuators, and receivers are used to “sense and/or hear” any perturbations caused by possible

hidden damage [6]. Numerous researchers have studied the passive smart structure using the bonded PZT patch on the composite for damage detection [1–5]. Embedding PZT in composite has some advantages, such as the protection of PZT from environmental effects, prevention of wire spoiling, and the increase of the PZT lifetime, compared with the bonding method. The result in this study shows that embedding the PZT patch method for passive smart structures is applicable to damage detection in a composite plate.

## 6. Conclusions

This paper presents experimental and theoretical investigations on impact localization on two piezocomposite plates, including one and two embedded PZT patches, through the cut-out method.

The signal from the embedded PZT patch was detected through the impact on the fabricated composite plate with an embedded one PZT patch. The value of external voltage was found to decrease by increasing the distance of the impact point from the PZT sensor. Therefore, the locus of the impact point can be identified using the output voltage if an impact occurs on the random points of the composite. The locus of the impact was a circle with  $R$  as the radius and the sensor as the center.

The current study attempts to determine the location of the impact points through the cut-out method and the two embedded PZT patches inside the four-layered composite plate. The fabricating process was conducted at a low temperature using the hand lay-up method to avoid wire spoiling and the decoupling of the PZT patch. The utilized fabrication process is a highly cost-effective manufacturing prototype model considering the cost advantages of using the PZT patch compared with the PZT wafer. The location of the impact points was determined by analyzing the output voltages of the PZT sensors, which were embedded among the composite layers. The applied impact to the page between the sensors resulted in the generation of voltage through the sensors. The output voltage of the sensors determined the distance of each of the imposed impacts from the sensors. The output voltage of the first sensor ( $V_1$ ) indicated the location of the impact based on the radial distance ( $R_1$ ) from the first sensor. The output voltage of ( $V_2$ ) indicated the location of the impact point based on the radial distance ( $R_2$ ) from the second sensor. The location of the impacts is obtained as two symmetric points and is generated as an intersection of the two circles. Therefore, determining the coordinates of the impact locations is necessary to obtain the locations of impacts. The coordinates of the two symmetrical impact points are defined with the origin of the intended coordinate system as the location of sensor 1.

## Abbreviations

PZT: Lead zirconate titanate ( $\text{Pb}[\text{Zr}(x)\text{Ti}(1-x)]\text{O}_3$ )  
 AE: Acoustic emission  
 WT: Wavelet transform

PSD: Passive sending diagnosis  
 CFRP: Carbon-fiber-reinforce plastic  
 $P$ : Pressure (Pa)  
 $F$ : Force (N).

## Acknowledgment

The authors would like to thank the Mechanical Department of University Putra Malaysia for providing the laboratory facilities and technical support.

## References

- [1] J. Wang, "Modeling dynamic of composite plate with PZT patches embedded by using FEMLAB3," in *Proceedings of the COMSOL Multiphysics User's Conference 2005 Stockholm*, 2005.
- [2] A. Zabihollah, R. Sedaghati, and R. Ganesan, "Active vibration suppression of smart laminated beams using layerwise theory and an optimal control strategy," *Smart Materials and Structures*, vol. 16, no. 6, pp. 2190–2201, 2007.
- [3] S. M. Yang, "Design and fabrication of a smart layer module in composite laminated structures," *Smart Materials and Structures*, vol. 14, no. 2, pp. 315–320, 2005.
- [4] S. G. Pierce, B. Culshaw, G. Manson, K. Worden, and W. J. Staszewski, "Application of ultrasonic Lamb wave techniques to the evaluation of advanced composite structures," in *Proceedings of the 7th Annual International Symposium on Smart Structures and Materials. International Society for Optics and Photonics (SPIE's '00)*, 2000.
- [5] M. M. S. Dezfouli, Z. Hashim, M. H. Ruslan et al., "Experimental investigation of solar hybrid desiccant cooling system in hot and humid weather of malaysia," in *Proceedings of the 10th International Conference on Environment, Ecosystems and Development (WSEAS '12)*, 2012.
- [6] M. Yocum, H. Abramovich, A. Grunwald, and S. Mall, "Fully reversed electromechanical fatigue behavior of composite laminate with embedded piezoelectric actuator/sensor," *Smart Materials and Structures*, vol. 12, no. 4, pp. 556–564, 2003.
- [7] F. Mustapha, G. Manson, K. Worden, and S. G. Pierce, "Damage location in an isotropic plate using a vector of novelty indices," *Mechanical Systems and Signal Processing*, vol. 21, no. 4, pp. 1885–1906, 2007.
- [8] M. M. S. Dezfouli, Z. Azran, M. H. Ruslan, K. Sopian, and B. Bakhtyar, "Experimental investigate of draying chilli by solar assisted heat pump dryer with multifunctional solar thermal collector," in *International Conference on Environment, Ecosystems and Development*, 2012.
- [9] W. J. Staszewski, S. Mahzan, and R. Traynor, "Health monitoring of aerospace composite structures—active and passive approach," *Composites Science and Technology*, vol. 69, no. 11–12, pp. 1678–1685, 2009.
- [10] Z. Guan and C. Yang, "Low-velocity impact and damage process of composite laminates," *Journal of Composite Materials*, vol. 36, no. 7, pp. 851–871, 2002.
- [11] D. Sung, C. Kim, and C. Hong, "Monitoring of impact damages in composite laminates using wavelet transform," *Composites Part B*, vol. 33, no. 1, pp. 35–43, 2002.
- [12] Z. Su, L. Ye, X. Bu, X. Wang, and Y. W. Mai, "Quantitative assessment of damage in a structural beam based on wave propagation by impact excitation," *Journal of Civil Structural*

- Health Monitoring*, vol. 2, no. 1, Article ID 145792, pp. 27–40, 2003.
- [13] K. Diamanti, J. M. Hodgkinson, and C. Soutis, “Detection of low-velocity impact damage in composite plates using lamb waves,” *Structural Health Monitoring*, vol. 3, no. 1, pp. 33–41, 2004.
- [14] A. Ghoshal, W. N. Martin, M. J. Schulz, A. Chattopadhyay, W. H. Prosser, and H. S. Kim, “Health monitoring of composite plates using acoustic wave propagation, continuous sensors and wavelet analysis,” *Journal of Reinforced Plastics and Composites*, vol. 26, no. 1, pp. 95–112, 2007.
- [15] I. Kim, H. Lee, and J. Kim, “Impact damage detection in composite laminates using PVDF and PZT sensor signals,” *Journal of Intelligent Material Systems and Structures*, vol. 16, no. 11-12, pp. 1007–1013, 2005.
- [16] J. Han, C. Kim, and J. Kim, “The propagation of Lamb waves in a laminated composite plate with a variable stepped thickness,” *Composite Structures*, vol. 76, no. 4, pp. 388–396, 2006.
- [17] D. Lee, *Fundamentals of Shock Wave Propagation in Solids*, Springer, Berlin, Germany, 2008.
- [18] C. Yoon, S. Lee, S. Lee, H. Kim, and K. Lee, “Transverse 1-3 piezoelectric ceramic/polymer composite with multi-layered PZT ceramic blocks,” *Sensors and Actuators*, vol. 134, no. 2, pp. 480–485, 2007.
- [19] J. Park, J. Kong, D. Kim, and D. Yoon, “Nondestructive damage detection and interfacial evaluation of single-fibre/epoxy composites using PZT, PVDF and P(VDF-TrFE) Copolymer sensors,” *Composites Science and Technology*, vol. 65, no. 2, pp. 241–256, 2005.
- [20] J. Barton, “Smart structures and materials Brian Culshaw,” in *Optics and Lasers in Engineering*, vol. 27, pp. 337–338, Artech House, Boston, MA, USA, 1997.
- [21] M. Arous, H. Hammami, M. Lagache, and A. Kallel, “Interfacial polarization in piezoelectric fibre-polymer composites,” *Journal of Non-Crystalline Solids*, vol. 353, no. 47-51, pp. 4428–4431, 2007.
- [22] D. Sung, C. Kim, and C. Hong, “Monitoring of impact damages in composite laminates using wavelet transform,” *Composites Part B*, vol. 33, no. 1, pp. 35–43, 2002.
- [23] S. W. Doebling, C. Farrar, and P. Cawley, “Damage identification and health monitoring of structural and mechanical systems from changes in their vibration characteristics: a literature review,” Los Alamos National Laboratory Report LA-13070-M, 1996.
- [24] Z. Su, L. Ye, X. Bu, X. Wang, and Y. Mai, “Quantitative assessment of damage in a structural beam based on wave propagation by impact excitation,” *Structural Health Monitoring*, vol. 2, no. 1, pp. 27–40, 2003.
- [25] J. D. Achenbach, *Wave Propagation in Elastic Solids*, vol. 16, North-Holland, Amsterdam, The Netherlands, 1973.
- [26] F.-H. Chou and J. D. Achenbach, “Three-dimensional Vibrations of Orthotropic cylinders,” *Journal of the Engineering Mechanics Division*, vol. 98, pp. 813–822, 1972.
- [27] S. J. Kirk and A. J. Dell’Isola, *Life Cycle Costing For Design Professionals*, McGraw-Hill, New York, NY, USA, 1995.
- [28] J. G. Webster, *The Measurement, Instrumentation, and Sensors Handbook*, Springer, 1999.

## Research Article

# Biopolymer Doped with Titanium Dioxide Superhydrophobic Photocatalysis as Self-Clean Coating for Lightweight Composite

Anika Zafiah M. Rus, S. R. Mohid, S. Nurulsaidatulasyida, and N. Marsi

*Sustainable Polymer Engineering, Advanced Manufacturing and Material Center (AMMC),  
Faculty of Mechanical and Manufacturing Engineering, Universiti Tun Hussein Onn Malaysia, 86400 Batu Pahat, Johor, Malaysia*

Correspondence should be addressed to Anika Zafiah M. Rus; [zafiah@uthm.edu.my](mailto:zafiah@uthm.edu.my)

Received 25 March 2013; Revised 24 April 2013; Accepted 24 April 2013

Academic Editor: Belal F. Yousif

Copyright © 2013 Anika Zafiah M. Rus et al. This is an open access article distributed under the Creative Commons Attribution License, which permits unrestricted use, distribution, and reproduction in any medium, provided the original work is properly cited.

The development of a lightweight composite (LC) based on Portland cement concrete with waste lightweight aggregate (WLA) additive was carried out to improve the sustainability and environmental impact and to offer potential cost savings without sacrificing strength. Treatment of the surface of the LC exposed to environmental attack by coating with biopolymer based on waste cooking oil doped with titanium dioxide photocatalysis (TOP) with superhydrophilic property was found to affect the mechanical properties of the LC in a systematic way. The results of compressive strength showed that the composite achieved the minimum required strength for lightweight construction materials of 17.2 MPa. Scratch resistance measurements showed that the highest percentages loading of superhydrophilic particles (up to 2.5% of biomonomer weight) for LC's surface coating gave the highest scratch resistance while the uncoated sample showed the least resistances. Scanning electron microscope (SEM) pictures revealed the difference between the surface roughness for LC with and without TOP coating. TOP is also formulated to provide self-cleaning LC surfaces based on two principal ways: (1) the development by coating the LC with a photocatalytic superhydrophilic, (2) if such a superhydrophilic is illuminated by light, the grease, dirt, and organic contaminants will be decomposed and can easily be swept away by rain.

## 1. Introduction

A large amount of waste lightweight aggregate (WLA) and waste cooking oil has become an environmental issue around the world. One useful application that WLA could find would be in the construction industry. Thus large amounts of WLA could be utilized as bitumen pastes, roofs, floor covers, pavement, ceiling roofs, and so forth. As regards, waste cooking oil can be recycled for biodiesel, paint, bio-bag plastic, pencil cases, containers, and so forth [1]. These approaches would reduce pollution and disposal problems. The concept of sustainable development, currently a very important issue, requires that society as a whole becomes aware of the necessity to make the most of all existing resources, combined with minimizing the creation of residues [2].

In this research, the fabrication of LC by WLA and its surface coating from biopolymer made from waste cooking oil was doped with superhydrophilic photocatalysis materials. LC can also be made cheaper by replacing some of the fine

aggregate with WLA. These WLA were produced through a process called continuous shredding, which is necessary to create WLA of particle size small enough to replace an aggregate as fine as sand. Such a type of concrete can be used to reduce the weight by as much as 35% as compared with the commercial standard concrete roof tile, and it offers a reduction in production cost while maintaining the mechanical strength.

A surface coating, known as TOP, was used and prepared based on biopolymer derived from waste cooking oil [3–5] doped with superhydrophilic metal oxide filler. The fabrication method for LC surfaces with or without fillers was formulated and the coating applied onto the surfaces. Physical and mechanical testing was conducted to observe the self-cleaning property of the additive in order to improve its quality as desired. In order for any further study or uptake of this new material to be successful, it is necessary to prepare them not just with the correct properties but also to determine their stability towards degradation from sunlight

and night humidity. This research is to establish a family of concrete mixes of WLA with Portland cement to produce LC with prescribed properties such as reducing cost and weight while maintaining the mechanical strength.

For example, investigation on the failure of rubberized concrete under flexural loading exhibited a ductile mode as compared to that of nonrubberized concrete. The RA concrete specimens could withstand larger deflection, indicating that they could absorb more energy [6]. This is largely due to the ability of RA to undergo a large deformation before failure. The replacement of natural aggregate with rubber particles resulted in a significant increase of flexural strength and tensile strain of concrete as well as better damping capacity. The addition of rubber particles is effective for reduction of concrete modulus of elasticity and increasing deformability of concrete. The tires rubber waste additives have great influence on concrete deformability after loading was reported [7, 8]. The strains of the concrete investigated with tires rubber in the beginning of stress increasing are higher as compared to the concrete without rubber waste [9].

The surface coating of LC surfaces by TOP was examined to observe the role of additives as self-clean upon exposure to sunlight and humidity and mechanical properties such as morphology of fracture surfaces by scanning electron microscopy (SEM), water droplet test, and scratch resistance by pencil test for coated and uncoated surface to assess its stability for outdoor applications.

## 2. Methodology

**2.1. Fabrication of LC.** Four standard samples were fabricated with a minimum required compressive strength of 17.2 MPa and flexural strength of 1.45 MPa based on standard lightweight concrete. The preparation of samples was carried out according to ASTM C170 and ASTM C99. The proportion varied in WLA percentages which are equivalent to weight of cement (wt/wt) by using 1 to 3 mm particle sizes. The mixture proportions of basic ingredients, that is, Portland cement, water, and 10% superplasticizer, were the same as the lightweight cube concrete samples. Table 1 and Figure 1 show the quantities of four standard samples (a), (b), (c), and (d) for concrete cubic meter.

The LC for cube test samples was cast into the cube mould with dimension of 100 mm in length, 100 mm in width, and 100 mm in depth and left to cure at room temperature for 3 days while the LC mixture was poured in the fiberglass mould with dimensions of 420 mm in length, 332 mm in width, and 12.5 mm in depth and cured at room temperature for about 24 hours.

**2.2. Preparation of TOP as Surface Coating.** Monomer based on waste cooking oil and its composites were prepared [3–5] by mixing with cross-linking agent and doped with different percentages of superhydrophilic photocatalysis fillers of  $\text{TiO}_2$  named as TOP which were 1.0%, 1.5%, 2.0%, and 2.5% equivalent to weight of monomer as shown in Table 2. The hand lay-up technique was used to coat the LC surfaces with TOP.

TABLE 1: Proportions ratio of LC samples preparation with WLA.

Materials	Proportions			
	a (wt/wt)	b (wt/wt)	c (wt/wt)	d (wt/wt)
Portland cement	1	1	1	1
Water	0.5	0.5	0.5	0.5
WLA (1–3 mm)	0.55	0.60	0.65	0.70

TABLE 2: Fabrication of LC coated with TOP for all test specimens.

No	Samples	LC surface coating treatment	TOP Thickness (mm)
1	A	Uncoated surface	0
2	B	Surface coated with neat biopolymer	0.30
3	C	Surface coated with TOP (1.0% $\text{TiO}_2$ wt/wt of biomonomer)	0.30
4	D	Surface coated with TOP (1.5% $\text{TiO}_2$ wt/wt of biomonomer)	0.30
5	E	Surface coated with TOP (2.0% $\text{TiO}_2$ wt/wt of biomonomer)	0.30
6	F	Surface coated with TOP (2.5% $\text{TiO}_2$ wt/wt of biomonomer)	0.30

**2.3. Compressive Strength Test for LC.** The compressive strength test for LC and standard samples (a), (b), (c), and (d) was conducted after 7 days of standard curing. A compressive test machine 2000 kN fully automatic, KalTest model no: QTC 2000, was used to determine the maximum compressive loads carried by various cubes. The load was applied at a rate of  $15 \text{ N/mm}^2$  per minute in accordance with ASTM C170 test method [10].

**2.4. Flexural Strength Test for LC.** The flexural strengths of LC and standard concrete specimens were determined after 7 days of standard curing. The beams were tested in the laboratory using Universal Testing Machine 1000 kN. The load was applied at a rate of  $0.16 \text{ N/mm}^2$  per second in accordance with the ASTM C99 test method. In the test, a load is applied through two rollers at the third points of the span until specimen breaks. Under these conditions, the lower surface of the beam is in tension. The beam fails by the growth of a crack from the tensile zone through the concrete. Using standard beam formula by (1), the failure stress can be calculated from dimension and load at the fracture [11]:

$$\sigma = \frac{3FL}{[2bd^2]}, \quad (1)$$

where  $F$  = load (force) at the fracture (N),  $L$  = length of the support system (mm),  $B$  = width of sample (mm),  $D$  = thickness of sample (mm),  $\Sigma$  = failure stress (MPa),  $M_c$  = weight of standard concrete roof tile, and  $m_{\text{LRT}}$  = weight of the lightweight roof tile by WLA.

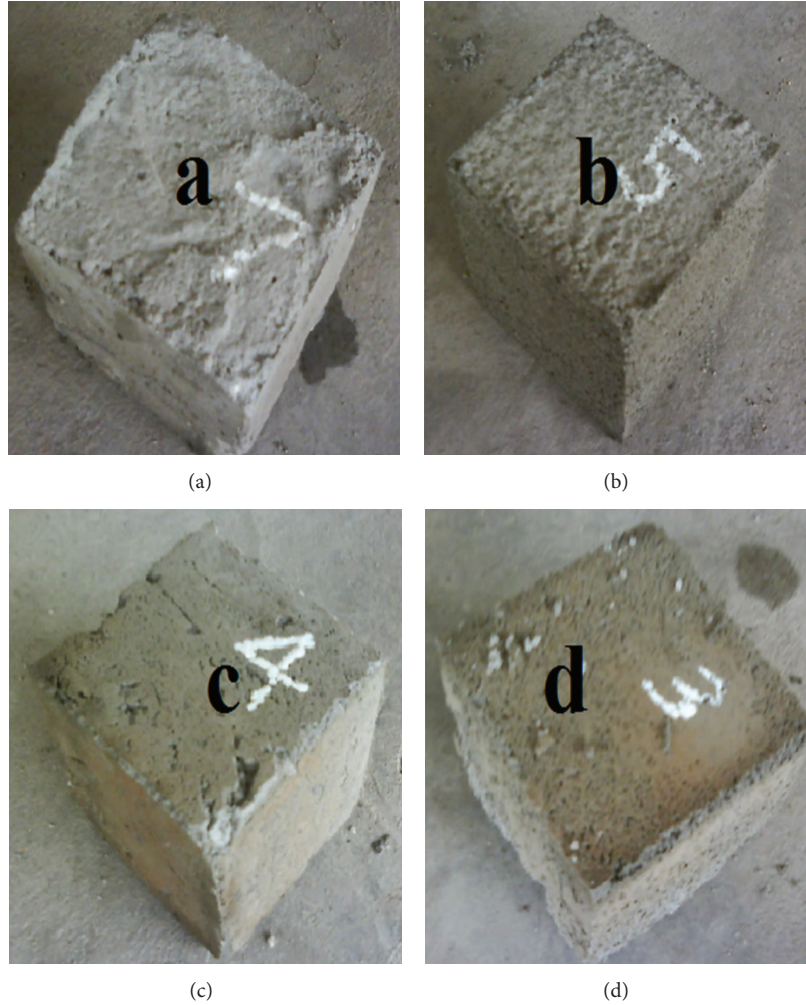


FIGURE 1: Samples of LC for cube test with different WLA proportion ratio: (a) 0.55, (b) 0.60, (c) 0.65, and (d) 0.70 wt/wt.

**2.5. Weight Reduction of LC.** The percentage weight of LC was compared with standard concrete as determined by (2). The reduction of weight percentage was calculated as

$$\% \text{weight} = \frac{(m_c - m_{LC})}{m_c} \times 100. \quad (2)$$

The percentage of weight reduction was taken from the average of three samples.

**2.6. Sunlight and Overnight Humidity Exposure of TOP Surface Coating.** This specification designates surface to be used as panels in weathering tests of coatings such as exterior solvent-borne or water-borne paints and other materials that are exposed to the sunlight and daily humidity. Referring to Figure 2, six categories of samples ((A), (B), (C), (D), (E), and (F)) with and without coating were exposed to sunlight and overnight humidity for eight weeks as shown in Figure 3 in accordance to ASTM D4258-05 [12]. This is to observe the self-clean properties of TOP indicated by colour change, sunburn, crack growth, dirt, oily deposition, and surface roughness.

**2.7. TOP Surface Coating of Exposed and Unexposed to Outdoor, Sunlight, and Overnight Humidity by SEM.** SEM has been used to analyze image of TOP before and after exposure to determine their surface before and after exposure to sunlight and humidity with different percentage of superhydrophilic fillers.

**2.8. Scratch Resistance of TOP Surface by Pencil Test.** Pencil hardness measurements have been used by the coating industry to determine the hardness of clear and pigmented organic coating films according to ASTM D3363 standard. The pencil consists of seventeen, ranging from 8H to 6B. The TOP surface coating with different percentages of photocatalysis superhydrophilic fillers was placed on a firm horizontal surface. The pencil was held firmly against 45° angle and pushed away in a smooth stroke with uniform pressure. The process was started with the hardest pencil and continued down the scale of hardness until the pencil used did not gouge or scratch the film [13].

**2.9. Water Droplet Test of TOP Surface Coating.** Water droplets come in contact with a superhydrophobic surface with

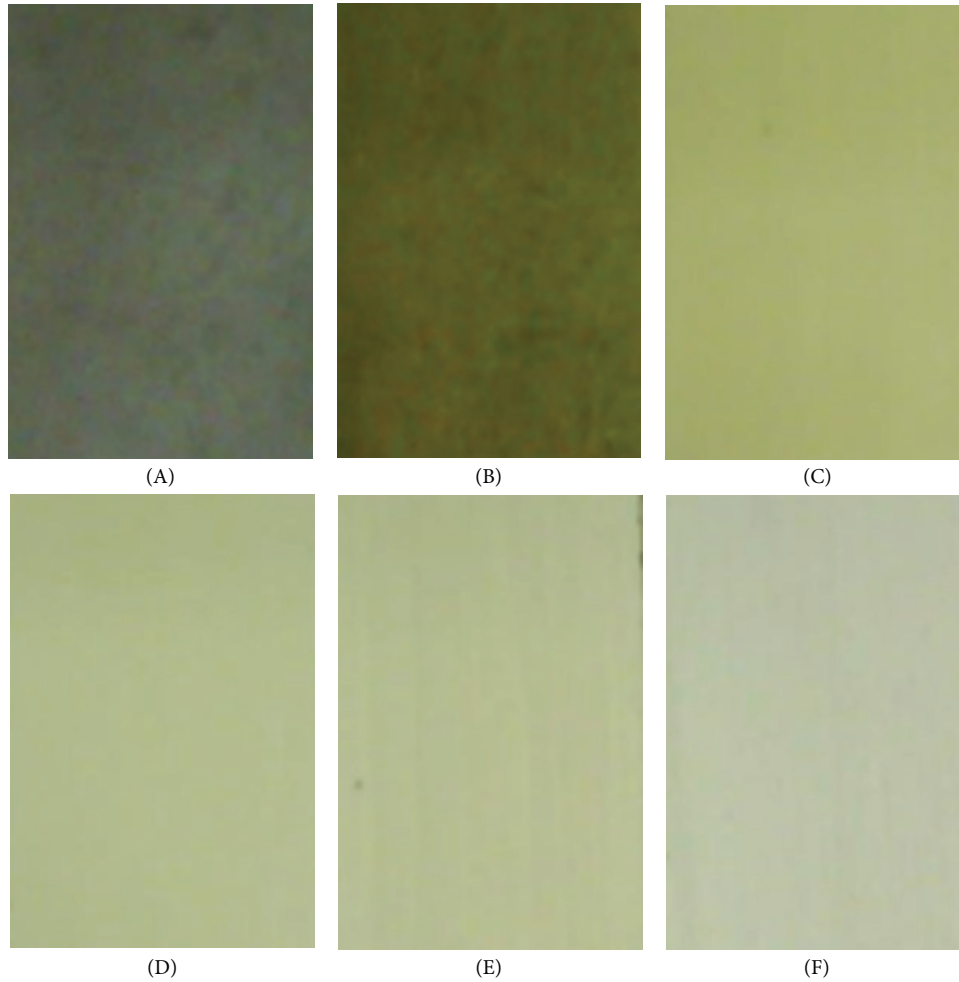


FIGURE 2: Samples of LC coated with TOP for outdoor exposure test.

contact angle higher than  $150^\circ$  to form nearly spherical beads. The contaminants, either inorganic or organic, on such surfaces are picked up by water droplets or adhered to the water droplet and are removed from the surface when the water droplets roll off. The combination of low surface energy microstructured features which certainly reduce the contact area between the surface and water droplets will form superhydrophobic surfaces [14].

### 3. Results and Discussion

**3.1. Compressive Strength Test of LC.** The compressive strength test was conducted to measure the effect of different percentages of WLA loading in the LC. A systematic reduction in compressive strength with the increase in WLA loading for the LC was revealed. The cube concrete of compressive strength test for 7 days immersion with 55% WLA (sample (C)) is 19.35 MPa was achieved the value of standard composition concrete which is 17.20 MPa. Meanwhile, LC compressive strength with 60% WLA loading (sample (B)), 65% WLA loading (sample (C)), and 70% WLA loading (sample (D)) are 16.95 MPa, 15.88 MPa, and 13.99 MPa, respectively, as shown in Table 3 and Figure 4.

The integrity of the bond between these particle sizes of rubber aggregate and cement paste is critical. If there is no bond, the aggregate effectively represent of weakness compressive strength of the lightweight concrete design mixture [15]. Large-sized coarse aggregates are increasingly used in compressive strength in lightweight concrete for economic and environmental reasons due the large coarse aggregates also require less energy for size reduction with increased production rates [16].

The possible reason for reduction in strength with the inclusion of rubber in concrete mixtures is due to, first, the rubber particles are much softer or elasticity deformable than the surrounding cement paste, on loading cracks are initiated quickly around the rubber particle in the mix, which accelerated the failure of the rubber cement matrix. Secondly, due to the lack of adhesion between rubber particles and the paste, soft rubber particles may be viewed as voids in the concrete matrix. The assumed increase in void content would certainly cause a reduction in strength. The third possible reason for the strength reduction is the fact that rubberized mixture is dependent greatly on the coarse aggregate, density, and size because the aggregates are partially replaced by rubber and the reduction of strength is anticipated [17].

TABLE 3: Compressive strength of standard and LC concrete with different ratio of WLA to cement (wt/wt).

Types of composite	Composite percentages (wt/wt)	Samples	Average compressive strength (MPa)	Density (kg/m <sup>3</sup> )	
Lightweight	WLA	55%	A	19.35	1750
		60%	B	16.95	1683
		65%	C	15.88	1580
		70%	D	13.99	1468
Standard composition	Commercial [8]		17.20	1900	

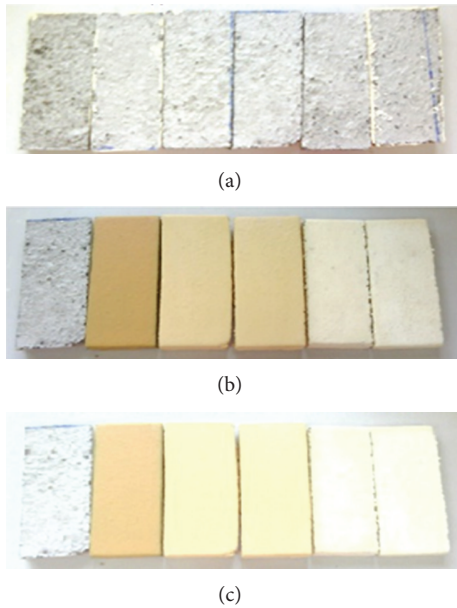


FIGURE 3: Samples of LC of (a) uncoated surface, (b) before being exposed to outdoor (sunlight and overnight humidity), and (c) after being exposed to outdoor (sunlight and overnight humidity).

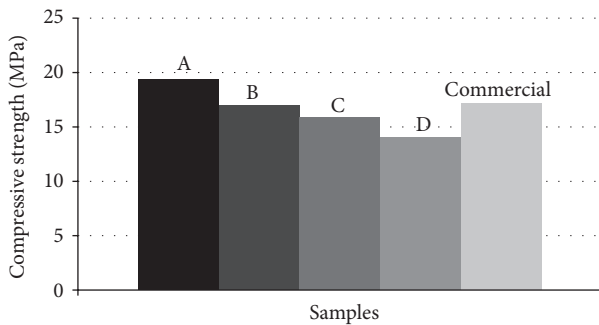


FIGURE 4: Compressive strength of standard lightweight cube concrete and LC with different ratio of WLA to cement (wt/wt) (A) 55%, (B) 60%, (C) 65%, and (D) 70%.

3.2. Flexural Strength Test of LC. The flexural strength behaviour of the mixtures is as shown in Table 4. Figure 5 shows the load-deflection curves for four groups of samples; the deflection was obtained by deducting the effect of the support deformation. The relationship between the load and longitudinal tensile strain (on the lowest surfaces of the beam) is shown in Figure 6.

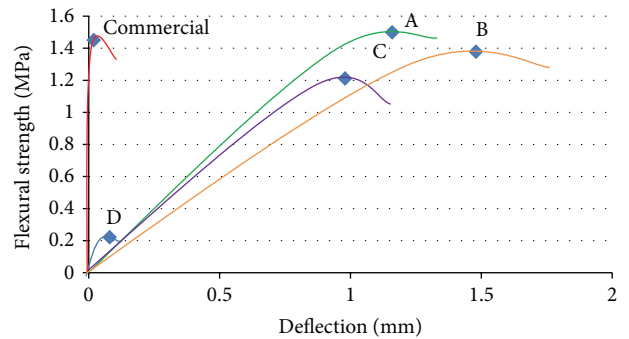


FIGURE 5: Flexural load against deflection of standard and lightweight cube concrete with different ratio of WLA to cement (wt/wt): (A) 55%, (B) 60%, (C) 65%, and (D) 70%.

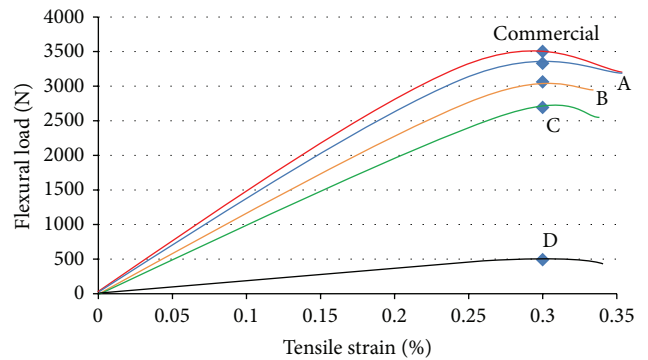


FIGURE 6: Flexural load against tensile strain of lightweight cube concrete with different ratio of WLA to cement (wt/wt): (A) 55%, (B) 60%, (C) 65%, and (D) 70%.

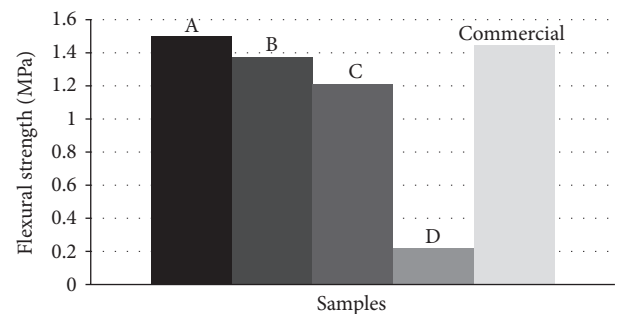


FIGURE 7: Flexural strength of lightweight cube concrete with different ratio of WLA to cement (wt/wt): (A) 55%, (B) 60%, (C) 65%, and (D) 70%.

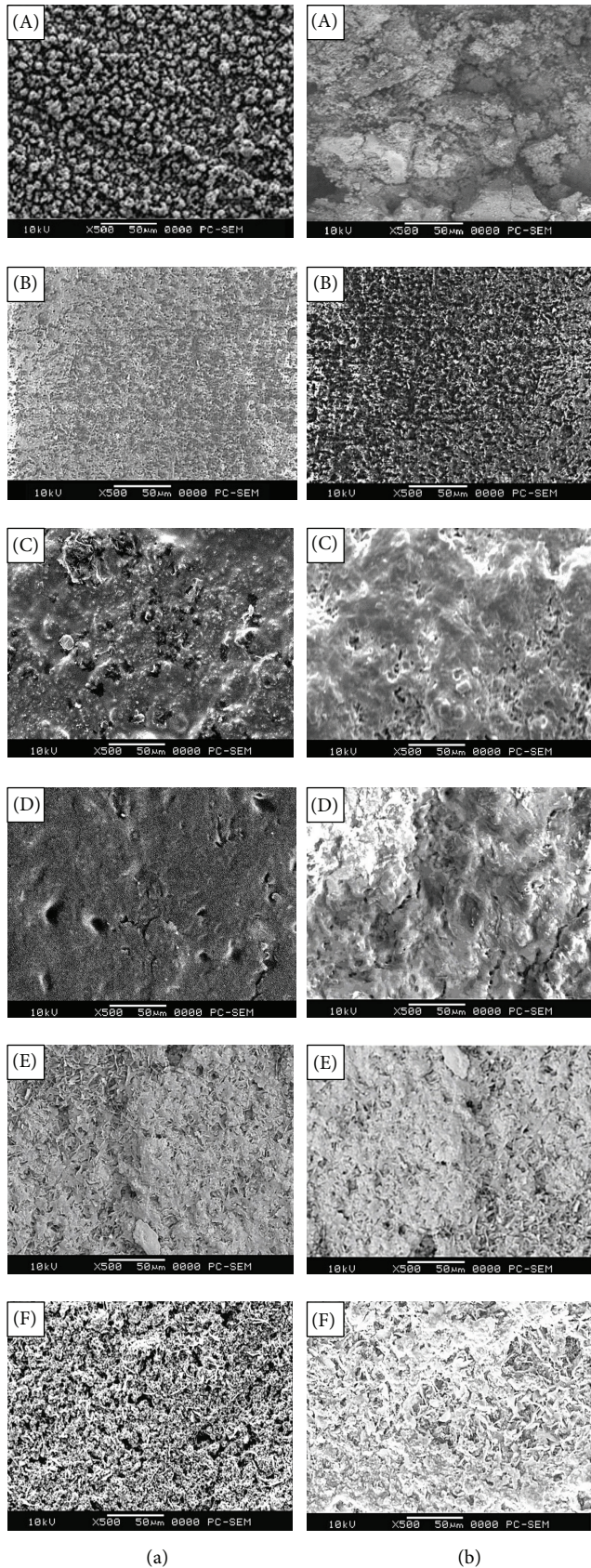


FIGURE 8: SEM morphology of LC coated with TOP for (a) being exposed and (b) after being exposed to sunlight and night humidity for samples (A), (B), (C), (D), (E), and (F).

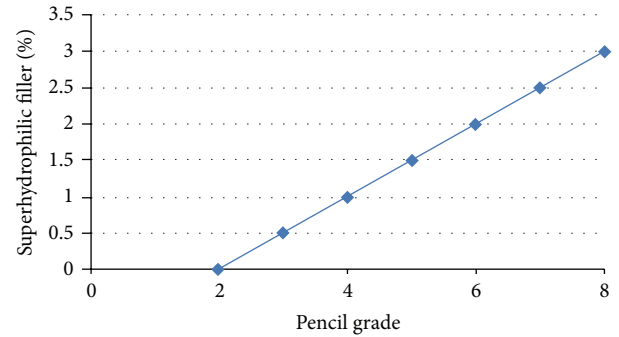


FIGURE 9: Influence of  $\text{TiO}_2$  superhydrophilic photocatalysis filler percentages against pencil grade that can gouge the TOP surfaces.

The flexural strength with minimum loading of 55% WLA concrete can sustain equivalent to the compressive strength behaviour of the standard concrete as referred to Table 3 and Table 4. Referring to Figure 7, the failure of 55%, 60%, and 65% of WLA loading for LC under flexural strength exhibited a ductile mode as compared to 70% WLA loading (sample (D)) in concrete. The WLA concrete specimens could withstand larger deflection, indicating that they could absorb more energy than the standard concrete. This is largely due to the ability of WLA to undergo a large deformation before failure [18].

The flexural load versus tensile strain curves as shown in Figure 6 indicate that the WLA concrete can undergo a much higher tensile strain before failure as compared to the standard concrete as referred to Table 4. WLA plays an important role in enhancing the strength of the lightweight concrete. When cracks occur, due to the strain capacity being exceeded, they propagate along the vertical direction. When a crack reached the WLA particles, due to the elastic properties, the WLA particles would elongate, while carrying a portion of load, until the bond between the WLA and the cement paste was broken [19].

**3.3. Weight Reduction of LC.** Lightweight composite (LC) was successfully being reduced in weight which offers 35% lighter than the commercial concrete as indicated in Table 5 according to (2). The reduction in weight of lightweight concrete was adequate while improvement and maintaining was successfully achieved its mechanical strength as shown in the above experimental results.

Physical properties including unit weight and consistency of rubberized concretes are measured and compared. The unit weight was calculated as summation of the weights of the different mixes. It was noticed that the unit weight of the concrete mixes containing rubber decreases with increasing of the percentages of rubber particles contents [20].

**3.4. Visual and SEM Morphology of Sunlight and Daily Humidity Exposure of LC Surface Coating of TOP.** The result was recorded in several categories such as colour change, sunburn, crack, dirt, oily deposition, and surface roughness as tabulated in Table 6.

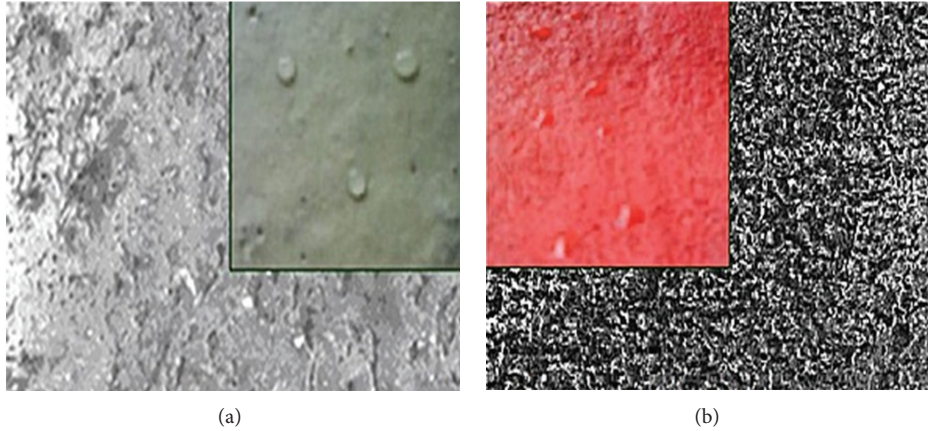


FIGURE 10: Water droplet test of LC, (a) with TOP of superhydrophobic and (b) without TOP of superhydrophobic property.

TABLE 4: Flexural strength and density of standard and lightweight cube concrete with different ratio of WLA to cement (wt/wt).

Types of composite	Composite percentages (wt/wt)	Samples	Load (N)	Flexural strength (MPa)	Deflection (mm)	
Lightweight	WLA	55%	A	3330	1.499	1.16
		60%	B	3060	1.377	1.48
		65%	C	2690	1.211	0.98
		70%	D	490	0.221	0.08
Standard composition	Commercial [8]		3500	1.450	0.02	

TABLE 5: Weight average of LC and standard commercial cube concrete.

Types of composite	Sample	Weight (kg)	Average weight (kg)
LC	Sample 1	2.96	3.03
	Sample 2	3.03	
	Sample 3	3.11	
Standard concrete	Commercial [8]		4.30

The observation of the physical properties was analyzed into two categories which are before and after exposure to sunlight and overnight humidity. As shown in Figure 3(b), for unexposed surface there are no physical changes observed such as color change, sunburn, crack, dirt, oily deposition, and surface roughness in room temperature for uncoated and coated surfaces. Meanwhile for exposed surfaces Figure 3(c) shows that the colours for sample (A) and (B) are dark brown upon exposure to sunlight and overnight humidity but did not show any crack, sunburn, dirt, oily deposition, or increase in surface roughness. Light brown colour for sample (C) was observed and no changes of colour for sample (E) and sample (F) can be observed. All the samples did not show any crack, sunburn, dirt, and oily deposition except surface roughness for sample (C), (D), (E), and (F); the surface roughness becomes smooth.

Through this observation, it is evident that the different percentages loading of TOP can affect the surface coating performance which can help to protect the changes of colour from deterioration upon environmental exposure especially

with harsh equatorial conditions. Referring to Figure 3(c), it is revealed that for, sample (F), coated surface with biopolymer doped with only 2.5% superhydrophilic particles stabilized the surface property of strong equatorial sunlight such as sunburn, crack, dirt, oily deposition, and surface roughness for longer period of time. This is due to the TOP as surface coating has the unique property of attracting rather than repelling water. The water lies flat on the surface and retained for approximately two days [21]. Furthermore, UV illumination of superhydrophilic filler leads to the formation of powerful agents with the ability to oxidize and decompose many types of bacteria and organic and inorganic materials. Hence, improvement of the quality property for surface finishing for outdoor application was observed. Longer period of exposure time should be proposed to further analyze the actual effect of surface properties as mentioned above [22].

The samples of LC with and without TOP were exposed to sunlight and overnight humidity for eight weeks. The result from SEM images was analyzed that dirt, bacteria, organic, and inorganic and other staining materials can easily be swept away with a stream of water.

As shown in Figure 8, sample (A), after being exposed to sunlight and overnight humidity, the surfaces become rough as grain raises, and the LC surface grows onto large crack; grain may loosen, loses its surface coherence, and becomes splinter, and fragments come off. All these effects brought about by a combination of light, water, mechanical forces, and heat.

The SEM micrograph of the LC surfaces before and after being exposed to sunlight and humidity exhibits that coated

TABLE 6: Observation on uncoated and coated LC samples before and after exposure to sunlight and overnight humidity.

Sample	Observation	Color change	Sunburn, crack, dirt, oily deposition	Surface roughness
A	Before	Cream	No	Rough
	After	Dark brown	Yes	Rough
B	Before	Cream	No	Low
	After	Dark brown	No	Low
C	Before	Cream	No	Low
	After	Light brown	No	Low/smooth
D	Before	Cream	No	Low
	After	Cream	No	Low/smooth
E	Before	Light cream	No	Low
	After	Light cream	No	Smooth
F	Before	Lighter cream	No	Low
	After	Lighter cream	No	Smooth

with renewable biopolymer based on waste cooking oil doped with superhydrophilic fillers (TOP) up to 2.5% shows the ability of coating to wash the surface dirt or other bacteria is high. It is also revealed that the coated surfaces with TOP have found to retain the original surface structure upon exposed to sunlight and humidity in a long term as compared to the sample (A) without coating. Therefore, no cracks, no sunburn, no dirt, and no oily deposition were found on the surfaces of coated sample after exposure.

**3.5. Scratch Resistance Test.** The pencil grade ranging from 2H to 8H can gouge or scratch the coated surface of biopolymer doped with different percentages of superhydrophilic fillers as shown in Figure 9. The higher the doped percentage of superhydrophilic as reinforcing fillers is, the higher the hardness of the pencil that can gouge or scratch the LC coated with TOP. This is due to the fact that the scratch resistance of the sample referred to the hardest pencil that will not gouge out the film. In general observation the coated sample with higher percentage of superhydrophilic has the optimum property of the scratch resistance while the uncoated sample shows the lowest value of scratch resistance by pencil test.

**3.6. Water Droplet Test.** Figure 10 shows the self-cleaning properties of TOP surfaces. The surfaces with superhydrophilic show that the self-cleaning mechanism has successfully been developed into TOP surfaces. The leaf of a lotus-plant has a water repellent wax cover which makes rain droplets just fall off the surface without spreading [23]. This is applicable or the main principal of the minimal contact between the TOP surfaces and the droplet of the water. This is due to the fact that the rain droplet that hits the TOP surfaces will immediately run off and on its way the droplet will catch dirt deposits from the surface, thus leaving the coated surface doped with TiO<sub>2</sub> clean.

#### 4. Conclusion

WLA with 55% loading equivalent to weight of cement ratio (wt/wt) has the highest capability to sustain both compressive

strength and flexural loads. It offered the weight reduction of 35% lighter than the commercial standard concrete roof tile. Considerable ductility of the WLA concrete can be observed when it is under compressive strength, especially under flexural loading. Such properties make it possible for these materials to be used in lightweight wall, pavement, floor, or road constructions where strength requirements are relatively low. Successful application of the material in these areas would be very promising. However, further investigation is needed before its practical application. For TOP as surface-coating results revealed different percentages loading of superhydrophilic filler that can be used to improve the material properties in practical use for outdoor application especially to enhance the stability of surface coating. The harsh equatorial environmental exposure test at certain period of time revealed that biopolymer from renewable resources doped with only 2.5% superhydrophilic shows no evidence of color or surface property changes such as sunburn, crack, dirt, oily deposition, and surface roughness. Therefore, by using TOP, it would benefit to improve the quality and stability of the surface finishing for outdoor and building application.

#### Acknowledgments

The authors would like to thank Universiti Tun Hussein Onn Malaysia (UTHM), Johor, and Malaysian Government for supporting this research under Malaysian Technical Universities Center of Excellent (MTUN-CoE), Vot C014.

#### References

- [1] C. Limbachiya and J. Roberts, *Construction Demolition Waste*, Thoemas, London, UK, 1994.
- [2] K. Singhai and K. Mehrotra, *Environmental Issues and Management of Waste in Energy and Mineral Production*, Taylor & Francis, Rotterdam, The Netherlands, 2000.
- [3] A. Z. M. Rus, "Degradation studies of polyurethanes based on vegetables oils. Part I. Photodegradatio," *Progress in Reaction Kinetics and Mechanism*, vol. 33, pp. 363–391, 2008.

- [4] A. Z. M. Rus, T. J. Kemp, and A. J. Clark, "Degradation studies of polyurethanes based on vegetable oils. Part 2. Thermal degradation and materials properties," *Progress in Reaction Kinetics and Mechanism*, vol. 34, no. 1, pp. 1–41, 2009.
- [5] A. Z. M. Rus, "Polymers from renewable materials," *Science Progress*, vol. 93, no. 3, pp. 285–300, 2010.
- [6] Z. Li, F. Li, and J. S. L. Li, "Properties of concrete incorporating rubber tyre particles," *Magazine of Concrete Research*, vol. 50, no. 4, pp. 297–304, 1998.
- [7] S. Gintautas and G. Audrius, "Deformation properties of concrete with rubber waste additive," *Material Science*, vol. 13, no. 3, pp. 219–223, 2007.
- [8] M. Anison, "An investigation into a hypothetical deformation and failure mechanism for concrete," *Magazine of Concrete Research*, vol. 6, no. 47, pp. 73–82, 1994.
- [9] M. C. Bignozzi and F. Sandrolini, "Tyre rubber waste recycling in self-compacting concrete," *Cement and Concrete Research*, vol. 36, no. 4, pp. 735–739, 2006.
- [10] B. D. Charles, *ASTM C 170-90, Test Method for Compressive Strength of Dimension Stone*, American Society for Testing and Materials, 2003.
- [11] B. D. Charles, *ASTM C 99, Modulus of Rupture of Dimension Stone*, American Society for Testing and Materials, 2003.
- [12] B. D. Charles, *ASTM D4258-05, Standard Practice for Surface Cleaning Concrete for Coating*, 2003.
- [13] B. D. Charles, *ASTM CD3363, Standard Test Method for Film Hardness by Pencil Test*, American Society for Testing and Materials, 2000.
- [14] A. Fujishima, K. Hishimoto, and T. Watanabe, *TiO<sub>2</sub> Photocatalysis: Fundamentals and Applications*, BKC, Tokyo, Japan, 1999.
- [15] V. R. Scahaefer, "An Overview of Previous Concrete Applications in Stormwater Management and Pavement Systems," 2006, <http://www.rmc-foundation.org/>.
- [16] P. D. Tennis, Portland Cement Characteristic. *Portland Cement Association*, 2004, <http://www.concretetechnologytoday.org/>.
- [17] P. K. Mehta and P. J. M. Monteiro, *Concrete, Properties and Materials*, Prentice Hall, Englewood Cliffs, NJ, USA, 2nd edition, 1993.
- [18] T. D. Biel and H. Lee, "Use of recycled tires in concrete, infrastructure new materials and methods of repair," in *Proceedings of the 3rd Materials Engineering Conference*, pp. 351–358, San Diego, Calif, USA, November 1994.
- [19] Z. K. Khatib and F. M. Bayomy, "Rubberized Portland cement concrete," *Journal of Materials in Civil Engineering*, vol. 11, no. 3, pp. 206–213, 1999.
- [20] M. M. Balaha, "Effect of ground waste tire rubber as fine aggregate on the behaviour of concrete structures," *ICI Journal*, vol. 3, pp. 22–30, 2007.
- [21] Danish, Use of Technical Textile Obtain Sustainable Self-cleaning Building Surface, 2006, <http://www.nordforsk.org/>.
- [22] A. Papadopoulos, J. B. Rout, L. Guiillot et al., *Innovative Self-Cleaning and De-Polluting Façade Surfaces*, Toronto, 2004.
- [23] L. J. Calbo, *Handbook of Coatings Additives*, Marcel Dekker, New York, NY, USA, 1992.

## Research Article

# Mechanical Properties of Palm Fibre Reinforced Recycled HDPE

**B. Aldousiri,<sup>1</sup> M. Alajmi,<sup>2</sup> and A. Shalwan<sup>2,3</sup>**

<sup>1</sup> Department of Power & Desalination Plants, Ministry of Electricity, Kuwait City, Kuwait

<sup>2</sup> Mechanical Production Engineering Department, College of Technological Studies, PAAET, Kuwait City, Kuwait

<sup>3</sup> Centre of Excellence in Engineered Fiber Composites (CEEFC), Faculty of Engineering and Surveying, University of Southern Queensland, Toowoomba, QLD 4350, Australia

Correspondence should be addressed to A. Shalwan; [abdullah.alajmi@usq.edu.au](mailto:abdullah.alajmi@usq.edu.au)

Received 16 April 2013; Accepted 27 April 2013

Academic Editor: Belal F. Yousif

Copyright © 2013 B. Aldousiri et al. This is an open access article distributed under the Creative Commons Attribution License, which permits unrestricted use, distribution, and reproduction in any medium, provided the original work is properly cited.

Recently, recycled thermoplastic polymers become an alternative resource for manufacturing industrial products. However, they have low mechanical properties compared to the thermosets. In this paper, an attempt has been made to enhance the mechanical properties of recycled high density polyethylene (HDPE) with chopped strand mat (CSM) glass fibres as a synthetic reinforcement and with short oil palm fibres as a biodegradable (natural) reinforcement. The effects of volume fraction of both synthetic and natural fibres on tensile, compression, hardness, and flexural properties of the HDPE were investigated. The failure mechanism of the composite was studied with the aid of optical microscopy. Tensile properties of the HDPE composites are greatly affected by the weight fraction of both the synthetic and the natural fibres. The higher strength of the composites was exhibited when at higher weight fraction of both natural and syntactic fibres which was about 50 MPa. Date palm fibre showed good interfacial adhesion to the HDPE despite the untreated condition used. On the other hand, treatment of the fibres is recommended for higher tensile performance of the composites.

## 1. Introduction

Polymers have emerged as the material used in different applications. This is due to their unique and attractive properties compared to the metal materials; that is, they own excellent impact and abrasion resistance, high strength-to-weight ratio, and high durability which fulfil the requirement for many designs in manufacturing components [1, 2]. However, there are several issues that limit the usage of such materials due to their need for synthetic reinforcements [3, 4]. Nowadays, there are regulations and carbon tax implemented in several developed countries which limits the usage of fossil products [5, 6]. This motivates the researchers and the mechanical designers to find alternative to the synthetic products. Natural fibres could be one of the most useful alternative reinforcements to the synthetic fibres such as glass, carbon, and Kevlar [7].

In the current decade, natural fibres such as coconut [8], oil palm [9], bamboo [7], and sugarcane fibres [10] are

attractive candidates and the usage of natural fibres to reinforce polymer has increased dramatically. However, there are still several potential fibres that have not been discovered yet. Date palm fibres are available in the Middle East in huge amounts [11, 12], and there is no much understanding of the mechanical properties of such fibre. This motivates the current work to be on the influence of the date palm fibre on the mechanical properties of the thermoplastic materials. Beside the aforementioned, thermoplastic materials have numerous applications in different industrial and academic sectors. Thermoplastics have the advantage of the recyclability compared to the thermoset polymers [13, 14]. High-density polyethylene is a potential recyclable matrix which showed excellent recyclability in several reported works [15, 16].

In the light of the above, the combination of environmental friendly characteristics of natural fibres and recycle HDPE polymer in developing a biorecyclable composite will be very attractive research. In the current study, the HPDE

is reinforced with date palm fibres and/or chopped glass fibres. Tensile, compressive, and hardness properties of the composites were evaluated at different weight fractions of fibres and orientations.

## 2. Materials and Experiments

Raw mesh (natural mat) surrounding the date palm tree stems was collected from a date palm farm in Kuwait. The fibres were separated from the meshes manually and washed with a tap water (2% detergent solution) to remove the contaminants and adhering dirt and dust. The extracted fibres were air-dried for 48 h at room temperature. At this stage, optical microscopy was used to check the fibre and select the desired ones. Also, the fibre diameter of  $0.7 \pm 0.05$  mm was selected in order to availability, and maturity of fibres at this diameter. In determining the fibre diameter, three measurements were taken at different cross-sections in each fibre and average diameter was calculated. Then the fibres were cut to the desired length and preserved in polyethylene bags. In this study, the extracted fibres are treated with sodium hydroxide (NaOH) for 24 h at room temperature. Then, the fibres are rinsed with fresh water and dried at room temperature for 24 h before preservation in right polyethylene bag to reduce the moisture absorption until they are used.

In the current study, several composites were prepared using hot press techniques. High density polyethylene reinforced with different weight fractions of chopped strand mar glass fibres and/or date palm fibres is prepared. Six types of composite blocks that have to be prepared are as follows:

- (1) pure HDPE,
- (2) HDPE with 6% chopped strand mat glass fibre (CSM),
- (3) HDPE with 6% palm fibre (OPF),
- (4) HDPE with 6% PF and 2% CSM,
- (5) HDPE with 6% PF and 4% CSM,
- (6) HDPE with 6% PF and 6% CSM.

Schematic drawing shows the fibre orientation in the composites presented in Figure 1. In the preparation, unidirectional geometry is selected since it is the recommended orientation in the literature [17].

**2.1. Experimental Procedure.** Mechanical properties of the developed composites were studied considering the tensile, compressive, and hardness characteristics. It is well known that when the fibre was oriented in the direction of the tensile applied load, the higher tensile strength can be achieved compared to other orientations [18–20]. Therefore, in the tensile testing, the composites were oriented in a way where the fibres are parallel to the direction of the applied load. On the other hand, since there is less work on the compressive and hardness of such composites [21–23], compressive and hardness tests were performed in two directions with respect to the applied load. In the horizontal direction, the applied load is perpendicular to the fibre mats, and, for the parallel, the fibre mats are parallel to the applied load.

## 3. Result and Discussion

Tensile, compressive, and hardness results are presented in Figures 2–8 including samples of the micrographs of the fractured samples. It should be mentioned here that the tensile experiments have been conducted in one orientation with respect to the fibre ends. In this orientation, the fibres were parallel to the applied load. However, in the compression and hardness tests, the samples were tested in two fibre orientations, that is, one parallel to the applied load and another opposite.

**3.1. Tensile Behaviour.** Figure 2 shows a sample of the tensile behaviour of the developed composites. From the figure, it is clear that all the composites exhibit ductile behaviour which is very desirable in the components design. It is well known that glass fibres are very brittle materials and always are not recommended as reinforcement for composites under fatigue loading conditions. In the current study, it can be seen that the addition of the date palm fibre preserves the ductility of the high density polyurethane despite the glass fibre addition in the composites. The summary of the three tests of each composite is listed in Table 1. In this table, it can be seen that the addition of either glass fibre or the date palm fibre enhances the mechanical properties of the HDPE since there is a significant increase in the tensile strength of the HDPE from 28 MPa to about 50 MPa. On the other hand, the addition of either fibre has slight effect on the modulus of elasticity (Young's modulus,  $E$ ). One can see that the addition of 6% natural fibres increases the tensile strength of HDPE to 38 MPa while synthetic glass fibre increases the tensile to 29 MPa only. This is mainly due to the fact that glass fibre has poor interfacial adhesion with the HDPE matrix. The combination of both synthetic and natural fibres assists in increasing the tensile strength of the HDPE to the maximum value of 50 MPa.

The SEM observation in Figure 3 indicates that there is low pull out of natural fibres since a good adhesion of the fibres appears. This shows the support of the natural fibres to the matrix during the loading conditions, [7]. In other works [1, 8, 24], the natural fibres like coconut should be treated with NaOH to gain good interfacial adhesion. It should be mentioned here that the natural fibres in [1, 8, 24] were reinforced with thermosets polymers. The high strength of thermoset compared to the thermoplastics demands high interfacial adhesion to the natural fibres. This is the main reason for the chemical treatments to the natural fibres when they are reinforced with thermosets.

**3.2. Compressive Behaviour.** The compressive experiments conducted in two orientations as the fibres were perpendicular or parallel to the applied load (Figures 4 and 5). Figure 4 shows the stress strain diagram of the typical compressive tests for all selected composites. The figure shows a ductile behaviour for all the composites which is similar to the tensile trend as shown before. However, the tensile strength of the composites seems to be much higher than the tensile strength of the neat HDPE, that is, about 50% more than

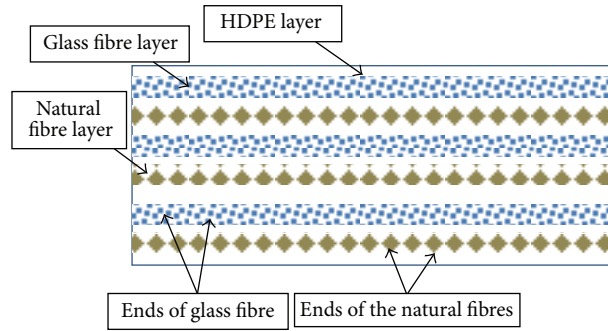


FIGURE 1: Schematic drawing shows the fibre orientation in the composites.

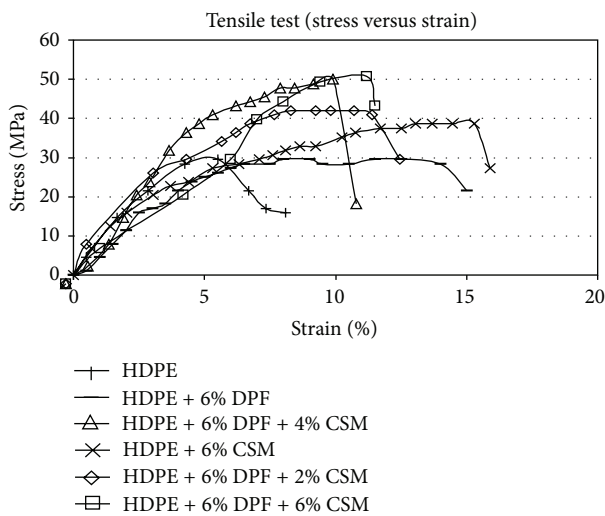


FIGURE 2: Tensile stress-strain diagram at various compositions.

TABLE 1: Ultimate tensile strength and Young’s Modulus for various compositions.

Type of composites	Ultimate tensile strength $\sigma_{UT}$ (MPa)	Young’s Modulus $E$ (MPa)
HDPE	$28 \pm 5$	350
HDPE + 6% CSM	$29 \pm 8$	200
HDPE + 6% DPF	$38 \pm 3$	330
HDPE + 6% DPF + 2% CSM	$40 \pm 6$	300
HDPE + 6% DPF + 4% CSM	$50 \pm 7$	250
HDPE + 6% DPF + 6% CSM	$50 \pm 3$	350

understanding the two orientations of the fibre with respect to the compressive applied load since there is less possibility of damage in the interface of the fibres with the matrix when the horizontal orientation was used. Similar findings were reported when the load was in tensile condition [20, 25].

the tensile strength in value. This can be observed with all the composites in horizontal direction. In this direction, the interfacial area between the fibre and the matrix is not exposed to any shear loading as in the tensile loading which in turn reduces the possibility of detachments of pull-out of fibres at high loads. The addition of either the natural fibre or the synthetic leads to higher compressive strength than the neat HDPE. Furthermore, the higher the amount of the fibres, the higher the compressive strength.

When the fibre is oriented parallel to the compressive load, the situation may change as can be seen in Figure 5 where the compressive strength reduces by about 30%–40% compared to another orientation of fibres. In the case of the fibre oriented parallel to the load, there is high possibility of detachments and decomposition of the composites. The compressive load transfers to shear force subjected between the fibre and the matrix along the fibre length which weakens the bonding area. Therefore, it is not recommended to use this composite in such loading condition. On the contrary, horizontal orientation is the recommended one which can bear high stress. To understand this further, a schematic drawing is developed and displayed in Figure 6. This assists in

3.3. *Hardness Characteristics.* The shore D hardness values of all the selected composites at both orientations (horizontal and vertical) are given in Figures 7 and 8, respectively. In both orientations, there is no remarkable influence of both types of fibres on the value of the HDPE hardness. Moreover, there is no effect of the fibre orientation on the hardness for all the composites. This can be explained by the fact that the hardness was measured on the neat HDPE surfaces especially in the case of the horizontal orientations. In the case of the vertical orientation, the hardness device needle is either on the HDPE matrix or on the interface of the fibre with the HDPE since the fibres ends are very small (cf. Figure 5). There are no reported works on the hardness of the thermoplastic materials reinforced with either synthetic or natural fibres. However, there are some works on the polyester and epoxy thermoset hardness [26, 27]. In those works, the hardness of the epoxy was very high compared to the reported ones in this work which was above 90 shore D. This is mainly due to the fact that the thermosets materials are always harder than the thermoplastic despite the fact that HDPE is reinforced with thermoset fibres (glass).

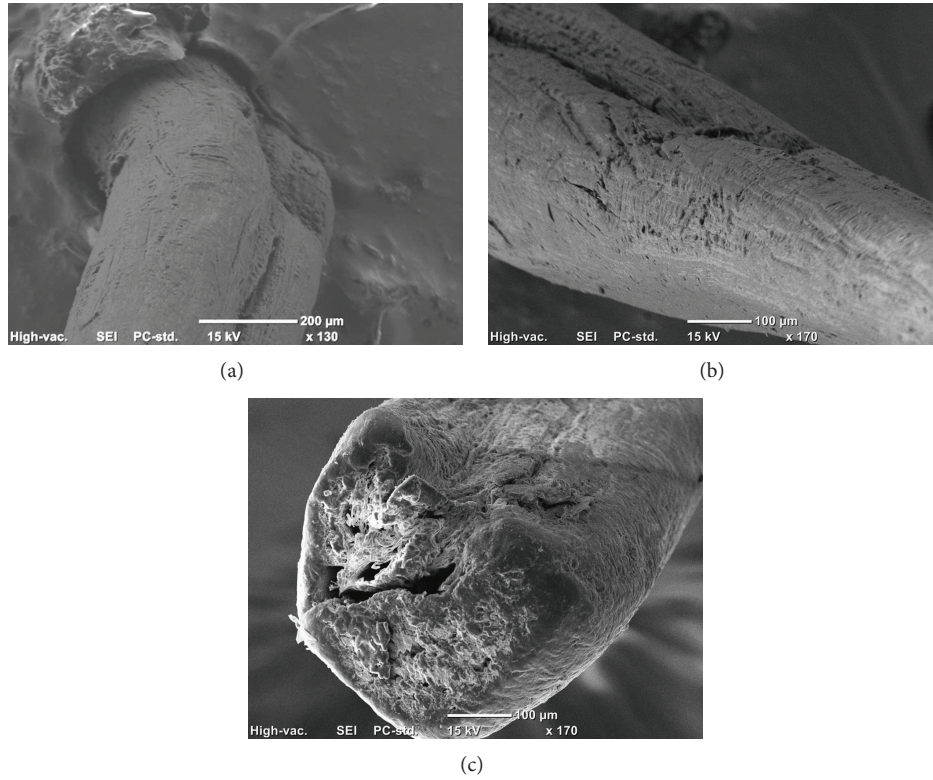


FIGURE 3: SEM micrographs of the date palm with the HDPE matrix.

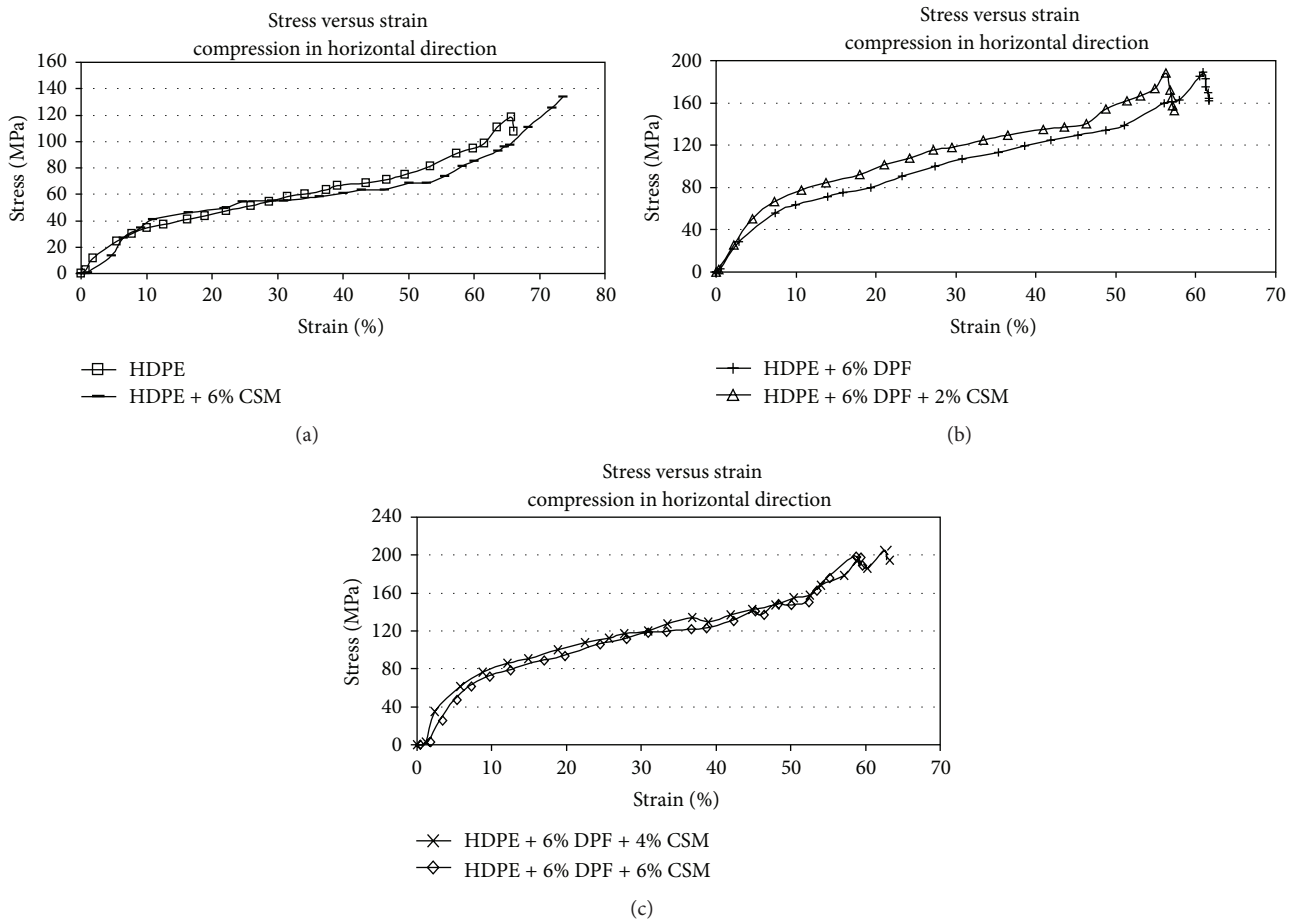


FIGURE 4: Compressive (horizontally) stress-strain diagram for various compositions.

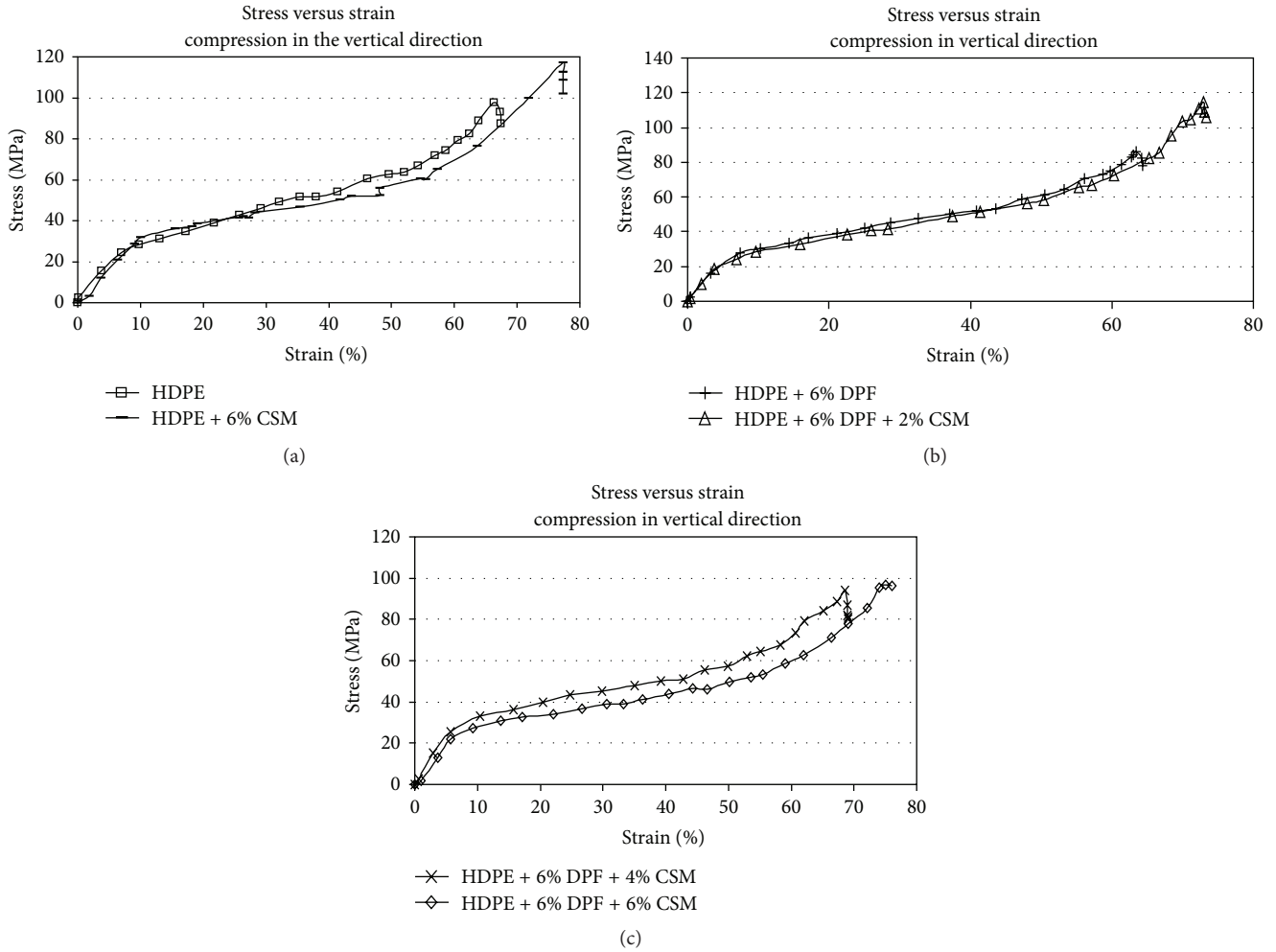


FIGURE 5: Compressive (vertically) stress-strain diagram for various compositions.

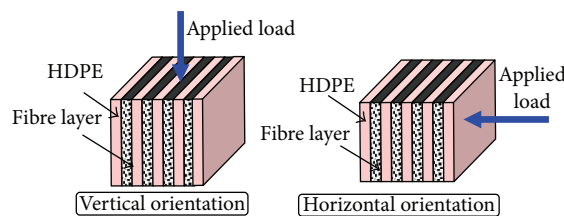


FIGURE 6: Schematic drawing showing the orientation of the fibres with respect to the applied load.

#### 4. Conclusions

After conducting the experiments and discussing the findings of the current work, few points can be concluded as follows.

- (1) Tensile properties of the HDPE composites are greatly affected by the weight fraction of both the synthetic and the natural fibres. The higher strength of the composites was exhibited when at higher weight fraction of both natural and syntactic fibres which was about 50 MPa.
- (2) Date palm fibre showed good interfacial adhesion to the HDPE despite the untreated condition used. However, treatment of the fibres is recommended for higher tensile performance of the composites.
- (3) Fibre orientation has very significant influence on compressive strength of the high density polyethylene composites. In the case of the vertical orientation, the composites suffered from detachments and delamination which resulted in low strength of the composites in this orientation. On the other hand, when the fibres were in horizontal orientation with respect to

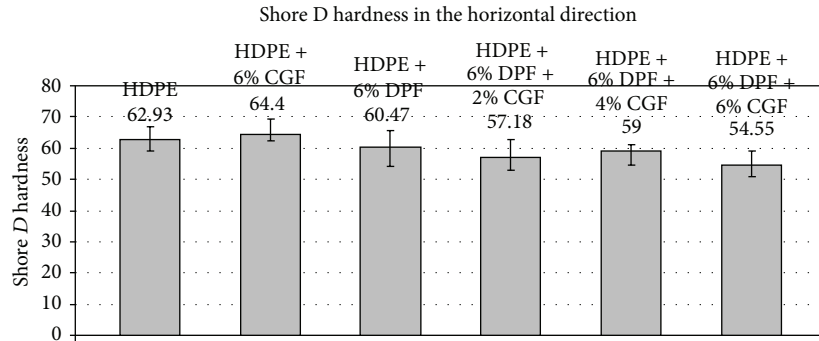


FIGURE 7: Shore D hardness values (horizontally) at various compositions.

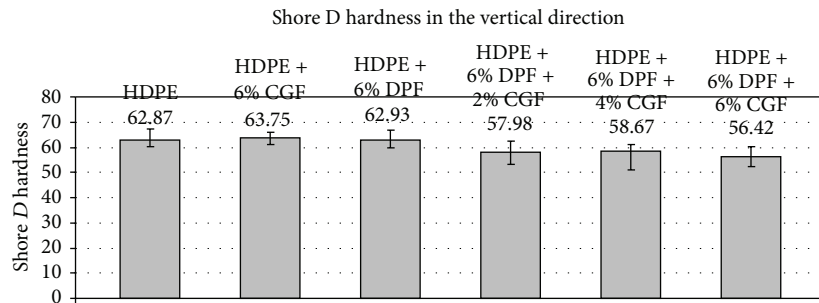


FIGURE 8: Shore D hardness values (vertically) at various compositions.

the applied load, higher resistance to the deformation was achieved.

- (4) There is no remarkable influence of both the amount and the orientation of natural and synthetic fibres on the shore D hardness since the hardness was measured on the composites surface and there is only neat HDPE presence there.

## References

- [1] B. F. Yousif, "Effect of oil palm fibres volume fraction on mechanical properties of polyester composites," *International Journal of Modern Physics B*, vol. 24, no. 23, pp. 4459–4470, 2010.
- [2] A. Shalwan and B. F. Yousif, "In state of art: mechanical and tribological behaviour of polymeric composites based on natural fibres," *Materials & Design*, vol. 48, pp. 14–24, 2013.
- [3] M. W. Chai, S. Bickerton, D. Bhattacharyya, and R. Das, "Influence of natural fibre reinforcements on the flammability of bio-derived composite materials," *Composites B*, vol. 43, no. 7, pp. 2867–2874, 2012.
- [4] S. M. Hejazi, M. Sheikhzadeh, S. M. Abtahi, and A. Zadhoush, "A simple review of soil reinforcement by using natural and synthetic fibers," *Construction and Building Materials*, vol. 30, pp. 100–116, 2012.
- [5] J. Jang, J. Lee, Y. J. Seol, Y. H. Jeong, and D. W. Cho, "Improving mechanical properties of alginate hydrogel by reinforcement with ethanol treated polycaprolactone nanofibers," *Composites B*, vol. 45, no. 1, pp. 1216–1221, 2013.
- [6] K. Majeed, M. Jawaid, A. Hassan et al., "Potential materials for food packaging from nanoclay/natural fibres filled hybrid composites," *Materials & Design*, vol. 46, pp. 391–410, 2013.
- [7] Z. N. Azwa, B. F. Yousif, A. C. Manalo, and W. Karunasena, "A review on the degradability of polymeric composites based on natural fibres," *Materials & Design*, vol. 47, pp. 424–442, 2013.
- [8] A. I. S. Brígida, V. M. A. Calado, L. R. B. Gonçalves, and M. A. Z. Coelho, "Effect of chemical treatments on properties of green coconut fiber," *Carbohydrate Polymers*, vol. 79, no. 4, pp. 832–838, 2010.
- [9] S. Shinoj, R. Visvanathan, S. Panigrahi, and M. Kochubabu, "Oil palm fiber (OPF) and its composites: a review," *Industrial Crops and Products*, vol. 33, no. 1, pp. 7–22, 2011.
- [10] S. M. Luz, A. Caldeira-Pires, and P. M. C. Ferrão, "Environmental benefits of substituting talc by sugarcane bagasse fibers as reinforcement in polypropylene composites: ecodesign and LCA as strategy for automotive components," *Resources, Conservation and Recycling*, vol. 54, no. 12, pp. 1135–1144, 2010.
- [11] Y. El may, M. Jeguirim, S. Dorge, G. Trouvé, and R. Said, "Study on the thermal behavior of different date palm residues: characterization and devolatilization kinetics under inert and oxidative atmospheres," *Energy*, vol. 44, no. 1, pp. 702–709, 2012.
- [12] M. A. AlMaadeed, R. Kahraman, P. N. Khanam, and S. AlMaadeed, "Characterization of untreated and treated male and female date palm leaves," *Materials & Design*, vol. 43, pp. 526–531, 2013.
- [13] D. Glew, L. C. Stringer, A. A. Acquaye, and S. McQueen-Mason, "How do end of life scenarios influence the environmental impact of product supply chains? Comparing biomaterial and petrochemical products," *Journal of Cleaner Production*, vol. 30, pp. 122–131, 2012.
- [14] S. Kumar, A. K. Panda, and R. K. Singh, "A review on tertiary recycling of high-density polyethylene to fuel," *Resources, Conservation and Recycling*, vol. 55, no. 11, pp. 893–910, 2011.

- [15] D. S. Achilias, C. Roupakias, P. Megalokonomos, A. A. Lappas, and Antonakou V., "Chemical recycling of plastic wastes made from polyethylene (LDPE and HDPE) and polypropylene (PP)," *Journal of Hazardous Materials*, vol. 149, no. 3, pp. 536–542, 2007.
- [16] A. Parada-Soria, H. F. Yao, B. Alvarado-Tenorio, L. Sanchez-Cadena, and A. Romo-Urbe, "Recycled HDPE-tetrapack composites. Isothermal crystallization, light scattering and mechanical properties," *MRS Proceedings*, vol. 1485, 2013.
- [17] S. B. Brahim and R. B. Cheikh, "Influence of fibre orientation and volume fraction on the tensile properties of unidirectional Alfa-polyester composite," *Composites Science and Technology*, vol. 67, no. 1, pp. 140–147, 2007.
- [18] K. Liu, H. Takagi, and Z. Yang, "Dependence of tensile properties of abaca fiber fragments and its unidirectional composites on the fragment height in the fiber stem," *Composites A*, vol. 45, pp. 14–22, 2013.
- [19] F. X. Espinach, F. Julian, N. Verdager et al., "Analysis of tensile and flexural modulus in hemp strands/polypropylene composites," *Composites B*, vol. 47, pp. 339–343, 2013.
- [20] A. Serrano, F. X. Espinach, F. Julian, R. del Rey, J. A. Mendez, and P. Mutje, "Estimation of the interfacial shears strength, orientation factor and mean equivalent intrinsic tensile strength in old newspaper fiber/polypropylene composites," *Composites B*, vol. 50, pp. 232–238, 2013.
- [21] A. Nevarez-Rascon, A. Aguilar-Elguezabal, E. Orrantia, and M. H. Bocanegra-Bernal, "Compressive strength, hardness and fracture toughness of  $Al_2O_3$  whiskers reinforced ZTA and ATZ nanocomposites: weibull analysis," *International Journal of Refractory Metals and Hard Materials*, vol. 29, no. 3, pp. 333–340, 2011.
- [22] B. Zhang, H. Fu, P. Sha et al., "Anisotropic compressive deformation behaviors of tungsten fiber reinforced Zr-based metallic glass composites," *Materials Science and Engineering A*, vol. 566, pp. 16–21, 2013.
- [23] J. Zhang, R. Luo, Q. Xiang, and C. Yang, "Compressive fracture behavior of 3D needle-punched carbon/carbon composites," *Materials Science and Engineering A*, vol. 528, no. 15, pp. 5002–5006, 2011.
- [24] B. F. Yousif and U. Nirmal, "Wear and frictional performance of polymeric composites aged in various solutions," *Wear*, vol. 272, no. 1, pp. 97–104, 2011.
- [25] Z. Rasheva, G. Zhang, and T. Burkhart, "A correlation between the tribological and mechanical properties of short carbon fibers reinforced PEEK materials with different fiber orientations," *Tribology International*, vol. 43, no. 8, pp. 1430–1437, 2010.
- [26] P. S. Babu, B. Basu, and G. Sundararajan, "The influence of erodent hardness on the erosion behavior of detonation sprayed WC-12Co coatings," *Wear*, vol. 270, no. 11-12, pp. 903–913, 2011.
- [27] B. F. Yousif, A. Shalwan, C. W. Chin, and K. C. Ming, "Flexural properties of treated and untreated kenaf/epoxy composites," *Materials & Design*, vol. 40, pp. 378–385, 2012.

## Research Article

# Reinforcement of Recycled Foamed Asphalt Using Short Polypropylene Fibers

Yongjoo Kim<sup>1</sup> and Tae-Soon Park<sup>2</sup>

<sup>1</sup> Highway Research Division, Korea Institute of Construction Technology, Daehwa-Dong 283, Goyangdae-Ro, Ilsanseo-Gu, Gyeonggi-Do, Goyang-Si 411-712, Republic of Korea

<sup>2</sup> Department of Civil Engineering, Seoul National University of Technology, 172 Gongneung 2 Dong, Nowon-Gu, Gongneung-Dong, Seoul 139-743, Republic of Korea

Correspondence should be addressed to Tae-Soon Park; [tpark@snut.ac.kr](mailto:tpark@snut.ac.kr)

Received 23 January 2013; Accepted 25 March 2013

Academic Editor: Md Mainul Islam

Copyright © 2013 Y. Kim and T.-S. Park. This is an open access article distributed under the Creative Commons Attribution License, which permits unrestricted use, distribution, and reproduction in any medium, provided the original work is properly cited.

This paper presents the reinforcing effects of the inclusion of short polypropylene fibers on recycled foamed asphalt (RFA) mixture. Short polypropylene fibers of 10 mm length with a 0.15% by weight mixing ratio of the fiber to the asphalt binder were used. The Marshall stability test, the indirect tensile strength test, the resilient modulus test, and wheel tracking test of the RFA mixtures were conducted. The test results were compared to find out the reinforcing effects of the inclusion of the fiber and the other mixtures, which included the conventional recycled foamed asphalt (RFA) mixtures; the cement reinforced recycled foamed asphalt (CRFA) mixtures; the semihot recycled foamed asphalt (SRFA) mixtures; and recycled hot-mix asphalt (RHMA) mixtures. It is found that the FRFA mixture shows higher Marshall stability than the RFA and SRFA mixtures, higher indirect tensile strength than the RFA mixture, and higher rut resistance than the RFA, SRFA, and RHMA mixtures as seen from the wheel tracking test.

## 1. Introduction

In recent years, pavement researchers are refocusing their efforts on using foamed asphalt due to environmental issues such as air pollution and recycling. The use of foamed asphalt as a recycling method for using reclaimed asphalt pavement (RAP) was once popular in the early of the 1980s in the United States, European countries and is still popular in African countries. However, the mixtures using the foamed asphalt method have been limited to low traffic volume roads due to lack of the strength and durability of the mixtures. Two reinforcing methods were used in order to improve the strength and durability of the foamed asphalt and recycled foamed asphalt (RFA). One is the use of the Portland cement as an additive, and the other is semihot RFA method [1]. It has been reported that both reinforcing methods provide a consistent quality of the mixture that is comparable to hot-mix asphalt (HMA) mixture. One of the important advantages of RFA is its ability to store the mixture at ambient temperatures for weeks. However, the inclusion

of the Portland cement and the semihot method limits the storage time to only a few hours. The use of the polypropylene fibers is expected to increase the strength and durability of the RFA mixture as found in the both hot- and cold-asphalt mixtures [2–5] and would also maintain its longer storage time. This study presents the mechanical properties and the enhanced performance of RFA mixtures when polypropylene fibers were included in the RFA mixtures. Four different kinds of RFA mixtures and a hot recycling asphalt mixture were tested and compared. The enhanced performance of the RFA mixture with fiber is discussed in terms of the Marshall stability, the indirect tensile strength, resilient modulus, the moisture susceptibility, and the dynamic stability.

## 2. Literature Review on Recycled Foamed Asphalt and Fiber Reinforced Asphalt Mixtures

*2.1. Recycled Foamed Asphalt (RFA) Mixtures.* The first foamed asphalt processes were introduced by Lee [6]. The

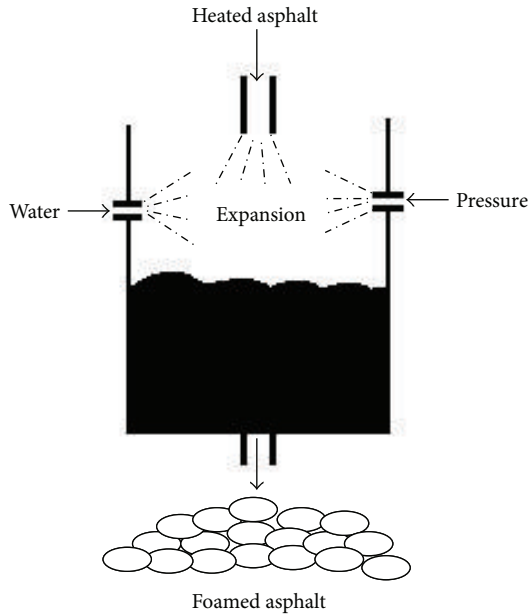


FIGURE 1: Schematic diagram of foaming system.

foamed asphalt technology has been used for low-volume roads and soil stabilization for many years in the past. The foaming technology has been continually developed using a low-pressure and cold-water system to improve the quality of the foamed asphalt mixture. Figure 1 is the schematic diagram of the foaming system.

Wijk and Wood [7], Brennen et al. [8], Roberts et al. [9], and Tia and Wood [10] have studied the use of foamed asphalt in recycling of an asphalt pavement. These studies demonstrated the feasibility of using RAP to produce a RFA mixture with new materials, such as new aggregates and binder. Portland cement was used as an additive to increase the strength of the RFA and decrease the curing time of the RFA. However, the inclusion of the Portland cement resulted in limiting of the storage time to one hour or so. Jenkins et al. [1] have developed the semihot treatment for the foamed asphalt. The treatment is that RAP and aggregate are heated to between 80°C and 95°C. The water and filler are added to the mixture during mixing. The process improves the binder coating of the RAP and aggregate, and the performance of the RAP is comparable to hot-mix asphalt (HMA). This process can significantly improve the quality of the RFA; however, the separate heating system is required to heat the RAP and aggregate and the storage time of the mixture cannot be kept as long as that of the conventional RFA mixture. Marquis et al. [11], Mohammad et al. [12], Loizos and Papavasiliou [13], and He and Wong [14] reported the performance in the field for medium- and low-volume roads. Kim and Lee [15] and Kim et al. [16] addressed a new mix design method and validation of the foamed asphalt mix. However, these studies did not address the reinforcing methods of the foamed asphalt mix.

**2.2. Fiber Reinforced Asphalt (FRA) Mixtures.** The previous studies showed that the use of polypropylene improved the performance and the crack resistance of both hot mix and cold mix, with most application in HMA. The use of short

polypropylene fibers in the HMA mixture showed that the strain energy measured at a low temperature (0°C and -18°C) was increased [2]. According to Button and Epps [17], small quantities of certain polypropylene fibers with good tensile properties can effectively retard reflective cracking in HMA mixture. Mills and Keller [18] also stated that the addition of polypropylene fibers does offer some improvement in the performance of the asphalt mixture by retarding the reflective crack. They emphasized the importance of the denier (a measurement that is used to identify the fiber thickness of individual thread), surface finishing, and the optimum fiber concentration for paving mixture.

Epps et al. [19] have conducted various tests and the test results showed that fibers in properly designed asphalt mixture have the potential to increase overall service life. The addition of fibers resulted in a decreased susceptibility to moisture damage [4]. Based on the results from the previous studies, with appropriate fiber quantities and distribution of fibers in the mixture, asphalt mixtures can resist cracking by redistributing stresses. The inclusion of the fiber in asphalt mixtures resulted in an increase in the optimum asphalt contents of between 0.5% and 1.0% [4].

### 3. Description of RFA Mixtures Evaluated

Four different types of RFA mixtures and a recycling HMA mixture were prepared to conduct mechanical laboratory tests. The descriptions of each mixture are as follows.

- (1) Conventional RFA mixture without the inclusion of fiber or additive and without heating; the mixture is named RFA.
- (2) RFA mixture including 2.0% of cement by the volume of the weight of the total mixture. The ratio of cement was adjusted to find the optimum ratio; 1.0%, 2.0%, and 3.0% were tried, and 2.0% was found to be the optimum ratio using the unconfined compression test: 3 days cured at 60°C as suggested by Bowering and Martin [20]. Lewis and Collings [21] and Marquis et al. [11] recommended the 2.0%–4.0% and 1.5%, respectively, the mixture is named CRFA.
- (3) Semihot RFA: the RAP and the virgin aggregate were heated to 90°C. (90°C was found as an optimum heating temperature at 60, 70, 80, 90, 100°C as a result of the aggregate coating) the mixture is named SRFA.
- (4) Mixture 1 (RFA) + polypropylene fiber (0.15% by the weight of asphalt mixture was used): the indirect tensile strength tests were used to find out the optimum contents of the fiber [19]; the mixture is named FRFA.
- (5) Recycling hot-mix asphalt: the mixture is named RHMA.

### 4. Selection of Materials Used in Mix Design

**4.1. Polypropylene Fiber.** Polypropylene fiber was used in this study having a singular shape and white to light gray color (Figure 2). The physical properties of the fiber are shown in Table 1. The 0.15% of the fiber by the weight of asphalt

TABLE 1: Physical properties of short polypropylene fiber used in the study.

Physical properties	Value	Test procedures
Denier	0.00189 ± 0.004 mm	ASTM D 1577
Length	10 ± 2 mm	—
Crimps	None	ASTM D 3987-82
Tensile strength	2,812 Kg/cm <sup>2</sup> min.	ASTM D 822-83
Elongation	33%, min.	ASTM D 2256-80
Specific gravity	0.91	—
Alkali resistance	99% strength retained	40% NaOH solution at 21°C for 1,000 hours
Acid resistance	99% strength retained	95% HCl solution at 21°C for 1,000 hours
Moisture regain at 70% and 65% relative humidity	Less than 0.1%	ASTM D 2654-76

mixture was used and the fiber was integrated while the RAP, aggregate, and the asphalt are mixing.

**4.2. Additive.** Portland cement was used as an additive. According to Bowering and Martin [20], Castedo et al. [22], Lewis and Collings [21], and Marquis et al. [11], the Portland cement can be used for reducing the curing times and increasing the marginal strength of foamed asphalt mixtures. The amount of 2.0% by the total weight of foamed asphalt mixture was used.

**4.3. Reclaimed Asphalt Pavement (RAP).** The RAP materials are collected from a 10-year-old pavement, which contains 5.3% asphalt content, with a penetration of 27 and viscosity of 6,860 Poise. The gradation of the RAP is within the specification; however, it is close to the upper limit in the coarse part and to the lower limit in the fine part of the specification. The gradation for the mix design was controlled by adding new aggregate bringing the gradation curve to the center portion of the specification limits. Figure 3 shows the gradation of the RAP and aggregate mixture.

**4.4. New Aggregates and Asphalt.** The specific gravity of fine aggregate is 2.71 and that of coarse aggregate is 2.64. A PG 64-22 asphalt binder is used to produce the foamed asphalt.

## 5. Mix Design

A Wirtgen laboratory scale unit manufactured in Germany was used to produce the foamed asphalt in this study. Foamed asphalt was produced by injecting cold water and hot asphalt with varying the air pressure in the air chamber. Expansion ratio and half-life were measured upon varying the temperature and chamber pressure. The temperature of the asphalt was varied between 160°C and 180°C. The foaming water content was varied between 1.0% and 3.0% by the volume of asphalt to find the optimum foaming asphalt moisture content. The air pressure was 179 kPa in this study.

**5.1. Determination of Optimum Moisture Content.** A unique procedure for the mix design of foamed asphalt is the determination of the optimum moisture contents for both aggregate and foamed asphalt binder. The optimum moisture

content for the aggregate and binder was determined in accordance with the South African specification [23]. The following procedures were used to determine the optimum foaming moisture contents for the production of the foamed asphalt binder:

- (1) asphalt binder was prepared to be produced at moisture contents ranging from 1.0% to 3.0% in an increment of 0.5%.
- (2) For each sample, allow the foam to discharge for 5 seconds into 20 liters steel drum and mark the maximum volume to which the foam expands. The time was measured in seconds that the foam takes to dissipate to half of its maximum volume (half-life).
- (3) The expansion ratio of the foamed asphalt was calculated by dividing the maximum foamed volume by the volume of asphalt in the drum after the foam has completely dissipated.

Using the expansion ratio and half-life relationship, the optimum foaming moisture content was determined to be 1.4% of the volume of asphalt. Figure 4 shows the relationship between the expansion ratio and the half-life of foamed asphalt in this study. The maximum dry density of the RAP and virgin aggregate is 2.1 g/cm<sup>3</sup> and the optimum moisture content is 5.9% using the modified proctor test [24].

**5.2. Optimum Foamed Asphalt Content.** In the past, Muthen [23] recommended that the optimum foamed asphalt content should be selected based on the relationship between indirect tensile strength and foamed asphalt content. Mohammad et al. [12] also determined the optimum foamed asphalt content based on the asphalt content that produced the maximum retained indirect tensile strength. To determine the optimum foamed asphalt content, the Basic Asphalt Recycling Manual [25] recommended the following test results: Marshall stability in dry and wet conditions and indirect tensile strength in dry and wet conditions. In this study, the average optimum foamed asphalt content (OFAC) was calculated by averaging four optimum foamed asphalt contents determined at highest Marshall stability and indirect tensile strength.

The OFAC was varied due to the inclusion of the fiber and also the different producing method of the recycled foamed



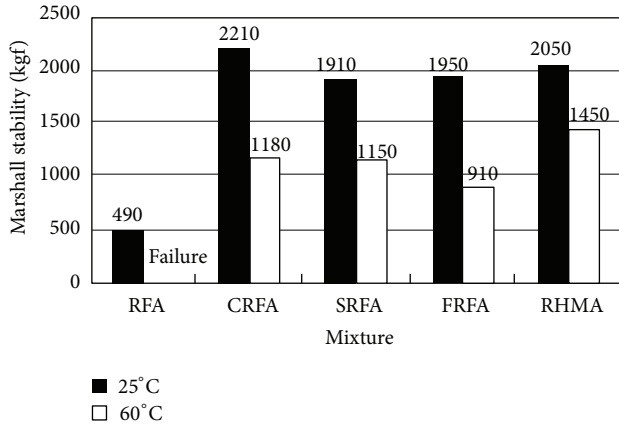


FIGURE 6: Marshall stability test results at 25°C and 60°C.

the Marshall stability test results. Based on the test results, the inclusion of the fiber resulted in the increase in the Marshall stability of the FRFA compared to that of the RFA mixture which failed at 60°C and that of SRFA and RHMA is comparable.

**6.2. Indirect Tensile Strength Test Results.** Indirect tensile strength is commonly used to characterize the crack resistance of hot-mix asphalt (HMA) pavement. For this study, indirect tensile strength values were measured for five different recycled mixtures in dry and wet conditions at 25°C. Figure 7 shows the indirect tensile strength test results. As shown in Figure 7, the indirect tensile strength is affected by the inclusion of the fiber and the cement as well as the semihot process. The effectiveness of the fiber is significant when the samples were in dry condition; however, such is not the case when the samples were tested in the wet condition. Because foamed asphalt mixture is susceptible to failure by moisture intrusion, it is postulated that moisture sensitivity is one of the major drawbacks of the RFA mixture. The wet and dry ratio of the indirect tensile strength of the FRFA mixtures improved compared to that of the RFA mixtures and less comparable to the other RFA mixtures. In comparison, the indirect tensile strength of RHMA mixture is superior to the all RFA mixtures tested in this study.

In Figure 8, the variation of the indirect tensile strength is shown as the storage time is increasing. The indirect tensile strength of the FRFA is dependent upon the storage times. However, that of the CRFA, SRFA, and RHMA mixtures is significantly decreased as the storage time is increased. It should be noted that the indirect tensile strength is strongly dependent upon the storage times and the reinforcing method of the RFA.

**6.3. Resilient Modulus Test Results.** Resilient modulus test is the most common method of measuring stiffness modulus for HMA. It has been shown that stiffer mixtures at low temperatures trend to crack earlier than more flexible mixtures. Figure 9 shows resilient modulus of five different recycled asphalt mixtures as a function of the testing temperature.

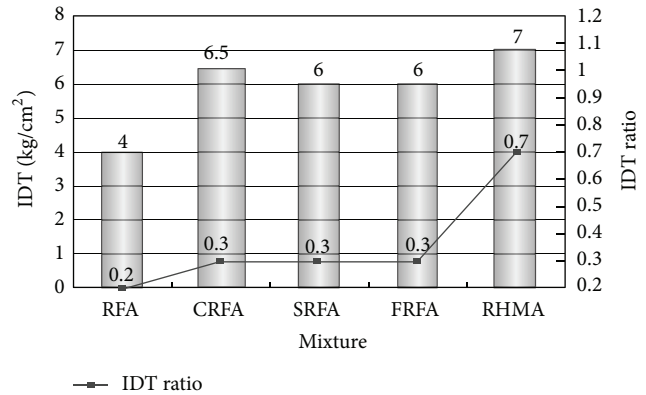


FIGURE 7: Indirect tensile strength test results and IDT ratio.

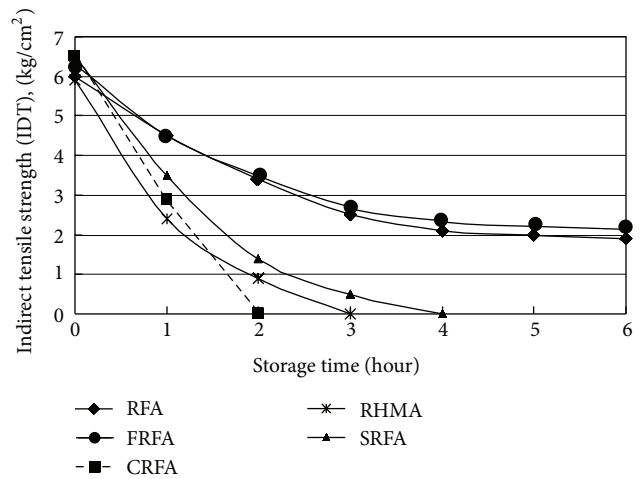


FIGURE 8: Effect of storage time on indirect tensile strength.

The interesting finding of Figure 9 is the difference in the shape of the curves for the mixtures. All RFA mixtures are less susceptible to the temperature changes except the RHMA mixture. The inclusion of the fiber in RFA increased the resilient modulus.

**6.4. Wheel Tracking Test Results.** Permanent deformation is an issue of critical distress in asphalt pavement and is defined as the accumulation of a small amount of unrecoverable strains due to traffic loading. It typically occurs under higher temperature when the pavement under traffic loading consolidates and/or there is a lateral movement of the HMA. Lateral movement is a shear failure and typically occurs in the upper portion of the pavement surface layer. As a result of permanent deformation, the pavement service life cycle is reduced due to vehicle hydroplaning at rutting area. The wheel tracking test was conducted to evaluate rutting resistance of five different recycled asphalt mixtures at 40°C. The results of the wheel tracking tests were evaluated in terms of the dynamic stability (cycle/mm). The dynamic stability defines the number of wheel paths that reach the 1 mm deformation (permanent deformation) in the mixture.

TABLE 2: Mean of three test properties and  $T$ -test analysis results.

Mean property	RFA	CREA	SRFA	FREA	RHMA	Prob. >  t									
						REA versus CREA	RFA versus SRFA	RFA versus FREA	RFA versus RHMA	CRFA versus SRFA	CRFA versus FREA	CRFA versus RHMA	SRFA versus RHMA	SRFA versus FREA	SRFA versus RHMA
Marshall stability (Kgf)	490	2210	1910	1950	2050	0.0001	0.0001	0.0001	0.0001	0.023	0.01	0.108	0.221	0.004	0.070
Indirect tensile strength (Kg/cm <sup>2</sup> )	4.0	6.5	6.0	6.0	7.0	0.0003	0.0006	0.0002	0.0009	0.086	0.079	0.092	0.5	0.017	0.013
Dynamic stability (cycle/mm)	800	1500	950	1200	350	0.0011	0.0674	0.0005	0.0005	0.0001	0.005	0.0001	0.003	0.0001	0.0001

TABLE 3: Summary of *t*-test results for the three properties.

Property	Method	RFA	CRFA	SRFA	FRFA	RHMA
Marshall stability (Kgf)	RFA	—	S	S	S	S
	CRFA		—	S	S	NS
	SRFA			—	NS	S
	FRFA				—	NS
	RHMA					—
Indirect tensile strength (Kgf/cm <sup>2</sup> )	RFA	—	S	S	S	S
	CRFA		—	NS	NS	NS
	SRFA			—	NS	S
	FRFA				—	S
	RHMA					—
Dynamic stability (cycle/mm)	RFA	—	S	NS	S	S
	CRFA		—	S	S	S
	SRFA			—	S	S
	FRFA				—	S
	RHMA					—

S: significant; NS: not significant.

TABLE 4: Analysis of variable result for Marshall stability.

Source	DF	Sum of squares	Mean square	F value	Pr > F
Mixture	4	9754400	2438600	220.09	<0.0001
Error	20	221600	11080		
Corrected total	24	9976000			

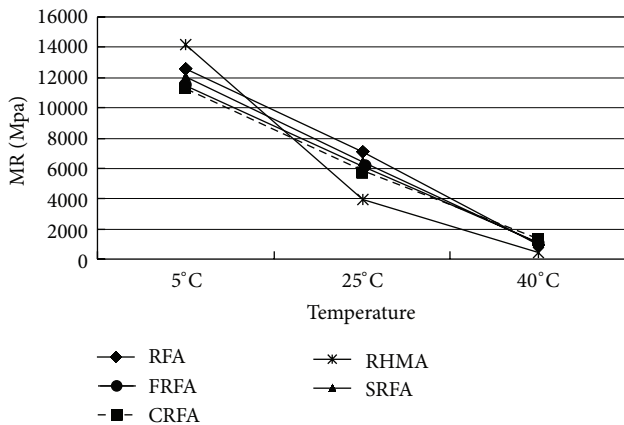


FIGURE 9: Resilient modulus test results at three different temperatures.

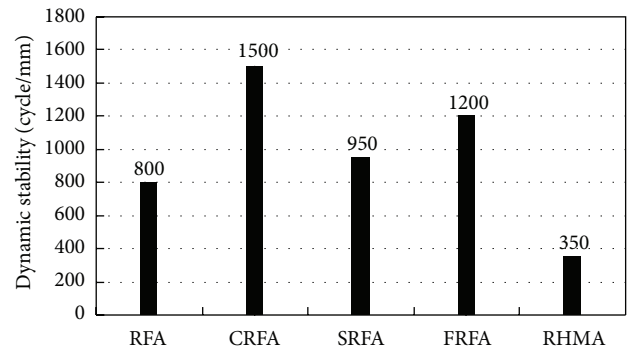


FIGURE 10: Wheel tracking test results.

Figure 10 shows the dynamic stability values for five different recycled asphalt mixtures. All RFA mixtures are resistant to the permanent deformation, and the CRFA and FRFA mixtures show the highest resistance to permanent deformation. On the other hand, the permanent deformation of the RHMA mixture is significantly higher than that of the RFA mixtures.

6.5. Summary. The inclusion of short polypropylene fibers improved the Marshall stability and the indirect tensile

strength. When the fiber is dispersed in the recycled foamed asphalt (RFA) mixture, the structure of foamed mixture is internally reinforced. However, the structure of the RFA and FRFA is weakened by water intrusion. Therefore, the improvement of the stability and the indirect strength was not significant when the samples were tested in a wet condition. Resilient modulus of FRFA mixture is increased with the inclusion of the polypropylene fiber. Button and Epps [17] have addressed the same results on the resilient modulus test. Resistance to permanent deformation of the FRFA mixture is another finding. All RFA mixtures showed good resistance to permanent deformation except semihot

TABLE 5: Analysis of variable result for the indirect tensile strength.

Source	DF	Sum of squares	Mean square	F value	Pr > F
Mixture	4	25.9816	6.4954	37.46	<0.0001
Error	20	3.4680	0.1734		
Corrected total	24	29.4496			

TABLE 6: Analysis of variable result for dynamic stability.

Source	DF	Sum of squares	Mean square	F value	Pr > F
Mixture	4	3845404.16	961351.04	138.54	<0.0001
Error	20	138778.80	6938.94		
Corrected total	24	3984182.96			

mixture and RHMA mixture. According to Ruckel et al. [25], this property is likely due to the discontinuous nature of the foamed-asphalt binding mechanism; that is, the binder formed a discontinuous random matrix of primarily fines and asphalt.

## 7. Statistical Analysis

The reinforcing effect of fiber on the recycled foamed asphalt mixtures was analyzed statistically. The statistical analysis was made in terms of the significance of the inclusion of the fiber and the improvement of performance in the laboratory for each mixture. Typical Student's *t*-test was conducted. The average of the three properties and results of Student's *t*-test at = 0.05 level were shown in Table 2. The mean data obtained were from equal number of samples (i.e., five each). If Prob. > |*t*| is lower than 0.05, the significant difference exists statistically. On the basis of Table 2, the significant difference was evaluated and summarized in Table 3. Table 3 showed that the inclusion of the fiber in RFA mixture had significant effect on the Marshall stability, the indirect tensile strength, and the wheel tracking (dynamic stability). When the performance of the FRFA mixtures was compared to that of the RFA and other RFA mixtures, the FRFA mixture showed statistically significant difference from the RFA mixture in Marshall stability and indirect tensile strength at = 0.05. The FRFA also showed a significantly higher rut resistance, measured by wheel tracking, from the RFA mixture at the same significant level. From this analysis, it was proved that the FRFA was improved statistically significantly in Marshall stability, tensile property, and permanent deformation resistance.

Tables 4, 5, and 6 show analysis results of variance (ANOVA) for the Marshall stability, the indirect tensile strength, and the dynamic stability, respectively. In all three properties, the probability of *F* value (Fisher statistics) shows highly significant level ("Pr > *F*" less than 0.0001 in each table) among five mixtures. This means that five mixtures made of different additive materials have different property levels and show statistically significant difference in each strength property.

## 8. Conclusions

Based upon the test results in the laboratory study using various recycled foamed asphalt (RFA) methods, the following

conclusions can be made. The inclusion of the polypropylene fibers in the RFA mixture is a viable method to improve the performance of the RFA mixture. Particularly, the Marshall stability and the indirect tensile strength of RFA mixture show higher values due to the inclusion of the polypropylene fiber. The temperature susceptibility of fiber-recycled foamed asphalt (FRFA) mixture is decreased. The permanent deformation resistance of FRFA mixture is another advantage when it is compared with that of recycling hot-mix asphalt (RHMA). Typical statistical analysis supports these findings. The inclusion of Portland cement and semihot method seems to provide the reinforcing effects to RFA mixture; however, the storage time is limited only to an hour or so. The FRFA mixture is equally susceptible to moisture as the other foamed asphalt mixtures. The fiber reinforcement did not make it more moisture susceptible though it did not improve the indirect tensile ratio.

## Acknowledgments

This study is funded by the Seoul National University of Science and Technology and supported by a Grant from a strategic research project "Development of Low-Carbon and Low-Cost Asphalt Pavements" funded by the Korea Institute of Construction Technology.

## References

- [1] K. J. Jenkins, Groot, D. JLA, M. Ven, and A. Molenaar, "Half-warm foamed bitumen treatment, a new process," in *Proceedings of the 7th Conference on Asphalt Pavements for Southern Africa*, pp. 1-17, 1999.
- [2] H. W. Busching, O. E. Achara, and S. E. Gaj, *Use of Short Polypropylene Fibers in Hot Mix Asphalt Concrete*, Resident Representative Clemson University, 1980.
- [3] M. Smith and R. A. Howden, *Final Evaluation of Hercules Fiber Pave 3010 in Cold Mix Pothole Patch Material*, Resident Representative Indiana DOT, 1982.
- [4] R. B. Freeman, J. L. Burati, S. N. Amirkhani, and W. C. Bridge, *Polyester Fibers in Asphalt Paving Mixtures*, Resident Representative Clemson University, Asphalt paving technology, 1989.
- [5] B. S. Bueno, W. R. Silvia, D. C. Lima, and E. Minete, "Engineering properties of fiber reinforced cold asphalt mixes," *Journal of Environmental Engineering*, vol. 129, no. 10, pp. 952-955, 2003.

- [6] D. Y. Lee, "Treating marginal aggregates and soil with foamed asphalt," *Association of Asphalt Paving Technologists*, vol. 50, pp. 150–211, 1981.
- [7] A. van Wijk and L. E. Wood, "Use of foamed asphalt in recycling of an asphalt pavement," *Transportation Research Record*, pp. 96–103, 1983.
- [8] M. Brennen, M. Tia, A. Altschaeffl, and L. E. Wood, "Laboratory investigation of the foamed asphalt for recycled bituminous pavements," *Transportation Research Record*, pp. 80–87, 1983.
- [9] F. L. Roberts, J. C. Engelbrecht, and T. W. Kennedy, "Evaluation of recycled mixtures using foamed asphalt," *Transportation Research Record*, pp. 78–85, 1984.
- [10] M. Tia and L. E. Wood, "Use of asphalt emulsion and foamed asphalt in cold-recycled asphalt paving mixtures," *Transportation Research Record*, pp. 315–321, 1984.
- [11] B. Marquis, R. L. Bradbury, S. Colson et al., *Design, Construction and Early Performance of Foamed Asphalt Full Depth Reclaimed(FDR) Pavement in Maine, CD-ROM*, Transportation Research Board of the National Academies, Washington, DC, USA, 2003.
- [12] L. N. Mohammad, M. Y. Abu-Farsakh, Z. Wu, and C. Abadie, "Louisiana experience with foamed recycled asphalt pavement base materials," *Transportation Research Record*, no. 1832, pp. 17–24, 2003.
- [13] A. Loizos and V. Papavasiliou, "Evaluation of foamed asphalt cold in-place pavement recycling using nondestructive techniques," *Journal of Transportation Engineering*, vol. 132, no. 12, pp. 970–978, 2006.
- [14] G. P. He and W. G. Wong, "Laboratory study on permanent deformation of foamed asphalt mix incorporating reclaimed asphalt pavement materials," *Construction and Building Materials*, vol. 21, no. 8, pp. 1809–1819, 2007.
- [15] Y. Kim and H. D. Lee, "Development of mix design procedure for cold in-place recycling with foamed asphalt," *Journal of Materials in Civil Engineering*, vol. 18, no. 1, pp. 116–124, 2006.
- [16] Y. J. Kim, H. D. Lee, and M. Heizman, "Validation of new mix design procedure for cold in-place recycling with foamed asphalt," *Journal of Materials in Civil Engineering*, vol. 19, no. 11, pp. 1000–1010, 2007.
- [17] J. W. Button and J. A. Epps, *Mechanical Characterization of Fiber Reinforced Bituminous Concrete*, Resident Representative Texas A & M University. Residence Foundation for Hercules, 1981.
- [18] D. R. Mills and T. J. Keller, *The Effectiveness of Synthetic Fiber Reinforced Asphaltic Concrete Overlays in Delaware*, Resident Representative Delaware DOT, 1982.
- [19] J. A. Epps, J. W. Button, and D. Little D, *Predicted Performance of Asphalt Paving Mixtures Containing Fibers*, Resident Representative Texas A & M. University, 1984.
- [20] R. H. Bowering and C. L. Martin, "Foamed bitumen production and application of mixtures, evaluation and performance of pavements," *Association of Asphalt Paving Technologists*, vol. 45, pp. 453–477, 1976.
- [21] A. Lewis and D. C. Collings, "Cold in place recycling: a relevant process for road rehabilitation and upgrading," in *Proceedings of the 7th Conference on Asphalt Pavement for South Africa (CAPSA '99)*, pp. 1–13, 1999.
- [22] H. Castedo, C. C. Beuadon, E. L. Wood, and A. G. Altschaeffl, "Durability characteristics of foamed asphalt mixtures," in *Proceedings of the 29th Annual Canadian Technical Asphalt Association Conference*, pp. 103–107, Montreal, Canada, 1984.
- [23] K. M. Muthen, "Foamed asphalt mixes design procedures," Contract Rep CR-98/077, CSIR Transportek, Pretoria, South Africa, 1999.
- [24] ASTM, "Standard test methods for laboratory compaction characteristics of soil using modified effort," Tech. Rep. ASTM D 1557-07, ASTM, West Conshohocken, Pa, USA, 2007.
- [25] P. J. Ruckel, L. L. Kole, F. Abel, R. E. Zator, J. W. Button, and J. A. Epps, "Foam mix asphalt advances, asphalt pavement construction: new materials and techniques," Tech. Rep. ASTM SPT 724, 1982.
- [26] ASTM, "Test method for resistance of plastic flow of bituminous mixtures using Marshall apparatus," Tech. Rep. ASTM D1559-89, ASTM, West Conshohocken, Pa, USA, 1989.
- [27] ASTM, "Standard test method for indirect tension test for resilient modulus of bituminous mixtures," Tech. Rep. ASTM D 4123-82, ASTM, West Conshohocken, Pa, USA, 1995.
- [28] Korea National Highway Corporation (KNHC), *Expressway Construction Guide Specification*, part 9, Asphalt Pavement for Surface Course, 2007.

## Research Article

# Effects of Fiber Orientation and Material Isotropy on the Analytical Elastic Solution of a Stiffened Orthotropic Panel Subjected to a Combined Loading

S. K. Deb Nath<sup>1,2</sup>

<sup>1</sup> Division of Mechanical and Automotive Engineering, Kongju National University, Republic of Korea

<sup>2</sup> Graduate School of Engineering Science, Osaka University, Japan

Correspondence should be addressed to S. K. Deb Nath; [sankar\\_20005@yahoo.com](mailto:sankar_20005@yahoo.com)

Received 4 December 2012; Accepted 23 February 2013

Academic Editor: Belal F. Yousif

Copyright © 2013 S. K. Deb Nath. This is an open access article distributed under the Creative Commons Attribution License, which permits unrestricted use, distribution, and reproduction in any medium, provided the original work is properly cited.

Using the displacement potential approach of orthotropic composite materials for the plane stress conditions, an orthotropic panel subjected to a combined loading at its right lateral edge is solved. Effects of fiber orientations and material isotropy on the elastic field of an orthotropic panel subjected to a combined loading are discussed. The analytical elastic solutions at different sections of the panel with fiber orientation  $\theta = 90^\circ$  are compared with those of finite element predictions to ensure the reliability of our present solutions.

## 1. Introduction

Recently in lightweight structures, the use of orthotropic composite material is increasing due to its higher strength weight ratio compared to its corresponding isotropic material. Aircraft wings which are generally made of aluminium are stiffened. Nowadays, boron/epoxy, graphite/epoxy orthotropic composite materials are used for manufacturing of aircraft panels. In structures, the stiffened panel experiences tension and bending at the same time. Effect of fiber orientation and material isotropy on the exact elastic field is necessary for designing purpose because strength, toughness, and all other mechanical properties of any orthotropic composite depend on its fiber orientation. Under loading, the stress and displacement components of any orthotropic composite vary with the variation of fiber orientation. This type of analysis is carried out by the finite element method. Exact analytical solution of this type of problem is hardly possible to carry out till now due to lack of effective elasticity formulations of orthotropic composite materials and boundary management techniques.

The limited progress in solution of the two-dimensional problems of elasticity theory for anisotropic bodies was

achieved by means of Lekhnitskii formalism [1, 2] and Stroh's formalism [3, 4]. Some solutions of the two-dimensional problems for anisotropic bodies were obtained by these approaches. An exposition of Stroh's formalism and its application to a limited number of two-dimensional problems was given by Ting [5]. The proof of the equivalence between the Lekhnitskii and Stroh formalisms was obtained by Barnett and Kirchner [6]. The stress analysis problems are still suffering from a lot of shortcomings in spite of becoming the fundamental subject in the field of elasticity and thus are being constantly investigated [7–15].

Elasticity problems are usually formulated either in terms of deformation parameters or stress parameters. Among the existing mathematical models of plane boundary-value stress problems, the stress function approach [15] and the displacement formulation [16] are noticeable. The application of the stress function formulation in conjunction with finite-difference technique has been reported for the solution of plane elastic problems where all of the boundary conditions are prescribed in terms of stresses only [7–15, 17, 18]. Further, Conway and Ithaca [18] modified the stress function formulation in the form of Fourier integrals to the case where the material is orthotropic and obtained analytical solutions for

a number of ideal problems. The shortcoming of the stress function approach is that it accepts boundary conditions only in terms of loadings of the structure. Boundary restraints specified in terms of the displacement components of the structure cannot be satisfactorily imposed on the stress function approach.

Stress analysis of composite structures is carried out using different analytical, semianalytical approaches where loading is applied along the perpendicular plane of the lamina of laminated composite [19–29] with limited mixed boundary conditions but along the directions of the plane of the composite laminas of the composite should be analyzed for the perfect design of composite structures with mixed boundary conditions. Kulikov and Plotnikova [19] focused on the use of efficient approach to exact elastic solutions of cross-ply and angle-ply composite plates. Interlaminar stresses resulting from bending of thick rectangular laminated plates with arbitrary laminations and boundary conditions are analyzed analytically based on a three-dimensional multiterm extended Kantorovich method (3DMTEKM) [20]. Using the principle of minimum total potential energy, three systems of coupled ordinary differential equations with nonhomogeneous boundary conditions are obtained [20]. Zhang and Hoa [21] proposed a limit-based approach to provide solution to the composite tube having cylindrical orthotropy. The Taylor series expansion method was used to derive new equations to replace those that are identically satisfied, while the other equations are kept to be same [21]. Singh and Shukla [22] presented the nonlinear response of laminated composite plates. The mathematical formulation of the actual physical problem of the laminated composite plate subjected to mechanical loading is presented utilizing higher order shear deformation theory and von-Karman nonlinear kinematics [10]. These nonlinear governing differential equations of equilibrium are linearized using quadratic extrapolation technique [22]. A meshfree technique based on multiquadric RBF is used for analysis of the problems, and isotropic, orthotropic, and laminated composite plates with immovable simply supported and clamped edges are analyzed [22]. A semianalytical method for bending of corrugated-core, honeycomb-core, and X-core sandwich panel is presented [23]. In the global displacement field, the governing equations of three sandwich panels are derived using energy variation principle and solved by employing Fourier series and Galerkin approach [23]. Shahbazi et al. [24] introduced a meshfree approach for analysis of isotropic/orthotropic cross-ply laminated plates with symmetric/non-symmetric layers. A series of exponential basis functions, satisfying the partial differential equations were used to approximate the solution on the whole domain [24]. The boundary conditions are enforced through a collocation approach on a set of boundary points [24]. Aifantis strain gradient elasticity theories and Zhang's two-variable method are used to study elastic bending problems of bilayered microcantilever beams, containing a gradient layer, subjected to a transverse concentrated load [25]. Based on three-dimensional theory of elasticity, axisymmetric static analysis of functionally graded circular and annular plates imbedded in piezoelectric layers is investigated using differential quadrature method [26].

TABLE I: Properties of composites used to obtain numerical results.

Material	Property	Boron/Epoxy
Fiber	$E_f$ ( $10^3$ MPa)	414
	$\nu_f$	0.20
Resin	$E_r$ ( $10^3$ MPa)	3.45
	$\nu_r$	0.35
Composite	$E_1$ ( $10^3$ MPa)	282.9
	$E_2$ ( $10^3$ MPa)	24.2
	$G_{12}$ ( $10^3$ MPa)	10.4
	$\nu_{12}$	0.27
	$\nu_{21}$	0.023

Liew et al. [27] discussed mainly on the developments of element free or meshless methods and their applications in the analysis of composite structures. Rodrigues et al. [28] proposed to use the Murakami's zig-zag theory for the static and vibration analysis of laminated plates, by local collocation with radial basis functions in a finite differences framework. Stürzenbecher and Hofstetter [29] presented an axiomatic equivalent single layer plate theory for cross-ply laminated composites, which is based on the work of Lekhnitskii and Ren and delivers accurate deformation and stress prognoses at the cost six solution variables.

Deb Nath et al. [30, 31] analyzed the elastic field of different stiffened composite structures analytically, with the verifications of the solution of FE (finite element) and FD (finite difference) methods. Deb Nath et al. [30, 31] studied the effect of fiber orientation on the elastic field of a stiffened orthotropic panel under tension. For the case of combined effects of bending and tension at the ends of the stiffened panel, effects of fiber orientation and material isotropy are not studied analytically till now which are necessary for the optimum design of orthotropic members in any loaded structure because during loading members of any structure experience tension and bending together. The present study presents the effects of fiber orientation and material isotropy on the elastic field of an orthotropic composite panel subjected to a combined loading at its tip. This analysis is carried out analytically using Fourier integral and the displacement potential formulation of orthotropic composite materials. Two types of fiber orientation are considered in the present analysis such as  $\theta = 0^\circ$  and  $\theta = 90^\circ$ . Appendix A illustrates the boundary and governing equations for isotropic panel and Appendix B illustrates the equations to derive the isotropic mechanical properties from orthotropic composite materials. The soundness and reliability of the present solution are shown comparing the present analytical solution at some particular sections with those of finite element predictions.

## 2. Analytical Model of the Present Problem

The geometry of a stiffened boron/epoxy panel subjected to a combined loading whose fiber orientation  $\theta = 90^\circ$  is shown

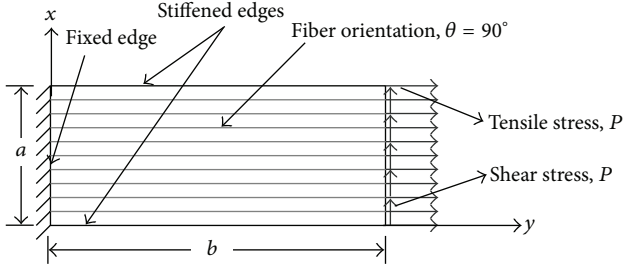


FIGURE 1: Model of an orthotropic composite panel subjected to a combined loading (uniform tension and shear).

in Figure 1. The supporting edge of the panel is rigidly fixed, two opposite edges are stiffened, and at the tip of the panel, uniform tension and shear are applied. Mechanical properties of the boron/epoxy composite used are given by Table 1. The applied tensile and shear stress on the tip of the panel is 41.4 MPa.

### 3. Displacement Potential Formulation of Orthotropic Materials for Plane Stress Conditions

With reference to a rectangular coordinate system  $(x, y)$ , the differential equations of equilibrium for the plane stress problems of orthotropic composite materials having fiber orientation  $\theta = 90^\circ$  [32] are as follows:

$$\begin{aligned} \frac{E_1 E_2}{E_1 - \nu_{12}^2 E_2} \frac{\partial^2 u_x}{\partial x^2} + \left( \frac{\nu_{12} E_1 E_2}{E_1 - \nu_{12}^2 E_2} + G_{12} \right) \frac{\partial^2 u_y}{\partial x \partial y} \\ + G_{12} \frac{\partial^2 u_x}{\partial y^2} = 0, \\ \frac{E_1^2}{E_1 - \nu_{12}^2 E_2} \frac{\partial^2 u_y}{\partial y^2} + \left( \frac{\nu_{12} E_1 E_2}{E_1 - \nu_{12}^2 E_2} + G_{12} \right) \frac{\partial^2 u_x}{\partial x \partial y} \\ + G_{12} \frac{\partial^2 u_y}{\partial x^2} = 0. \end{aligned} \quad (1)$$

The governing equation of the orthotropic material with fiber orientation  $90^\circ$  in terms of the function  $\psi$  is as follows [31]:

$$\begin{aligned} E_2 G_{12} \frac{\partial^4 \psi}{\partial x^4} + E_2 (E_1 - 2\nu_{12} G_{12}) \frac{\partial^4 \psi}{\partial x^2 \partial y^2} \\ + E_1 G_{12} \frac{\partial^4 \psi}{\partial y^4} = 0. \end{aligned} \quad (2)$$

The corresponding governing equation for isotropic materials can be obtained when the respective conditions [ $E_1 = E_2 = E$ ,  $\nu_{12} = \nu_{21} = \nu$ ,  $G_{12} = G = E/2(1 + \nu)$ ] are substituted in (2) which is as follows:

$$\frac{\partial^4 \psi}{\partial x^4} + 2 \frac{\partial^4 \psi}{\partial x^2 \partial y^2} + \frac{\partial^4 \psi}{\partial y^4} = 0. \quad (3)$$

The components of different displacement components with fiber orientation  $90^\circ$  [31] are as follows:

$$\begin{aligned} u_x(x, y) &= \frac{\partial^2 \psi}{\partial x \partial y}, \\ u_y(x, y) &= -\frac{1}{Z_{11}} \left[ E_1 E_2 \frac{\partial^2 \psi}{\partial x^2} + G_{12} (E_1 - \nu_{12}^2 E_2) \frac{\partial^2 \psi}{\partial y^2} \right]. \end{aligned} \quad (4)$$

The stress-strain relations of orthotropic composite lamina with fiber orientation  $\theta = 90^\circ$  in terms of the potential function  $\psi$  are obtained as follows [31]:

$$\begin{aligned} \sigma_{xx}(x, y) &= \frac{E_1 E_2 G_{12}}{Z_{11}} \left[ \frac{\partial^3 \psi}{\partial x^2 \partial y} - \nu_{12} \frac{\partial^3 \psi}{\partial y^3} \right], \\ \sigma_{yy}(x, y) &= \frac{E_1}{Z_{11}} \left[ E_2 (\nu_{12} G_{12} - E_1) \frac{\partial^3 \psi}{\partial x^2 \partial y} - E_1 G_{12} \frac{\partial^3 \psi}{\partial y^3} \right], \\ \sigma_{xy}(x, y) &= \frac{E_1 E_2 G_{12}}{Z_{11}} \left[ \nu_{12} \frac{\partial^3 \psi}{\partial x \partial y^2} - \frac{\partial^3 \psi}{\partial x^3} \right]. \end{aligned} \quad (5)$$

### 4. Solution of the Present Problem

4.1. *Solution of the Panel ( $\theta = 90^\circ$ )*. A stiffened rectangular boron/epoxy orthotropic composite panel is considered. Its fiber orientation is  $\theta = 90^\circ$ . Its supporting edge is rigidly fixed and the two opposing edges are stiffened. The panel is considered to be of unit thickness, and its configuration with respect to coordinate axes is illustrated in Figure 1. In this case, if the potential function  $\psi$  is assumed to be

$$\psi = \sum_{m=1}^{\infty} Y_m \sin \alpha x + Bx^3 + Cxy^2, \quad (6)$$

where  $Y_m$  is a function of  $y$  only, and  $\alpha = m\pi/a$ , then  $Y_m$  has to satisfy the ordinary differential equation

$$Y_m'''' - \left( \frac{E_2}{G_{12}} - \frac{2\nu_{12}E_2}{E_1} \right) \alpha^2 Y_m'' + \frac{E_2}{E_1} \alpha^4 Y_m = 0. \quad (7)$$

The general solution of the differential equation (7) can be given by

$$Y_m = A_m e^{m_1 y} + B_m e^{m_2 y} + C_m e^{m_3 y} + D_m e^{m_4 y}, \quad (8)$$

where

$$\begin{aligned} m_1, m_2 &= \frac{\alpha}{\sqrt{2}} \left[ \left\{ K_1 \pm \sqrt{K_1^2 - \frac{4E_2}{E_1}} \right\} \right]^{1/2}, \\ m_3, m_4 &= -\frac{\alpha}{\sqrt{2}} \left[ \left\{ K_1 \pm \sqrt{K_1^2 - \frac{4E_2}{E_1}} \right\} \right]^{1/2}, \\ K_1 &= \frac{E_2}{G_{12}} - \frac{2\nu_{12}E_2}{E_1}, \end{aligned} \quad (9)$$

where  $A_m, B_m, C_m,$  and  $D_m$  are arbitrary constants.

Now, combining (4) to (5) and (6), the expressions of displacement and stress components are obtained as follows:

$$\begin{aligned} u_x(x, y) &= \sum_{m=1}^{\infty} \alpha Y_m' \cos \alpha x + 2Cy, \\ u_y(x, y) &= \frac{1}{Z_{11}} \sum_{m=1}^{\infty} [-Z_{22} Y_m'' + E_1 E_2 \alpha^2 Y_m] \sin \alpha x \\ &\quad + (6BE_1 E_2 + 2CZ_{33}) x, \\ \sigma_{xx}(x, y) &= -\frac{E_1 E_2 G_{12}}{Z_{11}} \sum_{m=1}^{\infty} [\nu_{12} Y_m'''' + \alpha^2 E_1 Y_m'] \sin \alpha x, \\ \sigma_{yy}(x, y) &= \frac{E_1 E_2}{Z_{11}} \sum_{m=1}^{\infty} [Y_m' \alpha^2 (E_1 - \nu_{12} G_{12}) \\ &\quad - G_{12} Y_m''''] \sin \alpha x, \\ \sigma_{xy}(x, y) &= \frac{E_1 E_2 G_{12}}{Z_{11}} \sum_{m=1}^{\infty} [\alpha \nu_{12} Y_m'' + \alpha^3 Y_m] \cos \alpha x \\ &\quad - \frac{6BE_1 E_2 G_{12}}{Z_{11}} + \frac{2C\nu_{12} E_1 E_2 G_{12}}{Z_{11}}, \end{aligned} \quad (10)$$

where  $Z_{22} = G_{12}(E_1 - \nu_{12}^2 E_2)$ ,  $Z_{33} = (\nu_{12} E_2 Z_{11} - E_1^2 E_2)/(E_1 - \nu_{12}^2 E_2)$ .

Substituting the different derivatives of  $Y_m$  in the expressions of the displacement and stress components equations (10), we get

$$\begin{aligned} u_x(x, y) &= \sum_{m=1}^{\infty} [(m_1 A_m e^{m_1 y} + m_2 B_m e^{m_2 y} + m_3 C_m e^{m_3 y} \\ &\quad + m_4 D_m e^{m_4 y})] \alpha \cos \alpha x + 2Cy, \\ u_y(x, y) &= -\frac{1}{Z_{11}} \sum_{m=1}^{\infty} \left[ \begin{aligned} &(m_1^2 Z_{22} - \alpha^2 E_1 E_2) A_m e^{m_1 y} \\ &+ (m_2^2 Z_{22} - \alpha^2 E_1 E_2) B_m e^{m_2 y} \\ &+ (m_3^2 Z_{22} - \alpha^2 E_1 E_2) C_m e^{m_3 y} \\ &+ (m_4^2 Z_{22} - \alpha^2 E_1 E_2) D_m e^{m_4 y} \end{aligned} \right] \\ &\quad \times \sin \alpha x + (6BE_1 E_2 + 2CZ_{33}) x, \\ \sigma_{xx}(x, y) &= -\frac{E_1 E_2 G_{12}}{Z_{11}} \\ &\quad \times \sum_{m=1}^{\infty} \left[ \begin{aligned} &(m_1 \alpha^2 + m_1^3 \nu_{12}) A_m e^{m_1 y} \\ &+ (m_2 \alpha^2 + m_2^3 \nu_{12}) B_m e^{m_2 y} \\ &+ (m_3 \alpha^2 + m_3^3 \nu_{12}) C_m e^{m_3 y} \\ &+ (m_4 \alpha^2 + m_4^3 \nu_{12}) D_m e^{m_4 y} \end{aligned} \right] \sin \alpha x, \\ \sigma_{yy}(x, y) &= -\frac{E_1 E_2}{Z_{11}} \\ &\quad \times \sum_{m=1}^{\infty} \left[ \begin{aligned} &\{m_1 \alpha^2 (\nu_{12} G_{12} - E_1) + m_1^3 G_{12}\} A_m e^{m_1 y} \\ &+ \{m_2 \alpha^2 (\nu_{12} G_{12} - E_1) + m_2^3 G_{12}\} B_m e^{m_2 y} \\ &+ \{m_3 \alpha^2 (\nu_{12} G_{12} - E_1) + m_3^3 G_{12}\} C_m e^{m_3 y} \\ &+ \{m_4 \alpha^2 (\nu_{12} G_{12} - E_1) + m_4^3 G_{12}\} D_m e^{m_4 y} \end{aligned} \right] \sin \alpha x, \\ \sigma_{xy}(x, y) &= \frac{E_1 E_2 G_{12}}{Z_{11}} \sum_{m=1}^{\infty} \left[ \begin{aligned} &(\alpha^3 + \alpha m_1^2 \nu_{12}) A_m e^{m_1 y} \\ &+ (\alpha^3 + \alpha m_2^2 \nu_{12}) B_m e^{m_2 y} \\ &+ (\alpha^3 + \alpha m_3^2 \nu_{12}) C_m e^{m_3 y} \\ &+ (\alpha^3 + \alpha m_4^2 \nu_{12}) D_m e^{m_4 y} \end{aligned} \right] \cos \alpha x \\ &\quad - \frac{6BE_1 E_2 G_{12}}{Z_{11}} + \frac{2C\nu_{12} E_1 E_2 G_{12}}{Z_{11}}. \end{aligned} \quad (11)$$

**4.2. Boundary Conditions and Its Application.** For the present problem, it is observed that the boundary conditions on the two stiffened edges as observed in Figure 1 are

$$\begin{aligned} u_y(0, y) &= 0, & \sigma_{xx}(0, y) &= 0, \\ u_y(a, y) &= 0, & \sigma_{xx}(a, y) &= 0, \end{aligned} \quad (12)$$

satisfied automatically.

The associated boundary conditions of the supporting edge are

$$u_x(x, 0) = 0, \quad u_y(x, 0) = 0. \quad (13)$$

Now, the axial loading on the right lateral edge of the panel  $y = b$  can be expressed mathematically as follows:

$$\begin{aligned}\sigma_{yy}(x, b) &= P = \sum_{m=1}^{\infty} E_m \sin \alpha x, \\ \sigma_{xy}(x, b) &= P = E_0 + \sum_{m=1}^{\infty} \overline{E}_m \cos \alpha x,\end{aligned}\quad (14)$$

where  $E_m = (2/a) \int_0^a P \sin \alpha x dx = -4P/m\pi$ ,  $E_0 = (1/a) \int_0^a P dx = P$ ;  $\overline{E}_m = (2/a) \int_0^a P \cos \alpha x dx = 0$ .

Substituting the boundary conditions of (13) to (14) into the general expressions of (11), we get the following six equations in terms of the six unknown coefficients:

$$m_1 A_m + m_2 B_m + m_3 C_m + m_4 D_m = 0, \quad (15)$$

$$\begin{aligned}(m_1^2 Z_{22} - \alpha^2 E_1 E_2) A_m + (m_2^2 Z_{22} - \alpha^2 E_1 E_2) B_m \\ + (m_3^2 Z_{22} - \alpha^2 E_1 E_2) C_m + (m_4^2 Z_{22} - \alpha^2 E_1 E_2) D_m = 0,\end{aligned}\quad (16)$$

$$\begin{aligned}(m_1 \alpha^2 Z_{33} + m_1^3 G_{12} E_1) A_m e^{m_1 b} \\ + (m_2 \alpha^2 Z_{33} + m_2^3 G_{12} E_1) B_m e^{m_2 b} \\ + (m_3 \alpha^2 Z_{33} + m_3^3 G_{12} E_1) C_m e^{m_3 b}\end{aligned}\quad (17)$$

$$+ (m_4 \alpha^2 Z_{33} + m_4^3 G_{12} E_1) D_m e^{m_4 b} = \frac{-E_m Z_{11}}{E_1},$$

$$\begin{aligned}(\alpha^3 + \alpha m_1^2 \gamma_{12}) A_m e^{m_1 b} + (\alpha^3 + \alpha m_2^2 \gamma_{12}) B_m e^{m_2 b} \\ + (\alpha^3 + \alpha m_3^2 \gamma_{12}) C_m e^{m_3 b} + (\alpha^3 + \alpha m_4^2 \gamma_{12}) D_m e^{m_4 b} = 0,\end{aligned}\quad (18)$$

$$-3B + C\gamma_{12} = \frac{PZ_{11}}{2E_1 E_2 G_{12}}, \quad (19)$$

$$3BE_1 E_2 + CZ_{33} = 0. \quad (20)$$

Solution of the previous algebraic equations (15) to (18) yields the unknown constants  $A_m$ ,  $B_m$ ,  $C_m$ , and  $D_m$ .

From (19) and (20), we get the values of  $B$  and  $C$  as

$$\begin{aligned}B &= -\frac{PZ_{11}Z_{33}}{6G_{12}E_1 E_2 (\gamma_{12}E_1 E_2 + Z_{33})}, \\ C &= \frac{PZ_{11}}{2G_{12} (\gamma_{12}E_1 E_2 + Z_{33})}.\end{aligned}\quad (21)$$

Once the values of the unknowns are known, they are directly substituted into (11) to obtain the explicit expressions for the different parameters of interest, namely, the two displacement and the three stress components. Following the previous procedure, the panel having the orientation of fibers  $\theta = 0^\circ$  and isotropic material are solved.

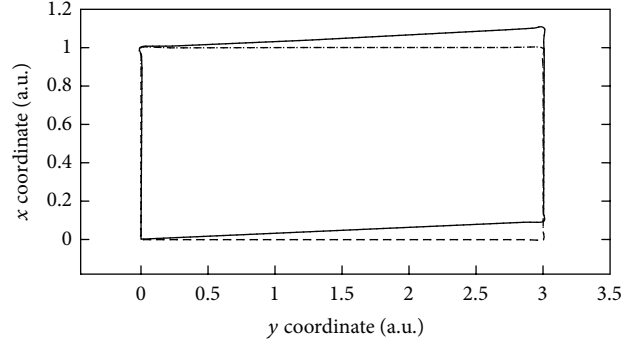


FIGURE 2: Deformed shape of the panel (deformation is magnified by multiplying factor of 1000).

## 5. Results and Discussions

**5.1. Elastic Analysis of of the Stiffened Panel ( $\theta = 90^\circ$ ).** Here, the deformed shape of the orthotropic beam panel subjected to a combined loading having fiber orientation  $\theta = 90^\circ$  under uniform tension and shear at its tip is shown in Figure 2. The effect of fiber orientation and material isotropy on the elastic field of the stiffened orthotropic panel is analyzed. Finally, the present elastic solutions of the supporting edge and the loaded tip are compared with those of finite element predictions.

**5.2. Effect of Fiber Orientation and Material Isotropy.** Effects of fiber orientation and material isotropy on the displacement and stress components are analyzed in this paper. Two different fiber orientations, such as  $\theta = 0^\circ$  and  $90^\circ$ , are taken into account for the purpose of the present analysis. Here, a serious attention is taken on the effect of fiber orientation and material isotropy of a boron/epoxy-stiffened panel subjected to a combined loading (tension and shear) at the tip. The aspect ratio of the panel  $b/a$ , as observed in Figure 1, is 3. The effective materials properties are given in Table 1. Effects of fiber orientation  $\theta = 90^\circ$  and  $\theta = 0^\circ$  are considered as case 1 and case 2, respectively, and material isotropy is considered in case 3.

The distribution of the lateral displacement component at the section  $y/b = 1.0$  for three different cases is shown in Figure 3(a). In this figure, there is observed slight effect on fiber orientations. Over the range  $0 < x/a < 1$ , for case 1, the lateral displacement with  $x/a$  at the section  $y/b = 1$  remains same with  $x/a$ . For case 2, the lateral displacement with  $x/a$  at the section  $y/b = 1$  increases. At the neutral axis,  $x/a = 0.5$ , the lateral displacement for case 1 and case 2 is equal. The lateral displacement at the section  $y/b = 1$  of the isotropic panel increases with  $x/a$ . The magnitude of lateral displacement component  $u_x$  of the isotropic panel at the section  $y/b = 1$  is the lowest. Figure 3(b) illustrates the effect of fiber orientation and material isotropy on the normalized axial displacement component  $u_y$  at the section  $y/b = 1.0$ . At two stiffened edges, the axial displacement component  $u_y$  is zero, which satisfies the physical boundary conditions of the problem. The axial displacement component  $u_y$  of the

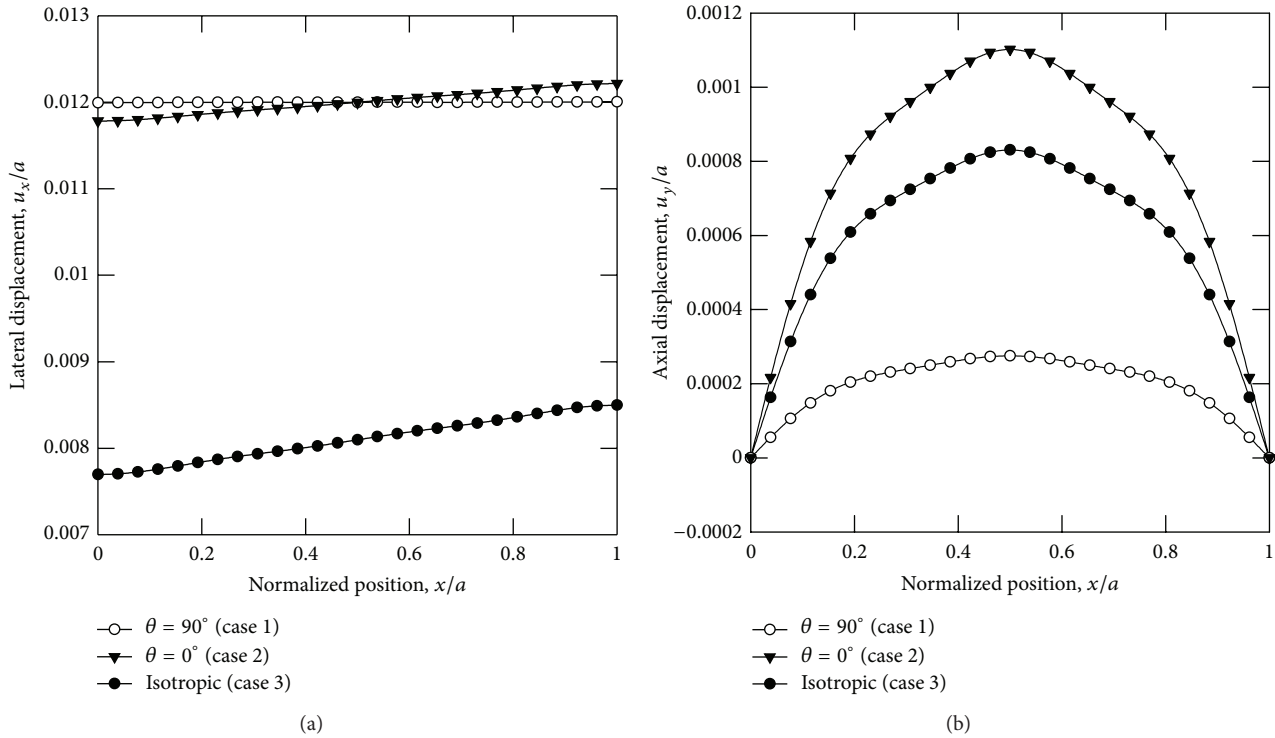


FIGURE 3: Effect of fiber orientation and material isotropy on the normalized displacement components at the section  $y/b = 1.0$  of the panel: (a) lateral displacement; (b) axial displacement.

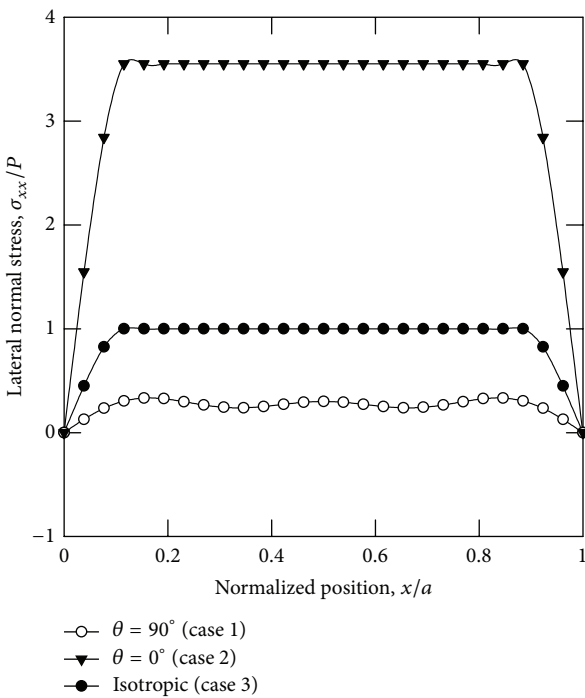


FIGURE 4: Effect of fiber orientation and material isotropy on the normalized lateral stress component at the section  $y/b = 1.0$  of the panel.

orthotropic panel is the highest for case 2 because in this case, the stiffness of the panel in  $y$ -direction is the lowest, and for case 1, the opposite phenomenon occurs due to having the highest stiffness in the same directions of the panels among three cases, and the axial displacement component  $u_y$  of the isotropic panel remains in between them due to having intermediate stiffness. From Figure 4, it is observed that at the section  $y/b = 1$ , for case 2, case 1, and case 3, the panel shows the highest, lowest, and intermediate lateral stress  $\sigma_{xx}$ , and the variation of the lateral stress occurs due to having different stiffness in  $x$ -direction of the panel; for example, for case 2, case 1, and case 3, in  $x$ -direction, the panel shows the highest, lowest, and intermediate stiffness. From Figure 5(a), it is observed that the lateral displacement at the section  $y/b = 0.5$  with  $x/a$  for case 2 remains constant with  $x/a$  but it decreases with  $x/a$  for case 1. At the neutral axis,  $x/a = 0.5$ , the lateral displacement at the section  $y/b = 0.5$  for case 1 and 2 is same. For case 3, the lateral displacement at the section  $y/b = 0.5$  is the lowest in compared to other two cases, 1 and 2. Figure 5(b) illustrates the comparison of the axial displacement components  $u_y$  at the section  $y/b = 0.5$  at different fiber orientation and material isotropy of the panel. The axial displacement component  $u_y$  at the section  $y/b = 0.5$  is the highest for the  $90^\circ$  fiber orientation (case 1) and the lowest for the isotropic material (case 3), and the displacement component of  $90^\circ$  fiber orientation (case 2) remains in between them. From Figure 6(a), it is shown that at the section  $y/b = 0.5$ , the isotropic panel shows the

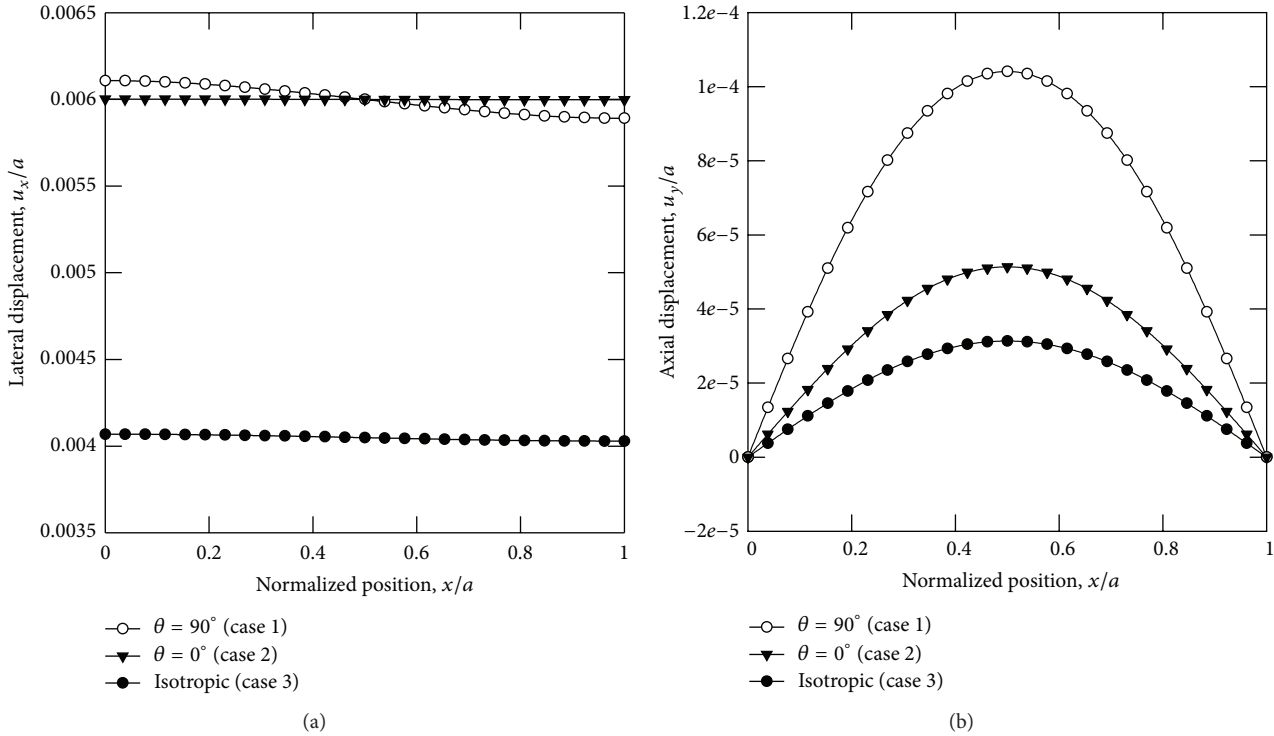


FIGURE 5: Effect of fiber orientation and material isotropy on the normalized displacement components at the section  $y/b = 0.5$  of the panel: (a) lateral displacement; (b) axial displacement.

highest lateral stress,  $\sigma_{xx}$  but effect of fiber orientation on the stress distribution is little. The panel whose fiber orientation is  $90^\circ$  shows highest axial stress  $\sigma_{yy}$  at the section  $y/b = 0.5$  as shown in Figure 6(b). From Figure 6(c), it is observed that at the section  $y/b = 0.5$ , the shear stress is the highest for case 1 and the lowest for case 2. The shear stress for case 3 at the section  $y/b = 0.5$  remains in between that of other two cases. Figure 7 shows the effect of fiber orientation and material isotropy on the shear stress distribution at the section  $x/a = 0.0$ . There is also observed effect of fiber orientation and material isotropy on the shear stress distribution.

### 6. Comparison with the Available Results

To compare the present solutions with those of FEM (finite element modeling), the panel made of boron/epoxy having fiber orientation  $\theta = 90^\circ$  is solved using the commercial software ANSYS. Rectangular orthotropic plane element is used to mesh the present model. To get higher accuracy of solutions, the numbers of elements are decreased or increased.

Figure 8 shows the comparison of solutions of lateral and axial displacement components at the section  $y/b = 1$  by the analytical and FE predictions. The lateral displacement component of the section  $y/b = 1$  obtained by FE and analytical method coincide each other as shown in Figure 8(a). Away from the stiffened edge to the neutral axis of the panel, the deviation between the solutions of axial displacement

obtained by FEM and analytical method increases, and axial displacement obtained by analytical method is higher than those of FEM as shown in Figure 8(b). From Figure 9, it is observed that the lateral stress of the section  $y/b = 1$  obtained by analytical and FEM is almost same in most of the regions of this section. Figure 10 illustrates the comparison of different stress components of the section  $y/b = 0$  by analytical and FE methods. From Figures 10(a) and 10(b), it is observed that the deviation between the solution of lateral stress obtained by the analytical and FE methods is significant; for the lateral stress, finite element method gives higher values than that of analytical method, but for the axial stress, the opposite phenomenon occurs. From Figure 10(c), it is clearly observed that the shear of the section  $y/b = 0$  obtained by analytical and FE methods is almost same. From the comparative analysis of the solutions between those of analytical and FEM methods, it is observed that in most of the cases, the solutions obtained by the analytical and FE methods quantitatively agree well, but in some cases, the solutions do not agree quantitatively but agree well qualitatively. So, the present analytical solutions are highly reliable for designing such type of structures.

### 7. Conclusions

The effects of fiber orientation and material isotropy on the stress and displacement components of the panels under

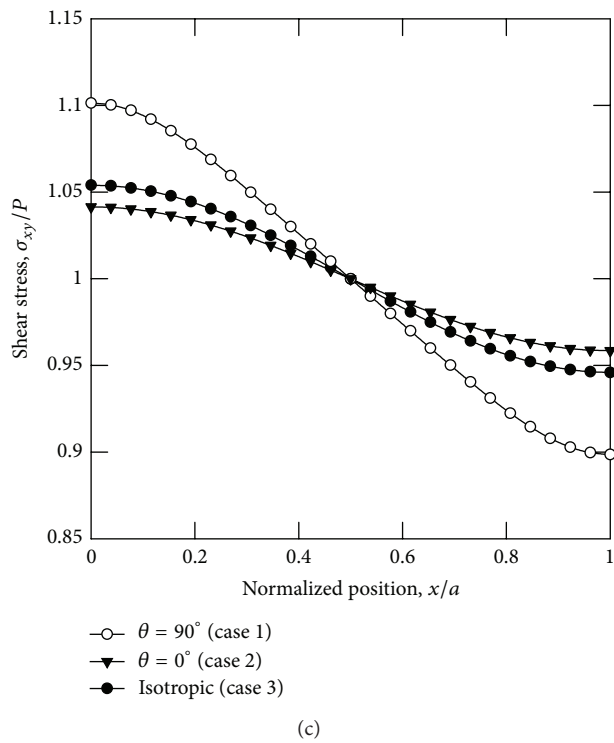
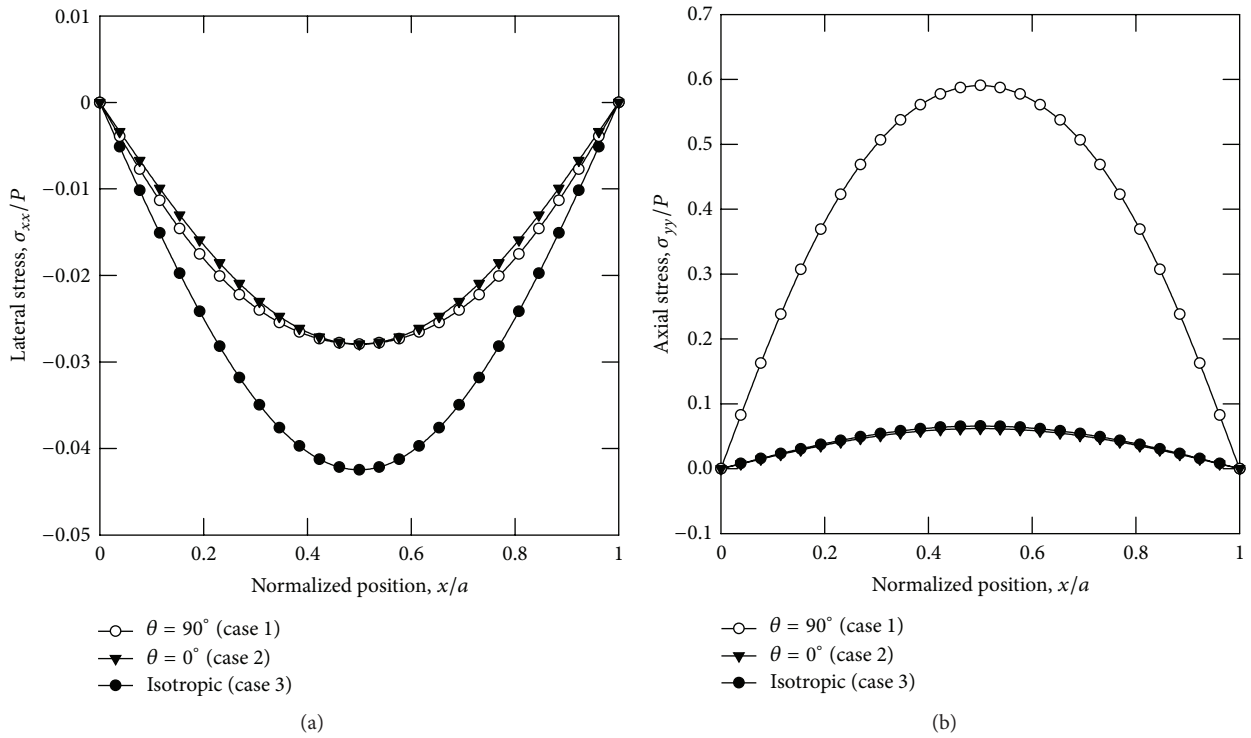


FIGURE 6: Effect of fiber orientation and material isotropy on the normalized stress components at the section  $y/b = 0.5$  of the panel: (a) lateral stress component; (b) axial stress component; (c) shear stress component.

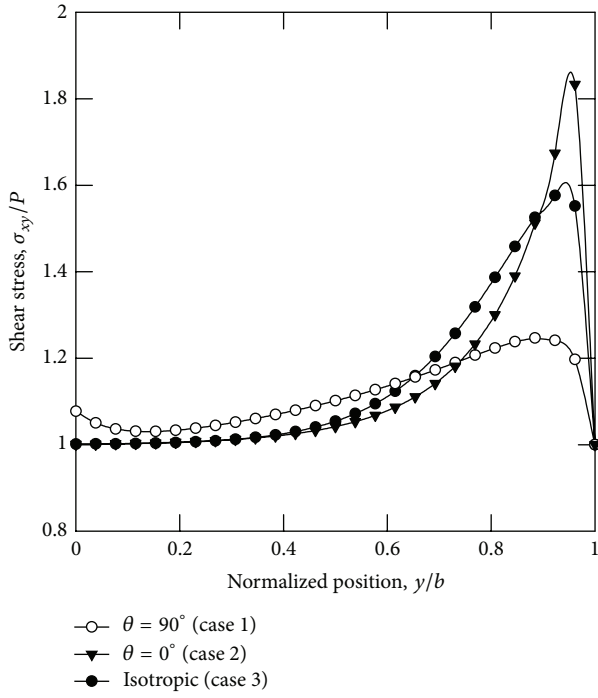


FIGURE 7: Effect of fiber orientation and material isotropy on the normalized shear stress component at the section  $x/a = 0$  of the panel.

uniform tension and shear at the tip of the panel are discussed. Effect of stiffeners is strongly observed in the solution. Due to stiffeners, maximum shear stress is observed at the stiffened edges. Significant effect of fiber orientation and material isotropy are observed on the displacement and stress components at different important sections of the panel. To check the reliability and soundness of the present solution, the present analytical solutions of the panel are compared with those of Finite element predictions.

## Appendices

### A. Solution of the Isotropic Panel

The mathematical background for the solution of isotropic stiffened panel using the present  $\psi$ -formulation is summarized in this appendix for ready reference of interested readers. Combining (3) and (6), the governing ordinary differential equation for the isotropic panel problem is obtained, which is

$$Y_m'''' - 2\alpha^2 Y_m'' + \alpha^4 Y_m = 0. \quad (A.1)$$

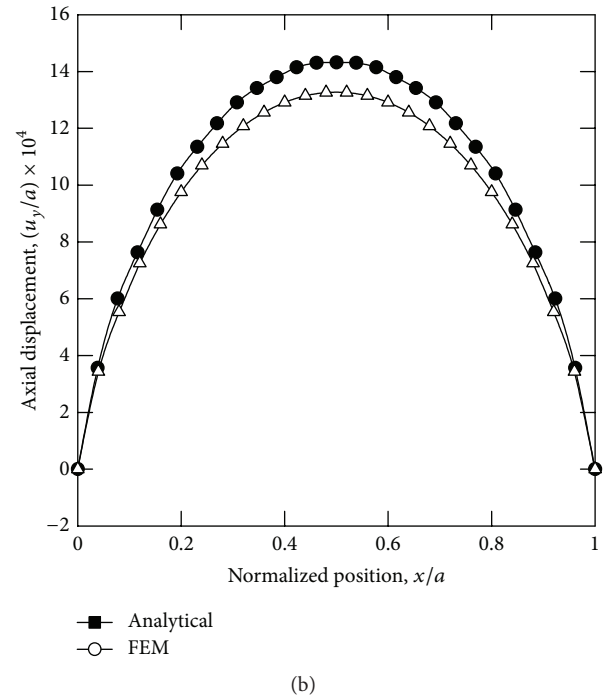
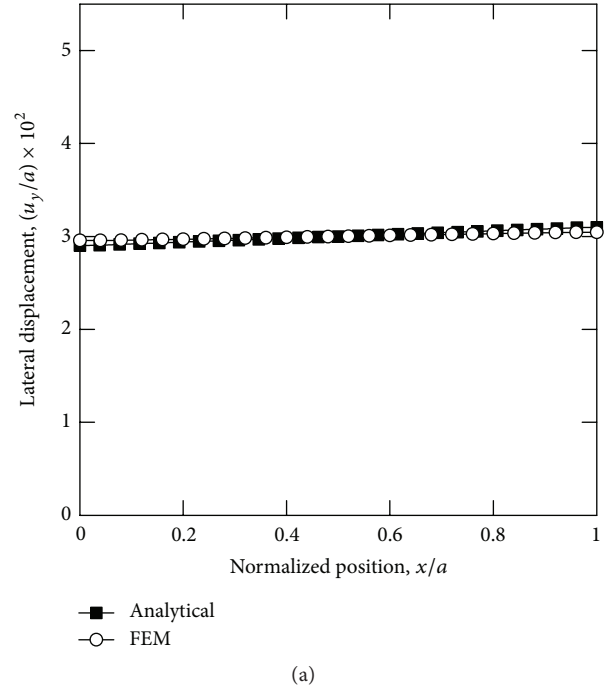


FIGURE 8: Comparison of solutions of different displacement components at the section  $y/b = 1$  of the beam by analytical and FE methods: (a) lateral displacement; (b) axial displacement.

The general solution of (A.1) is as follows:

$$Y_m = A_m \cosh \alpha y + B_m \alpha y \sinh \alpha y + C_m \sinh \alpha y + D_m \alpha y \cosh \alpha y. \quad (A.2)$$

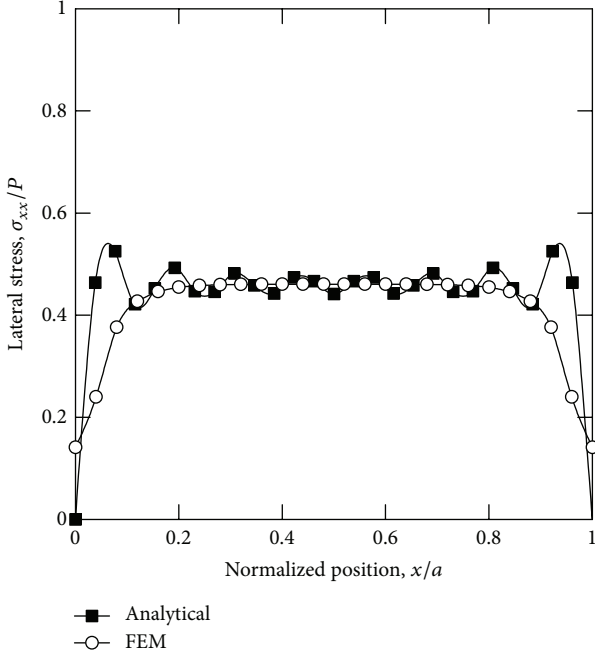


FIGURE 9: Comparison of solutions of the lateral stress component at the section,  $y/b = 1$  by analytical and FE methods.

The corresponding expressions for the displacement and stress components in terms of the four arbitrary constants are as follows:

$$\begin{aligned}
 u_x(x, y) &= \sum_{m=1}^{\infty} \alpha^2 [(A_m + B_m) \sinh \alpha y \\
 &\quad + (C_m + D_m) \cosh \alpha y + B_m \alpha y \cosh \alpha y \\
 &\quad + D_m \alpha y \sinh \alpha y] \cos \alpha x + 2Cy,
 \end{aligned} \tag{A.3}$$

$$\begin{aligned}
 u_y(x, y) &= \sum_{m=1}^{\infty} \alpha^2 [(A_m - 2tB_m) \cosh \alpha y \\
 &\quad + (C_m - 2tD_m) \sinh \alpha y \\
 &\quad + B_m \alpha y \sinh \alpha y \\
 &\quad + D_m \alpha y \cosh \alpha y] \sin \alpha x \\
 &\quad + \{6B + C(1 - \nu)\} E^2 x,
 \end{aligned} \tag{A.4}$$

$$\begin{aligned}
 \sigma_{xx}(x, y) &= - \sum_{m=1}^{\infty} \frac{E\alpha^3}{(1 + \nu)} [(A_m + t'B_m) \sinh \alpha y \\
 &\quad + (C_m + t'D_m) \cosh \alpha y \\
 &\quad + B_m \alpha y \cosh \alpha y + D_m \alpha y \sinh \alpha y] \sin \alpha x,
 \end{aligned} \tag{A.5}$$

$$\begin{aligned}
 \sigma_{yy}(x, y) &= - \sum_{m=1}^{\infty} \frac{E\alpha^3}{(1 + \nu)} [(A_m - tB_m) \sinh \alpha y \\
 &\quad + (C_m - tD_m) \cosh \alpha y \\
 &\quad + B_m \alpha y \cosh \alpha y \\
 &\quad + D_m \alpha y \sinh \alpha y] \sin \alpha x,
 \end{aligned} \tag{A.6}$$

$$\begin{aligned}
 \sigma_{xy}(x, y) &= \sum_{m=1}^{\infty} \frac{E\alpha^3}{(1 + \nu)^2} [\{A_m(1 + \nu) + 2\nu B_m\} \cosh \alpha y \\
 &\quad + B_m(1 + \nu) \alpha y \sinh \alpha y \\
 &\quad + \{C_m(1 + \nu) + 2\nu D_m\} \sinh \alpha y \\
 &\quad + D_m(1 + \nu) \alpha y \cosh \alpha y] \\
 &\quad \times \cos \alpha x \\
 &\quad + \frac{E}{(1 + \nu)^2} (-6B + 2C\nu),
 \end{aligned} \tag{A.7}$$

where  $t = (1 - \nu)/(1 + \nu)$  and  $t' = (1 + 3\nu)/(1 + \nu)$ .

Now, as before, solving (A.3), (A.4), (A.6), and (A.7) with the appropriate boundary conditions given by (12)–(14), the values of the four constants are evaluated.

## B. Effect of Material Isotropy on the Solution

It can be noted here that the corresponding isotropic material properties of the boron/epoxy orthotropic composite material are obtained by solving the following set of equations [33]:

$$\begin{aligned}
 V_m \frac{K_m - K}{3K_m + 4G} + V_f \frac{K_f - K}{3K_f + 4G} &= 0, \\
 V_m \frac{G_m - G}{G_m + \beta} + V_f \frac{G_f - G}{G_f + \beta} &= 0, \\
 E &= \frac{9KG}{3K + G}, \\
 G &= \frac{E}{2(1 + \nu)},
 \end{aligned} \tag{B.1}$$

where  $\beta = G(9K + 8G)/(6K + 12G)$ .

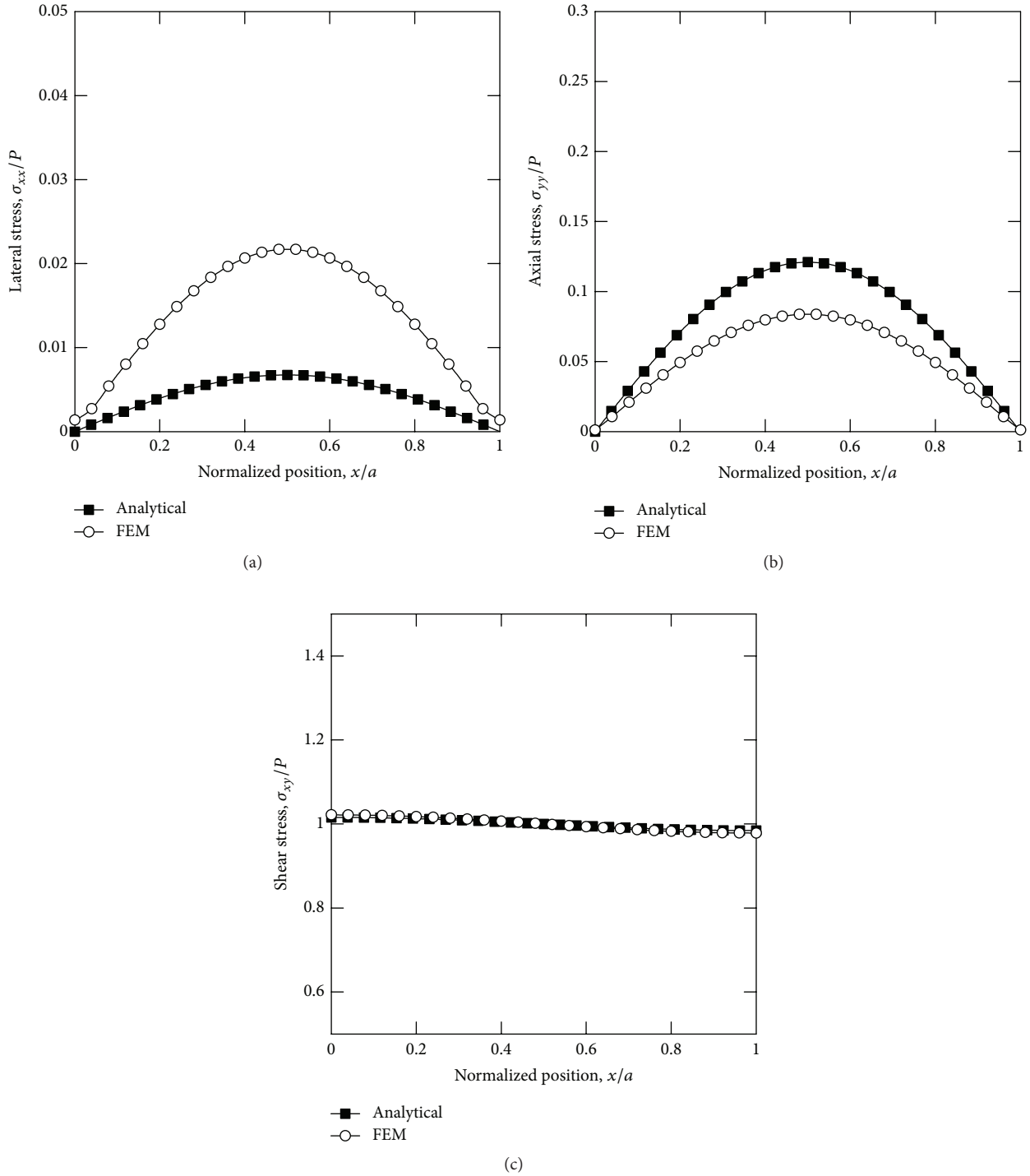


FIGURE 10: Comparison of solutions of different stress components at the section  $y/b = 0$  by analytical and FE methods: (a) lateral stress; (b) axial stress and (c) shear stress.

The solutions of the previous equations are carried out for a composite composition of 60% boron fiber and 40% epoxy resin. The supporting mathematical treatments required to solve the isotropic stiffened panel problem are given in Appendix A.

**Nomenclature**

- $E_1$  :Elastic modulus of the material in  $x$ -direction
- $E_2$ : Elastic modulus of the material in  $y$ -direction
- $\gamma_{12}$ : Major Poisson's ratio

$\nu_{21}$ : Minor Poisson's ratio  
 $\theta$ : Fiber orientation  
 $u_x$ : Displacement components in the  $x$  direction  
 $u_y$ : Displacement components in the  $y$  direction  
 $\sigma_{xx}$ : Normal stress components in the  $x$  direction  
 $\sigma_{yy}$ : Normal stress components in the  $y$  direction  
 $\sigma_{xy}$ : Shearing stress component in the  $xy$  plane  
 $\psi$ : Displacement potential function  
 $a$ : Width of the panel  
 $b$ : Length of the panel  
 $\sigma_{yy}^0$ : Uniformly distributed axial loading on the panel  
 $\sigma_{xy}^0$ : Uniform shear stress  
 $E$ : Elastic modulus of isotropic material  
 $\nu$ : Poisson's ratio of isotropic material.

## References

- [1] S. G. Lekhnitskii, *Theory of Elasticity of An Anisotropic Elastic Body*, Holden-Day, San Francisco, Calif, USA, 1963.
- [2] S. G. Lekhnitskii, *Anisotropic Plate*, Gordon and Breach, New York, NY, USA, 1968.
- [3] A. N. Stroh, "Dislocations and cracks in anisotropic elasticity," *Philosophical Magazine*, vol. 3, no. 30, pp. 625–646, 1958.
- [4] A. N. Stroh, "Steady-state problems in anisotropic elasticity," *Journal of Mathematical Physics*, vol. 41, pp. 77–103, 1962.
- [5] T. C. T. Ting, *Anisotropic Elasticity*, Oxford University Press, New York, NY, USA, 1996.
- [6] D. M. Barnett and H. O. K. Kirchner, "A proof of the equivalence of the Stroh and Lekhnitskii sextic equations for plane anisotropic elastostatics," *Philosophical Magazine A*, vol. 76, no. 1, pp. 231–239, 1997.
- [7] H. D. Conway, L. Chow, and G. W. Morgan, "Analysis of deep beams," *Journal of Applied Mechanics*, vol. 18, pp. 163–172, 1951.
- [8] L. Chow H. D. Conway and G. Winter, "Stresses in deep beams," *Trans ASCE Paper 2557*, 1952.
- [9] C. O. Horgan and J. K. Knowles, "Recent developments concerning Saint Venant's principle," *Advances in Applied Mechanics*, vol. 23, pp. 179–269, 1983.
- [10] D. F. Parker, "The role of Saint-Venant's solutions in rod and beam theories," *Journal of Applied Mechanics*, vol. 46, no. 4, pp. 861–866, 1979.
- [11] S. J. Hardy and M. K. Pipelzadeh, "Static analysis of short beams," *Journal of Strain Analysis*, vol. 26, pp. 15–29, 1991.
- [12] A. V. Krishna Murty, "Towards a consistent beam theory," *The American Institute of Aeronautics and Astronautics*, vol. 22, no. 6, pp. 811–816, 1984.
- [13] A. J. Durelli and B. Ranganayakamma, "On the use of photoelasticity and some numerical methods," in *Photomechanics and Speckle Metrology*, vol. 814 of *Proceedings of the SPIE*, pp. 1–8, 1987.
- [14] A. J. Durelli and B. Ranganayakamma, "Parametric solution of stresses in beams," *Journal of Engineering Mechanics*, vol. 115, no. 2, pp. 401–414, 1989.
- [15] S. Timoshenko and V. N. Goodier, *Theory of Elasticity*, McGraw-Hill, New York, NY, USA, 3rd edition, 1979.
- [16] M. W. Uddin, *Finite Difference Solution of Two-Dimensional Elastic Problems with Mixed Boundary Conditions [M.S. thesis]*, Carleton University, Ottawa, Canada, 1966.
- [17] R. Chapel and H. W. Smith, "Finite difference solutions for plane stresses," *The American Institute of Aeronautics and Astronautics*, vol. 6, pp. 1156–1157, 1968.
- [18] H. D. Conway and N. Y. Ithaca, "Some problems of orthotropic plane stress," *Journal of Applied Mechanics, Trans ASME Paper*, no. 52-A-4, pp. 72–76, 1953.
- [19] G. M. Kulikov and S. V. Plotnikova, "Exact 3D stress analysis of laminated composite plates by sampling surface method," *Composite Structures*, vol. 94, pp. 3654–3663, 2012.
- [20] M. Tahani and A. Andakhshideh, "Interlaminar stresses in thick rectangular laminated plates with arbitrary laminations and boundary conditions under transverse loads," *Composite Structures*, vol. 94, pp. 1793–1804, 2012.
- [21] C. Zhang and S. V. Hoa, "A limit-based approach to the stress analysis of cylindrically orthotropic composite cylinders (0/90) subjected to pure bending," *Composite Structures*, vol. 94, pp. 2610–2618, 2012.
- [22] J. Singh and K. K. Shukla, "Nonlinear flexural analysis of laminated composite plates using RBF based meshless method," *Composite Structures*, vol. 94, pp. 1714–1720, 2012.
- [23] L. He, Y. -S Cheng, and J. Liu, "Precise bending stress analysis of corrugated-core, honey comb-core and X-core sandwich panels," *Composite Structures*, vol. 94, pp. 1656–1668, 2012.
- [24] M. Shahbazi, B. Boroomand, and S. Soghrati, "A mesh-free method using exponential basis functions for laminates modeled by CLPT, FSDT and TSDT - Part I: formulation," *Composite Structures*, vol. 93, pp. 3112–3119, 2011.
- [25] N. H. Zhang, W. L. Meng, and E. C. Aifantis, "Elastic bending analysis of bilayered beams containing a gradient layer by an alternative two-variable method," *Composite Structures*, vol. 93, pp. 3130–3139, 2011.
- [26] A. Alibeigloo and V. Simintan, "Elasticity solution of functionally graded circular and annular plates integrated with Sensor and actuator layers using differential quadrature," *Composite Structures*, vol. 93, pp. 2473–2486, 2011.
- [27] K. M. Liew, X. Zhao, and A. J. M. Ferreira, "A review of meshless methods and functionally graded plates and shells," *Composite Structures*, vol. 93, pp. 2031–2041, 2011.
- [28] J. D. Rodrigues, C. M. C. Roque, A. J. M. Ferreira, E. Carrera, and M. Cinefra, "Radial basis functions-finite differences collocation and a unified formulation for bending, vibration and buckling analysis of laminated plates, according to Murakami's zig-zag theory," *Composite Structures*, vol. 93, no. 7, pp. 1613–1620, 2011.
- [29] R. Stürzenbecher and K. Hofstetter, "Bending of cross-ply laminated composites: an accurate and efficient plate theory based upon models of Lekhnitskii and Ren," *Composite Structures*, vol. 93, no. 3, pp. 1078–1088, 2011.
- [30] S. K. Deb Nath and A. M. Afsar, "Analysis of the effect of fiber orientation on the elastic field in a stiffened orthotropic panel under uniform tension using displacement potential approach," *Mechanics of Advanced Materials and Structures*, vol. 16, no. 4, pp. 300–307, 2009.
- [31] S. K. Deb Nath and S. R. Ahmed, "Investigation of elastic field of a short orthotropic composite column by using finite-difference

technique,” *Proceedings of the Institution of Mechanical Engineers G: Journal of Aerospace Engineering*, vol. 222, no. 8, pp. 1161–1169, 2008.

- [32] R. M. Jones, *Mechanics of Composite Materials*, McGraw-Hill, 1975.
- [33] C. W. Nan, R. Z. Yuan, and L. M. Zhang, “The physics of metal/ceramic functionally gradient materials,” in *Ceramic Transaction. Functionally Gradient Materials*, J. B. Holt et al., Ed., vol. 34, pp. 75–82, American Ceramic society, Westerville, Ohio, USA, 1993.

## Research Article

# Behavior of Concrete Columns Repaired with Polymer Mortar and Epoxy Fiber Panel

**Sungnam Hong and Sun-Kyu Park**

*Department of Civil and Environmental Engineering, Sungkyunkwan University, Suwon 440-746, Republic of Korea*

Correspondence should be addressed to Sun-Kyu Park; [skpark@skku.edu](mailto:skpark@skku.edu)

Received 12 November 2012; Accepted 30 January 2013

Academic Editor: Md Mainul Islam

Copyright © 2013 S. Hong and S.-K. Park. This is an open access article distributed under the Creative Commons Attribution License, which permits unrestricted use, distribution, and reproduction in any medium, provided the original work is properly cited.

Underwater structures are not easy to check for the degree of damage or to repair and strengthen damaged regions. Even during repair and strengthening, quality control is very difficult, because the work is done under water. Moreover, underwater structures severely deteriorate, owing to special environmental conditions. If this deterioration continues, the structures face serious structural problems, because of the corrosion of steel rods and the loss of concrete sections. Repairing or strengthening underwater structures requires effective, economic underwater repair and reinforcement techniques that allow the same working conditions as on the ground while maintaining dry condition for the repair sections. However, systematic studies on the repair and strengthening techniques for underwater structures are insufficient. This study proposes a new repair method for underwater structures, which applies epoxy fiber panel forms and shear connectors. To demonstrate the repair effects, this study compared and evaluated the failure modes and repair effects by the surface condition of repair sections, by applying various repair methods, in consideration of the ground and underwater conditions.

## 1. Introduction

When concrete structures are constructed in a river, lake, or sea, a part of the structure is placed under water, and the underwater structures are subjected to damages such as concrete spalling and exfoliation, due to aging, faulty construction, and various deterioration factors [1]. Such structures urgently need repairs and reinforcements. In particular, the substructures of bridges in water are subjected to damages by such environmental factors as the scouring of foundations by water flow, erosion of members, and the corrosion of steel rods [2], in addition to the damages that may occur to structures above ground.

Structural engineers have extensive experience of repairing concrete structures above water [3–6]. The conventional approach to the repair of reinforced concrete columns that have shallow damages, however, is to use patch repair for the damaged zones where cracking and spalling occur [7, 8]. For patch repair to be structurally effective, the appropriate material should be applied in the damaged concrete section.

A limited range of materials is available for use in underwater repair. They can be divided into two mortar types: cementitious and resin based. Generally, normal epoxy or polyester resins are unsuitable for underwater use, as they often fail to bond to the damaged concrete and can be adversely affected by reaction between the hardener and the water [9]. However, cementitious mortars can range from conventional mortars and grouts to materials with greatly enhanced properties achieved by the use of admixtures. In particular, the use of polymers can result in cohesiveness, high rates of strength gain, greater workability, resistance to washout of cement, and reduction in bleed and shrinkage [10–12]. From these advantages, polymer mortar has been utilized in a range of mortar and concrete repair and primary construction applications [13–15].

For effective repair and reinforcement of underwater structures, the damaged regions must be maintained in dry condition. However, installing coffer and caissons for partial defects under water requires a long period of work, much manpower, and heavy equipment, so causing much loss

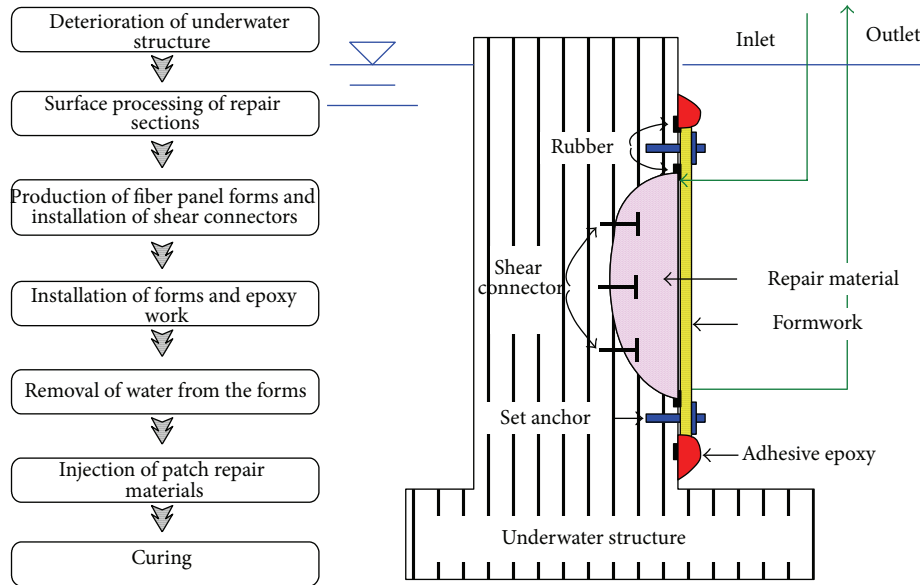


FIGURE 1: Schematic diagram of the newly proposed repair method.

in time and money [16]. Therefore, we need effective and economic underwater repair and reinforcement techniques that allow working in the same conditions as on the ground while maintaining a dry condition. However, systematic studies on the repairs and reinforcements of underwater structures are insufficient.

Accordingly, this study proposes a repair method for underwater structures, which applies epoxy fiber panel forms and shear connectors. To demonstrate the repair effects, this study compared and evaluated the repair effects, by applying various repair methods, in consideration of various underwater and ground conditions.

## 2. Newly Proposed Underwater Repair Method

Existing repair methods for underwater structures can be largely classified into three groups, as shown below [17].

- (1) Repairing the damaged sections after installing coffer.
- (2) Repairing by installing underwater caissons.
- (3) Repairing with underwater repair materials by divers.

Repair methods that use coffers and caissons greatly increase time and construction cost, including materials cost, so they are uneconomical for partial repair works. Furthermore, the direct repair method by divers is also inappropriate, because it causes environmental problems such as the leakage of materials, quality control is difficult, and effective repair work is impossible.

The underwater repair method proposed by this study has been newly developed to apply to underwater structures with deteriorations such as concrete spalling and exfoliation, cracks, and corrosion of steel rods. Because the outside water is perfectly blocked by fiber panel forms, underwater epoxies, and rubber packings, while the damaged sections are

repaired [18], this method maximizes the repair effects and enables economical work. Furthermore, the shear connectors installed on the repair sections give shear resistance at interfaces and prevent the elimination of repair materials; anchor bolts fix the forms, to provide binding force. The work procedure and a schematic diagram of the proposed underwater repair method are shown in Figure 1.

## 3. Experimental Program

**3.1. Test Variables.** To evaluate the performance of the proposed underwater repair method, control columns and repaired columns were produced, as shown in Table 1. The repaired columns were produced under water and above ground, to evaluate the effects of different working conditions. The proposed underwater repair method used the epoxy fiber panels and shear connectors in numbers 19 to 22 in Table 1.

It should be noted that the test columns were planned for the pilot test in the laboratory. Therefore, full-scale field tests should be conducted, to derive a general application for the proposed repair system.

**3.2. Material Properties.** The concrete mix proportion for the control and repaired columns are shown in Table 2. For the compressive strength and splitting tensile strength of concrete by atmospheric curing and water curing of concrete aged 28 days, three columns were produced and tested, and the mean values are summarized in Table 2.

For repair materials, inorganic polymer mortar with a polymer/cement ratio of 20%, which was specially manufactured for underwater use, was used. The strength characteristics of the underwater repair material were determined by compressive strength test and splitting tensile strength test



FIGURE 2: Column production process.

at the age of 28 days. The mean values of the three columns obtained from these tests are summarized in Table 3.

**3.3. Production of Columns.** For columns, control and repaired columns were produced under the assumption that the concrete was damaged as shown in Figure 2. The shape and dimensions of the sections of columns are shown in Figure 3. To obtain the repaired columns, two damaged columns whose depths of damage were 5 cm and 7 cm were repaired, in accordance with the test variables.

For G-D-D series columns, acrylic forms were attached to the sides of the repair sections on the ground, and underwater repair materials were injected in such a way that the repair materials would not flow out. For G-D-F-D series columns, epoxy fiber panel forms were fixed to the repair sections with anchors on the ground, and the underwater repair materials were injected through an inlet connected to the forms.

For U-W-F-D series columns, epoxy fiber panel forms were fixed under water, the gaps in the forms and columns were waterproofed using underwater epoxies, and underwater repair materials were injected without removing water

TABLE 1: Variables of test columns.

No.	Columns	Cut-out preparation	Form	Damage	Curing condition	Remarks	
1	M1	M series (Control)	No cutout	*	*	No repair	
2	M2						
3	G-D-D1-1	G-D-D series	Cast	Acrylic plate	Air		
4	G-D-D1-2		Chipping				
5	G-D-D2-1		Cast				
6	G-D-D2-2		Chipping				
7	G-D-F-D1-1	G-D-F-D series					
8	G-D-F-D1-2						
9	G-D-F-D2-1						
10	G-D-F-D2-2						
11	U-W-F-D1-1	U-W-F-D series					
12	U-W-F-D1-2						
13	U-W-F-D2-1						Epoxy fiber panel
14	U-W-F-D2-2						Chipping
15	U-D-F-D1-1	U-D-F-D series			Underwater		
16	U-D-F-D1-2						
17	U-D-F-D2-1						
18	U-D-F-D2-2						
19	U-D,S-F-D1-1	U-D,S-F-D series					
20	U-D,S-F-D1-2						
21	U-D,S-F-D2-1						Epoxy fiber panel/shear connector
22	U-D,S-F-D2-2						

G: ground, U: underwater, D: dry, W: wet, S: shear connector, F: form (epoxy fiber panel), D1: damage1 (depth 5 cm), D2: damage2 (depth 7 cm), and 1/2: serial number.

TABLE 2: Mix proportion and mechanical properties of concrete.

(a) Mix proportion						
Water/cement ratio (%)	Unit weight (kg/cm <sup>3</sup> )					Sand/aggregate ratio (%)
	Cement	Water	Fine aggregate	Coarse aggregate	Admixture	
54.7	335	183	825	930	1.68	47.5
(b) Mechanical properties						
Curing condition	Compressive strength (MPa)		Tensile strength (MPa)		Elastic modulus (MPa)	
Atmospheric curing	20.0		1.7		20901.2	
Water curing	21.1		1.7		21604.6	

from the forms. For columns U-D-F-D series, epoxy fiber panel forms were fixed under water, the gaps in the forms and columns were waterproofed using underwater epoxies, water was removed from the forms, and then underwater repair materials were injected into them. For columns U-D,S-F-D series, anchors that play the role of shear connectors were inserted into the repair sections, the forms were fixed, water was removed, and the patch repair materials were injected.

All the columns were waterproofed for gaps in the forms and columns, using underwater epoxies after the forms were fixed.

3.4. *Forms.* The forms used in this experiment were manufactured with epoxy fiber panels with waterproof rubber packing. As shown in Figure 3, the repair sections were

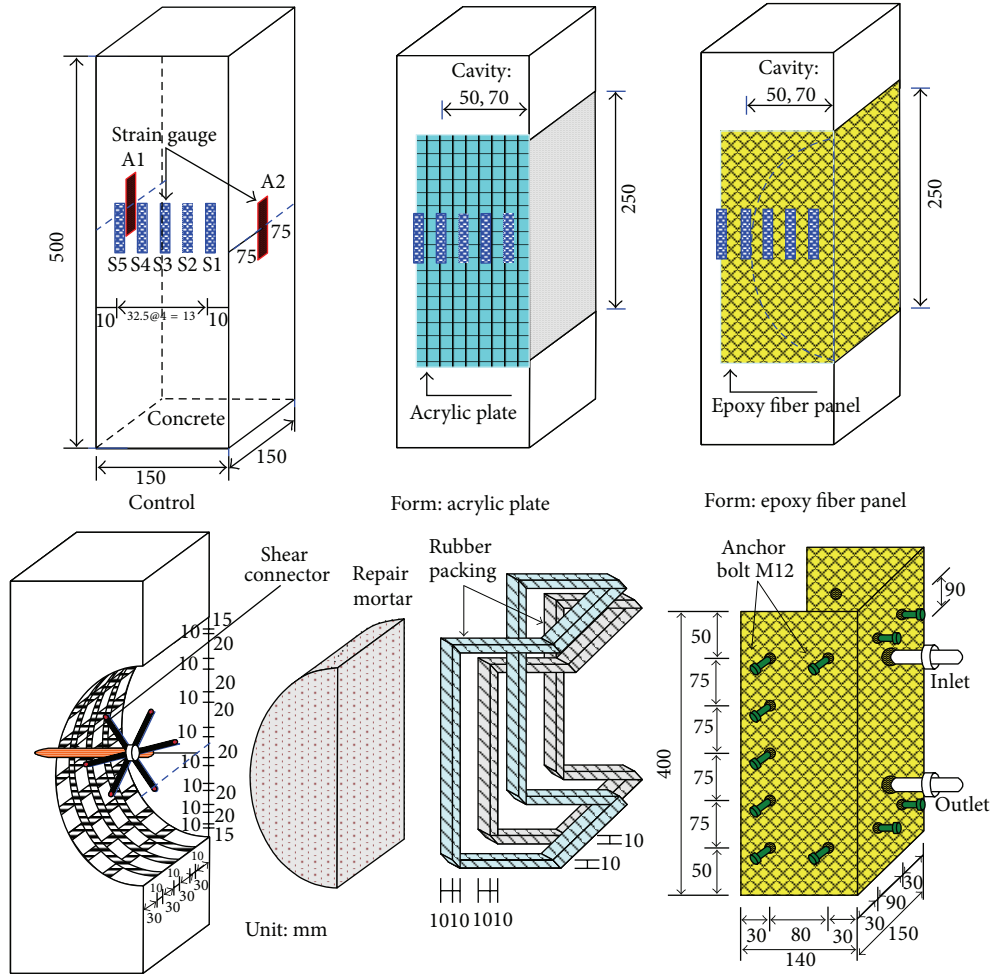


FIGURE 3: Column details.

TABLE 3: Mix proportion and mechanical properties of polymer mortar.

(a) Mix proportion			
Cement/sand (by weight)	Polymer/cement (%)	Water/cement (%)	Flow (mm)
1:2	20	32	168
(b) Mechanical properties			
Curing condition	Compressive strength (MPa)	Tensile strength (MPa)	Elastic modulus (MPa)
Atmospheric curing	52.6	2.6	24515.0
Water curing	58.1	2.3	25662.0



FIGURE 4: Shear connector.

wrapped up on three sides, and holes were made to insert anchor bolts underwater repair materials through them. The shear connector that was installed at the center of the repair sections to resist shear force from the repair sections, and to prevent the elimination of the repair material, is

shown in Figure 4. Also, the dimensional and mechanical characteristics of the shear connector are shown in Table 4.

TABLE 4: Dimensions and mechanical properties of shear connector.

Type of anchor bolt	Length (mm)	Diameter (mm)	Diameter of umbrella ribs (mm)	Tensile strength (MPa)	Pullout strength (MPa)
M10	100	10	120	293	25

TABLE 5: Significant values for load and strain at ultimate state.

Column	Ultimate load			Strain at ultimate load			
	Measured (kN)	Average (kN)	Ratio	Measured ( $\mu\epsilon$ )	Average ( $\mu\epsilon$ )	Ratio -	
Control	M1	555.1	558.0	1	2079.1	2013.2	1
	M2	560.9			1947.2		
Repaired (ground)	G-D-D1-1	513.9	513.9	0.92	1312	1312.0	0.65
	G-D-D1-2	554.1	554.1	0.99	2235.5	2235.5	1.11
	G-D-D2-1	518.7	518.7	0.93	1466.7	1466.7	0.73
	G-D-D2-2	544.3	544.3	0.98	2223.3	2223.3	1.10
	G-D-F-D1-1	567.8	568.8	1.02	2740.5	2798.6	1.39
	G-D-F-D1-2	569.8			2856.6		
	G-D-F-D2-1	551.1	549.2	0.98	2211.1	2235.3	1.11
	G-D-F-D2-2	547.2			2259.5		
Repaired (underwater)	U-W-F-D1-1	514.8	517.8	0.93	1899.9	1875.4	0.93
	U-W-F-D1-2	520.7			1850.9		
	U-W-F-D2-1	527.6	529.6	0.95	1851.8	1851.4	0.92
	U-W-F-D2-2	531.5			1850.9		
	U-D-F-D1-1	N.A.	519.8	0.93	N.A.	2115.3	1.05
	U-D-F-D1-2	519.8			2115.3		
	U-D-F-D2-1	506	509.5	0.91	2139.3	2164.3	1.08
	U-D-F-D2-2	512.9			2189.3		
	U-D,S-F-D1-1	578.6	564.9	1.01	2319.2	2409.6	1.20
	U-D,S-F-D1-2	551.1			2499.9		
	U-D,S-F-D2-1	567.8	565.4	1.01	2043.2	2091.3	1.04
	U-D,S-F-D2-2	562.9			2139.3		

3.5. *Loading and Gauge Installation.* To examine the stresses and deformations of the concrete and patch repair materials, gauges (A1, A2, S1, S2, S3, S4, and S5) were installed, as shown in Figure 3. A strain gauge was installed to measure the vertical strain of the existing section A1 and the repaired section (the surface of epoxy fiber panel or repair material) A2. Furthermore, to compare strains at different locations in the interface between the existing concrete section and the repaired section, strain gauges were installed at S1 to S5. For loading device, a universal testing machine (UTM) with a capacity of 980 kN was used, and the strain and load data of the concrete and forms were measured with a data logger.

#### 4. Test Results and Discussion

To examine the repair effects of the underwater repair method applied to damaged underwater structures, a loading experiment was conducted. The measured maximum load

(failure load) and the vertical strains of the concrete at the maximum load for each column are summarized in Table 5.

4.1. *Failure Mode.* The failure modes of the columns can be largely divided into interface failure at the interface between underwater repair materials and concrete and concrete failure. Interface failure occurs suddenly, as shown in Figures 5(a) and 5(b), when the repair sections were smooth, and when water was not removed from the forms and repair sections. These are undesirable failure modes in the repair and reinforcement of structures.

Concrete failures are illustrated in Figures 6(a) and 6(b). They occur in concrete with lower strength than repair materials, by the effect of the binding force of the forms, and the role of the shear connectors when the load shear at the interface is smooth. However, concrete failure would not occur in actual structures, because the repair sections are larger than the existing concrete sections.

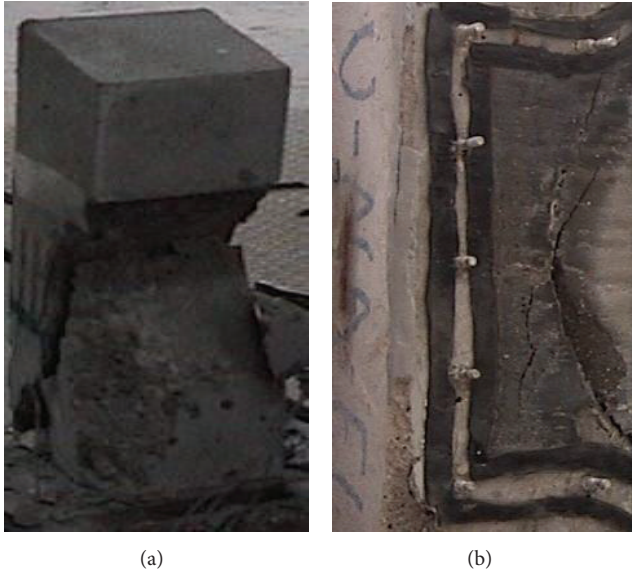


FIGURE 5: Interface failure.

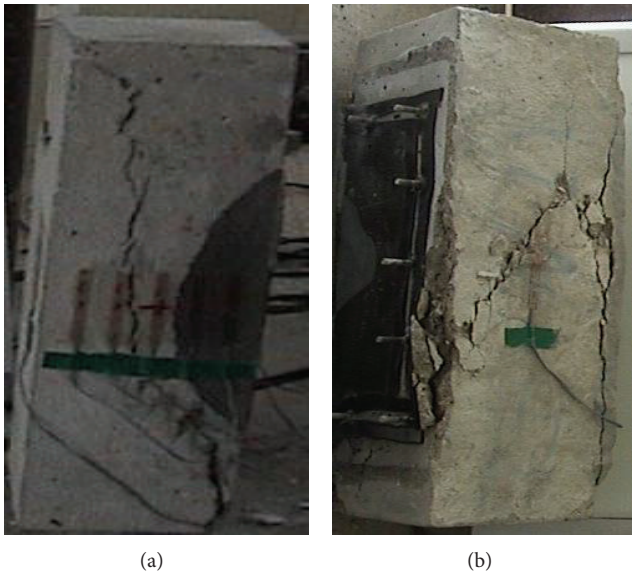


FIGURE 6: Concrete failure.

4.2. *Control Columns.* The maximum loads of control columns M1 and M2 were 555.1 kN and 560.9 kN. The mean strains at maximum load measured at A1 and A2 of the columns were 2079  $\mu\epsilon$  and 1947  $\mu\epsilon$ . These results are shown in Figure 7. Figure 8 shows the strains of M1 at S1 to S5. As the load increased, the strains were constant at various points on the side, and stress was evenly distributed on the shear surface of the concrete.

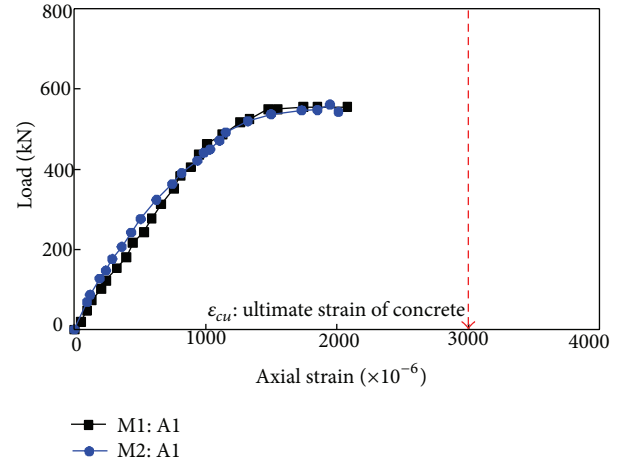


FIGURE 7: Load-axial strain curve: M1 and M2.

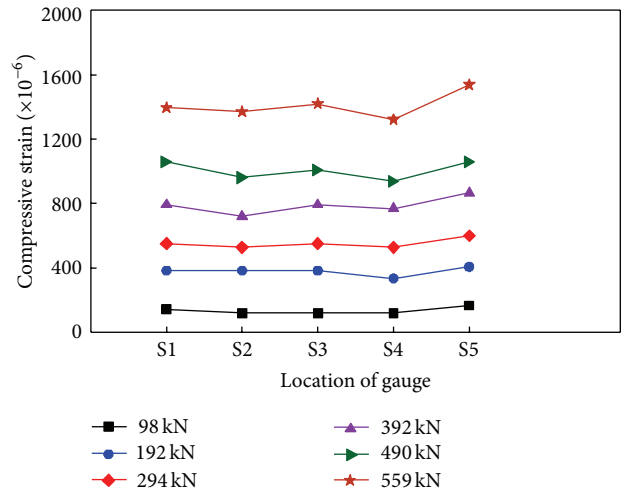


FIGURE 8: Strain distribution: M1.

### 4.3. Repaired Columns

4.3.1. *G-D-D Series.* The results of the loading experiment on the repaired columns G-D-D series are shown in Figures 9 and 10. The axial strains of concrete at maximum load A1 and A2 of the columns G-D-D1-1 and G-D-D2-1 with smooth repair sections were 1312  $\mu\epsilon$  and 1466  $\mu\epsilon$ , respectively, which were lower than the strain at maximum load of the control columns. The reason for this result is that the columns did not fail by the failure of the concrete or repair material, but by sudden interface failure, due to decreased bond strength at the interface.

For columns G-D-D1-2 and G-D-D2-2 whose repair sections were surface treated (chipping), the strain of the concrete surface reached the maximum compressive strain, and the columns failed by concrete failure. The reason for this result is that the interface failure did not occur due

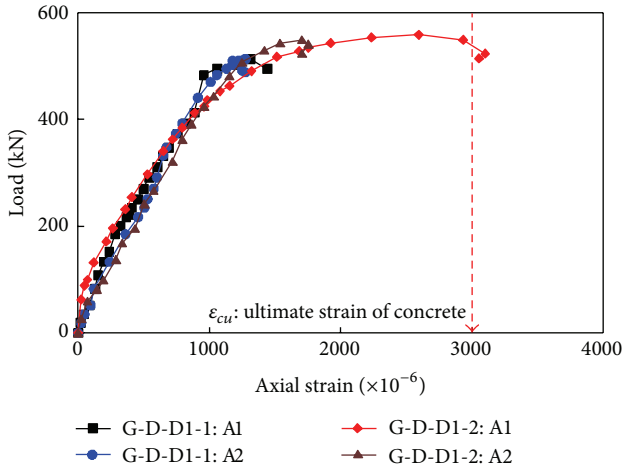


FIGURE 9: Load-axial strain curve: G-D-D1 columns.

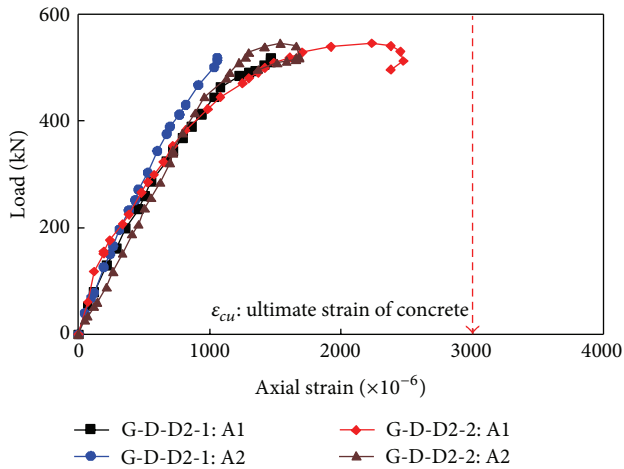


FIGURE 10: Load-axial strain curve: G-D-D2 columns.

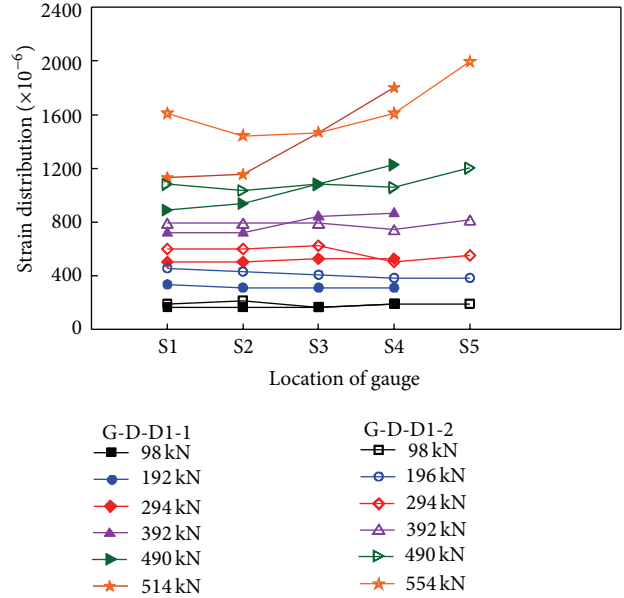


FIGURE 11: Strain distribution: G-D-D1 columns.

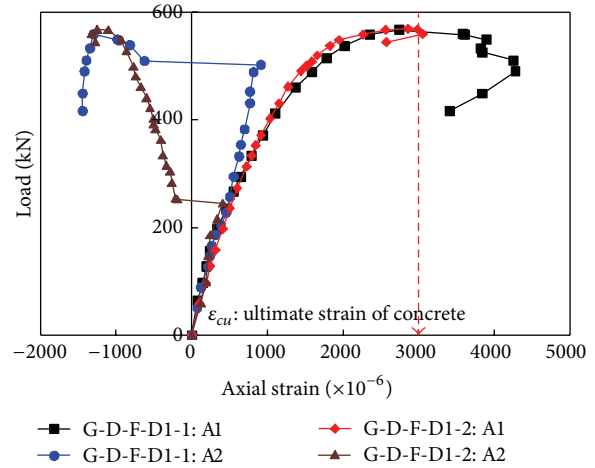


FIGURE 12: Load-axial strain curve: G-D-F-D1 columns.

to increased bond strength by the surface treatment of the repair sections and the excellent dynamic characteristics of the repair materials, and the load was concentrated on the concrete with lower strength. It was found that chipping of the repaired section increased maximum load by 8% and the strain at maximum load by 70%. These results were similar, regardless of the degree of damage.

Figure 11 shows the strains of the column with smooth surface of repair sections and the chipped column. For the smooth surface column, the strain steadily increased up to 392 kN at various locations but rapidly increased in weak concrete from 490 kN until failure. However, for the chipped column, strain steadily increased to 490 kN and then rapidly increased in concrete at failure. The reason for this is that the bond strength between concrete and repair material increased by the surface treatment of the repair sections, and the load was smoothly transmitted through the interface. As

a result, no interface failure occurred, but the weak concrete failed suddenly, as cracks were generated by the increased strain. This result indicates that the surface treatment for damaged sections of structures has great influence on repair effects. Repair materials with different material characteristics exhibited different behaviors. Austin and Robins [19] and Emberson and Mays [20] also found similar results.

4.3.2. *G-D-F-D Series.* As shown in Figure 12, the maximum load of the column G-D-F-D1-1 was 567.8 kN, and the strains of the fiber panel form of the repaired surface and the concrete surface showed similar behaviors until 294.2 kN. At

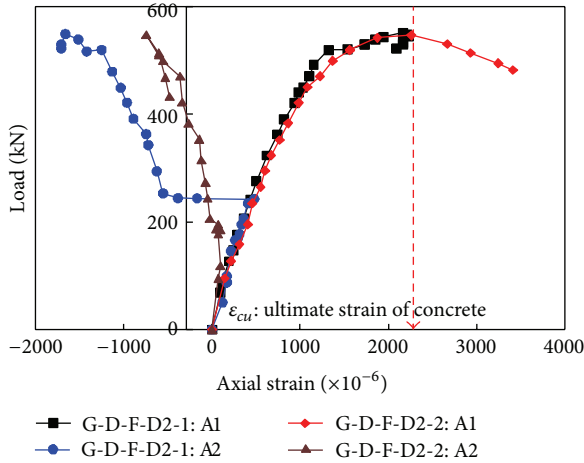


FIGURE 13: Load-axial strain curve: G-D-F-D2 columns.

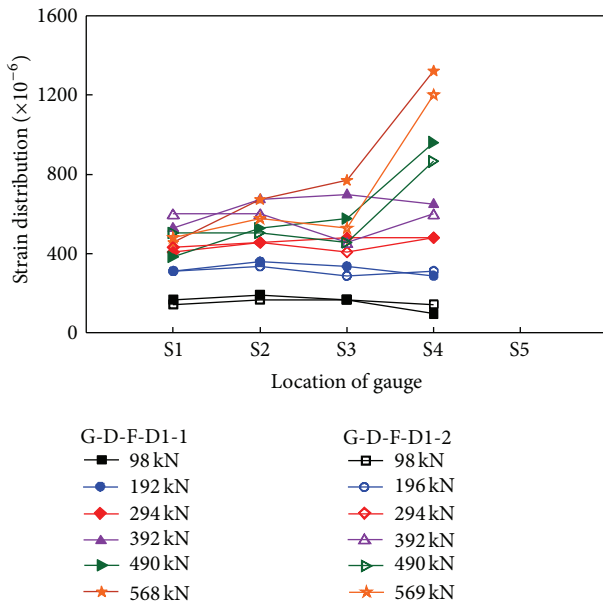


FIGURE 14: Strain distribution: G-D-F-D1 columns.

500.1 kN, the strain changed to the tensile region simultaneously with the failure of the epoxy finishing at the joint of the forms, and binding force was exhibited until the column reached the maximum load. For the column G-D-F-D1-2, as shown in Figure 12, the strain of the form changes to the tensile region at 245.2 kN. This difference between columns in the load at which the strain of the form changes to the tensile region seems to be due to work errors of the epoxy.

Figure 13 shows the results of the columns G-D-F-D2-1 and G-D-F-D2-2. It can be seen that the epoxy fiber panel form is changed from compressed condition to tensile condition at 242.2 kN and 196.1 kN, and the binding force is exhibited until the columns reach the maximum load.

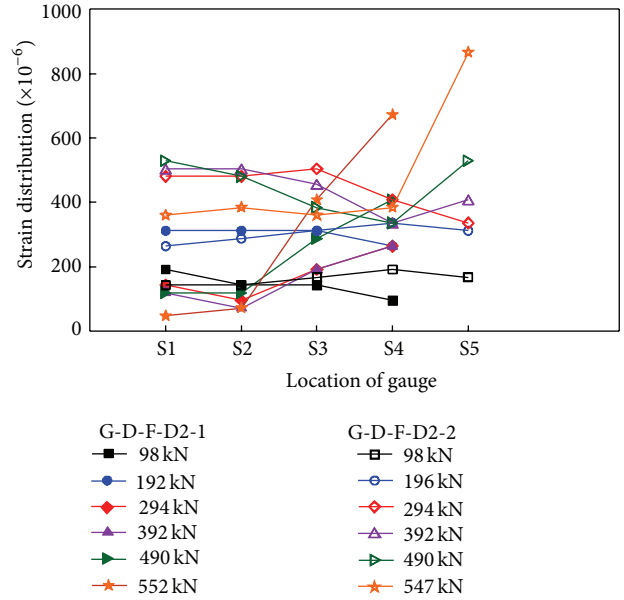


FIGURE 15: Strain distribution: G-D-F-D2 columns.

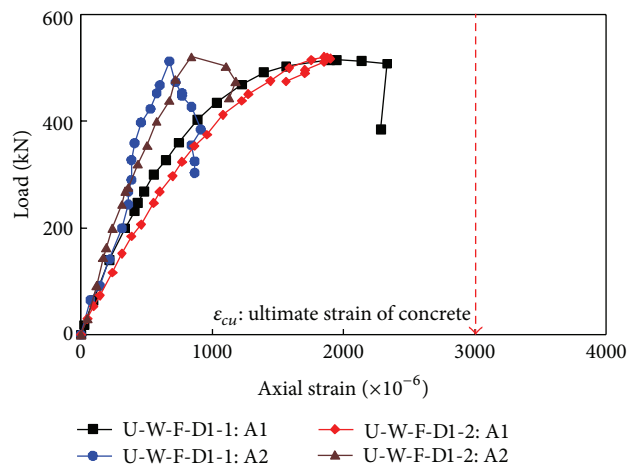


FIGURE 16: Load-axial strain curve: U-W-F-D1 columns.

As the load increases, the fiber panel form fixed to the column initially shows behaviors similar to concrete, but as the load increased further, the form binds the expanding concrete, and the axial strain of the form changes from the compressive region to the tensile region. Thus, the forms and the anchors that fix the forms exhibited binding force to the repair sections, and the maximum load increased more than that of the control columns. Furthermore, the strain of concrete also increased, and ductility increased greatly by the binding force of the forms, particularly in columns with a low degree of damage.

Figures 14 and 15 show the strains S1 to S5 by loading steps at different locations of the columns that were repaired

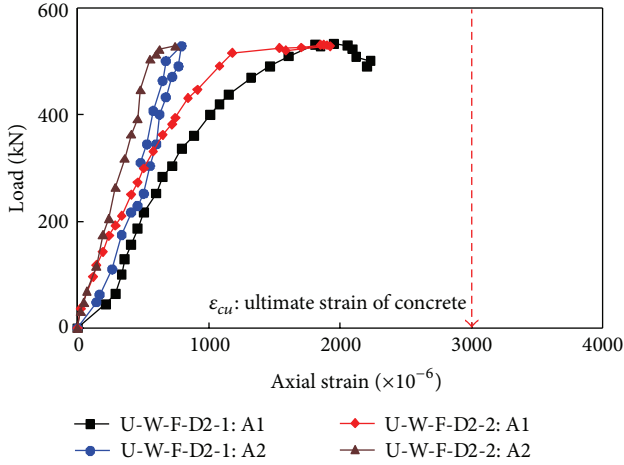


FIGURE 17: Load-axial strain curve: U-W-F-D2 columns.

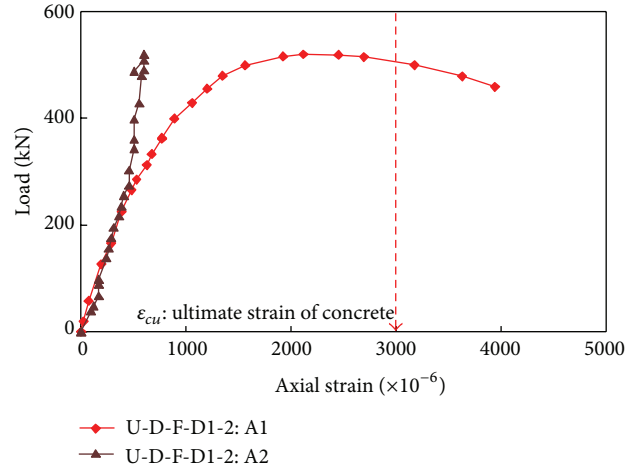


FIGURE 19: Load-axial strain curve: U-D-F-D1-2 column.

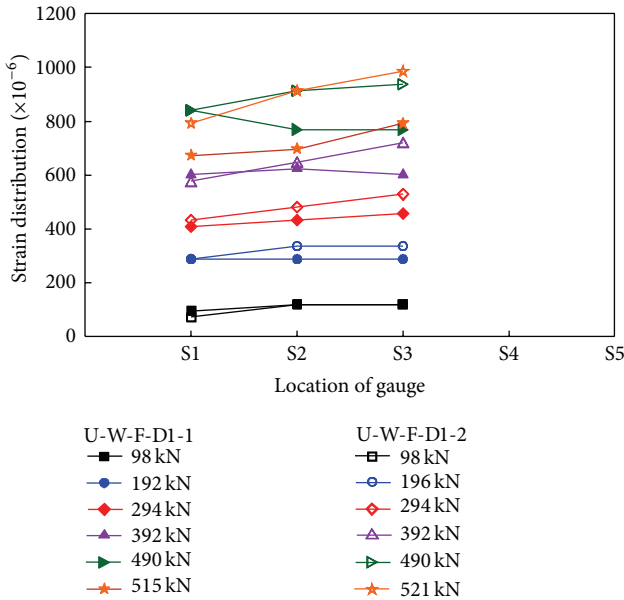


FIGURE 18: Strain distribution: U-W-F-D1 columns.

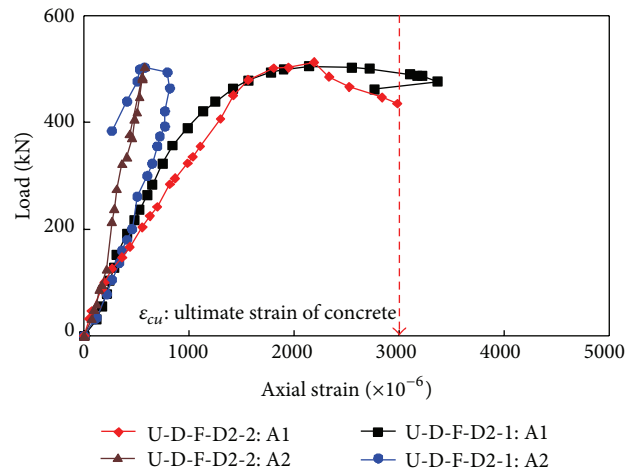


FIGURE 20: Load-axial strain curve: U-D-F-D2 columns.

using fiber panel forms on the ground. No interface failure occurred due to the increased bond strength at the interface by chipping and the binding force of the fiber panel forms and anchor bolts. However, when the load increased over 490.3 kN, the strain of concrete rapidly increased, and failure occurred at the load of 539.4 kN or higher. The reason for this result seems to be that the bond strength at the interface increased by chipping, and the binding force of the forms and anchors inhibited expansion and failure, thus improving the repair effects.

4.3.3. *U-W-F-D Series.* The loading experiment results for the columns U-W-F-D series are shown in Figures 16 and 17. The

columns failed at the maximum load of 509.9 to 529.6 kN, and the axial strain A1 at maximum load was 1850  $\mu\epsilon$  to 1899  $\mu\epsilon$ , smaller than that of the control column.

Unlike the results for the columns produced on the ground (G-D-F-D series), the strain of the epoxy fiber panel forms of the columns produced under water was measured in compressed condition until failure.

These results seem to have been caused by the special underwater working condition. In other words, for the forms to exhibit definite binding forces, the repair materials and the existing concrete sections must be completely bonded, and the load must be transmitted smoothly. However, due to the underwater working condition, the water in the forms reduced the bonding force between the repair materials and the repair sections, and interface failure developed before the forms exhibited binding force.

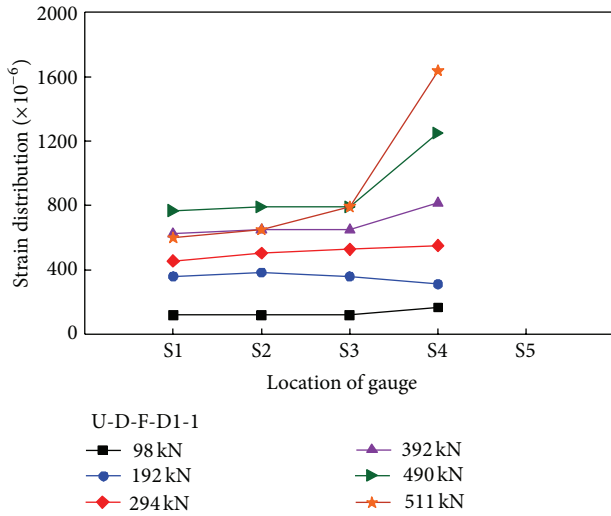


FIGURE 21: Strain distribution: U-D-F-D1-1 column.

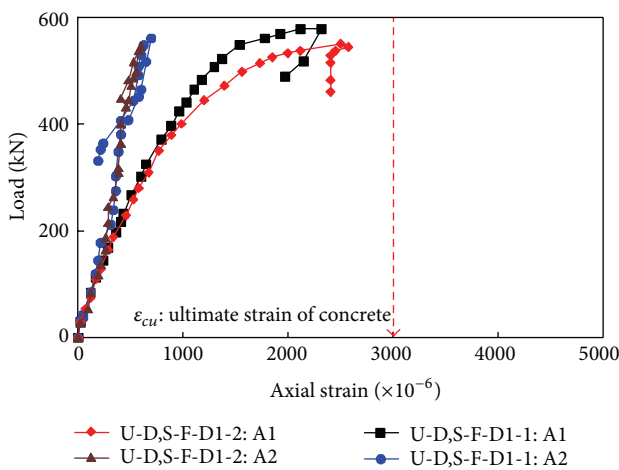


FIGURE 22: Load-axial strain curve: U-D,S-F-D1 columns.

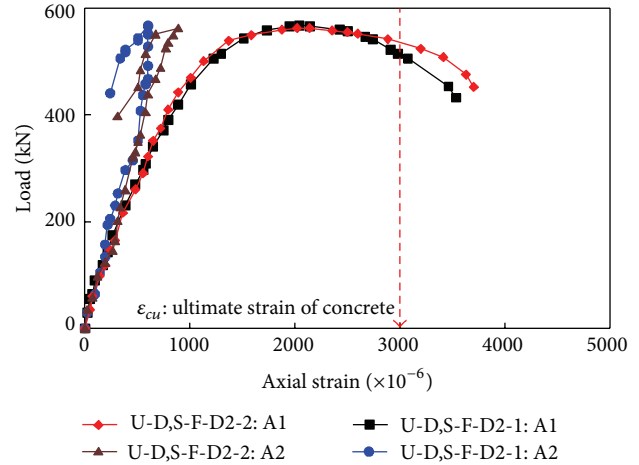


FIGURE 23: Load-axial strain curve: U-D,S-F-D2 columns.

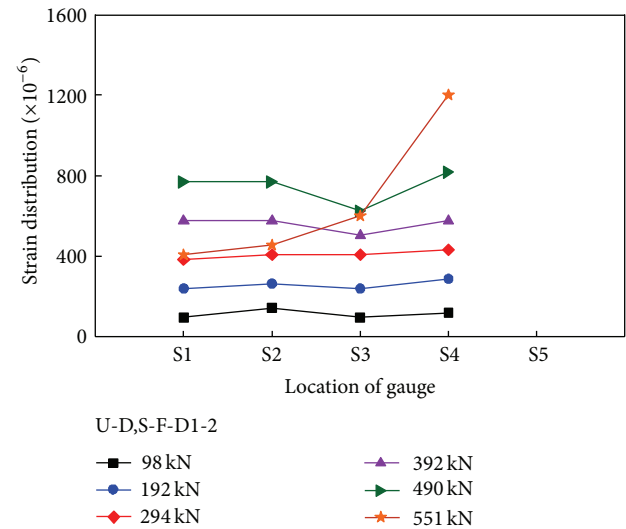


FIGURE 24: Strain distribution: U-D,S-F-D1-2 column.

Therefore, to improve the repair effects of underwater structures using forms, the water between repair sections and forms must be removed, so as to inhibit the washing and leaking of the patch repair materials.

Figure 18 shows the distribution of strains at different locations on the sides of the concrete and repair materials, for the columns U-W-F-D1. The changes of strains by increasing load at different locations were not clear, and the concrete and repair materials did not fail, either. The reason for this seems to be the occurrence of interface failure, which prevented the transmission of load to the repair sections, thus decreasing maximum load and strain.

4.3.4. *U-D-F-D Series.* The loading experiment results for the columns U-D-F-D series are shown in Figures 19 and 20. The maximum load of the repaired columns U-D-F-D series

ranged from 500.1 to 519.8 kN, which was lower by 7–9% than that of the control column. However, the strain of concrete was 2100  $\mu\epsilon$  or higher, by the binding force between forms and anchors.

Columns U-D-F-D series, which were repaired by underwater work, showed lower maximum loads, compared to the repaired columns produced by ground repair work. However, interface failure, which is important in repair works, did not happen. The reason for this seems to be that the proposed underwater repair method inhibited the interface failure between underwater repair materials and concrete, by the water removal process before injection of the underwater repair materials, and the water tightness provided by the epoxy fiber panel forms.

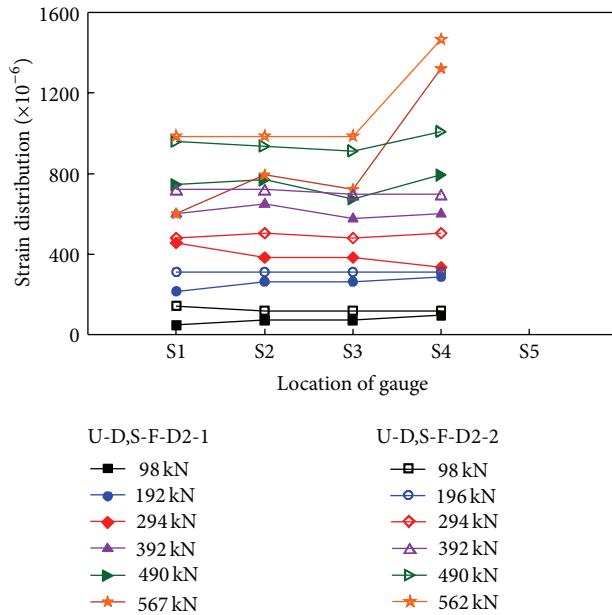


FIGURE 25: Strain distribution: U-D,S-F-D2 columns.

Figure 21 shows the strains at different locations on the sides of the underwater repair materials and concrete for the column U-D-F-D1-1. Concrete failure occurred at 509.9 kN, as strain on the concrete suddenly increased. In other words, the strains of concrete sections and repaired sections also steadily changed until failure. The reason for this seems to be that the water tightness by forms increased the bond force of the repaired sections and facilitated the smooth transmission of load. Removing the water from the forms and repair sections before injecting underwater repair materials inhibited the leaking and washing of the repair materials, thus increasing the bond force at the interface. Furthermore, the water tightness and binding force by forms were effective in underwater working conditions and increased the bonding force of the repair materials and concrete sections at the interface, thus improving repair effects.

**4.3.5. U-D,S-F-D Series.** The loading experiment results for the columns U-D,S-F-D series are shown in Figures 22 and 23. The maximum load of the columns U-D,S-F-D series was 559 kN regardless of the maximum load, which is the same strength as that of the control column.

Furthermore, for the column that did not use shear connectors, concrete suddenly failed after the maximum load, and failure occurred at the interface of concrete and underwater repair materials. However, for the columns U-D,S-F-F2-1 and U-D,S-F-F2-2, which used shear connectors, the maximum compressive strain of concrete increased to 3000  $\mu\epsilon$  or higher after the maximum load, showing a greatly improved strain capacity, and no interface failure occurred. The reason for this seems to be that the binding force of the forms and the shear connectors effectively resisted

the interface failure between concrete and repair materials, greatly improving the ductility of the members.

Figures 24 and 25 show the strains at different locations of concrete and underwater repair materials. The vertical strain steadily increased with the increasing load, and the strain of concrete sections sharply increased at failure. The reason for this result seems to be that the binding and water tightness of the forms resisted the shear force at the interface of the underwater repair materials and concrete, thus inhibiting interface failure, and the load was evenly transmitted to the concrete sections and repaired sections, but the concrete sections that were relatively weaker failed.

## 5. Conclusion

This study applied an underwater repair method to the damaged sections of underwater structures to solve problems during underwater works and conducted experiments to demonstrate the repair effects. The study arrived at the following conclusions.

- (1) The columns repaired with the proposed underwater repair method showed a maximum load that was similar to that of the control columns. This result seems to be due to the binding force of forms and anchors and the influence of the resistance of shear connectors at the interface between underwater repair materials and the existing concrete.
- (2) The proposed underwater repair method fully removes water from the forms after installation of the forms and maintains perfect water tightness by the installation of rubber packings and the epoxy finishing after the installation of forms. As a result, the underwater repair materials are injected when the repaired sections are in dry condition, so they are not subject to the washing, loss, or impact of the patch repair materials, thus increasing the bonding force of the interface and maximizing repair effects. Therefore, interface failure between patch repair materials and existing structures, which may result from a patch repair using heterogeneous materials, does not occur.
- (3) The proposed underwater repair method improved repair effects by 4%, as demonstrated by the comparison of strength between the control columns and the repaired columns, and also greatly improved ductility, as demonstrated by the comparison of strain at maximum load.

## Acknowledgment

This work was supported by the Postdoctoral Research Program of Sungkyunkwan University (2012).

## References

- [1] A. C. I. Committee 546, *Guide to Underwater Repair of Concrete*, America Concrete Institute, Colo, USA, 2006.

- [2] I. Lasa, R. Powers, and R. Kessler, "Practical application of cathodic protection systems for reinforcing steel substructures in marine environment," in *Proceedings of the International Seminar on Repair and Rehabilitation of Reinforced Concrete Structures*, pp. 16–31, Maracaibo, Venezuela, May 1997.
- [3] K. Han, S. Hong, and S. Park, "Seismic performance evaluation of retrofitted bridge by isolation bearings," *Baltic Journal of Road and Bridge Engineering*, vol. 4, no. 3, pp. 134–142, 2009.
- [4] D. Y. Cho, S. K. Park, and S. N. Hong, "Bond-slip behavior of CFRP plate-concrete interface," *Mechanics of Composite Materials*, vol. 47, no. 5, pp. 529–538, 2011.
- [5] K. B. Han, S. Hong, and S. K. Park, "RC slabs repaired and strengthened by alumina/polymer mortar and prestressing strands in the tension zone: experimental investigation under static and fatigue loadings," *Mechanics of Composite Materials*, vol. 48, no. 5, pp. 587–602, 2012.
- [6] S. Hong and S. K. Park, "Effect of prestress levels on flexural and debonding behavior of reinforced concrete beams strengthened with prestressed carbon fiber reinforced polymer plates," *Journal of Composite Materials*, 2012.
- [7] D. Cambel-Allen and H. Roper, *Concrete Structures: Material, Maintenance and Repair, Concrete Design and Construction Series*, Longman, Singapore, 1991.
- [8] J. L. Ramírez, "Ten concrete column repair methods," *Construction and Building Materials*, vol. 10, no. 3, pp. 195–202, 1996.
- [9] Departments of the Army and Air Force (Headquarters), "Repair of rigid pavements using epoxy-resin grouts, mortars, and concrete (ch 10)," TM 5-822-9/AFM 88-6, Washington, DC, USA, 1989.
- [10] G. W. Depuy, "Polymer modified concrete-properties and applications," *Construction Repair*, vol. 10, no. 2, pp. 63–67, 1996.
- [11] Y. Ohama, *Handbook of Polymer-Modified Concrete and Mortars Properties and Process Technology*, Noyes Publications, Park Ridge, NJ, USA, 1995.
- [12] UEG, "The influence of methods and materials on the durability of repairs to concrete coastal and offshore structures," UEG Publication UR 36(CIRIA/UEG), London, UK, 1986.
- [13] B. Herroelen, D. Van Gemert, and K. Broesen, "Repair and strengthening of a swimming pool roof structure using polymer concrete and CFRP laminates," in *Proceedings of the 9th ICPIC*, pp. 419–425, Bologna, Italy, 1998.
- [14] V. A. Lissenko, "Durability and structure formation of polymer composites for restoration and conservation of ancient architectural heritage," in *Proceedings of the 9 ICPIC*, pp. 699–708, Bologna, Italy, 1998.
- [15] K. S. Rebeiz, D. W. Fowler, and D. R. Paul, "Recycling plastics in polymer concrete for construction applications," *Journal of Materials in Civil Engineering*, vol. 5, no. 2, pp. 237–248, 1993.
- [16] G. Mullins, R. Sen, K. Suh, and D. Winters, "Underwater fiber-reinforced polymers repair of prestressed piles in the Allen Creek Bridge," *Journal of Composites for Construction*, vol. 9, no. 2, pp. 136–146, 2005.
- [17] J. Y. Yeom, *Underwater Concrete Repairing*, Lotte Engineering and Construction, Seoul, South Korea, 2005.
- [18] S. Bazinet, L. Cereone, and F. Worth, "Composite FRP moves into underwater repair applications," *SAMPE Journal*, vol. 39, no. 3, pp. 8–16, 2003.
- [19] S. A. Austin and P. J. Robins, "Development of patch test to study behavior of shallow concrete patch repairs," *Magazine of Concrete Research*, vol. 45, no. 164, pp. 221–229, 1993.
- [20] N. K. Emberson and G. C. Mays, "Significance of property mismatch in the patch repair of structural concrete—part 2: axially loaded reinforced concrete members," *Magazine of Concrete Research*, vol. 48, no. 1, pp. 45–57, 1996.